

# Novel Functional Polymeric Nanomaterials for Energy Harvesting Applications



Yeonsik Choi

St Edmund's College  
University of Cambridge

Supervisor: Dr. Sohini Kar-Narayan

This dissertation is submitted for the degree of  
*Doctor of Philosophy*  
August 2018



# Declaration

This dissertation is the result of my own work and includes nothing which is the outcome of work done in collaboration, except as declared in the Preface and specified in the text. It is not substantially the same as any that I have submitted, or, is being concurrently submitted for a degree or diploma or other qualification at the University of Cambridge or any other University or similar institution, except as declared in the Preface and specified in the text. I further state that no substantial part of my dissertation has already been submitted, or, is being concurrently submitted for any such degree, diploma or other qualification at the University of Cambridge or any other University or similar institution, except as declared in the Preface and specified in the text. It does not exceed the word limit of 60,000 words including abstract, tables, footnotes and appendices, but excluding table of contents, figure captions, list of figures/tables, list of abbreviations/acronyms, bibliography and acknowledgements.

Yeonsik Choi

August 2018

# Acknowledgements

All praise, honour and glory to my Lord Jesus Christ for His richest grace and mercy for the accomplishment of this thesis.

First and foremost, I wish to place on record my sincere thanks to my supervisor Sohini Kar-Narayan for her encouragement, guidance, inspiration and support throughout this project across all areas.

My sincere thanks to the current and past members of the Kar-Narayan group, in which this project was undertaken, for their contributions, collaborations and general discussions in this research area. This includes Michael Smith, Anuja Datta, Chess Boughey, Canlin Ou, Yonatan Calahorra, Qingshen Jing, Tommaso Busolo, Sung Kyun Kim, Richard A Whiter, and Abhijeet Sangle. I would also like to thank Dineo Lioma, Patrick Hutchinson, and Findlay Williams for their enthusiasm and patience whilst supervising them.

I thank James A. Elliott for his guidance on molecular simulation, Thomas D. Bennett for helpful discussion on polymer physics, Mary E. Vickers for guidance and support on X-ray diffraction analysis as well as all of the Device Materials Group for sharing facilities.

I thank the Cambridge Commonwealth, European & International Trust for my studentship funding and in addition, the Engineering and Physical Sciences Research Council Centre for Doctoral Training in Nanotechnology for additional financial support and equipment access as an associate of this programme. The Royal Society and the European Research Council is also thanked for my supervisor's grants in which I benefited in the form of facilities, consumables and stipend.

My sincere thanks to my dearest parents for their constant prayers. Finally, my deepest gratitude to my dearest wife, Ji Yoon Yun, for her patient, kindness, prayer, and love.

# Abstract

## Novel Functional Polymeric Nanomaterials for Energy Harvesting Applications

Yeonsik Choi

Polymer-based piezoelectric and triboelectric generators form the basis of well-known energy harvesting methods that are capable of transforming ambient vibrational energy into electrical energy via electrical polarization changes in a material and contact electrification, respectively. However, the low energy conversion efficiency and limited thermal stability of polymeric materials hinder practical application. While nanostructured polymers and polymer-based nanocomposites have been widely studied to overcome these limitations, the performance improvement has not been satisfactory due to limitations pertaining to long-standing problems associated with polymeric materials; such as low crystallinity of nanostructured polymers, and in the case of nanocomposites, poor dispersion and distribution of nanoparticles in the polymer matrix. In this thesis, novel functional polymeric nanomaterials, for stable and physically robust energy harvesting applications, are proposed by developing advanced nanofabrication methods. The focus is on ferroelectric polymeric nanomaterials, as this class of materials is particularly well-suited for both piezoelectric and triboelectric energy harvesting.

The thesis is broadly divided into two parts. The first part focuses on Nylon-11 nanowires grown by a template-wetting method. Nylon-11 was chosen due to its reasonably good ferroelectric properties and high thermal stability, relative to more commonly studied ferroelectric polymers such as polyvinylidene fluoride (PVDF) and polyvinylidene fluoride-trifluoroethylene (P(VDF-TrFE)). However, limitations in thin-film fabrication of Nylon-11 have led to poor control over crystallinity, and thus investigation of this material for practical applications had been mostly discontinued, and its energy harvesting potential never fully realised. The work in this thesis shows that these problems can be overcome by adopting nanoporous template-wetting as a versatile tool to grow Nylon-11 nanowires with controlled crystallinity. Since the template-

grown Nylon-11 nanowires exhibit a polarisation without any additional electrical poling process by exploiting the nanoconfinement effect, they have been directly incorporated into nanopiezoelectric generators, exhibiting high temperature stability and excellent fatigue performance. To further enhance the energy harvesting capability of Nylon-11 nanowires, a gas-flow assisted nano-template (GANT) infiltration method has been developed, whereby rapid crystallisation induced by gas-flow leads to the formation of the ferroelectric  $\delta'$ -phase. The well-defined crystallisation conditions resulting from the GANT method not only lead to self-polarization but also increases average crystallinity from 29 % to 38 %.  $\delta'$ -phase Nylon-11 nanowires introduced into a prototype triboelectric generator are shown to give rise to a six-fold increase in output power density as observed relative to the  $\delta'$ -phase film-based device. Interestingly, based on the accumulated understanding of the template-wetting method, Nylon-11, and energy harvesting devices, it was found that thermodynamically stable  $\alpha$ -phase Nylon-11 nanowires are most suitable for triboelectric energy generators, but not piezoelectric generators. Notably, definitive dipole alignment of  $\alpha$ -phase nanowires is shown to have been achieved for the first time via a novel thermally assisted nano-template infiltration (TANI) method, resulting in exceptionally strong and thermally stable spontaneous polarization, as confirmed by molecular structure simulations. The output power density of a triboelectric generator based on  $\alpha$ -phase nanowires is shown to be enhanced by 328 % compared to a  $\delta'$ -phase nanowire-based device under the same mechanical excitation.

The second part of the thesis presents recent progress on polymer-based multi-layered nanocomposites for energy harvesting applications. To solve the existing issues related to poor dispersion and distribution of nanoparticles in the polymer matrix, a dual aerosol-jet printing method has been developed and applied. As a result, outstanding dispersion and distribution. Furthermore, this method allows precise control of the various physical properties of interest, including the dielectric permittivity. The resulting nanocomposite contributes to an overall enhancement of the device capacitance, which also leads to high-performance triboelectric generators.

This thesis therefore presents advances in novel functional polymeric nanomaterials for energy harvesting applications, with improved performance and thermal stability. It further offers insight regarding the long-standing issues in the field of Nylon-11, template-wetting, and polymer-based nanocomposites.

# Contents

<b>Declaration.....</b>	<b>i</b>
<b>Acknowledgements.....</b>	<b>ii</b>
<b>Abstract.....</b>	<b>iii</b>
<b>Contents .....</b>	<b>v</b>
<b>Publications and Presentations .....</b>	<b>ix</b>
<b>List of Figures.....</b>	<b>xi</b>
<b>List of Tables .....</b>	<b>xv</b>
<b>Nomenclature.....</b>	<b>xvi</b>
<b>1 Introduction.....</b>	<b>1</b>
1.1 Issues and motivations .....	3
1.2 Thesis outline .....	4
<b>2 Background and Theory.....</b>	<b>6</b>
2.1 Piezoelectric energy harvesting.....	7
2.1.1 Fundamental principle.....	7
2.1.2 Piezoelectric materials .....	10
2.1.3 Piezoelectric energy generators.....	11
2.2 Triboelectric energy harvesting.....	13
2.2.1 Fundamental principle.....	14
2.2.2 Theoretical model.....	17
2.2.3 Strategies to improve performance .....	24
2.2.4 Perspectives and challenges .....	32
2.3 PVDF and its copolymer .....	34

2.3.1	PVDF .....	35
2.3.2	P(VDF-TrFE) .....	36
2.3.3	Confronting issues .....	37
2.4	Nylon-11 .....	38
2.4.1	Structures of Nylon-11 .....	39
2.4.2	Post-treatment techniques .....	44
2.4.3	Perspectives and challenges .....	47
2.5	Polymer-based nanocomposite .....	48
2.5.1	Dispersion and distribution issue .....	48
2.5.2	Multi-layered nanocomposite .....	50
2.6	Template-wetting method .....	51
2.6.1	Background .....	51
2.6.2	Comparison: polymer nano-structuring methods .....	52
2.6.3	Fundamental principles .....	54
2.6.4	Properties of template-grown polymer nanostructures .....	56
2.6.5	Conclusion .....	59
<b>3</b>	<b>Experimental and Computational Methods .....</b>	<b>61</b>
3.1	Fabrication .....	61
3.1.1	Conventional film preparation method .....	61
3.1.2	Nanostructured polymer fabrication method .....	64
3.1.3	Aerosol-jet printing .....	69
3.2	Characterization .....	78
3.2.1	Polymer characterisation .....	78
3.2.2	Scanning probe microscopy characterisation .....	83
3.2.3	Electrical property characterization .....	91
3.2.4	Modelling .....	93

<b>4</b>	<b>Nano-Piezoelectric Generator based on Nylon-11 Nanowires Grown by Template-Wetting Method.....</b>	<b>97</b>
4.1	Growth mechanism of Nylon-11 nanowire.....	98
4.2	Crystal structure of Nylon-11 nanowires grown by template-wetting.....	103
4.3	Thermal behaviour of Nylon-11 nanowires.....	105
4.4	Nanowire-based nano-piezoelectric generator.....	107
4.5	Conclusions.....	112
<b>5</b>	<b><math>\delta'</math>-phase Nylon-11 Nanowires Fabricated by Gas-Assisted Nano-Template Infiltration (GANT) method for Triboelectric Generators.....</b>	<b>113</b>
5.1	Nylon-11 for triboelectric generators.....	114
5.2	Gas-flow assisted crystal structure control.....	117
5.3	Self-poled $\delta'$ -phase nanowires through GANT method.....	122
5.4	Nanowire-based triboelectric generators.....	124
5.5	Conclusions.....	134
<b>6</b>	<b><math>\alpha</math>-phase Nylon-11 Nanowires Fabricated by Thermally-Assisted Nano-Template Infiltration (TANI) Method for Triboelectric Generators.....</b>	<b>135</b>
6.1	Ideal remanent polarization calculation.....	136
6.2	Thermally-assisted crystal structure control.....	139
6.3	Spontaneous polarization in $\alpha$ -phase nanowires.....	146
6.4	Nanowire-based triboelectric generators.....	150
6.5	Conclusions.....	152
<b>7</b>	<b>Phase Tunable Nanoconfined Polymer Crystallisation Method for Nylon-11 Nanowires : A Comparative Study.....</b>	<b>154</b>
7.1	Nanowire growth mechanism.....	155
7.1.1	Evaporation-driven crystallisation.....	155
7.1.2	Capillary-infiltration.....	160

7.1.3	Processing parameters for crystallisation in the nanopores.....	162
7.1.4	Three different methods to control the crystal structure of Nylon-11 nanowires .....	168
7.2	Thermal behaviour .....	174
7.2.1	DSC analysis .....	174
7.2.2	X-ray diffractograms .....	178
7.3	Electromechanical characteristics .....	180
7.3.1	Mechanical stiffness of Nylon-11 single nanowire.....	180
7.3.2	Piezoelectric response of nanowire arrays .....	184
7.4	Conclusions.....	187
<b>8</b>	<b>Multi-layered Nanocomposites by Dual Aerosol-Jet Printing Method for Energy Applications .....</b>	<b>188</b>
8.1	Route to nanocomposites with ideal dispersion .....	189
8.2	Nanoparticle dispersion in aerosol-jet printed nanocomposite .....	190
8.3	Dielectric properties of multi-layered nanocomposite .....	196
8.4	Multi-layered nanocomposite-based triboelectric generator.....	199
8.5	Conclusions.....	200
<b>9</b>	<b>Conclusions and Future Work.....</b>	<b>202</b>
	<b>Appendix A .....</b>	<b>207</b>
	<b>Appendix B .....</b>	<b>212</b>
	<b>Bibliography .....</b>	<b>221</b>

# Publications and Presentations

## Publications

1. **Choi, Y. S.**; Kim, S. W.; Kar-Narayan S. “Advanced Materials for High-Performance Triboelectric Energy Harvesting Devices,” *In Preparation*.
2. **Choi, Y. S.**; Williams, F.; Kim, S. K.; Elliot, J. A.; Kar-Narayan S. “Unprecedented Spontaneous Self-Polarization of Non-Ferroelectric  $\alpha$ -Phase Nylon-11 for Energy Harvesting Applications,” *In Preparation*.
3. Jing, Q.; **Choi, Y.S**; Smith, M.; Ou, C.; Kar-Narayan S. “Aerosol Jet Printed Freestanding Conductive Structures for Stretchable Electronics and Sensing Applications,” *Submitted*.
4. Jing, Q.; **Choi, Y.S**; Smith, M.; Catic, N.; Ou, C.; Kar-Narayan S. “Aerosol Jet Printed Triboelectric Sensors with Fine Structures for Motion Sensing,” *Advanced Materials Technologies* **2018**, *Accepted*.
5. **Choi, Y. S.**; Kim, S. K.; Williams, F.; Calahorra, Y.; Elliot, J. A.; Kar-Narayan S. “The Effect of Crystal Structure on the Electromechanical Properties of Piezoelectric Nylon-11 Nanowires,” *Chemical Communications* **2018**, *54*, 5863.
6. **Choi, Y. S.**; Jing, Q.; Datta, A.; Boughey, C.; Kar-Narayan S. “A Triboelectric Generator Based on Self-poled Nylon-11 Nanowires Fabricated by Gas-flow Assisted Template Wetting,” *Energy and Environmental Science* **2017**, *10*, 2180.
7. Datta, A.; **Choi, Y. S.**; Chalmers, E.; Ou, C.; Kar-Narayan S. “Piezoelectric Nylon-11 Nanowire Arrays Grown by Template Wetting for Vibrational Energy Harvesting Applications,” *Advanced Functional Materials* **2017**, *27*, 1604262.
8. Smith, M.; **Choi, Y. S.**; Boughey, C.; Kar-Narayan S. “Controlling and Assessing the Quality of Aerosol Jet Printed Features for Large Area and Flexible Electronics,” *Flexible and Printed Electronics* **2017**, *2*, 015004.
9. Wang, T.; Farajollahi, M.; **Choi, Y. S.**; Lin, I.; Marshall, J. E.; Thompson, N. M.; Kar-Narayan S.; Madden, J. D. W.; Smoukov, S. K. “Electroactive Polymers for Sensing,” *Interface Focus* **2016**, *20160026*.

## Patent applications

1. Kar-Narayan, S.; **Choi, Y. S.** “Triboelectric generator, method for manufacture thereof and elements thereof” **2017**, International Patent Appl. No. PCT/EP2017/072742.
2. Kar-Narayan, S.; **Choi, Y. S.** “Triboelectric generator, method for manufacture thereof and elements thereof” **2017**, International Patent Appl. No. PCT/EP2017/068810.

## Oral presentations

1. “Printed Polymer Nanocomposites with High Uniformity for Triboelectric Nanogenerators,” International Conference on Nanogenerators and Piezotronics, Seoul, S. Korea, May **2018**.
2. “Highly-Uniform and Well-Dispersed Polymer Nanocomposites for Energy Harvesting Application,” 2018 Materials Research Society (MRS) Spring Meeting, Phoenix, USA, Apr **2018**.
3. “Nanoconfined  $\gamma$ -Phase Ferroelectric Nylon Nanowire for Energy Harvesting Devices,” 2017 Materials Research Society (MRS) Spring Meeting, Phoenix, USA, Apr **2017**. (**Best Graduate Student Presentation Award**).
4. “Device using Static Electricity,” Maxwell Centre Annual Research Showcase, Cambridge, UK, Mar **2017**.
5. “Nano-confined Ferroelectric Polymer Nanowires for Triboelectric Nanogenerators,” International Conference on Nanogenerators and Piezotronics, Rome, Italy, Jun **2016**.

## Poster presentations

1. “Advanced Printing Technique for Polymer Nanocomposites,” Innovations in Large-Area Electronics Conference (innoLAE 2018), Cambridge, UK, Jan **2018**. (**Best Poster Award**).
2. “Nanogenerators for Energy Harvesting” Nanoshowcase 2017, Cambridge, UK, Nov **2017**.
3. “Self-poled Nylon-11 Nanowires for Triboelectric Energy Harvesting Devices,” Armourers and Brasiers' Cambridge Forum, Cambridge, UK, Jun **2017**.
4. “Nano-confined Ferroelectric Polymer Nanowires for Triboelectric Nanogenerators,” Ministry of Defence Poster Session, Cambridge, UK, May **2017**.
5. “Design Rules for the Multi-layered and Multi-grated Free-standing Triboelectric Nanogenerator,” Innovations in Large-Area Electronics Conference (innoLAE 2017), Cambridge, UK, Feb **2017**.

# List of Figures

Fig. 2-1 Schematic representation of the piezoelectric effect .....	7
Fig. 2-2 Configuration of piezoelectric energy generators.....	12
Fig. 2-3 Prototype polymer-based piezoelectric generator.....	13
Fig. 2-4 Four fundamental working modes of the triboelectric generators .....	16
Fig. 2-5 Schematics of the contact-separation mode triboelectric generators with two different assumptions.....	21
Fig. 2-6 Theoretical relationship between short-circuit transferred charge and thickness .....	23
Fig. 2-7 Various strategies to improve the performance of triboelectric generators.....	26
Fig. 2-8 Schematic drawing of molecular structure of $\beta$ -phase PVDF .....	35
Fig. 2-9 Schematic drawing of molecular structure of P(VDF-TrFE). .....	37
Fig. 2-10 Schematics of molecular chain structure of Nylon.....	39
Fig. 2-11 Schematics of conventional synthesis techniques of polymer nanocomposite.....	49
Fig. 2-12 Schematic of dispersion and distribution of nanoparticles in polymer matrix .....	50
Fig. 2-13 Schematics of polymer nanostructure synthesis techniques .....	52
Fig. 2-14 Schematic of partially wetting of liquid droplet on the solid substrate. ....	54
Fig. 3-1 Reference Nylon-11 films with $\alpha$ -, $\alpha'$ -, and $\delta'$ -phase.....	63
Fig. 3-2 SEM image of $\alpha$ -phase Nylon-11 film .....	64
Fig. 3-3 Morphology of AAO template .....	65
Fig. 3-4 Image analysis for effective surface area of AAO template calculation .....	65
Fig. 3-5 XRD patterns of melt-pressed Nylon-11 nanostructures.....	66
Fig. 3-6 SEM images of Nylon-11 nanostructures fabricated by the melt-infiltration method...	67
Fig. 3-7 Schematics of Nylon-11 nanowire growth mechanisms.....	68
Fig. 3-8 Schematic of the aerosol-jet process.....	71
Fig. 3-9 Schematic of ultrasonic atomization mechanism .....	72
Fig. 3-10 Schematics of pneumatic atomisation mechanism. ....	73
Fig. 3-11 Schematic of the aerosol flow profile at the printer nozzle .....	74

Fig. 3-12 The influence of two gas-flows on printed-line morphology.....	77
Fig. 3-13 Background XRD patterns.....	79
Fig. 3-14 X-ray diffraction mechanism in Bragg-Brentano geometry.....	80
Fig. 3-15 Schematics for the operational mechanisms of Kelvin probe force microscopy.....	84
Fig. 3-16 KPFM characteristics Au sample.....	86
Fig. 3-17 Schematic for the operational mechanisms of piezoresponse force microscopy.....	87
Fig. 3-18 PFM characteristics of calibration sample (LiNbO <sub>3</sub> ).....	88
Fig. 3-19 Operation mechanism of quantitative nanomechanical property mapping.....	89
Fig. 3-20 QNM characteristics of calibration sample (PS).....	91
Fig. 3-21 Schematic diagram and photograph of energy harvesting setup.....	93
Fig. 3-22 The symmetry geometry used in the simulation.....	94
Fig. 4-1 Schematic of the growth mechanism of Nylon-11 nanowires by capillary infiltration within AAO template.....	98
Fig. 4-2 Cross-section SEM images of Nylon-11 filed AAO template.....	99
Fig. 4-3 Effect of concentration on the microstructure of Nylon-11 nanowires.....	101
Fig. 4-4 SEM images of nanowires and nanowire mat.....	102
Fig. 4-5 XRD patterns of Nylon-11 nanowires.....	103
Fig. 4-6 Room temperature FT-IR spectra of Nylon-11 nanowires.....	104
Fig. 4-7 DSC thermograms of nanowires before and after template dissolution in comparison with parent pellets and film.....	106
Fig. 4-8 Nylon-11 nanowire-based nano-piezoelectric generator.....	108
Fig. 4-9 Electrical output with various input signals.....	109
Fig. 4-10 The change of power according to the time under 10M $\Omega$ load resistance.....	109
Fig. 4-11 High-temperature operation of Nylon-11 nanowire-based piezoelectric device.....	111
Fig. 4-12 Fatigue test results of nano-piezoelectric device.....	112
Fig. 5-1 Triboelectric series of common materials.....	115
Fig. 5-2 Nylon-11 nanowires fabricated by GANT method.....	116
Fig. 5-3 Cross-section SEM image of a nanowire-filled AAO template.....	117
Fig. 5-4 XRD patterns of Nylon-11 nanowires fabricated by GANT method.....	119
Fig. 5-5 Numerical simulation results of turbulence flow generated by assisted gas-flow.....	121

Fig. 5-6 Schematic of the polymer crystallisation process in the nano-dimensional pore of the GANT infiltration method .....	121
Fig. 5-7 FT-IR absorbance spectra of $\delta'$ -phase nanowires and additionally stretched film .....	122
Fig. 5-8 KPFM analysis of $\delta'$ -phase nanowires and film .....	123
Fig. 5-9 Schematic of the structure of triboelectric generator .....	124
Fig. 5-10 Electrical output of GANT fabricated nanowire-based triboelectric device .....	125
Fig. 5-11 Electrical output of the device with load resistors .....	125
Fig. 5-12 Electrical output of the device under various input conditions .....	126
Fig. 5-13 Reliability test of the triboelectric device .....	127
Fig. 5-14 Template-freed nanowire-based triboelectric generators .....	128
Fig. 5-15 Charge accumulation trend of the nanowire-based device with respect to time.....	129
Fig. 5-16 LED lightning test for $\delta'$ -phase nanowire-based triboelectric generators.....	130
Fig. 5-17 Calculated electric potential distribution at different surface charge density .....	132
Fig. 5-18 The short circuit current of various triboelectric generators.....	133
Fig. 6-1 Molecular structure and chain packing of Nylon-11 .....	138
Fig. 6-2 Morphology of nano-template and resulting polymer nanowires.....	139
Fig. 6-3 XRD patterns of nanowires crystallised at various temperatures .....	141
Fig. 6-4 Comparison of XRD patterns of $\alpha$ -phase film and nanowires.....	143
Fig. 6-5 FT-IR absorbance spectra of $\alpha$ -phase template-freed nanowires and film .....	143
Fig. 6-6 Comparison of calculated and experimentally achieved XRD patterns .....	145
Fig. 6-7 KPFM analysis of film and nanowires .....	146
Fig. 6-8 Comparison of XRD patterns before and after thermal annealing .....	148
Fig. 6-9 Charge accumulation capability of $\alpha$ -phase, $\delta'$ -phase nanowires, and $\alpha$ -phase film ..	149
Fig. 6-10 Triboelectric generator device performance.....	151
Fig. 6-11 Electrical output of the device under various input condition .....	152
Fig. 7-1 Temperature variation according to time in temperature- and evaporation-driven crystallisation method.....	156
Fig. 7-2 XRD patterns of Nylon-11 films fabricated by temperature-driven and evaporation-driven methods.....	156
Fig. 7-3 XRD patterns of Nylon-11 films fabricated by evaporation-driven crystallisation.....	159
Fig. 7-4 Schematics of two different template-wetting methods .....	161

Fig. 7-5 Schematic for evaporation-driven crystallisation .....	162
Fig. 7-6 Characteristics of reference Nylon-11 nanowires.....	165
Fig. 7-7 Changes in XRD patterns with different processing conditions.....	166
Fig. 7-8 Schematics of Nylon-11 nanowire growth mechanisms.....	169
Fig. 7-9 XRD patterns of Nylon-11 nanowires without and within AAO template.....	171
Fig. 7-10 XRD peak analysis of Nylon-11 nanowires with different crystal structures. ....	173
Fig. 7-11 DSC thermograms (heating) for Nylon-11 films and nanowires.....	175
Fig. 7-12 DSC thermograms (cooling) for Nylon-11 films and nanowires .....	177
Fig. 7-13 Comparison of XRD patterns of nanowires before and after thermal annealing.....	179
Fig. 7-14 QNM characteristics of various nanowire phases.....	180
Fig. 7-15 Average DMT modulus of $\alpha$ -phase, $\delta'$ -phase and conventional nanowires .....	181
Fig. 7-16 Numerical simulation results of nano-indentation.....	182
Fig. 7-17 QNM characteristics of $\alpha$ -phase Nylon-11 film .....	183
Fig. 7-18 QNM characteristics of $\alpha$ -phase Nylon-11 nanowire and film.....	183
Fig. 7-19 Piezoelectric response amplitude of $\alpha$ -, $\delta'$ -phase, and reference nanowires.....	185
Fig. 7-20 PFM characteristics of AAO template filled with $\delta'$ -phase nanowires.....	185
Fig. 7-21 PFM characteristics of AAO template filled with $\alpha$ -phase nanowires .....	186
Fig. 7-22 PFM characteristics of AAO template filled with reference nanowires .....	186
Fig. 8-1 Schematic of Y-shape connector for aerosol-jet printed nanocomposite. ....	190
Fig. 8-2 XRD patterns of aerosol printed PI/Ag NPs nanocomposite.....	191
Fig. 8-3 Microstructure of aerosol printed PI/Ag NPs nanocomposite .....	192
Fig. 8-4 SEM image analysis data for the calculation of degree of dispersion .....	193
Fig. 8-5 XRD patterns of aerosol-jet printed P(VDF-TrFE)/Ag NPs nanocomposite. ....	194
Fig. 8-6 SEM images of aerosol-jet printed P(VDF-TrFE)/Ag NPs nanocomposite.....	195
Fig. 8-7 SEM images of aerosol-jet printed film-typed nanocomposite .....	196
Fig. 8-8 Room temperature dielectric properties of nanocomposite .....	198
Fig. 8-9 Design and properties of multi-layered nanocomposite .....	199
Fig. 8-10 Aerosol-jet printed nanocomposite-based triboelectric generators.....	200

# List of Tables

Table 2-1 Triboelectric series.....	15
Table 2-2 Property comparison of ferroelectric polymers: PVDF and P(VDF-TrFE).....	37
Table 2-3 Various crystal structures of Nylon-11 .....	42
Table 2-4 Proposed unit cell parameters of Nylon-11 .....	43
Table 2-5 Advantages and disadvantages of nanostructured-polymer synthesis techniques .....	53
Table 3-1 Summary of processing parameters and affecting factors .....	76
Table 3-2 Region, assignments and peak positions of the infrared bands of Nylon-11 .....	82
Table 3-3 A comparison between the unit cell parameters .....	95
Table 5-1 Dimensions of the triboelectric generator .....	133
Table 7-1 Four processing conditions for evaporation driven crystallisation. ....	158
Table 7-2 Indices of crystallographic planes of Nylon-11 films fabricated by different processing conditions of evaporation-driven crystallisation methods .....	159
Table 7-3 Optimum processing conditions for each method.....	168
Table 7-4 Summary of XRD peak analysis.....	173
Table 7-5 The $T_m$ , $T_c$ , and $\chi$ of various phases of Nylon-11 films and nanowires.....	177
Table 8-1 Setting values of sheath, pneumatic atomizer, and ultrasonic atomizer gas-flow rate for nanocomposite printing.....	191

# Nomenclature

## Greek Symbols

$\alpha, \alpha', \beta, \gamma, \gamma', \delta, \delta'$	Crystalline phases
$\gamma$	Surface tension
$\varepsilon$	Permittivity
$\varepsilon'$	Dielectric constant
$\varepsilon_0$	Vacuum permittivity
$\varepsilon_r$	Relative permittivity
$\eta_S$	Figure of merit normalized by applied squared strain
$\eta_T$	Figure of merit normalized by applied squared stress
$\theta$	Incident beam angle in X-ray diffraction
$\theta_c$	Contact angle
$\lambda$	Wavelength
$\mu$	Viscosity / Mobility
$\rho$	Concentration of solution
$\sigma$	Charge density
$\Phi$	Work function
$\varphi_f$	Volume fraction
$\chi$	Degree of crystallinity
$\chi'$	Device efficiency
$\omega$	Oscillation / Angular (or natural) frequency

## Subscripts

hkl	Crystallographic axis
i	Direction of the induced electric field (polarization) / Direction of the applied voltage
j	Direction of the applied stress / Direction of the induced strain

## Other Symbols

$A$	Device area
$C$	Capacitance
$D$	Electric displacement
$d$	Piezoelectric strain (or charge) constant / Thickness / Crystal size / Diameter
$d_{ij}$	Piezoelectric strain (or charge) coefficient
$D_p$	Crystallite size
$E$	Electric field / modulus
$E_s$	Young's modulus
$E_c$	Coercive field
$E_F$	Fermi energy level
$F$	Force
$f$	Frequency
$F_{el}$	Electrostatic force
$g$	Piezoelectric voltage constant / Gravity
$g_{ij}$	Piezoelectric voltage coefficient
$H$	Enthalpy
$h$	Height
$H_{vap}$	Heat of vaporisation
$I$	Current
$i$	Number of layer
$I_{SC}$	Short-circuit current
$J_{SC}$	Short-circuit current density
$k$	Relative dielectric constant
$k_e$	Coulomb's constant
$L$	Device thickness / length
$M_w$	Molecular weight
$n$	Integer / Number of X-ray diffraction peaks
$P$	Polarization
$p$	Pressure
$P_r$	Remanent polarization

$Q$	Electric charge / Transferred charge
$q$	Transferred charge / Scattering vector
$Q_a$	Aerosol-jet flow rate
$Q_s$	Sheath gas flow rate
$Q_{sc}$	Short-circuit transferred charge
$R$	Resistance
$r$	Radius
$Re$	Reynolds number
$S$	Strain / Surface area / Spreading factor
$s$	Elastic compliance
$R$	Radius
$r$	Distance
$T$	Applied stress / Period of one cycle
$t$	Time
$T_c$	Curie temperature / Crystallisation temperature
$T_g$	Glass transition temperature
$T_m$	Melting temperature
$U$	Energy
$V$	Voltage
$\nu$	Poisson's ratio
$V_E$	Electrostatic potential
$V_{OC}$	Open-circuit voltage
$Y$	Young's modulus
$x$	Displacement / Thickness of layer
$z$	Height / Separation
$z_h$	Lift scan height

### **Acronyms / Abbreviations**

1D	One-Dimensional
2D	Two-Dimensional
3D	Three-Dimensional
AAO	Anodic Aluminium Oxide

AC	Alternating Current
add.	additional
AFM	Atomic Force Microscope
Al	Aluminium
APTES	3-Aminopropyltriethoxysilane
Ag	Silver
AJP	Aerosol-Jet Printing
Au	Gold
BTO	Barium Titanate (BaTiO <sub>3</sub> )
C	Carbon
CNT	Carbon Nanotube
COMPAS	Condensed-phase Optimised Molecular Potentials for Atomistic Simulation
CPD	Contact Potential Difference
Cu	Copper
dep-	deposition
DC	Direct Current
DI	De-Ionised
DMF	Dimethylformamide
DMT	Derjaguin–Muller–Toporov
DSC	Differential Scanning Calorimetry
Eq.	Equation
EXP	Extrusion-based Printing
F	Fluorine
FEM	Finite Element Method
FEP	Fluorinated Ethylene Propylene
Fig.	Figure
FOM	Figure-of-Merit
FOTS	Trichloro(1H,1H,2H,2H- perfluorooctyl) Silane
FR	Focus Ratio
FT-IR	Fourier Transform Infrared
FWHM	Full Width at Half-Maximum

GANT	Gas-flow Assisted Nano-Template infiltration
GO	Graphene Oxide
GPTES	3-Glyci-doxypropyltriethoxysilane
H	Hydrogen
high- <i>k</i>	High dielectric constant
HT	High Temperature
IJP	Inkjet Printing
ITO	Indium Tin Oxide ( $\text{In}_2\text{O}_3 \cdot (\text{SnO}_2)_x$ )
KPFM	Kelvin Probe Force Microscopy
LED	Light-Emitting Diode
LiNbO <sub>3</sub>	Lithium Niobate
MoS <sub>2</sub>	Molybdenum Disulfide
N	Nitrogen
NMP	N-Methyl-2-Pyrrolidone
NP	Nanoparticle
NT	Nanotube
NW	Nanowire
Nylon	Polyamide
OH	Hydroxide
O	Oxygen
PA	Pneumatic Atomizer
PAA	Polyamic Acid
PC	Polycarbonate
PDMS	Polydimethylsiloxane
Pd	Palladium
PEDOT:PSS	Poly(3,4-ethylenedioxythiophene) Polystyrene Sulfonate
PET	Polyethylene Terephthalate
PFM	Piezoresponse Force Microscopy
PI	Polyimide
PMMA	Poly(methyl methacrylate)
PS	Polystyrene
PSPD	Position Sensitive Photodetector

Pt	Platinum
PtBA	Poly(tert-butyl acrylate)
PTFE	Polytetrafluoroethylene
PTrFE	Poly(trifluoroethylene)
PVA	Polyvinyl Alcohol
PVDF	Polyvinylidene Fluoride
P(VDF-TrFE)	Polyvinylidene Fluoride-trifluoroethylene
PZT	Lead Zirconium Titanate ( $\text{PbZr}_x\text{Ti}_{1-x}\text{O}_3$ )
QNM	Quantitative Nanomechanical Mapping
rGO	reduced Graphene Oxide
RMS	Root Mean Square
rpm	Revolutions Per Minute
RT	Room Temperature
SAM	Self-Assembled Monolayer
SEM	Scanning Electron Microscopy
Si	Silicon
SiO <sub>2</sub>	Silicon Dioxide
SPM	Scanning Probe Microscopy
sPS	syndiotactic Polystyrene
TANI	Thermally-Assisted Nano-template Infiltration
TEG	Triethylene Glycol
TFA	Trifluoroacetic Acid
TFPS	Trichloro(3,3,3-trifluoropropyl) Silane
TiO <sub>x</sub>	Titanium Oxide
TrFE	Trifluoroethylene
UA	Ultrasonic Atomizer
w/o	without
wt %	Weight percent
XRD	X-Ray Diffraction



# Chapter 1

## Introduction

The rapidly growing demand for energy solutions for portable and wearable electronic devices and wireless sensor applications has prompted great interest towards environment-friendly energy harvesting devices. Among various alternative energy sources, scavenging mechanical energy from vibrations and frictional motion has attracted worldwide attention as these are easily available from ambient sources, regardless of time and environmental condition. Piezoelectric and triboelectric generators are well-known energy harvesting methods which are able to transform such vibrational and friction energy into electrical energy, using electrical polarization in a material and contact electrification, respectively.

In order to realise piezoelectric and triboelectric generators, materials selection is crucial since materials determine not only the performance of the device but also the range of application. In the field of piezoelectric generators, research has been focused on inorganic materials due to their high energy conversion efficiency. However, as a result of harsh processing conditions, toxicity, and increasing needs for mechanical flexibility, polymeric materials with piezoelectric properties have been proposed as substitutes. Furthermore, in the case of triboelectric generators, common polymers show better device performance than inorganic materials. However, in general, the low energy conversion

efficiency and thermal stability of polymer-based energy harvesting devices are still insufficient for introduction into practical applications.

Possible approaches to enhance the requisite properties of polymeric materials are through nanoconfinement and also by considering polymer-based nanocomposites. Nanoconfinement methods, such as nanoporous template-wetting, serve to enhance molecular ordering in nanostructures, hence it has been widely investigated as a means to improve the piezoelectric performance of polymers. The formation of polymer nanocomposites, in which functional and high-performance nanoparticles embedded within a polymer matrix, also allows for tuning of dielectric properties, which are required for triboelectric performance. However, the performance improvement to date has not been satisfactory due to limitations pertaining to long-standing problems associated with polymeric materials, such as low crystallinity of nanostructured polymers, and in the case of nanocomposites, poor dispersion and distribution of nanoparticles in the polymer matrix.

In this thesis, to overcome such limitations, novel functional polymeric nanomaterials with stable and robust energy harvesting performance are proposed by developing advanced nano-fabrication techniques. We showcase the literature regarding vibration-based energy harvesting mechanisms, possible energy harvesting materials, and nano-fabrication techniques. Based on the issue therein, solutions for high-performance energy harvesting devices are then suggested with detailed fabrication and characterization methods. The experimental results and discussions sections are broadly divided into the following parts: (i) growth of Nylon-11 nanowires by the template-wetting method; and (ii) dual aerosol-jet printed multi-layered nanocomposites. The conclusions of this thesis and possible future work are summarised at the end.

<b>Category</b>	<b>Part</b>	<b>Chapter</b>
Literature review	- Energy harvesting mechanisms	2.1, 2.2
	- Energy harvesting materials	2.3 ~ 2.5
	- Nano-fabrication techniques	2.6
Methods	Fabrication and characterization	3
Results and discussions	- Growth of Nylon-11 nanowires by template-wetting method	4 ~ 7
	- Aerosol-jet printed multi-layered nanocomposite	8
Conclusions	Conclusions and future work	9

## 1.1 Issues and motivations

The material-related issues in the field of piezoelectric and triboelectric energy harvesting devices can be summarised as follows:

1. Development of thermally stable piezoelectric polymers.
2. Developing tribo-positive (i.e. charge donating) materials.
3. Investigating materials with high-intensity spontaneous polarization.
4. Solving the issue of high-voltage poling process for spontaneous polarization.
5. Developing polymer-based nanocomposites.
6. Investigating the multi-layered structure for triboelectric devices.

### 1) Nylon-11 nanowires fabricated by template-wetting method

Nylon-11 can circumvent issue No. 1 ~ 3 because, as an exceptional synthetic material among tribo-positive materials, Nylon-11 has much higher thermal stability and compatible ferroelectric properties compared to polyvinylidene fluoride (PVDF) and polyvinylidene fluoride-trifluoroethylene (P(VDF-TrFE)). Furthermore, template-wetting method enables self-polarization of ferroelectric Nylon-11 via preferential crystal orientation without high-voltage poling process (issue No. 4). However, the harsh processing conditions and metastable property of ferroelectric Nylon-11 are long-standing problems. Furthermore, conventional template-wetting method also has serious issues regarding low crystallinity of resulting nanowires and limited available crystal structures. Above all, alternative synthesis methods for Nylon-11 nanowires have rarely been attempted, and the understanding of their piezoelectric and triboelectric properties of Nylon-11 nanowires has been yet to be reported.

Therefore, this thesis aims to develop Nylon-11 nanowires for piezoelectric and triboelectric energy harvesting applications (Chapter 4 ~ 7). It demonstrates the conventional template-wetting method as a versatile tool to grow Nylon-11 nanowires and suggests two different novel and scalable nano-template infiltration methods for Nylon-11 nanowires with enhanced crystallinity and control of the crystal phase. This also provides various characterization routes to measure their properties at bulk and single nanowire scale.

Detailed Nylon-11 crystallisation mechanisms in the nanostructure are also studied and resulting nanowires are compared, where the aim is to show that suggested method can be generalized and applied to other materials. Piezoelectric and triboelectric energy harvesting capabilities of the developing Nylon-11 nanowires are provided in order to show how the molecular scale nanoconfinement effect influence the bulk scale energy applications.

## **2) Dual aerosol-jet printed polymer nanocomposite**

Although the polymer-based nanocomposite (issue No. 5) and multi-layered structure (issue No. 6) have been suggested to improve the performance of triboelectric energy harvesting devices, poor dispersion and distribution of nanomaterials in polymer matrix and limited variety of available polymers are still challenges that need to be overcome.

In this thesis, aerosol-jet printing is suggested for multi-layered polymer-based nanocomposites (Chapter 8). It demonstrates the optimum processing conditions for novel non-mixable dual printing technique and the corresponding image analysis for evaluating the degree of nanoparticle dispersion. It also provides dielectric property measurements of the resulting nanocomposites in order to display the design capability of this technique. To show the possibility of aerosol-jet printed multi-layered nanocomposite, preliminary research for triboelectric energy harvesting application is provided.

## **1.2 Thesis outline**

In this thesis, novel functional polymeric nanomaterials, for stable and robust energy harvesting performance, are proposed by developing advanced nanofabrication methods. In Chapter 2, the background and context of energy harvesting mechanisms, energy harvesting materials, and nano-fabrication techniques are provided. In Chapter 3, the methodology for functional polymeric nanomaterials' fabrication and property characterization techniques are clearly presented so that all the results should be reproducible. In Chapter 4, the method to grow Nylon-11 nanowires by template-wetting is described. Since the resulting Nylon-11 nanowires exhibit a polarisation without

additional electrical poling process by exploiting the nanoconfinement effect of the template-wetting process, they have been directly incorporated into nano-piezoelectric generators successfully, exhibiting high temperature stability and excellent fatigue performance. In Chapter 5, to further enhance the energy harvesting capability of Nylon-11 nanowires, a gas-flow assisted nano-template (GANT) infiltration method is proposed. The well-defined fast crystallisation conditions resulting from the GANT method not only leads to self-polarization of the ferroelectric  $\delta'$ -phase but also increases average crystallinity.  $\delta'$ -phase Nylon-11 nanowires introduced into a prototype triboelectric generator are shown to give rise to a six-fold increase in output power density as observed relative to the  $\delta'$ -phase film-based device. In Chapter 6, thermodynamically stable  $\alpha$ -phase Nylon-11 nanowires are presented. Notably, definitive dipole alignment of  $\alpha$ -phase nanowires is shown to have been achieved for the first time via a novel thermally assisted nano-template infiltration (TANI) method, resulting in exceptionally strong and thermally stable spontaneous polarization, as confirmed by molecular structure simulations. The output power density of a triboelectric generator based on  $\alpha$ -phase nanowires is shown to be enhanced by 328 % compared to a  $\delta'$ -phase nanowire-based device under the same mechanical excitation. In Chapter 7, the crystallisation mechanism of three different template-wetting methods; conventional template wetting, GANT and TANI methods, is investigated in more detail. Additionally, the resulting nanowires' crystal structures and characteristics are compiled. In Chapter 8, multi-layered nanocomposites are fabricated via a modified aerosol-jet printing method. Due to the novel aerosol-based printing technique, outstanding dispersion and distribution of the nanoparticles in the polymer matrix has been achieved. The resulting nanocomposite contributes to the enhancement of the device capacitance, which also leads to high-performance triboelectric generators. The concluding remarks and on-going projects are presented in the final chapter.

# Chapter 2

## Background and Theory

In this chapter, we explain in more detail the backdrop against which this research is undertaken. This chapter consists of three parts: energy harvesting mechanisms, energy harvesting materials, and nano-fabrication techniques as follows:

<b>Part</b>	<b>Chapter and content</b>
A. Energy harvesting mechanisms	2.1 Piezoelectric energy harvesting 2.2 Triboelectric energy harvesting
B. Energy harvesting materials	2.3 PVDF and its copolymers 2.4 Nylon-11 2.5 Polymer-based nanocomposite
C. Nano-fabrication techniques	2.6 Template-wetting

The fundamental mechanisms and context of piezoelectric and triboelectric generators are addressed. As an energy harvesting material, ferroelectric polymers, including PVDF with its copolymers and Nylon-11, and polymer-based nanocomposite are introduced. Lastly, the operating principle of nano-fabrication technique, such as template-wetting, is provided. Some of the work presented here is adapted from the previous works

by the author.[1]–[4] Copyright permission and authors' contributions are given in Appendix A.

## **Part A. Energy harvesting mechanism**

### **2.1 Piezoelectric energy harvesting**

This section provides a concise introduction to piezoelectric energy harvesting, including fundamental background, piezoelectric materials, and configuration of piezoelectric energy harvesting devices.

#### **2.1.1 Fundamental principle**

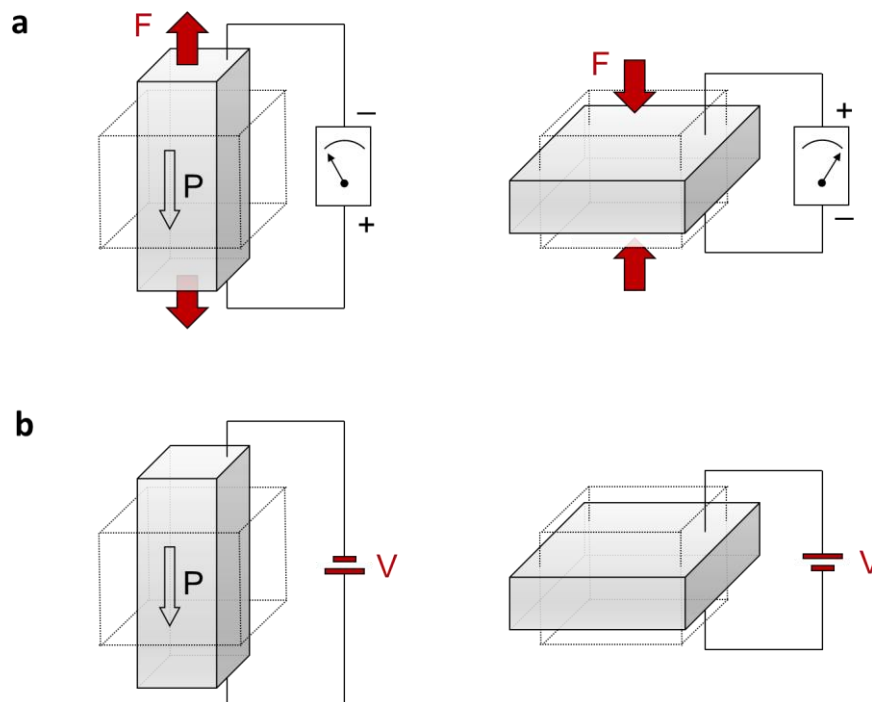


Fig. 2-1 Schematic representation of the piezoelectric effect: (a) The direct piezoelectric effect and (b) the converse piezoelectric effect.  $F$ ,  $P$ , and  $V$  indicate applied external force, the direction of net polarization, and applied external voltage. A cube with dotted edges indicates the shape of the original material.

The piezoelectric effect was first discovered by Jacques and Pierre Curie.[5] The term ‘piezoelectric’ originates from the Greek word ‘piezo’, which means ‘pressure’, and refers to the propensity of certain materials to generate electrical charge on their surfaces in response to applied pressure (Fig. 2-1a). Therefore, piezoelectricity can be described as a function of applied stress ( $T$ ), which is applied force ( $F$ ) per unit area ( $A$ ), and the induced electric displacement<sup>1</sup> ( $D$ , surface charge per unit area).[6] In three-dimensional space,  $T$  is described as a second rank tensor ( $T_{ij}$ ) by two vectors ( $i, j$ ) because the vector  $F$  with direction  $i$  ( $F_i$ ) is normal to the vector  $A$  with the direction  $j$  ( $A_j$ ). Thus, the diagonal and off-diagonal elements of  $T_{ij}$  represent “normal” and “shear” stress, respectively. In the linear electrical behaviour of the material,  $D$  is defined by Gaussian theorem as follows:

$$D = \varepsilon E \quad (2-1)$$

where  $\varepsilon$  is the permittivity, and  $E$  is the electric field<sup>2</sup>. (Details of the Gaussian theorem are discussed in Appendix B1.) As  $D$  and  $E$  can be presented as vectors  $D_i$  and  $E_j$  in three-dimensions,  $\varepsilon$  is also described by a second rank tensor  $\varepsilon_{ij}$ . In addition, based on Hooke’s Law, the strain ( $S$ ) can be defined by

$$S = sT \quad (2-2)$$

where  $s$  is the elastic compliance. Considering  $T$  and  $E$  are independent,  $D$  is specified by

$$D = dT + \varepsilon^T E \quad (2-3)$$

where  $d$  is the piezoelectric strain constant (or piezoelectric charge constant) of the material and is represented by a third rank tensor, and  $\varepsilon^T$  is the permittivity at constant stress. In matrix form,  $[d]$  represents the direct piezoelectric effect, and  $[D]$  can be represented by

---

<sup>1</sup> D (electric displacement): Electric field induced by only free charges in material.

<sup>2</sup> E (electric field): Fundamental field in Maxwell equation. The amplitude of E depends on all charges in vacuum.

$$\begin{bmatrix} D_1 \\ D_2 \\ D_3 \end{bmatrix} = \begin{bmatrix} d_{11} & d_{12} & d_{13} & d_{14} & d_{15} & d_{16} \\ d_{21} & d_{22} & d_{23} & d_{24} & d_{25} & d_{26} \\ d_{31} & d_{32} & d_{33} & d_{34} & d_{35} & d_{36} \end{bmatrix} \begin{bmatrix} T_1 \\ T_2 \\ T_3 \\ T_4 \\ T_5 \\ T_6 \end{bmatrix} + \begin{bmatrix} \varepsilon_{11} & \varepsilon_{12} & \varepsilon_{13} \\ \varepsilon_{21} & \varepsilon_{22} & \varepsilon_{23} \\ \varepsilon_{31} & \varepsilon_{32} & \varepsilon_{33} \end{bmatrix} \begin{bmatrix} E_1 \\ E_2 \\ E_3 \end{bmatrix} \quad (2-4)$$

To identify the directions in the piezoelectric system, terms 1, 2, and 3 corresponding to x-, y-, and z-axes are used.<sup>3</sup>

Conversely, when an electric potential is applied across the material, mechanical deformation in the form of strain results (Fig. 2-1b). Under short circuit condition with constant  $E$ ,  $S$  is then specified by

$$S = s^E T + d_t E \quad (2-5)$$

where  $d_t$  is the transpose of  $d$  and the matrix form of  $d_t$  ( $[d_t]$ ) represent the converse piezoelectric effect.  $s$  is then represented by a 4th-rank tensor, while  $d_t$  is a 3rd rank tensor. Under open circuit condition with constant  $D$ ,  $S$  is specified by

$$S = s^D T + g D \quad (2-6)$$

where  $g$  is the piezoelectric voltage constant, which is the electric field produced by a mechanical stress. From these equations, piezoelectric coefficients can be derived as follows:<sup>4</sup>

$$d_{ij} = \left( \frac{\partial D_i}{\partial T_j} \right)^E \quad (2-7)$$

$$g_{ij} = - \left( \frac{\partial E_i}{\partial T_j} \right)^D = \left( \frac{\partial S_j}{\partial D_i} \right)^T \quad (2-8)$$

---

<sup>3</sup> The terms 4, 5, 6 are defined by combination of the directions of 23, 13, and 12, respectively.

<sup>4</sup> Unit of piezoelectric charge (or strain) coefficient ( $d$ ) and piezoelectric voltage coefficient ( $g$ ) are (C/N) and (V<sub>m</sub>/N), respectively.

The piezoelectric coefficient for resulting strain ( $d_{ij}$ ) and voltage ( $g_{ij}$ ) are used to assess the piezoelectric material's capability for actuator and energy harvesting (or sensor) applications, respectively.[7], [8] The relationship between two different coefficient  $d$  and  $g$  can be defined as follows:

$$g = \frac{d}{\varepsilon} \quad (2-9)$$

### 2.1.2 Piezoelectric materials

The piezoelectric effect is closely related to the change in electrical polarisation in a piezoelectric material. When an external stress is applied to a crystal, the resultant deformation of atomic structure leads to ion (or molecular) movement. As a result, a dipole moment is induced in the unit cell, and a net polarization (or net dipole moment) is formed across the whole material.[9] In crystallography, piezoelectric materials have to have non-centrosymmetric crystal structure<sup>5</sup> to generate a net polarization, otherwise the induced dipole moments cancel out by the surrounding dipoles. Therefore, the piezoelectric effect is observed in 20 non-centrosymmetric crystals out of the 32 crystal classes. Half of these non-centrosymmetric crystals exhibit “polar” crystal structures, meaning that the induced polarization can be maintained unless there is an application of external electric field or mechanical load. These classes of materials with spontaneous polarization are called “ferroelectric” materials. In contrast, the polarization of “non-polar” crystals is only induced by mechanical stress and cannot be retained without external stimulus.[10]

In the case of polar piezoelectric materials (i.e. ferroelectric materials), electrical poling (or mechanical stretching in some cases) is conducted to maximize polarization because microscale domains with dipole moments are randomly oriented. By applying electric fields greater than the coercive field ( $E_c$ ), and with heating close to the Curie temperature ( $T_c$ ), the dipoles can be aligned, and spontaneous polarization is enhanced after cooling.[11]

---

<sup>5</sup> Non-centrosymmetric crystal structure: Crystals without a centre of symmetry

In general, most of the well-known piezoelectric materials are inorganic materials[12]–[15], such as barium titanate ( $\text{BaTiO}_3$ , BTO) and lead zirconium titanate ( $\text{PbZr}_x\text{Ti}_{1-x}\text{O}_3$ , PZT), due to their high piezoelectric strain constant. However, these piezoelectric ceramics are rigid and require high processing temperatures. In addition, to gain the highest performance, lead-containing materials, such as PZT,[16], [17] are used. To counter these drawbacks, polymer piezoelectric materials, including PVDF and its copolymers, polyamides (Nylon), liquid-crystalline polymers, and polyureas, have been proposed as substitutes.[10] These piezoelectric polymers have significant advantages; in addition to their soft elasticity, both the materials and processing equipment required are inexpensive.[6], [18], [19] Furthermore, although piezoelectric polymers have lower piezoelectric strain constants, they present better piezoelectric voltage constants due to the low dielectric permittivity of the polymer, as described in Eq. (2-9). This indicates that piezoelectric polymers are particularly well-suited to energy harvesting applications.[7], [8] However, much higher electric fields ( $\sim 1 \text{ MV/cm}$ ) are required for the electrical poling process of piezoelectric polymers than that of inorganic single crystals ( $\sim 1 \text{ kV/cm}$ ). Furthermore, only low operating temperatures of polymer-based piezoelectric devices are achievable due to their typically low melting point ( $\sim 100 \text{ }^\circ\text{C}$ ) and low  $T_c$ .

### 2.1.3 Piezoelectric energy generators

In general, the electrical poling direction or the direction of crystal orientation is defined as the z-direction (polar axis) in polar and non-polar piezoelectric materials, respectively. In these cases, the polar axis and all directions in the plane at right angles to the polar axis are referred to as the ‘3’ and ‘1’ direction, respectively.[20] Then, the electrical response to stress along the polar axis or at right angles to it can be described by piezoelectric coefficient of  $d_{33}$  and  $d_{31}$  respectively, and these two configurations commonly used for piezoelectric energy generators for the conversion of mechanical stress/strain into an electric charge (Fig. 2-2).

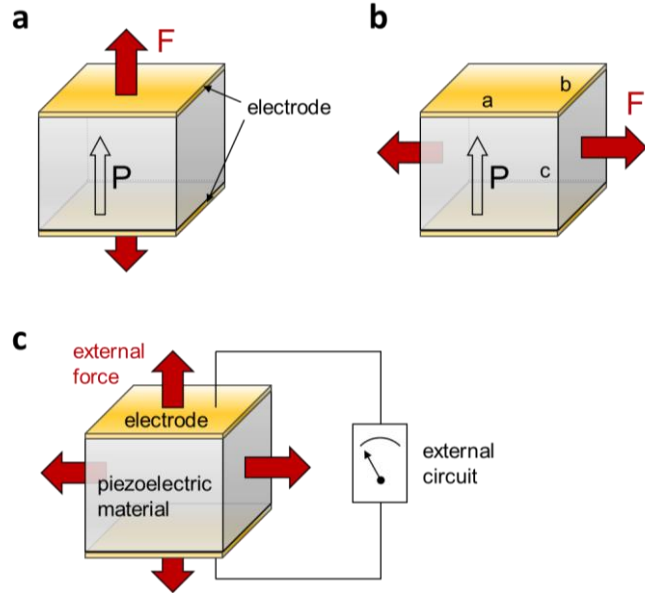


Fig. 2-2 Configuration of piezoelectric energy generator: (a) 33 mode and (b) 31 mode generator. a, b, and c indicate the length of each corner of piezoelectric material. (c) A schematic of piezoelectric generator.

As shown in Fig. 2-2c, the design of a piezoelectric generator is that of a two-plate capacitor with top and bottom electrodes and the piezoelectric material as a dielectric layer, where the applied force induces a charge or voltage across the capacitor that can be sensed by an external circuit. The electric charge ( $Q$ ) and induced voltage ( $V$ ) of 33 and 31 mode piezoelectric generators can be defined respectively by

$$Q (V = 0) = (d_{33} F) \text{ or } \left( \frac{a}{c} d_{31} F \right) \quad (2-10)$$

and

$$V (Q = 0) = \left( \frac{c}{ab} g_{33} F \right) \text{ or } \left( \frac{1}{b} g_{31} F \right) \quad (2-11)$$

(Detailed development processes are described in Appendix B2.) The maximum energy per cycle ( $U_m$ ) is also defined respectively by

$$U_m = \left( \frac{c}{ab} d_{33} g_{33} F^2 \right) \text{ or } \left( \frac{1}{b} d_{31} g_{31} F^2 \right) \quad (2-12)$$

Fig. 2-3a presents a schematic of a prototype piezoelectric generator. A spin-coated and electrically poled film of P(VDF-TrFE) is introduced as a piezoelectric material. (Detailed properties of P(VDF-TrFE) are given in Chapter 2.3) Fig. 2-3b illustrates typical output voltage characteristics of the piezoelectric generator under low-frequency vibration (5 Hz). The magnitude and frequency of applied stress should be considered as significant factors since the shape of the output signal is determined by those.[21] This device shows an alternating current shaped output signal with a peak voltage of 0.3 V under the strain rate of  $0.1 \% s^{-1}$ . [1] This result is a simple demonstration of how a piezoelectric generator transforms an induced strain from an applied force into an electrical output, such as a voltage or electric current, via changes in electrical polarization.

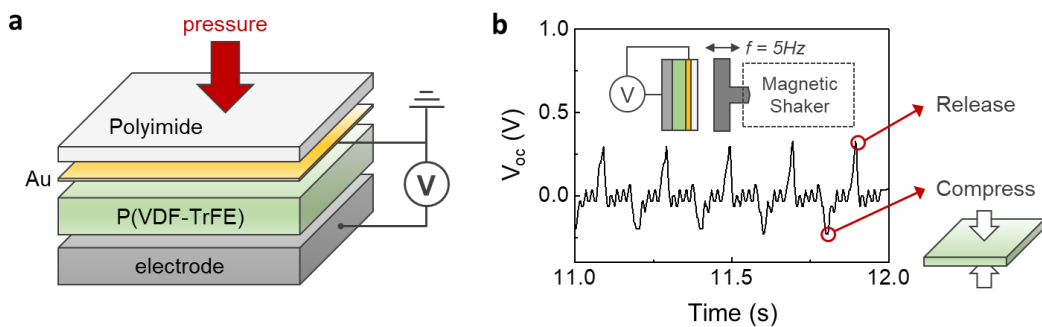


Fig. 2-3 Prototype polymer-based piezoelectric generator. (a) A schematic representation of a P(VDF-TrFE)-based piezoelectric generator. (b) Output voltage of P(VDF-TrFE) based piezoelectric device when impacted with low-frequency vibrations ( $f = 5 \text{ Hz}$ ) using a magnetic shaker. Red circles indicate the deformation states of the ferroelectric polymer film. Fig. (a) and (b) are taken from the author's work from Ref. [1], reproduced with permission from The Royal Society Publishing.

## 2.2 Triboelectric energy harvesting

Here, we review the fundamentals of the triboelectric energy harvesting and various ways to enhance the performance of triboelectric generators. In particular, the choice of material and functionalization route of materials are discussed predominantly based on triboelectric charge collection and storage mechanism.

## 2.2.1 Fundamental principle

### 1) Operating mechanism

The key mechanisms of triboelectric energy generator are contact electrification and subsequent electrostatic induction.[22], [23]

Contact between two different materials causes a charge transfer between the surfaces of the materials.[24]–[26] The material which gains charge becomes negatively charged, and the material which loses charge becomes positively charged; this phenomenon is known as “contact electrification”. Such charge transfer is attributed to electron[27]–[30], ion[31], and/or material[32] movement between two materials with different charge affinity. The charge affinity of materials sometimes referred to as “triboelectricity”, thus such charge transfer phenomena and the resulting transferred charge on the surface are called “triboelectric effect (or triboelectrification)” and “triboelectric charge”, respectively. Since a number of factors, such as electron affinity, electronegativity, surface roughness, affect triboelectricity, researchers have come up with an empirical arrangement of materials according to their ability to gain or lose charge when two materials are contacted, and this arrangement is called a “triboelectric series”.[33] Table 2-1 shows the triboelectric series for common materials.[34] Materials located in the positive region, called tribo-positive materials, easily lose charge when they come in contact with other materials, and those on the negative region, called tribo-negative materials, tend to gain charge upon contact. Materials that are far apart with respect to their position in the series are thus desirable for greater charge transfer upon contact. When transferred charge (i.e. triboelectric charge) are generated on the surfaces of materials, such charge can be moved or stored within the materials. In some cases, the transferred charge can be lost through a connected electrode or the surrounding atmosphere. Therefore, contact electrification can be further divided into three subprocesses: charge transfer, charge storage and charge loss.

In general, triboelectric generators consist of a pair of dielectric materials and attached electrodes (or at least one of them is an insulator with an attached electrode). When two contacted materials are separated, transferred charges on the top surfaces of both materials induce a potential difference across the electrodes. This results in electron flow from one electrode to the other; this phenomenon is called “electrostatic induction”. A periodic

potential difference can thus be generated across the materials as a result of periodic relative motion between the two.

Table 2-1 Triboelectric series.[34] All known materials have different charge affinities and exhibit a contact electrification when two materials are contacted. Positive (or negative) means materials have a tendency to lose (or gain) charge during contact motion.

+	Air	Polyethylene terephthalate (PET)	
↑	Human skin	Polyvinyl butyral	
	Human hair	Polychlorobutadiene	
	Polyamide 11 (Nylon-11)	Nature rubber	
	Polyamide 6-6 (Nylon-6,6)	Polyacrylonitrile	
	Wool, knitted	Acrylonitrile-vinyl chloride	
	Silk, woven	Polybisphenol carbonate	
	Cellulose	Polychloroether	
	Cotton, woven	Polyvinylidien chloride (Saran)	
	Polyurethane elastomer (PU)	Polystyrene (PS)	
	Styrene-butadiene copolymer	Polyethylen (PE)	
	Wood	Polypropylene (PP)	
	Hard rubber	Polyimide (Kapton)	
	Acetate, Rayon	Polyvinyl Chloride (PVC)	
	Polyvinyl alcohol (PVA)	Polytrifluoroethylene	
	Polyester (Dacron)	Polydimethylsiloxane (PDMS)	
	Polyisobutylene	Polytetrafluoroethylene (Teflon)	-

## 2) Geometry of a triboelectric generator

Regarding the geometry of triboelectric generators, four different modes have been introduced (Fig. 2-4): the vertical contact-separation mode, the lateral sliding mode, the single-electrode mode, and the free-standing mode.[23] Although each geometry shares the same fundamental energy harvesting mechanism, such as contact electrification and electrostatic induction, they have different working parameters and energy harvesting efficiencies according to their structure. To develop a triboelectric generator, therefore, device geometry should be carefully considered depending on target applications. In this thesis, all triboelectric generators are developed based on the vertical contact-separation mode (Fig. 2-4a) in order to focus on the influence of materials on the device performance. In this mode, due to the presence of electrodes on the bottom side of each material, the transferred charge creates an electrical potential between the two electrodes under open-circuit conditions during separation motion. In the short-circuit condition, the resulting electrical potential causes the flow of electrons in order to attain equilibrium.

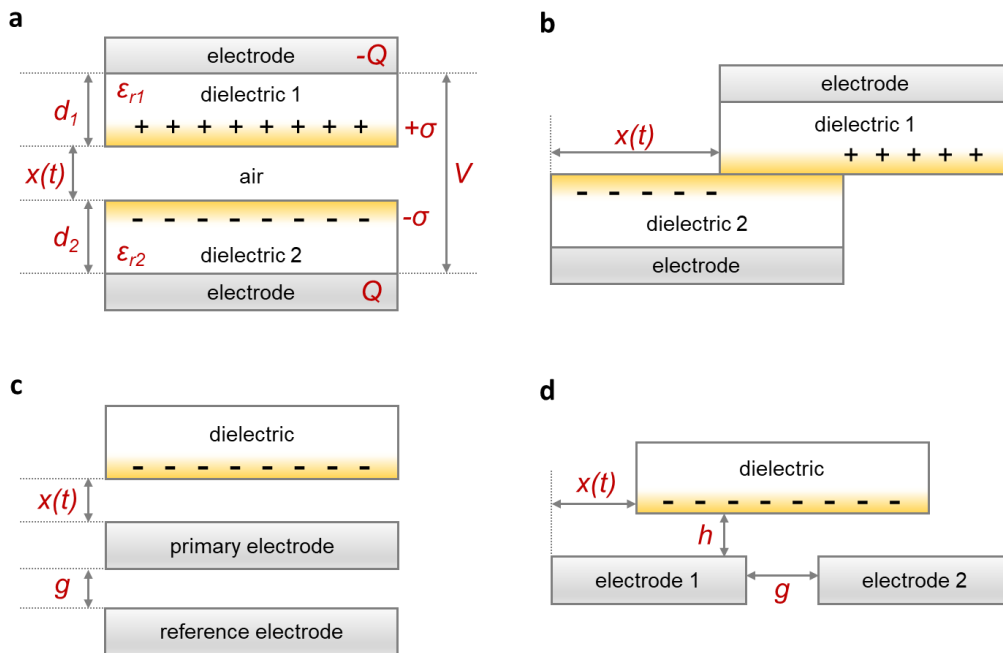


Fig. 2-4 Four fundamental working modes of the triboelectric generators. (a) The vertical contact-separation mode, (b) the lateral sliding mode, (c) the single-electrode mode, and (d) the free-standing mode.

## 2.2.2 Theoretical model

In order to predict the output behaviour of a triboelectric generator, several theoretical models have been proposed, and they can be classified into two different categories: 1) device-related model and 2) material-related model. All device-related models assumed that an equal density of opposite triboelectric charge are uniformly distributed on the contact surfaces, and their densities are unchanged once the surfaces are charged. Whereas, the movement and loss of triboelectric charge are considered separately in material-related models.

### 1) Device-related model

**Classical model.** Researchers have developed a theoretical model based on a planar circuit element.[35]–[38] In the dielectric-to-dielectric contact-separation mode triboelectric generators (Fig. 2-4a),[35] the electric field strength ( $E$ ) of one dielectric part is derived by Gauss's law (Eq. (2-1)) and given by

$$E = \frac{Q}{S \varepsilon_0 \varepsilon_r} \quad (2-13)$$

where  $Q$  is the value of transferred charge between the two electrodes,  $S$  the area of the electrode,  $\varepsilon_0$  the permittivity of the vacuum ( $8.854 \times 10^{-12}$  F m<sup>-1</sup>), and  $\varepsilon_r$  the relative permittivity (i.e. dielectric constant) of dielectric material. The electric potential difference ( $\Delta V$ ) between two electrodes can be thus given by

$$\begin{aligned} \Delta V &= E_1 d_1 + E_2 d_2 + E_{air} x(t) \\ &= \left[ -\frac{Q}{S \varepsilon_0 \varepsilon_{r1}} d_1 \right] + \left[ -\frac{Q}{S \varepsilon_0 \varepsilon_{r2}} d_2 \right] + \left[ \frac{S \sigma - Q}{S \varepsilon_0} x(t) \right] \\ &= -\frac{Q}{S \varepsilon_0} \left( \frac{d_1}{\varepsilon_{r1}} + \frac{d_2}{\varepsilon_{r2}} + x(t) \right) + \frac{\sigma x(t)}{\varepsilon_0} \end{aligned} \quad (2-14)$$

where  $d_1$  and  $d_2$  are the thickness of the two dielectric materials,  $x(t)$  the distance between two contact surfaces,  $t$  the time,  $\sigma$  the triboelectric charge density, and  $\varepsilon_{r1}$  and  $\varepsilon_{r2}$

the dielectric constants of the two dielectric materials. (In the conductor-to-dielectric structure,  $t_1/\epsilon_{r1}$  can be ignored because the metal layer acts as both triboelectric layer and electrode.) Under open-circuit conditions, the value of transferred charge ( $Q$ ) become zero since no charge is transferred between electrodes. Thus, if we assume the electric potential of the bottom electrode to be zero, the equation for the open-circuit voltage ( $V_{oc}$ ) can be calculated to be

$$V_{oc} = \frac{\sigma}{\epsilon_0} x(t) \quad (2-15)$$

From the experimentally determined  $V_{oc}$  of each triboelectric generator, the theoretical triboelectric charge density ( $\sigma$ ) can be estimated by

$$\sigma = \frac{V_{oc} \epsilon_0}{x(t)} \quad (2-16)$$

Under short-circuit conditions ( $V = 0$ ), the short-circuit transferred charge ( $Q_{sc}$ ) is given by

$$Q_{sc} = \frac{S \sigma \epsilon_{r1} \epsilon_{r2} x(t)}{d_1 \epsilon_{r2} + d_2 \epsilon_{r1} + \epsilon_{r1} \epsilon_{r2} x(t)} \quad (2-17)$$

The value of  $Q_{sc}$  can therefore vary as a function of  $x$ . In the case of conductor-to-dielectric structure,  $Q_{sc}$  is given by

$$Q_{sc} = \frac{S \sigma x(t)}{d + x(t)} \quad (2-18)$$

Since we can measure the short-circuit current ( $I_{sc} = dQ_{sc} / dt$ ), the  $Q_{sc}$  is also calculated using the integration of experimentally achieved  $I_{sc}$ . (Example of calculation can be shown in Fig. 5-18.)

Based on these classical model, a figure-of-merit (FOM) of triboelectric generator has been suggested,[39] as described in the following equation

$$FOM_s = \frac{2\varepsilon_0}{\sigma^2} \frac{E_m}{S \cdot x_{max}} \quad (2-19)$$

where  $FOM_s$  is the dimensionless structural FOM,  $E_m$  the largest possible output energy per cycle, and  $x_{max}$  is the maximum displacement between two different materials.[39]

**Distance-dependent electric field model.** Although this classical model has been widely used to demonstrate the experimental results of triboelectric devices, it cannot clearly explain the mechanism of polarization of the dielectric layer and free-charge induction on the electrodes. This is because the classical model assumed that electric field perpendicular to a charged plane is uniform throughout the intervening space, and the magnitude of the electric field does not change with the distance from the charged surface.[40] Dharmasena et al. subsequently introduced an advanced theoretical model using the concept of a distance-dependent electric field.[40], [41] To calculate the variation of electric field with distance, the z-axis electric field ( $E_z$ ) above the midpoint (along with the z-axis) of a charged surface in free space is defined by Gauss's law. In the dielectric-to-dielectric contact-separation mode triboelectric generator, the electric field ( $E$ ) at the dielectric-electrode interface is given by

$$E = \frac{\sigma}{\pi \varepsilon_{r1}} [f(d) - f(x + d)] \quad (2-20)$$

where

$$f(d) = \arctan\left(\frac{1}{2(d/L)\sqrt{4d^2/L^2 + 2}}\right) \quad (2-21)$$

Assuming that  $L$  is the dimension of a square-shaped dielectric material, the  $V_{oc}$  can be calculated by

$$V_{oc} = \frac{\sigma}{\pi \varepsilon_{r1}} [M(d)]_{d_1}^{d_1+x} + \frac{\sigma}{\pi \varepsilon_{r2}} [M(d)]_{d_2}^{d_2+x} \quad (2-22)$$

where

$$M(d) = x \arctan\left(\frac{L}{2d\sqrt{4d^2/L^2 + 2}}\right) - \frac{L}{w} \ln\left(\frac{1 + \sqrt{4d^2/L^2 + 2}}{-1 + \sqrt{4d^2/L^2 + 2}}\right) \quad (2-23)$$

(Detailed development processes are described in Appendix B3.) Under short-circuit conditions ( $V = 0$ ), the short-circuit transferred charge ( $Q_{sc}$ ) is given by

$$Q_{sc} = \frac{\sigma S \left[ \frac{1}{\epsilon_{r1}} [M(d)]_{d_1}^{d_1+x} + \frac{1}{\epsilon_{r2}} [M(d)]_{d_2}^{d_2+x} \right]}{\left( \frac{1}{\epsilon_{r1}} + \frac{1}{\epsilon_{r2}} \right) [M(d)]_0^{d_1+d_2+x}} \quad (2-24)$$

Consideration of the electric field variation with the distance results in non-zero overall electric field, which depends on the separation distance, and this enabled the explanation of dielectric polarization and electron rearrangement.

**The resistance-capacitance product matching model.** From a practical point of view, a different FOM for maximum power density was also presented by Peng et al.[42] They pointed out that the periodic mechanical motion of contact-separation mode triboelectric generators changes the distance ( $x$ ) between two dielectric surfaces and results in the time-varying capacitance of dielectric layer and air gap. Furthermore, they assured that, to achieve the most effective generator with maximum power density, the mechanical motion with constant frequency ( $\omega$ ) should be matched with the characteristic frequency of the circuit ( $1/RC_{total}$ ). By matching the resistance-capacitance (RC) product to  $\omega$ , the device FOM ( $FOM_{device}$ ) for the maximum power density is defined by

$$FOM_{device} = 0.064 \cdot \frac{\sigma^2 \cdot \bar{v}}{\epsilon_0} \quad (2-25)$$

where  $\bar{v} = \omega x_{max}/\pi$  is the average speed of the mechanical motion. It shows that  $\sigma$  is the only material-related parameter that needs to be considered for the maximum power density.

## 2) Material-related model

**Dynamic charge model.** According to the Eq. (2-17) and (2-24), the triboelectric charge density, which is the density of transferred charge on the surface, is the only material-related parameter for the performance of triboelectric generator. This means that charge transfer is the only critical process that needs to be considered for the highly efficient device. However, it must be noted that such device-related models assumed that triboelectric charge are placed only on the top surface of dielectric material and do not move or dissipate (Fig. 2-5a). (As a result, these conventional models are also called “static charge models”.) Considering the motion of triboelectric charge in the dielectric layer, it is obvious that the charge storage and loss process should also be considered. Cui et al. have suggested a “dynamic charge model” to elucidate the motion of charge in the dielectric layer.[43] Given that the movement of charge are determined by the properties of material, this model would be classified as ‘material-related model’.

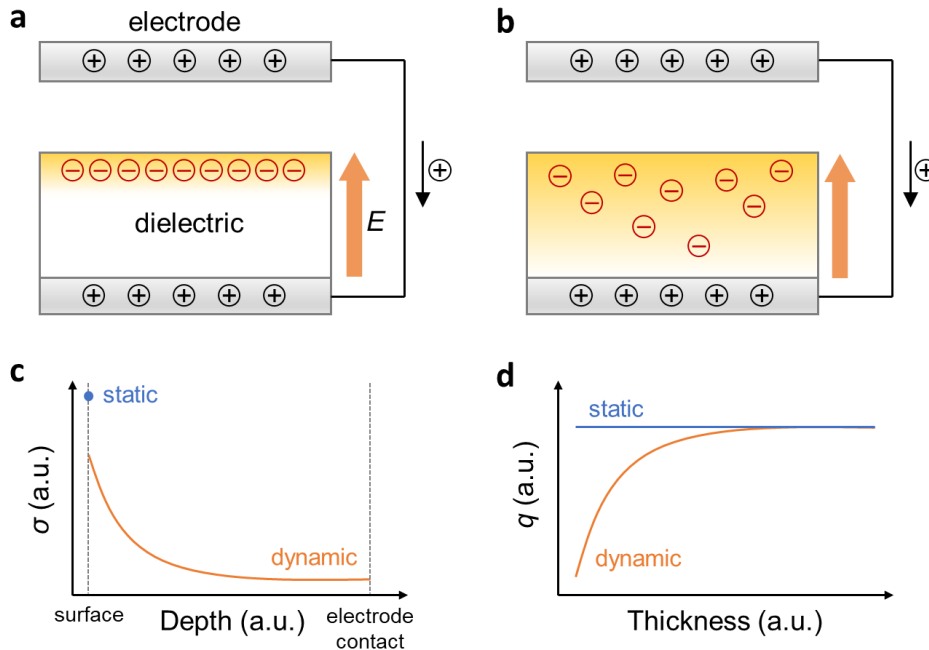


Fig. 2-5 Schematics of the contact-separation mode triboelectric generators with two different assumptions: (a) conventional static charge model and (b) dynamic charge model. Red and blue circles indicate transferred electron by contact electrification and induced positive charge, respectively. (c) Theoretical triboelectric charge distribution in the dielectric layer of (blue) static and (orange) dynamic charge model. (d) Theoretical relationship between the quantity of triboelectric charge ( $q$ ) and thickness of the dielectric layer.

As shown in Fig. 2-5b, the dynamic charge model assumes that triboelectric charge can be moved and stored (or lost) in the dielectric layer by two different mechanisms: an electric field-induced drift and recombination with the charge on the electrode, respectively. (In order to simplify the model, diffusion caused by the concentration gradient, an impact of trap level, and the absorbance of charge from the atmosphere were ignored. In addition, large electric field ( $E$ ) and a much larger surface area than thickness were also assumed.) As a result, triboelectric charge are distributed within the whole dielectric layer (Fig. 2-5c). In addition, the quantity of triboelectric charge ( $q$ ) can vary with thickness of the dielectric layer due to the loss process (Fig. 2-5d). In static charge models, the value of  $q$  is constant regardless of thickness of the dielectric layer because it is assumed that  $q$  is determined by contact electrification and is not altered. In contrast, in the case of the dynamic model,  $q$  increase with dielectric layer thickness because charge can be lost easily in thin dielectric materials. If the dielectric layer is expressed as discrete  $n$  sub-layers in direction parallel to the surface, space and time-dependent electric field ( $E_{x,t}$ ) of each layer is defined by

$$E_{x,t} = \frac{\sum_0^i q(i,t)}{\epsilon_0 \epsilon_r S} \quad (2-26)$$

where  $q(i,t)$  is the triboelectric charge quantity,  $i$  the number of sub-layer, and  $S$  the surface area of dielectric layer. Then, the Gaussian probability density function for the drift distance of charge is given by

$$f(i, t) = \frac{1}{\sigma\sqrt{2\pi}} e^{-\frac{1}{2}\left(\frac{x-\mu E_{i,t}}{\sigma}\right)^2} \quad (2-27)$$

where  $\mu$  is the electron mobility in the dielectric materials, and  $\sigma$  the standard deviation. The quantity of triboelectric charge carried in  $i$  th sub-layer can be described as

$$q_{(i,t+\Delta t)} = \sum_0^i [q_{(i-1,t)} \cdot f(i, t)] - q_{(i,t)} \int_{i\Delta x}^{n\Delta x} f(i, t) \quad (2-28)$$

where  $\Delta x$  is the thickness of each sub-layer. The electron drift modelling confirms that a large amount of triboelectric charge are lost in the thin dielectric layer. When the thickness of dielectric layer increases, the total amount of triboelectric charge increases and is saturated at certain thickness because triboelectric charge cannot reach the dielectric/electrode interface by induced electric field in the thick dielectric film (Fig. 2-5d, orange).

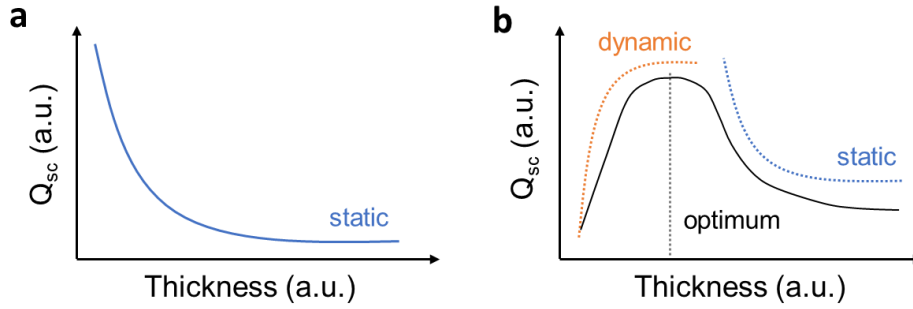


Fig. 2-6 Theoretical relationship between short-circuit transferred charge ( $Q_{sc}$ ) and thickness based on (a) static charge model and (b) dynamic and static charge model.

This dynamic charge model gives interesting insight regarding the output performance of triboelectric generators. Typically, researchers predicted that much more short-circuit transferred charge ( $Q_{sc}$ ) could be achieved from triboelectric generator with a thinner dielectric layer based on the conventional static charge model. This is because the dielectric layer is assumed as a capacitor with constant voltage (through constant triboelectric charge), and the capacitance ( $C$ ) is defined as

$$C = \frac{\epsilon_0 \epsilon_r S}{d} \quad (2-29)$$

where  $\epsilon_r$  is the dielectric constant of the dielectric layer,  $S$  the surface area, and  $d$  the thickness of dielectric layer. As a result, according to the Eq. (2-17) and Eq. (2-18), short-circuit transferred charge ( $Q_{sc}$ ) (and  $I_{sc}$ ) is inversely proportional to the thickness of dielectric layer in the contact-separation mode triboelectric generators (Fig. 2-6a).

However, as discussed, if triboelectric charge are moved and lost by combining with induced charge at the dielectric/electrode interface, increasing effect of  $C$  would be cancelled out by voltage drop in thin dielectric layer (Fig. 2-6b). The relationship between electric force (or electrostatic force,  $F_{el} = E \times Q$ ) and dielectric thickness ( $d$ ) is simply derived by Coulomb's law:

$$F_{el} = \frac{k_e q Q_{sc}}{d^2} \quad (2-30)$$

where  $k_e$  the Coulomb's constant,  $q$  the triboelectric charge, and  $Q_{sc}$  short-circuit transferred charge (i.e. induced charge on electrode).[44] When the dielectric is thick enough, despite the triboelectric charge being preserved, only a small amount of  $Q_{sc}$  can be moved through the electrode because  $F_{el}$  is inversely proportional to the thickness. In contrast, when the dielectric layer is too thin, triboelectric charge with drift mobility ( $\mu$ ) can easily be moved and combined with charge in the electrode by electric field, resulting in low  $Q_{sc}$  at the equilibrium condition. These results indicate that there is an optimum thickness for the maximum  $Q_{sc}$  (b). Considering that  $\mu$  is the material-related factor, the dynamic charge model implies that the triboelectric charge storage and loss mechanism can also be controlled through material processing.

### 2.2.3 Strategies to improve performance

As an alternative energy source, triboelectric energy harvesting research has focused on the enhancement of energy conversion efficiency. To realise an efficient triboelectric device, the majority of research to date has focused on finding the best pair of materials as this is critical to charge transfer. Versions of the triboelectric series have been used to select appropriate pairs of materials because it is known that materials that are further apart in the series result in a greater relative charge transfer. Thus, triboelectric generators based on pairs of materials located on the extreme opposite ends of the triboelectric series are expected to show superior energy harvesting capabilities. For example, the combination of fluorinated polymers and metals have been the most commonly used materials in triboelectric generator research to date. However, purely

triboelectric series-based material selection has shown limited performance enhancement. In addition, this would not be a reliable approach because such tables are empirically arranged.

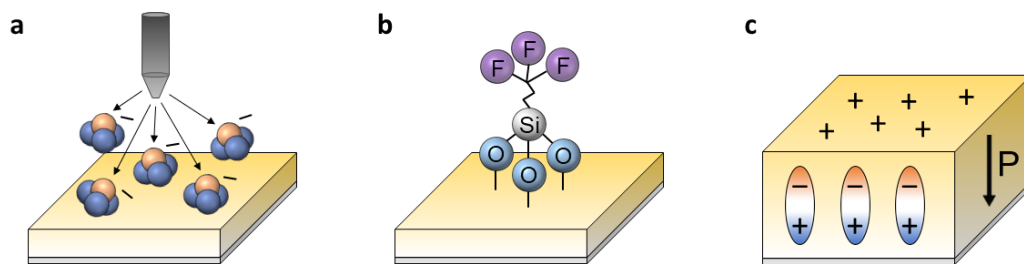
The second major approach is morphological tuning of the contact surfaces. Forming nanostructures, such as nanowires or nanotubes, or patterns of pyramid-, square-, or hemisphere-based micro- or nanopatterns were shown to improve the effective contact area, resulting in output generation enhancement.[45]–[50] However, these rough structures increase the frictional force, causing a reduction of energy conversion efficiency. Furthermore, lifetimes of such polymer nano- and micro-structures severely affect the reliability of the device performance.

Recently, material-related performance enhancement approaches have been proposed. By introducing functional materials or by functionalizing the material itself, further improvement of device performance can be achieved. The methods are divided into two parts based on the property manipulating mechanism: charge generation and charge storage. Fig. 2-7 displays the schematics of each method.

### **1) Charge generation**

By transferring charge during contact, triboelectric charge is induced and placed on the surface of a material, and the resulting triboelectric charge density is one of the critical material-related factors which affects the output of a triboelectric generator. Therefore, additional generation of triboelectric charge or increasing surface charge density is an effective approach to improve the device performance. (To clarify, both term ‘triboelectric charge density’ and ‘surface charge density’ should be defined separately. Triboelectric charge density should be limited to transferred charge on the surface by contact electrification. In contrast, surface charge density can be defined as density of the total charge on the surface regardless of origin. The density of surface charge can be measured using Kelvin Probe Force Microscopy (KPFM). This method is addressed in more detail in Chapter 3.2.2.)

### Charge generation



### Charge storage

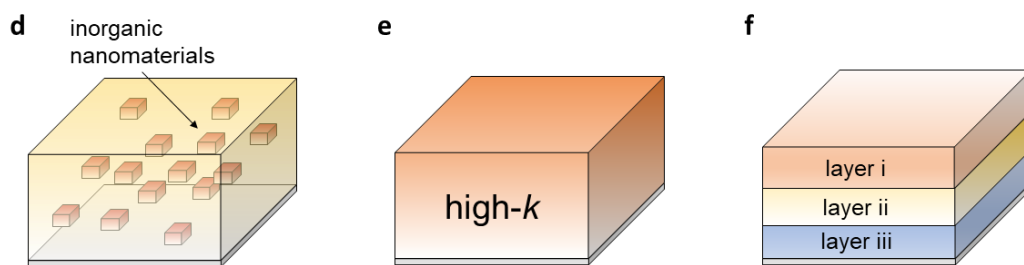


Fig. 2-7 Various strategies to improve the performance of triboelectric generators: (a) Charge injection by the corona discharging using the air-ionization gun. Possible charged molecules are  $\text{CO}_3^-$ ,  $\text{O}_3^-$ , and  $\text{NO}_3^-$ . (b) Surface chemical functionalization by a self-assembled monolayer (SAM). (c) Realization of spontaneous polarization in ferroelectric materials. (d) Polymer-based nanocomposite with inorganic nanoparticles. (e) High dielectric constant (high- $k$ ) dielectric layer. (f) Multi-layered structures with charge transfer, trap, storage, and blocking layers.

**Ion-injection.** By injecting single-polarity charged particles/ions on the dielectric surface via corona discharging, surface charge density has been directly modulated (Fig. 2-7a).[51] The charged particles/ions are injected using air-ionization gun on grounded dielectric layers. The surface charge density increased with a number of injections and reached a maximum level due to air breakdown. As a result, 25-fold enhancement of triboelectric output performance was reported at the maximum surface charge density ( $\sigma_{max}$ ). The relationship between  $\sigma_{max}$  and the thickness of the dielectric film was also investigated by comparing the threshold voltage for the air breakdown and the actual voltage drop across the air gap in the triboelectric generator. The theoretical and experimental research revealed that a larger  $\sigma_{max}$  could be achieved in a thinner film. By reducing the thickness of fluorinated ethylene propylene (FEP) dielectric layer to the range of hundreds of nanometres, the surface charge density could be enhanced by a factor of two, with 4-fold improvement of output power. It must be noted that the  $\sigma_{max}$ -thickness relationship and  $Q_{sc}$ -thickness relationship in Fig. 2-6 are different. This is because the main consideration of ion-injection is charge storage capability in dielectric layer and the air-breakdown. In contrast the  $Q_{sc}$  relationship assumes the same triboelectric charge density and focuses on the possibility of charge loss. In other words, the ion-injection method only considers the relatively thick dielectric layer with negligible charge loss. The injected charge showed good stability on the surface of the dielectric material. The density of injected surface charge on the thick FEP layer was reduced  $\sim 16.6\%$  during the first 20 days and maintained the 80 % level over an additional 100 days. Depending on the materials, ion-injection method showed significant variation of charge storage capability. Despite the same quantity of charge ( $\sim 240 \mu\text{C}/\text{m}^2$ ) initially injected, more than 80 % of surface charge density was lost in a Kapton film within 5 days, indicating that the charge storage (or loss) efficiency varies with material properties.

**Surface functionalization.** Triboelectric charge density can also be manipulated by modification of surface chemical structure. To functionalize the surface of a dielectric material, self-assembled monolayers (SAMs) have been introduced via dip-coating or vapour deposition method (Fig. 2-7b). Poly-L-lysine and trichloro(1H,1H,2H,2H-perfluorooctyl) silane (FOTS) coated polyethylene terephthalate (PET) film resulted in positively and negatively charged surfaces, respectively.[52] 3-aminopropyltriethoxysilane (APTES), 3-glycidypropyltriethoxysilane (GPTES), FOTS, and trichloro (3,3,3-

trifluoropropyl) silane (TFPS) were also applied onto polydimethylsiloxane (PDMS) layer for negative (APTES, GPTES) and positive (FOTS, TFPS) surface potentials.[53] With more sophisticated characterization, Shin et al. produced functionalized PETs with 10 different surface potentials using halogen-terminated aryl-silane derivatives and aminated materials.[54] These functionalization processes manipulate the surface potential of the dielectric layer through highly polarized functional groups, such as -F, -Cl, -NH<sub>2</sub>, and amide groups. As a result, the tendency of electrostatic potential is consistent with the sequence of electron affinity of halogen atoms in the gas phase (Cl > F > Br), indicating modification of charge affinity (triboelectricity) of the polymer surface. Thus, if surface modification processes result in a more positive (or negative) surface potential, the driving force for contact electrification is increased, leading to enhancement of the triboelectric charge density on the contact surface and improvement of output performance in a triboelectric generator. Surface functionalization research proposes interesting ideas regarding contact electrification mechanism: the parameters related to charge affinity of surface molecules, such as electronegativity or electron density, is one of the key factors for the charge transfer process. As all other variables related to the property of dielectric layer, including capacitance and mechanical stiffness, are fixed in surface functionalization studies, resulting trends give important evidence for the arrangement of a triboelectric series. For example, it is possible to explain why the materials with negative functional groups (-F), such as fluorinated polymers, are located on the negative edge, but the materials containing positive groups (-NH<sub>2</sub>, and amide group), such as Nylon, are placed on the positive region in the triboelectric series. In some of the literature, the output performance was further improved by the combination of the morphological tuning and chemical functionalization.[55], [56] Despite the outstanding efficiency of surface modification methods, durability of SAMs is a critical limitation because monolayered functionalized molecules are vulnerable to frictional motion. As a substitute, Ryu et al. suggested solid polymer electrolyte-based triboelectric generators.[57] The addition of various ions successfully changed the surface potential of polyvinyl alcohol (PVA) electrolyte, improving triboelectric output performance with high durability (more than 30,000 cycles).

**Spontaneous polarization.** Spontaneous polarization (or remanent polarization) is the polarization which remains in a ferroelectric polymer when an applied electric field is

reduced to zero. Recent investigations have proposed that this spontaneous polarization can enhance triboelectric charge density (Fig. 2-7c). Bai et al. demonstrated the substantial enhancement of the output power density of triboelectric devices using electrically polarized PVDF.[58] Lee et al. showed evidence of the changes in surface potential of P(VDF-TrFE) depending on the polarization direction.[59] When a P(VDF-TrFE) film was poled negatively, films acted as a tribo-positive material. In contrast, positively poled film showed tribo-negative properties, increasing the output voltage compared to an unpoled film. This indicates that the spontaneous polarization of the ferroelectric polymer can alter the triboelectric charge density as well as device performance. Based on piezoresponse force microscopy (PFM) and KPFM analysis, the effect of spontaneous polarization on the triboelectric charge density has been demonstrated in more detail.[60] When P(VDF-TrFE) films were poled by an atomic force microscope (AFM) tip with different magnitude and direction of electric field, the KPFM measurement after rubbing process, which imitates the frictional motion of triboelectric generator, showed that the spontaneous polarization further enhanced the amount of surface charge. This is possibly due to the modulation of work function between the ferroelectric polymer and contact material.[61] The electrical poling caused the polarization-induced Fermi level shift in ferroelectric polymer and led to transfer of more charge from the metal counterpart to the ferroelectric polymer surface. The great advantage of this spontaneous polarization approach is the durability of the device. This is because such spontaneous polarization is induced by the modification of the “internal” molecular structure of the materials, while ion-injection and surface modification manipulate the “surface” property of dielectric materials.

## 2) Charge storage

During the contact and separation motion of triboelectric generator, free-charge are introduced into the electrodes to achieve an equilibrium state with the triboelectric charge. However, as discussed, triboelectric charge can be dissipated, and this loss process is determined by the property of the dielectric layer. There has been much research regarding ways to reduce the loss of triboelectric charge by modification of the dielectric layer.

**Dielectric constant.** In the triboelectric generator, the dielectric layer is assumed as a capacitor with constant voltage (through constant triboelectric charge), and  $C$  increases

with a decrease in the thickness and/or an increase in the relative permittivity ( $\epsilon_r$ , dielectric constant) of the dielectric layer. However, as discussed, since the charge recombination and loss process hinder the reduction of thickness, researchers have suggested ways to increase the dielectric constant of the polymer dielectric layer instead of decreasing dielectric thickness. In this respect, polymer-based nanocomposites have been proposed to improve the dielectric constant (Fig. 2-7d). It was found that the a 3-fold increase in  $V_{oc}$  can be obtained by embedding barium titanate ( $\text{BaTiO}_3$ ) nanoparticles into a PDMS dielectric layer compared to pure PDMS-based triboelectric generators.[62] In addition, it could be clearly seen that the output performance of the triboelectric device increased with increasing volume ratio of  $\text{BaTiO}_3$  nanoparticles. Based on Maxwell model, the  $\epsilon_r$  of composite ( $\epsilon_{r,composite}$ ) is given by

$$\epsilon_{r,composite} = \epsilon_{r,polymer} \left[ 1 + 3\varphi_f / \left( \frac{\frac{\epsilon_{r,NPs}}{\epsilon_{r,polymer}} + 2}{\frac{\epsilon_{r,NPs}}{\epsilon_{r,polymer}} - 2} - \varphi_f \right) \right] \quad (2-31)$$

where  $\epsilon_{r,polymer}$  is the relative permittivity (i.e. dielectric constant) of the polymer matrix,  $\varphi_f$  the volume fraction of nanoparticles, and  $\epsilon_{r,NPs}$  the relative permittivity of nanoparticles. This indicates that the relative permittivity increases with the increase of volume ratio of nanoparticles. The same effect of high dielectric constant (high- $k$ ) nanocomposite on device performance has been confirmed through studies of triboelectric generators with Ag-exchanged zeolite[63] and graphite particle-based nanocomposite.[64] (The ways to control the dielectric constant of polymers by adding micro- or nano-sized materials are well-established in the field of nanocomposite with reviews.[65], [66] Therefore, we opted not to deal with it in more detail in this section.) To further enhance the performance of triboelectric generators, nanoparticles have been introduced into mesoporous dielectric layers. By mixing PDMS with Au/water solution, a mesoporous structure was achieved after subsequent evaporation of the water. This Au nanoparticle-embedded mesoporous film-based triboelectric generator showed 5-fold power enhancement compared to a flat film-based device. This is because the pores forming in the dielectric layer effectively reduce the thickness, while preventing electric shorting between top and bottom electrodes.[67] As a result, the capacitance could be improved by

both high- $k$  nanoparticles and decreased thickness (by mesoporous structure). Furthermore, pores in the dielectric layer enlarged the surface contact area during contact electrification, increasing triboelectric charge density. This is the reason why a synergetic effect could be achieved by nanoparticles and pores, despite the air ( $\epsilon_r=1$ ) in the pores reducing the total dielectric constant of the nanocomposite ( $\epsilon_{r,composite}$ ). A triboelectric generator with a high- $k$  polymer dielectric was proposed by Lee et al (Fig. 2-7e).[68] Instead of adding inorganic nanoparticles, the  $\epsilon_r$  of PVDF layer was controlled by a poly(tert-butyl acrylate) (PtBA) grafting ratio. Due to the  $\pi$ -bonding and polar characteristics of the ester functional groups in the PtBA, the PtBA-grafted PVDF was mainly composed of  $\alpha$ -phase with increasing dielectric constant, generating twice the enhancement in triboelectric output power compared to a pristine PVDF-based generator.

**Charge trap.** To reduce the loss of triboelectric charge and improve the charge storage capability, additional charge trap materials have been introduced into the polymer dielectric (Fig. 2-7f). The first approach was adding polymer interlayers. This is because the physical defects (amorphous free volume, crosslinking points, or imperfections of crystal lattice) and chemical defects (dangling bonds or functional groups) in polymer materials can act as a charge trap site.[69]–[71] The preliminary study regarding multi-layered polymer structures was suggested by Cui et al. with the dynamic charge model.[54] By adding polystyrene (PS) ‘charge storage’ layer on the bottom of the PVDF friction layer (or charge transfer layer), the resulting triboelectric generator showed 7-fold improvement of total charge density compared to a single PVDF-based device because most of the triboelectric charge were stored in the PS layer. A three-layered structure was also proposed to further enhance the performance. To reduce the triboelectric charge attenuation effect during contact electrification by accumulated charge in PS layer, a highly conductive carbon nanotubes (CNTs) ‘charge transport’ layer was added between PS and PVDF layer. As a result, this three-layered structure raised the total charge density by a factor of 11.2. The charge storage effect of multi-layered structure was also reported by Feng et al.[72] After adding a polyimide (PI) charge storage layer under the PVDF friction layer, the triboelectric device exhibited a 6-fold enhancement of short-circuit current. In comparison to PET and cellulose (i.e. paper), PI showed the best device performance as a charge storage layer because non-uniform energy levels along the aromatic rings in the PI chains generate much more trapping sites.[73] Kim et al. demonstrated a triboelectric generator with PDMS

interlayer.[44] Due to the physical traps in amorphous phase and the crosslinking networks, and chemical traps in the functional groups, the triboelectric generator with PDMS interlayer showed 173-fold increased output power density compared to single layered device. When compared the charge storage capability to PS, PDMS-PVDF double-layered structure exhibited much higher surface potential (- 421 V) than PS-PVDF device because the trap density in PDMS is much higher than that of PS. The other approach for charge trapping was introduction of inorganic materials into polymer matrix. Wu et al. reported that the two-dimensional (2D) materials, such as reduced graphene oxide (rGO) and molybdenum disulfide ( $\text{MoS}_2$ ), could suppress the loss of triboelectric charge in the polymer dielectric because the large surface area and quantum confinement effect enabled the charge trapping.[74], [75] As a result, the triboelectric generator with PI/ $\text{MoS}_2$ /PI structure exhibited 120 times greater power density than that of the device without  $\text{MoS}_2$ . A titanium oxide ( $\text{TiO}_x$ ) based electron ‘blocking’ layer was reported by Park et al.[76] The  $\text{TiO}_x$  film with thickness of 100 nm was introduced on the dielectric-electrode interface to “block” charge recombination, while other methods have focused on “storage” of triboelectric charge by manipulating the dielectric layer. Furthermore, high permittivity of  $\text{TiO}_x$  enabled additional polarization of dielectric layer, causing improvement of surface charge density. As a result, due to the coupling effect of electron blocking and enhanced polarization, 25 times greater output power was observed in the triboelectric generator with PDMS/ $\text{TiO}_x$  double-layer relative to that of single-layered PDMS device.

#### **2.2.4 Perspectives and challenges**

Based on the review, the issues and problems that need to be addressed for further improvement of triboelectric generators are summarised as follows:

- Understanding the fundamental mechanisms of contact electrification. Although a few hypotheses have been proposed, no substantial conclusion has been reached.[23] Using advanced scanning probe microscopy (SPM) techniques, contact electrification can be investigated in more detail.
- Developing reliable tribo-positive materials. The triboelectric generators based on pairs of materials located at the extreme opposite ends of the triboelectric series are expected

to show superior energy harvesting capabilities. However, the majority of the research to date has almost exclusively focused on tribo-negative materials, such as polytetrafluoroethylene (PTFE), PVDF, and PDMS. Furthermore, these materials have been paired with aluminium or copper as the tribo-positive (or electron-donating) counterpart, even though these metals are not located on the extreme positive end of the triboelectric series. This is because the vast majority of materials on the positive side of the triboelectric series are biological or natural materials, such as human skin and cotton, and have relatively low mechanical stiffness and/or formability. Therefore, development of robust tribo-positive material is crucial for high-performance triboelectric generators.

- Investigating mechanically durable functionalized layer. Since the triboelectric device is a mechanical contact-based energy generator, abrasion of contact surface is inevitable. In this respect, despite ion-injection being the most effective way to increase the surface charge density, the persistence of injected charge should be confirmed in advance. Otherwise additional equipment for constant charge injection needs to be introduced, but it is practically unfavourable. In addition, although the surface functionalization method is scientifically meaningful to investigate the contact electrification mechanism, it cannot be applied to practical devices due to the low durability of functionalized layer. Therefore, advanced functionalization method and/or functionalized layer should be developed.
- Development of a polymer material with a high-intensity spontaneous polarization. In the durability respect, spontaneous polarization is the most feasible method among various triboelectric charge generating techniques, because it relies on altered internal molecular structures of the dielectric layer. Therefore, a material with high-intensity spontaneous polarization would be a good approach to enhance the device performance. However, the required additional electrical poling process with high electric field needs to be addressed.
- Improving the dynamic charge model. The dynamic charge model has given outstanding insight regarding charge storage and loss phenomena. It should be extended to the device level, merging with latest device-related models, such as distance-dependent electric field model and/or capacitor-resistance optimization model.

- Developing polymer-based nanocomposites. The approaches for output performance improvement, including tuning the dielectric constant and charge trapping, can be further investigated through nanocomposite structures. Although various nanocomposites have been suggested already, a myriad of combinations of materials can be introduced to triboelectric generator research. Furthermore, applying the techniques and ideas in the well-established nanocomposite field, to enhance triboelectric generator performance, would be a good approach.
- Investigating the multi-layered structure. The role of additional layers, including charge storage, charge transfer, and electron blocking layers, need to be studied in more detail. In addition, various combinations of materials should be proposed for multi-layered structures. Considering the dielectric constant of whole device, polymer-based nanocomposite can be also applied as an interlayer. Recently, multi-layered nanocomposite has attracted considerable interest in the field of energy storage device. Therefore, the studies regarding an advanced multi-layered structure would be meaningful for both energy harvesting and energy storage applications.

## **Part B. Energy harvesting materials**

We now consider specific polymeric materials investigated in this thesis.

### **2.3 PVDF and its copolymer**

As a ferroelectric polymer material, PVDF and its copolymer P(VDF-TrFE) have been widely studied and exploited in various applications, including energy harvesting devices. This is because, despite exhibiting weaker piezoelectric properties than commonly used ceramics, such as BTO and PZT, PVDF and P(VDF-TrFE) possess a range of advantages over ceramics that render them mechanically stable, chemically robust, and possibly biocompatible. The following section briefly describes the structure and properties of PVDF and P(VDF-TrFE) as energy harvesting materials.

### 2.3.1 PVDF

PVDF is a well-known semi-crystalline polymer, with crystalline regions dispersed within amorphous regions. Therefore, the relative amount of crystalline and amorphous region affect the properties of PVDF. For instance, the mechanical properties of PVDF change above the glass transition temperature ( $T_g$ ) of  $-35\text{ }^\circ\text{C}$  because the amorphous regions become glassy or rubbery, decreasing in Young's modulus at room temperature. The degree of crystallinity of PVDF is typically 50 ~ 60 % and varies depending on crystal structures and thermal history.[10]

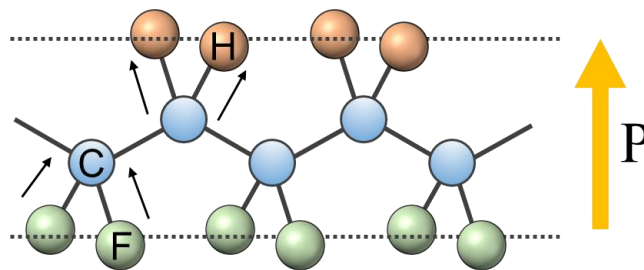


Fig. 2-8 Schematic drawing of molecular structure of  $\beta$ -phase PVDF with an all-*trans* configuration and its dipole moment ( $P$ ). Black arrows indicate the dipole moment. Orange, blue and green spheres indicate hydrogen, carbon, and fluorine atoms.

The molecular structure of PVDF is shown in Fig. 2-8. PVDF has a spatially symmetrical arrangement of fluorine (F) and hydrogen (H) atoms along the polymer chain. Due to the difference in electronegativity<sup>6</sup>, dipole moments are generated along C-F and C-H bonds. If the directions of C-F and C-H bonds are aligned within all-*trans* chain conformation, a macroscopic net polarization of PVDF occurs across the carbon backbone. Such chain conformation of PVDF is called  $\beta$ -phase, and it exhibits ferroelectric behaviour due to the net polarization. Including  $\beta$ -phase, PVDF has at least four different crystal structures (the  $\alpha$ ,  $\beta$ ,  $\gamma$  and  $\delta$ -phases).[77], [78] The  $\alpha$ -phase is thermodynamically the most stable phase, while it is non-polar and paraelectric because of the centrosymmetric unit cell

---

<sup>6</sup> Electronegativity: The tendency of an atom to attract a shared pair of electrons (or electron density) towards itself. According to the Pauling scale, Fluorine, which is the most electronegative element is assigned a value of 4.0. Carbon and Hydrogen are assigned a value of 2.55 and 2.2, respectively.

structure with *trans-gauche-trans-gauche* conformation.  $\gamma$ -PVDF has a chain conformation in between that of the  $\alpha$  and  $\beta$ -phases, and also shows ferroelectric behaviour. However, the  $\gamma$ -phase is experimentally hardly accessible because it requires extreme temperature control and high pressures. The  $\delta$ -phase is a polar version of the  $\alpha$ -phase and shows ferroelectric property.  $\delta$ -PVDF is synthesized from  $\alpha$ -phase sample by electro-forming with high electric field (170 MV/m).

The most common and widely-studied ferroelectric  $\beta$ -phase PVDF can be achieved via biaxial stretching or electrical poling with a high electric field ( $\sim 130$  MV/m) of thick  $\alpha$ -PVDF films. It is noted that the induced polarization and resulting piezoelectricity of typical ferroelectric polymers degrade with increasing temperature and vanishes at its Curie temperature ( $T_c$ ).<sup>[10]</sup> In the case of  $\beta$ -PVDF, the polarization is stable up to melting temperature ( $T_m$ ) because the  $T_c$  ( $\sim 195$  °C) is higher than the  $T_m$  ( $\sim 166$  °C), and it enables the high temperature operation of PVDF-based ferroelectric devices.<sup>[77], [79]</sup>

### 2.3.2 P(VDF-TrFE)

As shown in Fig. 2-9, P(VDF-TrFE) is a random copolymer generated by integration of two homopolymers: PVDF and poly(trifluoroethylene) (PTrFE).<sup>[79]</sup> Thus, P(VDF-TrFE) has similar physical strength, flexibility<sup>7</sup> and chemical stability to PVDF. Additional side group of PTrFE helps the polymer crystallize into the ferroelectric  $\beta$ -phase with all-*trans* conformation because of steric effects, which eliminates the need for mechanical stretching. This is why the research and applications with P(VDF-TrFE) have been more common than those with PVDF.

---

<sup>7</sup> Mechanical flexibility: It means that a material has a low Young's modulus and changes its shapes considerably under elastic loads. Young's modulus can be defined as the resistance of a material to elastic deformation under load.

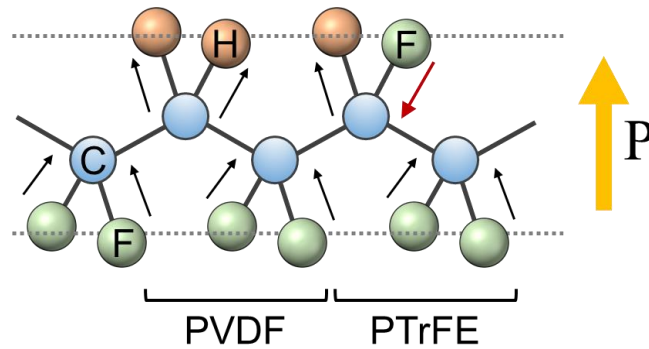


Fig. 2-9 Schematic drawing of molecular structure of P(VDF-TrFE) and its dipole moment ( $P$ ). Black and red arrows indicate the dipole moment. Orange, blue and green spheres indicate hydrogen, carbon, and fluorine atoms.

In addition, P(VDF-TrFE) has a higher solubility in common organic solvents and can easily be processed into ferroelectric thin films via thermal annealing close to the crystallisation temperature.[10] However, due to the F atoms in the middle of H atoms and resulting dipole moment with opposite direction to others, the magnitude of net polarization ( $P$ ) is smaller than that of PVDF. Furthermore, the reduced dipole interaction gives rise to lower  $T_c$  of 110 °C, resulting in limited thermal stability of the spontaneous polarization. Reported properties of PVDF and P(VDF-TrFE) are given in Table 2-2.[10]

Table 2-2 Property comparison of ferroelectric polymers: PVDF and P(VDF-TrFE)

Polymer	$T_c$ (°C)	$T_m$ (°C)	$d_{31}$ (pC/N)
PVDF	195	175	20 ~ 28
P(VDF-TrFE)	110	150	12

### 2.3.3 Confronting issues

PVDF and P(VDF-TrFE) are the most cited and widely used ferroelectric polymer materials.[6], [18] PVDF has a high piezoelectric strain constant (20 ~ 28 pC/N) and a good thermal stability, while additional mechanical stretching or electric poling with high electric field is required to generate a device with ferroelectric property. In contrast, ferroelectric phase can easily be achieved in P(VDF-TrFE) due to the additional side group. However, the magnitude of net polarization and resulting piezoelectric strain constant (12 pC/N) is much smaller than that of PVDF. Furthermore, the low  $T_c$  and  $T_m$  of P(VDF-TrFE)

limit their use in applications, such as actuator and sensor, at higher temperatures. There is thus a growing need to explore alternative ferroelectric polymers with a high intensity of polarization and enhanced thermal stability, which can offer reliable energy harvesting performance at higher temperatures.

## 2.4 Nylon-11

Odd-numbered Nylons, such as Nylon-11, with relatively high melting temperatures are known to possess ferroelectric (and piezoelectric) characteristics, that are comparable to PVDF at room temperature, by virtue of the high degree of hydrogen bonding and dipole orientation resulting from the arrangement of amide molecules within adjacent chains upon crystallisation.

Nylon-11 is also an attractive material in the field of triboelectric energy generators because it is a notable exception among tribo-positive materials, being synthetic in nature with excellent mechanical properties, such as tenacity, abrasion resistancy, and elasticity, that allow for easy control of its shape and subsequent integration into triboelectric generators (Table 2-1). In contrast, the vast majority of materials on the positive side of the triboelectric series are biological or natural materials, such as human skin and cotton, and have relatively low mechanical stiffness and/or shape controllability.[80] Therefore, an investigation into Nylon as a potential tribo-positive candidate is essential to enhance triboelectric performance and extend the range of triboelectric generator applications.

In this section, we discuss Nylon-11 as a material for energy harvesting applications. In the first half of this review, the structures of Nylon-11, including molecular structures and crystal structures, are presented. In the second part, the reported post-treatment techniques are presented. The development of piezoelectric and ferroelectric properties of Nylon-11 are also discussed in chronological order. Lastly, we summarise the general characteristics and confronting issues of Nylon-11.

## 2.4.1 Structures of Nylon-11

### 1) Molecular structure

Nylon is a semi-crystalline polymer with repeating units linked by amide bonds, and these amide bonds generate hydrogen bonding which is one of the most important characteristics of Nylon. The hydrogen bonding is formed between the oxygen atom in one amide group and a hydrogen atom which is bound to another adjacent nitrogen atom, resulting in electrostatic attraction between two Nylon chains. The crystalline region consists of stacking of chains with multiple hydrogen bonds and contributes to the mechanical and dielectric properties of Nylon.

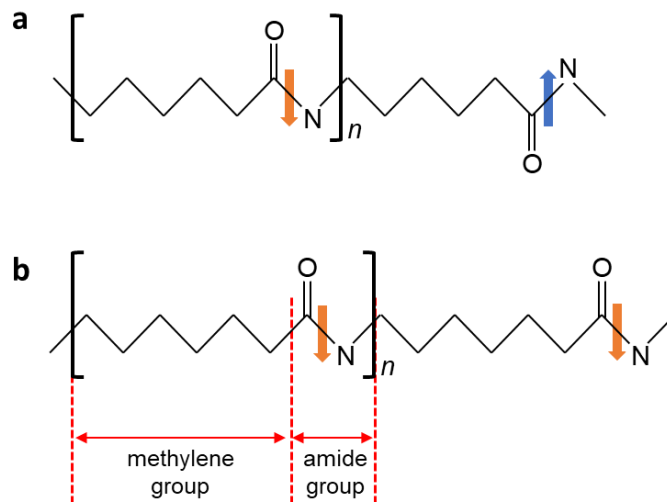


Fig. 2-10 Schematics of molecular chain structure of Nylon: (a) even-numbered (Nylon-6) and (b) odd-numbered Nylon (Nylon-7). Colour arrows indicate the direction of the dipole moment, which is nearly parallel to the C=O bond.

The chemical structure of both Nylons is shown in Fig. 2-10. In one repeating unit, Nylon- $n$  has a methylene group  $(\text{CH}_2)_{n-1}$  and an amide group. Depending on the number of carbon atoms ( $n$ ) in a repeating unit, it is called “even-numbered” or “odd-numbered” Nylon. The amide group has a permanent electric dipole moment, and the configuration of dipole moments varies on the number of carbon atoms. As a result, even-numbered Nylon has no “net” polarization due to the alternating amide groups. In contrast, all of the dipoles

in odd-numbered Nylon point in the same direction, resulting in net polarization. Thus, odd-numbered Nylon has “polar” properties, and this is the reason why odd-numbered Nylon is recognised as a “ferroelectric” polymer. (In reality, even-numbered Nylon also exhibits ferroelectric behaviour. It will be discussed in the following subsection.) In this work, we focus specifically on Nylon-11.

## 2) Crystal structures

At an early stage, most of the studies of Nylon-11 had focused on its crystal structures and changes in crystalline morphology with processing conditions because Nylon-11 has an extensive degree of polymorphism.[81]–[86] The crystal structures of Nylon-11 and their producing methods are summarised in Table 2-3.

The crystal structures observed for Nylon-11 fall into two categories: (1)  $\alpha$ ,  $\alpha'$  and  $\beta$  phases; (2) pseudo-hexagonal phase ( $\gamma$ ,  $\gamma'$ ,  $\delta$ ,  $\delta'$ ).[87] The triclinic  $\alpha$ -phase has been produced by precipitation from Nylon-11 solution in *m*-cresol with decreasing temperature from 150 °C to room temperature.[88] Thus, it is considered as the most thermodynamically stable crystal structure, consisting of stacks of well-defined hydrogen-bonded sheets. The  $\alpha'$ -phase has been achieved by slow cooling ( $\sim 2$  °C/min) of melted Nylon-11.[88] It shows almost identical crystal structures to the  $\alpha$ -phase; a polar, triclinic unit cell with hydrogen-bonded sheets shifting progressively along the chain axis. Thus, the X-ray diffraction (XRD) patterns of the  $\alpha'$ -phase at room temperature are very similar to the  $\alpha$ -phase. However, the  $\alpha'$ -phase can be assumed to be a defective  $\alpha$ -form because the calculated crystal perfection index value of  $\alpha'$  is lower than that of  $\alpha$ -phase (Appendix B4).[89] In addition, the reversible phase transition at high temperature, as known as the “Brill transition”, is observed only in the  $\alpha'$ -phase, indicating that the  $\alpha'$ -phase is a thermally tunable (i.e. unstable) crystal structure.[89] The  $\beta$ -phase was not found to be distinct, probably involving a small modification of the  $\alpha$  phase. There is no definitive crystal structure, and this form is not of practical interest. It is generally accepted that the molecular chains in the  $\gamma$ -form are slightly contracted from that of the fully extended planar zigzag found in the  $\alpha$ -form of Nylon-11. Kawaguchi et al. found that the  $\beta$  angle in the pseudo-hexagonal  $\gamma$ -phase was 118.5° (rather than 120° for perfect hexagonal crystals).[81] The  $\delta$ - and  $\delta'$ -phases, like  $\gamma$ , have a pseudo-hexagonal crystal structure. The  $\delta$ -phase can be viewed

as the high temperature  $\alpha$ -form, as they are the result of the Brill transition in  $\alpha'$  at  $\sim 100^\circ\text{C}$  (quoted by Newman[90] as  $95^\circ\text{C}$ , although the exact temperature is dependent on nature of the sample and heating rate).[89] It is not yet clear exactly how the hydrogen bonding arrays are arranged in the  $\delta$ -phase; the sheet-like structure from the  $\alpha'$ -phase may or may not be preserved above the Brill transition temperature. The  $\delta'$ -phase has been produced by ice quenching of melted Nylon-11, resulting in a metastable smectic pseudo-hexagonal crystal structure with a random distribution of hydrogen bonds along the chain axis. (This metastable crystal structure remains intact even when left for extended periods of time.[91]) The relationship between  $\delta$ - and  $\delta'$ -phase has never been investigated, but  $\delta'$ -phase is presumed to be a less ordered  $\delta$ -phase because both phases show similar diffraction patterns.

Table 2-3 Various crystal structures of Nylon-11[81], [82], [89], [92]–[94]

phase	unit cell	sample preparation method	$(hkl) = 2\theta$ (°)	$d$ (Å)
$\alpha$	triclinic	Precipitated from solution in <i>m</i> -cresol	(001) = 7.5 (200) = 20 (210/010) = 23.5	11.7 4.44 3.79
$\alpha'$	triclinic	Melt and slow cooling	(001) = 7.4 (200) = 20.4 (210/010) = 23.4	11.9 4.35 3.80
$\beta$	monoclinic	Precipitated from solution in triethylene glycol (TEG)	(010) = 5.89 (001) = 12.2 (200) = 20.08 (210) = 20.94	15.0 7.25 4.42 4.24
$\gamma$	monoclinic	Solution casting from trifluoroacetic acid (TFA) based solution	(001) = 5.91 (200) = 21.34 (220/020) = 21.87	14.9 4.16 4.06
$\gamma$	pseudo-hexagonal	Solvent treatment on $\alpha$ -phase	(020) = 6.01 (200/210) ~ 21.5 (001) = 22.4	14.7 4.13 3.97
$\gamma'$	pseudo-hexagonal	Solvent treatment on $\delta'$ -phase	(002) = 12.5 (100) = 21.5	7.08 4.13
$\delta$	pseudo-hexagonal	High temperature phase of $\alpha'$ -phase	(001) = 7.4 (200), (210/010) = 21.1	11.9 4.21
$\delta'$	smectic pseudo-hexagonal	Melt and ice-quenching	(001) = 7.2 (hk0) = 21.6	12.2 4.11

Although the detailed structure of Nylon-11 including atomic coordinates is not available in the literature, several unit cell parameters of Nylon-11 crystalline forms have been proposed based on theoretical calculation and some experimental results compared with the studies of well-known Nylon, such as Nylon-6 or Nylon-66 (Table 2-4).

Table 2-4 Proposed unit cell parameters of Nylon-11

crystal structure	unit cell parameters						parallel/anti-	Ref.
	<i>a</i> (Å)	<i>b</i> (Å)	<i>c</i> (Å)	$\alpha$ (deg)	$\beta$ (deg)	$\gamma$ (deg)		
Triclinic $\alpha$	9.6	4.2	15.0	72	90	63.5	A	[83]
	9.81	4.65	14.45	68.5	90	66	A	[84]
	9.8	5.25	14.9	50.5	90	72	A	[89]
	9.52	5.35	14.9	48.5	90	74.7	A	[82]
	4.9	5.4	14.9	49	77	63	P	[85]
	4.78	4.13	13.1	81.5	75.2	65.4	P	[86]
Monoclinic $\beta$	9.75	15	8.02	90	65	90	A	[81]
	9.52	14.9	4	90	67.5	90	A	[82]
Monoclinic $\gamma$	9.48	29.4	4.51	90	118.5	90	A	[81]

In particular, unit cell parameters of  $\alpha$ -phase have been studied dominantly because  $\alpha$ -phase is the most stable and basic crystal structure of Nylon-11. There were two main debates regarding chain conformation and configuration of  $\alpha$ -phase. First, literature evokes the chain conformation of both fully extended chain and zigzag chain around a single bond, corresponding to *c* value of 15.0 Å and 13.1 Å, respectively. However, a majority of studies have suggested that  $\alpha$ -phase Nylon-11 has a fully extended chain conformation with the *c* length of around 15.0 Å. Second, the chain configuration was also a controversial issue because theoretically, the odd-numbered Nylons have equal energy to form hydrogen bonding in both parallel and antiparallel configuration. However, at this moment, the antiparallel chain configuration is generally rather accepted based on experimental results.[82]

Regarding ferroelectric (and piezoelectric) properties, although all the phases of Nylon-11 have a polar crystal structure due to its molecular configuration, only pseudo-hexagonal  $\delta'$ -phase has been investigated extensively. This is because sparse and randomly oriented crystal structures with less hydrogen bonding in pseudo-hexagonal phase ( $\gamma$ ,  $\gamma'$ ,  $\delta$ ,  $\delta'$ ) enabled field induced dipole reversal.[95]–[97] Whereas, in the case of  $\alpha$ -phase, the

field induced dipole rotation was restricted up to the electrical breakdown due to the highly-packed hydrogen bonding and well-ordered crystal structure.

## **2.4.2 Post-treatment techniques**

The research regarding crystal structures of Nylon-11 was carried out with three different post-treatment techniques: thermal annealing, mechanical drawing, and electrical poling.

### **1) Thermal annealing**

Most of the thermal annealing studies were related to Brill transition phenomenon of Nylon-11,[88], [93], [98], [99] and they are well-summarised by Pepin et al.[89] According to the literature, triclinic  $\alpha'$  and smectic pseudo-hexagonal  $\delta'$ -phase Nylon-11 displayed a phase transition around 100 °C inducing the formation of pseudo-hexagonal  $\delta$ -phase, and they became triclinic  $\alpha'$ -phase during the cooling process. In contrast, the  $\alpha$ -phase keeps its lattice symmetry up to the melting point due to the persistence of the hydrogen-bonded sheet-like structure. At high-pressure condition, the temperature for the Brill transition increased because greater energy is required for equalisations of the lattice spacings in  $\delta$ -phase.[90], [100]

### **2) Mechanical drawing**

It must be noted that the mechanical drawing of Nylon-11 does not give rise to a phase transition but does improve both crystallinity and molecular orientation.[101] Zhang et al. reported that the XRD peak of  $\delta'$ -phase became sharper and stronger with the increase of drawing ratio, indicating the enhancement of the degree of crystallinity.[91] Similar increasing trend of crystallinity with strain rate was observed from  $\alpha'$ -phase.[102] The influence of stretching on the molecular orientation was proved by Wu et al.[101] They showed that the remanent polarisation of  $\delta'$ -phase film was improved by mechanical drawing because of improved molecular orientation.

### 3) Electrical poling

As briefly mentioned, the high-voltage poling process generates piezoelectric and ferroelectric Nylon-11, and this was one of the major research topics in the field of Nylon-11. Here, the studies regarding piezoelectricity and ferroelectricity of Nylon-11 is introduced in chronological order because such arrangement would be helpful to understand the current status of Nylon-11 work and to suggest new research directions.

Based on the studies of piezoelectric properties of PVDF and its copolymers, it has been known that the piezoelectricity in semi-crystalline polymers is proportional to the volume fraction of polar crystallites with preferred dipole orientation.[103] As a result, it had been supposed that Nylon-11 should have the large piezoelectric properties due to all-*trans* conformation with large dipole moment in aligned amide group. However, the reported piezoelectric strain coefficients of Nylon-11 in the early stage work were two orders of magnitude less than that of oriented PVDF.[104] This was because the piezoelectric activities of Nylon-11 are quite sensitive to crystal structure and poling conditions.[103] In 1980, Newman et al. first investigated the influence of hydrogen bonding in the Nylon-11 during the electrical poling process.[103] They found that the energy barrier for  $\alpha'$ -phase dipole realignment is too high due to the well-ordered hydrogen bonding, while melt-quenched  $\delta'$ -phase could be poled without breakdown and showed much improved piezoelectric constants ( $d_{31}$ ) of 3 pC/N. In 1984, the effect of uniaxial drawing on piezoelectric response was reported by Mathur et al.[105] In both  $\alpha'$ - and  $\delta'$ -phase case, the magnitude of the piezoelectricity of the stretched film was much higher than that of the unstretched film due to the dipole reorientation. The origin of  $\delta'$ -phase's high piezoelectric coefficient was confirmed by Wu et al. in 1986.[106] Using various crystal structures of Nylon-11, they showed that the lower regularity in the dipole orientation within the  $\delta'$ -phase makes it relatively easier to rearrange the dipoles in parallel to the electric field in the poling process. Takase et al.'s investigation of Nylon-11 showed much higher  $d_{31}$  value at high temperature.[107] At a temperature between 100 and 200 °C, stretched and poled  $\delta'$ -phase exhibited  $d_{31}$  value of 14 pC/N, which was much higher than that of PVDF (~ 5 pC/N). Furthermore, this sample displayed little decay of  $d_{31}$  even after annealing at 185 °C, while PVDF samples showed a significant decay in response, indicating much better thermal stability of Nylon-11 as compared to PVDF. In 1999, the

highest piezoelectricity of Nylon-11 was reported by Wu et al.[101] From stretched (3.5:1) and electrically poled  $\delta'$ -phase film,  $d_{31}$  value of 20 pC/N was achieved at 120 °C, indicating that the orientation of molecular chains and increased crystallinity enhanced the piezoelectricity.

The ferroelectric behaviour of Nylon-11 was firstly achieved by Lee et al. in 1991.[108] Before this literature, researchers concluded that the Nylon-11 samples do not reveal any ferroelectric behaviour, such as electric displacement ( $D$ ) versus electric field ( $E$ ) hysteresis loops. However, via high-voltage poling process,  $D$ - $E$  hysteresis with remanent polarisation value of 68 mC/m<sup>2</sup> was achieved from the cold-drawn or low-temperature annealed (< 100 °C)  $\delta'$ -phase samples. In contrast,  $\alpha'$ -phase and high-temperature annealed  $\delta'$ -phase did not show any ferroelectric behaviour even after electric poling process. The same group also discovered an increased coercive field and a decreased spontaneous polarisation with increasing annealing temperature.[109] Takahashi et al. explained such phenomenon using phase transition from a pseudo-hexagonal  $\delta'$ -phase containing distorted conformation into all-*trans* triclinic  $\alpha'$ -phase.[110] They attributed the origin of the increased ferroelectric switching time after thermal annealing (> 100 °C) to the enlarged potential barrier against the chain rotation in the  $\alpha'$ -phase. The effect of mechanical drawing on the ferroelectric properties was investigated by Wu et al.[101] Interestingly, both undrawn and drawn (3.5:1) films exhibited  $D$ - $E$  hysteresis loops with coercive voltages of 73 and 63 MV/m, respectively. It means that such drawing process gave rise to molecular orientation, so that electric field-induced dipole reorientation became easier in the sample with drawing process. Furthermore, assuming that the dipole switching occurred in the crystalline region, the increased crystallinity via drawing would increase the number of oriented dipoles, resulting in reorientation of more dipoles during the poling process. In 2016, Zhang et al. reported  $D$ - $E$  hysteresis from even-numbered Nylons (Nylon-6 and -12) with mesomorphic (or metastable) melt-quenched phase.[97] Although the size of the hysteresis loop was smaller than that of Nylon-11, high voltage electric poling enabled Nylon-12 to undergo dipolar switching of the dangling bonds and weak hydrogen bonds. It means that that odd-numbered Nylons with polar crystalline structures are not pre-requisites for ferroelectricity. Instead, mesophases with enlarged interchain spacing and disordered hydrogen bonds are the key factors for ferroelectric behaviour of Nylon.

### 2.4.3 Perspectives and challenges

Due to the hydrogen bonding and fast crystallisation speed, Nylon-11 has an extensive degree of polymorphism, and among various phases, thermodynamically stable triclinic  $\alpha$ -, defective triclinic  $\alpha'$ -, and metastable pseudo-hexagonal  $\delta'$ -phases have been studied mainly. The post-treatment techniques of Nylon-11 can be classified into three methods: thermal annealing, mechanical drawing, and electrical poling. The thermal annealing process resulted in phase transition of  $\alpha'$ - or  $\delta'$ -phase to  $\delta$ -phase, and such phenomenon was called Brill transition. The mechanical drawing process did not change the crystal structures but improved the molecular orientation and crystallinity. The electrical poling process enabled Nylon-11 to show piezoelectric and ferroelectric properties. Furthermore, pre-stretched and poled Nylon-11 showed outstanding thermal stability with much higher piezoelectric and ferroelectric behaviours comparable to PVDF.

However, the limitations of the Nylon-11 should also be considered:

- Harsh processing condition for  $\delta'$ -phase fabrication. Such piezoelectric and ferroelectric properties of Nylon-11 were achieved only in the pseudo hexagonal  $\delta'$ -phase, and this is typically produced through extremely fast crystallisation that is required to avoid the formation of large crystal domain. As a result, most of the studies regarding the  $\delta'$ -phase Nylon-11 have been carried out on films grown via melt and ice-quenching. Although several alternative techniques, such as spin coating,[93] vapour deposition,[111] electrospinning,[112] and adding carbon nanostructures,[113] have been suggested, most of these reported approaches resulted in a lower crystallinity and/or still require harsh processing conditions, such as high temperature (290 °C) and/or vacuum condition.
- High-voltage poling process. In order to realise such piezoelectric and ferroelectric behaviour in the  $\delta'$ -Nylon-11, mechanical stretching and/or electrical poling process under high voltage ( $\sim 140$  MV/m) are required. However, such processes are practically unfavourable, thus these are major processing issues that need to be overcome.
- Metastable  $\delta'$ -phase. As discussed, the key to piezoelectric and ferroelectric behaviour is not a polar crystal structure of Nylon-11 but a metastable crystal structure with enlarged interchain spacing and disordered hydrogen bonds because the field induced dipole rotation is restricted up to the electrical breakdown in the well-ordered crystal

structure with highly-packed hydrogen bonding. However, such a concept of metastable crystal structure is inconsistent with the commonly held notion in the field of ferroelectric polymers: that polymers with ordered crystal structures and higher crystallinity generate a better ferroelectric response.

## **2.5 Polymer-based nanocomposite**

With increasing demand for high performance and multi-functional polymers, polymer-based nanocomposites have been proposed and investigated for more than five decades.[114], [115] It was shown, for instance, that the electrical and mechanical properties of polymers can be manipulated significantly by adding a small number of inorganic nanoparticles.[65], [66], [116]

### **2.5.1 Dispersion and distribution issue**

Despite many advantages of polymer-based nanocomposite, the use of nano-insertions in nanocomposites to date has been limited by challenges in nanoparticle dispersion and distribution in polymer matrix.

So far, the fabrication of polymer-based nanocomposite has mainly been achieved by melt-extrusion or doctor-blading techniques. [117], [118]

Melt-extrusion is a well-known process of applying heat and pressure to melt a polymer and mix polymer with inorganic nanoparticles (i.e. nano-insertions) (Fig. 2-11a). Thermoplastic polymer pellets and inorganic nanoparticles are fed together (or separately) through the feeder. A screw of the extruder then forces the mixture of polymer melt and nanoparticles through a hole in a continuous process, resulting in polymer-based nanocomposite. The melt-extrusion method enables high-throughput fabrication of polymer-based nanocomposites, but the aggressive mechanical shearing by screw severely damages the surface of the nano-insertions and deteriorates their mechanical and electrical performance.[119] In addition, it is difficult to obtain decent degree of dispersion via melt-extrusion due to high viscosity of polymer melt.

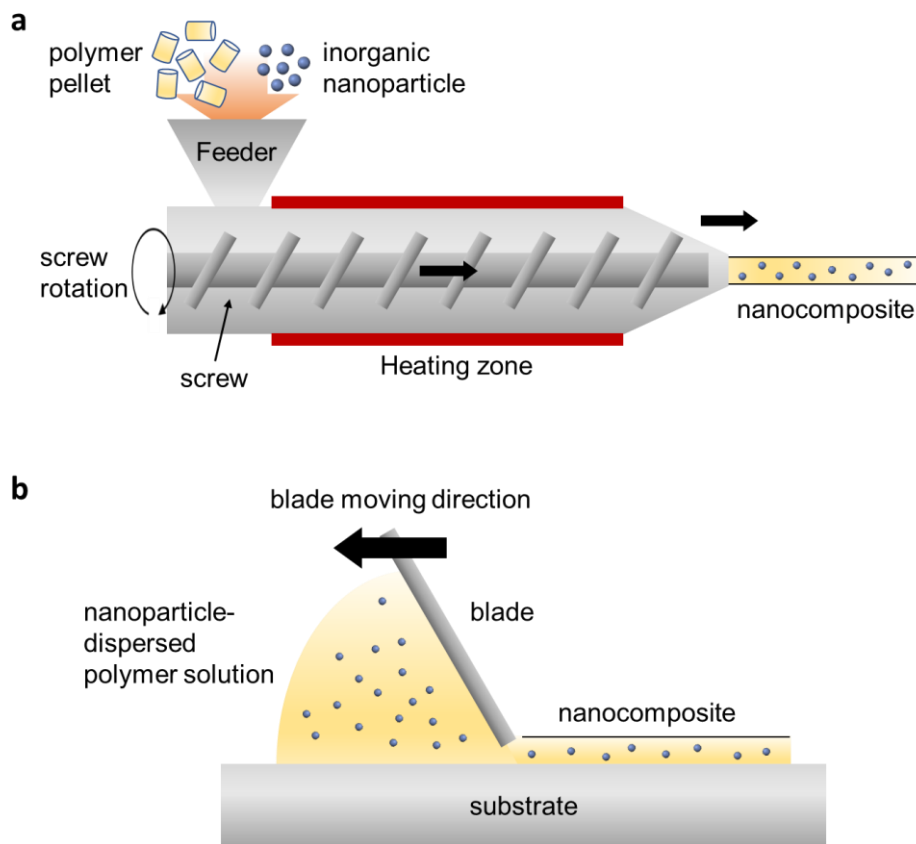


Fig. 2-11 Schematics of conventional synthesis techniques of polymer-based nanocomposite: (a) melt-extrusion and (b) doctor-blading.

As for doctor-blading methods, they enable fabrication of nanocomposites with improved dispersion of nano-insertions by using nanoparticle-dispersed polymer solution (Fig. 2-11b). However, they also suffer from performance degradation of nano-insertions because the extremely high energy input ( $\sim 20,000$  W/L) from ultrasonication is required to disperse nanoparticles in polymer solution. Furthermore, to maintain the degree of dispersion in the solution, destructive or non-destructive functionalization process should be preceded. However, surface defects of nano-insertions by destructive functionalization or phase separation by non-destructive method also decline the performance of resulting nanocomposite.[120] In addition, preparation of nanoparticle-dispersed polymer solution lack in versatility; the process for functionalization or design of surfactant need to be modified and re-optimized for every new material combination.

Lastly, although only the dispersion of nanoparticles in polymer matrix has been focused dominantly in the nanocomposite study, the issue of distribution should also be considered. As shown in Fig. 2-12, nanoparticles can be poorly distributed in the polymer matrix even they are well-dispersed. In this case, the nanocomposite shows large difference of device performance with low reliability depending on the measuring position. However, the ways to solve this distribution issue have not been suggested in the field of nanocomposite because of the intrinsic limitation of aforementioned fabrication processes.

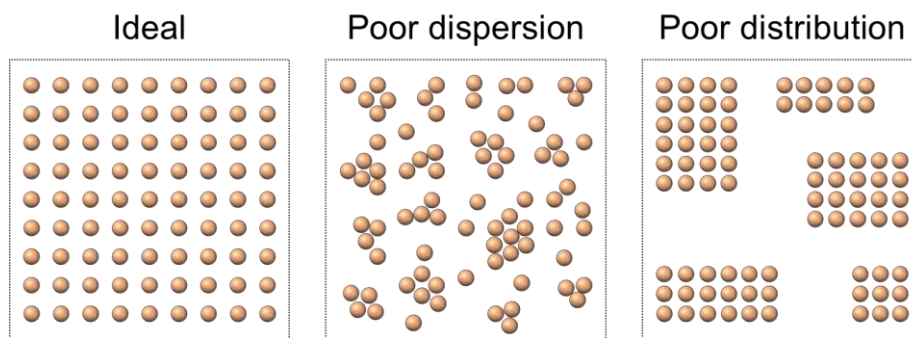


Fig. 2-12 Schematic of dispersion and distribution of nanoparticles in polymer matrix: (left) ideal dispersion and distribution; (middle) poor dispersion with uniform distribution; and (right) well dispersion with poor distribution.

## 2.5.2 Multi-layered nanocomposite

Recently, multi-layered nanocomposites have attracted considerable interest for energy applications, such as capacitor type energy storage device[118], [121], [122] and triboelectric energy harvesting device[43], [75], due to their superior dielectric properties and electrical stabilities. This multi-layered nanocomposite is also fabricated via melt-extrusion and doctor-blading techniques. [117], [118] This means that only thermoplastic polymers can be selected for melt-extrusion method. Furthermore, only cross-linked polymers (i.e. thermoset polymers) or highly viscous polymer solution can be used in the doctor-blade method because solvent in the additional layers can dissolve the former layer. This limited variety of available polymers is a severe issue for the energy applications. Since, in the case of triboelectric generator, properties of polymers, such as charge affinity and mechanical stiffness, should also be considered to realize high-performance device.

Therefore, development of a novel fabrication method which can circumvent these limitations of nanocomposites is essential not only to further enhance the performance of energy harvesting devices and but to extend the range of energy harvesting device applications.

## **Part C. Nano-fabrication technique**

We now discuss the nano-fabrication method crucial to this work.

### **2.6 Template-wetting method**

In this section, details of template-wetting method, which is one of the traditional structure manipulating methods that has emerged in the past two decades as a promising technique to prepare advanced nanomaterials, are discussed. In the first half of this section, the background and underlying fundamentals of the template-wetting method are introduced. In the second half, properties of template-grown polymer nanostructures are presented as compared to their bulk counterpart. Lastly, the achievements and limitations of previous studies are summarised.

#### **2.6.1 Background**

The origin of template-wetting method is a “membrane-based synthesis”, which entails production of the desired materials within the pores of a nanoporous membrane.[123] Because the membranes contain cylindrical pores of uniform diameter, monodispersed nanocylinders of the desired materials, whose dimensions can be carefully controlled, are obtained.[124] Above all, the nano-sized confinement effect was the reason why such synthesis method attracted attention because molecular ordering can be enhanced through this effect. As a result, this membrane-based synthetic method had been used to enhance the electric conductivities of conductive polymers[125]–[127] and studied as a different

crystallisation mechanism of nanoconfined insulating polymers, such as engineering plastics or block-copolymers.[128]–[131] It was widely believed that polymer melt or solution could not infiltrate the small pores in the membrane, thus polymeric nanostructures had usually been achieved via this method with i) additional pressure (melt-press, polymer solution-based vacuum filtration) or ii) smaller particles than pore sizes (polymerisation, monomer vapour deposition).[129] However, in 2002, Stenhardt *et al.* proposed a versatile “template-wetting method”.[132] They showed that polymer melts or solutions could infiltrate nano-sized pores of the template via “wetting” without additional force due to the high surface energy porous templates. Since then, a number of studies regarding novel properties of polymeric nanocylinders have been investigated based on the template-wetting method.

### 2.6.2 Comparison: polymer nano-structuring methods

Polymeric materials with nanoscopic dimensions not only have potential technological applications based on the surface and interface properties but also are of fundamental interest because the physical, chemical, optical, electrical, and structural properties of polymers can change in this dimension of transition between the bulk and molecular scales.

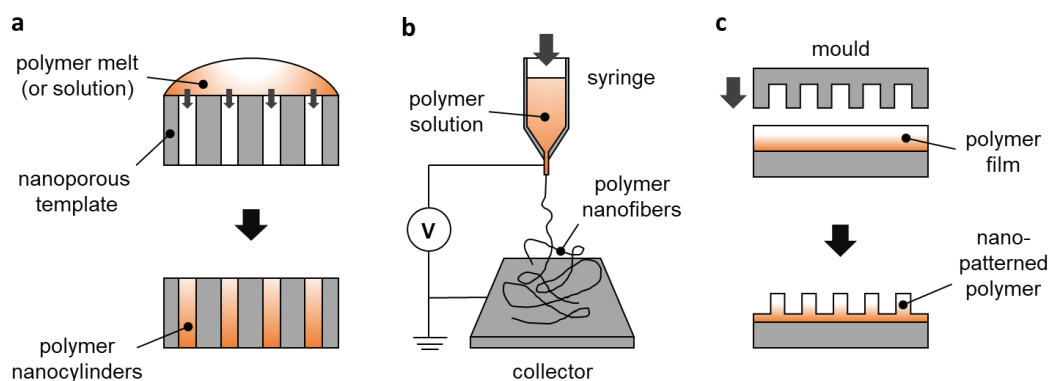


Fig. 2-13 Schematics of polymer nanostructure synthesis techniques: (a) template-wetting, (b) electrospinning, and (c) nanoimprinting methods.

Nanostructured polymers are typically synthesised by three main methods; template-wetting, electrospinning; and nanoimprinting (Fig. 2-13).[133] Template-wetting method produces polymer nanostructures by infiltration of polymer melt or solution into a nanoporous template. In the case of electrospinning, the polymer solution is extruded through a nozzle, where a high electric-field is applied, and deposited on a grounded surface.[134]–[136] Strong drawing and electrical poling during the process result in dipole alignment in the nanofibers. Nanopattern or regular arrays of polymer nanostructures can also be achieved via nanoimprinting.[137]–[139] If the polymer film is pressed above the glass-transition temperature of the polymer by nano-patterned mould, the inverse patterned polymer structure occurs. Table 2-5 shows the advantages and disadvantages of each nanoconfinement method.

Table 2-5 Advantages and disadvantages of three different polymer nanostructure synthesis techniques

	<b>Advantage</b>	<b>Disadvantage</b>
<b>Template-wetting</b>	- preferential crystal orientation - template embedded structure	- limited length of nanocylinder
<b>Electrospinning</b>	- preferential crystal orientation - continuous process - unlimited nanowire length	- less-uniform morphology - high-voltage process
<b>Nanoimprinting</b>	- preferential crystal orientation	- high temp. and pressure process - nanostructure size limitation

All methods have an advantage of preferential crystal orientation, and all with their specific requirements and applicability. In terms of vibrational energy harvesting, the template-embedded structure from template-wetting method would be a significant advantage because such structure not only enables the alignment of polymer nanostructures but also enhance the mechanical stability. Electrospinning is likely to be more appropriate for large surface area application, such as sensor and membrane, due to continuous process and unlimited nanofiber length.

### 2.6.3 Fundamental principles

Template-wetting method involves the mechanisms of wetting, capillarity, and hydrodynamic flow of liquids in cylindrical pores.

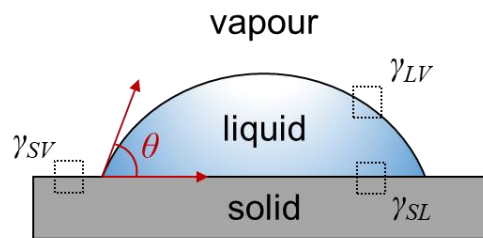


Fig. 2-14 Schematic of partially wetting of liquid droplet on the solid substrate.

When we drop a liquid droplet on a flat substrate, the interaction between liquid and solid substrate can be described by the contact angle ( $\theta$ ). In this case, three different interfacial tensions need to be considered (Fig. 2-14):

- The surface energy of the solid ( $\gamma_{SV}$ )
- The surface tension of the liquid ( $\gamma_{LV}$ )
- The solid-liquid interfacial energy ( $\gamma_{SL}$ ).

The  $\theta$  is determined by the balance of these three interfacial tensions of  $\gamma_{SV}$ ,  $\gamma_{LV}$ , and  $\gamma_{SL}$ , as is defined by Young's equation:

$$\cos \theta = \frac{\gamma_{SV} - \gamma_{SL}}{\gamma_{LV}} \quad (2-32)$$

If  $\theta < 90^\circ$ , wetting will occur, while a system is non-wetting if  $\theta > 90^\circ$ . These wetting regimes can be classified differently according to the spreading factor ( $S$ ), [140]–[142] which is defined by

$$S = \gamma_{SV} - \gamma_{SL} - \gamma_{LV} \quad (2-33)$$

$S$  indicates the interfacial energy difference between the bare substrate and the substrate covered with a liquid. Therefore,  $S \geq 0$  corresponds to complete wetting, and a liquid droplet will spread on the solid substrate spontaneously until complete coverage of the substrate and form a thin liquid film. In contrast,  $S < 0$  corresponds to partial wetting, so that an equilibrium shaped liquid droplet is placed on the substrate with  $\theta$ . When the substrate has a high surface energy ( $\gamma_{SV} = 0.1 \sim 0.5 \text{ J m}^{-2}$ )[143], such as glass, metals, metal oxides, and ionic crystals, liquid with low surface tensions ( $\gamma_{LV} \downarrow$ , including polymer melt and solution) immediately cover (or wet) the surface of the substrate because covering the solid surface and deformation of the liquid droplet are energetically favourable.[144] Interfacial energies ( $\gamma_{SL}$ ) are determined by the intrinsic properties of the solid and liquid.

Capillarity is the tendency of a liquid to fill the capillary tube (or pore) spontaneously. The driving force of capillary infiltration is also surface tension. The capillary pressure difference ( $\Delta p$ ) across a hemispherical meniscus can be described by the Laplace equation:

$$\Delta p = \frac{2\gamma_{LV} \cdot \cos \theta}{r} \quad (2-34)$$

where  $r$  is the pore radius. Thus, if  $\theta < 90^\circ$  (wetting condition), infiltration occurs spontaneously, and if  $\theta > 90^\circ$  (non-wetting condition), capillary infiltration cannot exist unless nanosized droplets are placed outside the capillary.[145] However, in the case of the typical template-wetting method, such situation with nanosized droplets can be ignored.

The hydrodynamic flow of liquids in cylindrical pores can be described for Newtonian liquids by the Lucas-Washburn equation:

$$x(t) = \sqrt{\frac{r \cdot \gamma_{LV} \cdot t \cdot \cos \theta}{2\mu}} \quad (2-35)$$

where  $x(t)$  is a time-dependent displacement of liquid in a cylindrical pore,  $t$  the time,  $\mu$  the viscosity of the liquid.[146], [147] Based on this equation, the rate ( $dx/dt$ ) of the flow of liquid in the cylindrical pores can be estimated by[148]

$$\frac{dx}{dt} = \frac{r \cdot \gamma_{LV} \cdot \cos \theta}{4\mu x} \quad (2-36)$$

Because the  $\mu$ , in turn, depends on the temperature, the filling rate is controlled by the processing temperature. Zhang et al. demonstrated a transition from the partial to complete wetting of polystyrene melt when the annealing temperature was raised above a critical temperature.[142] According to the literature, tailored polymeric nanostructures (nanorods or nanotubes) can be obtained via the template-wetting method simply by controlling the annealing temperature.

#### **2.6.4 Properties of template-grown polymer nanostructures**

As briefly mentioned, the property of confined polymeric structures is different as compared to the bulk. In particular, when the size of the template pores is in the nanometre-scale, the changes in the polymer characteristics are called “nanoconfinement effect”. Many processing parameters of template-wetting affect the nanoconfinement effect and properties of resulting polymer nanostructures. Thus, in this subsection, the parameters are classified into three types: 1) pore-size; 2) temperature; and 3) interfacial interaction changes.

##### **1) Pore-size**

A dominant research topic in the field of template-wetting is the effect of pore-size on the properties of polymer nanostructure. First, the thermal behaviour changes of polymer nanocylinders were reported based on differential scanning calorimetry (DSC) analysis. Both the melting and crystallisation temperature of P(VDF-TrFE) nanowires within pores of < 40 nm diameter were depressed, while the Curie transition was only slightly affected.[149] The melting point depression ( $\Delta T_m$ ) can be explained by Gibbs-Thomson equation:

$$\Delta T_m = T_m - T_m(d) = \frac{4 \gamma_{SL} T_m}{d \Delta H_f \rho_s} \quad (2-37)$$

where  $T_m$  is the normal melting point of bulk,  $T_m(d)$  the melting point of resulting nanomaterials,  $\gamma_{SL}$  the surface tension of the solid-liquid interface,  $d$  the size of resulting nanomaterial,  $\Delta H_f$  the bulk enthalpy of fusion (per g of material), and  $\rho_s$  the density of the solid.[150] According to the equation,  $T_m(d)$  decreases as the dimension of material decreases. The pore size also influence on polymer crystallisation mechanism: nucleation can be changed from heterogenous to homogenous with decreasing pore diameter. Homogeneous nucleation means that only a few defects initiate nucleation and growth crystals due to the small diameter of pores.[149] Such crystallisation temperature reduction was investigated in the polyethylene[151], [152], and semi-crystalline block copolymer[153], [154] nanocylinders. This melting and crystallisation temperature depression behaviour is noticeable at small pore sizes (< 50 nm) where the lamellae are forced to be thinner due to a reduction in the space available to crystallise.[155] It must be noted that the crystallinity of resulting polymer nanostructures was also found to decrease with decreasing pore-size, and was much lower than that of bulk.[151] Second, the polymorphism of polymers could be varied by template pore-diameter. Hamilton et al. reported on pore-size dependent formation of metastable amorphous and thermodynamically stable crystalline phases.[156] Using XRD analysis, Ha et al. demonstrated that a mixture of form II and III of anthranilic acid were observed in 24 nm template, and only form II was observed in 7.5 nm due to the critical nucleus size.[157] Crystal phase transition of PVDF in the nanopores was also observed.[158], [159] Garcia-Gutierrez et al. showed that the arrays of isolated ferroelectric  $\gamma$ -phase nanorods connected by paraelectric  $\alpha$ -phase supporting film could be achieved by template-wetting method (The pore diameter is 200 nm).[158] In the case of P(VDF-TrFE), the portion of ferroelectric  $\beta$ -phase crystals was enhanced and the non-ferroelectric phase was suppressed below the pore size of < 40 nm diameter.[149] Lastly, the pore-diameter affect the dielectric properties of polymer nanostructures. Choi et al. demonstrated P(VDF-TrFE) “nanowires” using 80 nm pores and their piezoelectric properties.[160] The resulting nanowires with thick lamellar and higher crystallinity showed piezoelectric polarization without any treatment. It was also found that a piezoelectric response, in the absence of any poling or

stretching, is obtained upon nanoconfinement on the PVDF and P(VDF-TrFE), which does not show any polarization when in bulk or film form without poling.[161] This is because the nanoconfinement effect attribute the preferential orientation of crystals in the pores and results in polarization without additional stretching or electric poling process, which is referred to as “self-polarization”.

## 2) Temperature

Since processing temperature also plays a vital role in polymer crystallisation, many research have been conducted regarding property changes of polymer nanostructures depending on the temperature. The effect of processing temperature on the crystal structures of syndiotactic Polystyrene (sPS) was reported by Wu et al.[162] By the slow cooling of the melt sPS,  $\beta$ -phase nanorods with preferential crystal orientation could be achieved. In contrast,  $\alpha$ -sPS fabricated by annealing of the melt-quenched amorphous nanorods had no preferred orientation, meaning that the preferred crystal orientation is formed during the crystallisation process *within* the nanopores. Lee et al. showed the way to change the morphology of PVDF nanostructures by very low crystal growth temperature.[163] As a result of placing the solution filled template on a liquid nitrogen contacted plate ( $< 100$  °C), directional cooling crystallisation occurred, and various nanostructures, ranging from spheres to nanofibers, were produced depending on polymer solution concentration (wt %).

## 3) Interfacial interaction

Changing the solid-liquid interfacial energy ( $\gamma_{SL}$ ) also affect the properties of polymer nanostructures because it affects the wetting mechanism. Fu et al. showed that the crystal structure of PVDF nanostructure could be tuned by  $\gamma_{SL}$ . [164] The surface treatment by 3-aminopropyltriethoxysilane (APTES) resulted in stronger interaction between the hydrogen atoms on  $\text{NH}_2$  groups in APTES and the fluorine atoms on the PVDF chains. It was also found that highly polar hydroxyl groups on the template surface induced by plasma-treatment bring out the improvement of polar  $\beta$ -phase proportion in the PVDF

nanowires. Xue et al. reported that the interfacial interaction modified the morphology and crystallisation of Nylon-6 nanowires.[165] While enhancing the interaction of Nylon-6 and the surface of template pores by immersion precipitation, the morphology of nanostructures changed from solid nanofibers, mesoporous, to bamboo-like, increasing the domains of metastable  $\gamma$ -phase. A double-solution wetting method also showed the impact of the solid-liquid interaction in the pores to final morphology.[166] When polystyrene (PS) solution in dimethylformamide (DMF) and poly(methyl methacrylate) (PMMA) solution in acetic acid were infiltrated into the nanopores sequentially, due to the stronger interaction between acetic acid and aluminium oxide template, peapod-like PS/PMMA core-shell nanostructures were obtained.

### 2.6.5 Conclusion

Template-wetting has a great potential for the preparation of polymer nanostructures. Based on the wetting (and capillary infiltration) mechanism, polymer melt or solution can easily infiltrate high surface energy nano-pores and result in the various nanostructures, such as nanotubes, nanowires, nanoparticles. The key boundary conditions for the template-wetting method are pore-size, temperature, and interfacial interaction. Several general trends of template-wetted polymer nanostructures can be extracted from this review section:

- The melting and crystallisation temperature decreases with pore size reduction, and such thermal behaviours are noticeable at small pore sizes.
- The degree of crystallinity of template-grown polymer nanostructures is much lower than that of bulk polymers, and the crystallinity further decreases with pore size reduction.
- Regardless of pore-size or other processing parameters, preferential crystal orientation is achieved in most of the reported polymer nanostructures with perpendicular direction to the cylinder axis.[167], [168] The “self-polarisation” in nanoconfined ferroelectric polymers would be a practical application of this phenomenon because it takes away the need for drawing or electric poling process.

- Polymer crystallisation in the nanopores can be affected by temperature and interfacial interaction, manipulating polymorphism or nanostructures.
- The template-wetting method can be applied to a wide variety of polymer materials, such as general, engineering, functional polymers, and block copolymers.

In summary, the distinct advantage of the template-wetting method is preferential crystal orientation. However, considering that most of the favourable properties of semi-crystalline ferroelectric polymers originate from the crystalline regions, the crystallinity depression would be a severe drawback of the template-wetting method. Therefore, ways to improve the crystallinity of nanoconfined polymer nanostructures should be developed.

# Chapter 3

## Experimental and Computational Methods

This chapter provides an overview of the experimental methods used in the following chapters. The details of sample fabrication are provided with results of reference samples. In addition, characterization techniques of the properties of the polymers used, scanning probe microscopy, electrical measurements, and modelling methods are described.

### 3.1 Fabrication

#### 3.1.1 Conventional film preparation method

Typically, Nylon-11 films were fabricated by melt-pressing, drop-casting, and spin-coating, and the resulting films have different crystal structures depending on processing conditions.

**Melt-pressing.** This method generates  $\alpha'$ - and  $\delta'$ -phase Nylon-11 film. Nylon-11 pellets (molecular weights ( $M_w$ ) of 201.31g/mol, Sigma-Aldrich) were placed on an aluminium

foil on a hot-plate, and then the temperature of the hot-plate was increased up to 230 °C. When the pellet became a molten film, a glass-slide was placed upon the polymer melt and pressure was applied using a tensile machine (Instron 8501) with a force of 200 N. The molten polymer was then crystallised by slow-cooling or ice-quenching methods. In the case of slow-cooling, the temperature of the hot-plate was decreased from 230 °C to room temperature with a cooling rate of 5 °C/min, resulting in  $\alpha'$ -Nylon-11 film.  $\delta'$ -phase could be achieved by quenching the molten film into an ice bath.

**Drop-casting.** Nylon-11 solution was prepared by dissolving Nylon-11 pellets in formic acid (Sigma-Aldrich, Reagent grade > 95%) under constant stirring at 80 °C. Using a pipette (Research Plus 100  $\mu$ L ~ 1,000  $\mu$ L, eppendorf), 800  $\mu$ L Nylon-11 solution was dropped on a silicon wafer and then allowed to dry naturally over 30 min at room temperature. The silicon wafer was used to achieve the films with flat and smooth surfaces. Depending on the targeting crystal structures, the drying process of the polymer solution can be modified. For instance, if the Nylon-11 solution can be dried slowly in a roughly sealed and heated system (where a lid was placed over the sample to fill the environment with vapour of formic acid, and the sample was then placed on a hot plate at 80 °C) the most stable  $\alpha$ -phase Nylon-11 film can be achieved. Details of various drying processes and resulting crystal structures are given in Chapter 8.

**Spin-coating.** Spin-coating is used to generate a thin film of polymer material, and  $\delta'$ -phase Nylon-11 film also achieved by this method. The Nylon-11 solution was dropped on a silicon substrate, which is held by a vacuum pump on a spin coater, and the substrate was spun with a speed of 2,000 revolutions per minute (rpm) for 60 sec. The setting values can be varied to achieve the target thickness and evaporation rate. The spin coater used here was Model WS-650 Mz-23NPPB (Laurell Technologies).

Fig. 3-1 shows the XRD patterns and photographs of Nylon-11 films. As described,  $\alpha'$ - and  $\delta'$ -phase films were produced by a melt-pressing method with slow-cooling and ice-quenching, respectively. The patterns of diffractograms and peak positions are in good agreement with the reported data (Table 2-3).

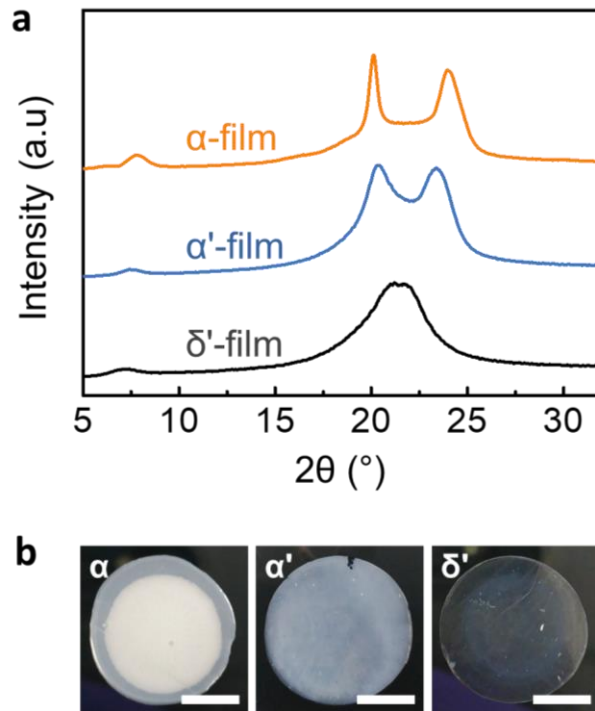


Fig. 3-1 Reference Nylon-11 films with  $\alpha$ -,  $\alpha'$ -, and  $\delta'$ -phase. (a) XRD patterns of each film. (b) Photographs of each film. Scale bar indicates 1 cm.

Inspection of the photograph of films (Fig. 3-1b) allows us to speculate the crystal conformation and degree of crystallinity. The  $\alpha$ -phase film fabricated by drop-casting and slow-cooling method showed white colour due to the well-ordered crystal structures and the highest crystallinity ( $\sim 48\%$ ). In contrast, opaque colour was achieved in the melt and slow cooling film due to the defective crystal structure of  $\alpha'$ -phase. In the case of melt and ice-quenched process, the resulting film was almost transparent because melt-quenched process suppressed crystal growth and formed  $\delta'$ -phase with the lowest crystallinity of  $38\%$ . Fig. 3-2 displays the surface morphology of  $\alpha$ -phase Nylo-11 film as measured by SEM. It shows a rough surface with grain boundaries between spherulite structures.

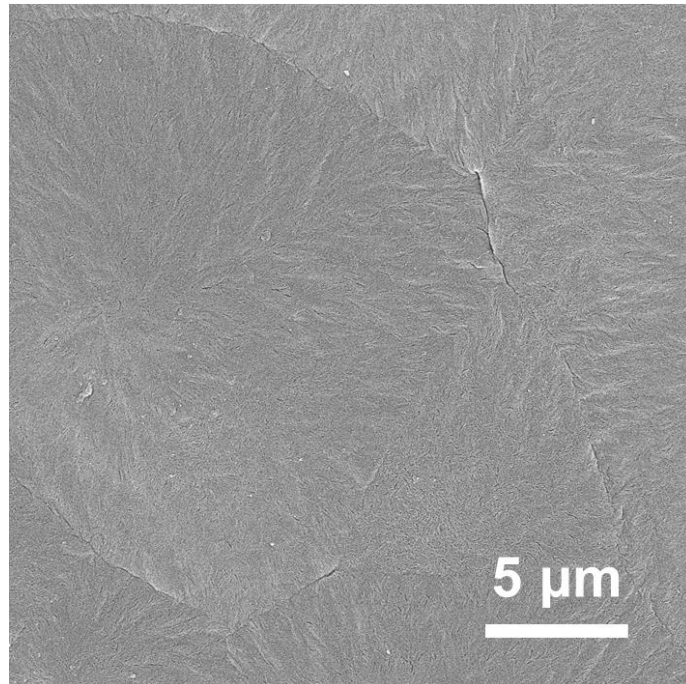


Fig. 3-2 SEM image of  $\alpha$ -phase Nylon-11 film fabricated by drop-casting and slow-cooling method. Microstructure shows the spherulite structures of Nylon-11 with grain boundaries.

### 3.1.2 Nanostructured polymer fabrication method

Polymer nanostructures were fabricated via melt-pressing or template-wetting methods using anodic aluminium oxide (AAO) template (Whatman). The diameter and length (i.e. template thickness) of pores in the AAO template are about 200 ~ 250 nm and 60  $\mu\text{m}$ , respectively (Fig. 3-3). Cross-section of AAO template shows uniform and continuous vertical pores across the template. The effective surface area of nano-pores can be calculated by an image analyser using a SEM image of bare AAO template. According to the SEM images (Fig. 3-4), nano-pores take up approximately 50% area of the AAO template.

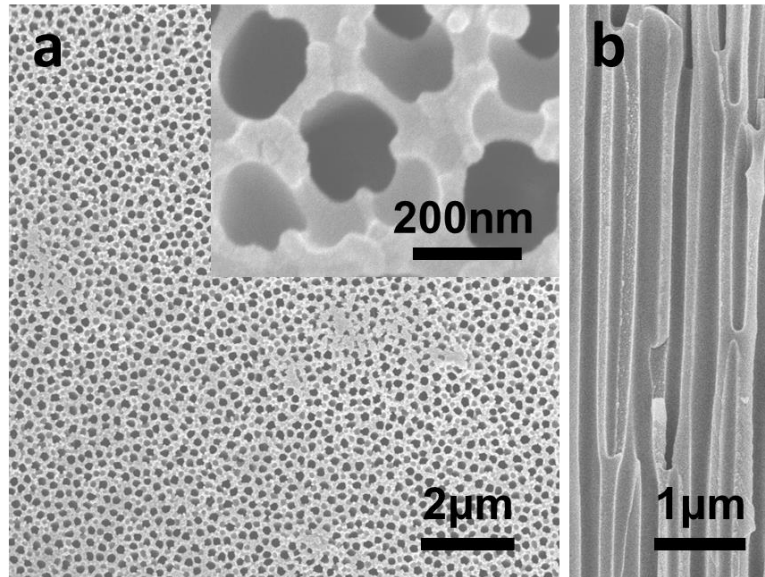


Fig. 3-3 Morphology of AAO template: (a) Surface image and (inset) magnified image of the pores, and (b) cross-section image. Fig. (a) and (b) are taken from the author's work from Ref. [2], reproduced with permission from Royal Society of Chemistry.

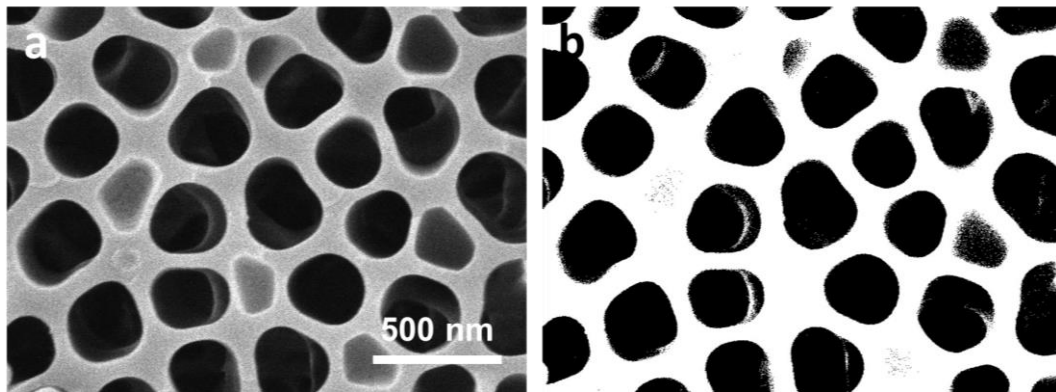


Fig. 3-4 Image analysis for the effective surface area of AAO template calculation. The SEM image (a) was transformed into the black and white image (b). The number of black pixels (pores) were counted and divided by the total number of pixels (whole surface area of the template). As a result, the average effective area was calculated to be  $\sim 48.25\%$ . Fig. (a) and (b) are taken from the author's work from Ref. [2], reproduced with permission from Royal Society of Chemistry.

### 1) Melt-pressing method

As a reference, Nylon-11 nanostructures were fabricated by the melt-pressing method. As before, Nylon-11 pellets were melted on an aluminium foil using a hot-plate, and an AAO template was placed on the molten polymer. Pressure was applied to the AAO template using the tensile machine, then polymer melt can infiltrate into the pores. The crystal structure of melt-pressed Nylon-11 nanostructures is also determined by the crystallisation process followed.

Fig. 3-5 displays the XRD patterns of melt-pressed Nylon-11 nanostructures. The diffractograms of slow-cooling (SC) and melt-quenched (MQ) nanostructures are well-matched with that of  $\alpha'$ - and  $\delta'$ -phase films, respectively. However, the slow-cooled nanostructures show a much sharper peak at  $20^\circ$ , indicating that melt-pressing process resulted in preferential crystal orientation. In the case of  $\delta'$ -phase (melt-quenched sample), XRD patterns of both melt-pressed nanostructure and film were almost the same.

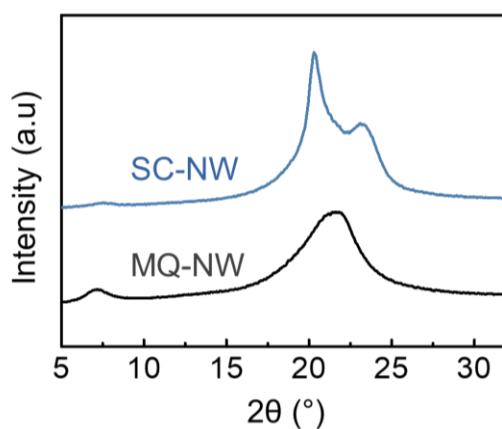


Fig. 3-5 XRD patterns of melt-pressed Nylon-11 nanostructures crystallized by (blue) slow-cooling and (black) melt-quenching methods. SC, NW, MQ indicate slow-cooling, melt-quenching, and nanowire.

The morphology of resulting melt-pressed nanostructures is displayed in Fig. 3-6. To obtain the template-free nanostructures, the nanostructure-filled AAO template was immersed in a 40 vol % phosphoric acid solution for 4 h. The resulting nanostructure mat was then washed in de-ionised water and left to air-dry. As shown in Fig. 3-6e, melt-

pressing technique generated “nanotube” structure with the pore size of  $\sim 200$  nm. In addition, the length of the nanotubes was shorter than that of AAO template. These results indicate that polymer melt did not completely infiltrate the nano-pores during the melt-pressing process. From the macroscopic point of view,  $\alpha'$ -phase nanotubes seem straight (Fig. 3-6a~c). In contrast,  $\delta'$ -phase nanotubes seem to lean over (Fig. 3-6f~h). This phenomenon is likely to be attributed to the difference of mechanical and/or dielectric properties of nanotubes with different crystal structures.

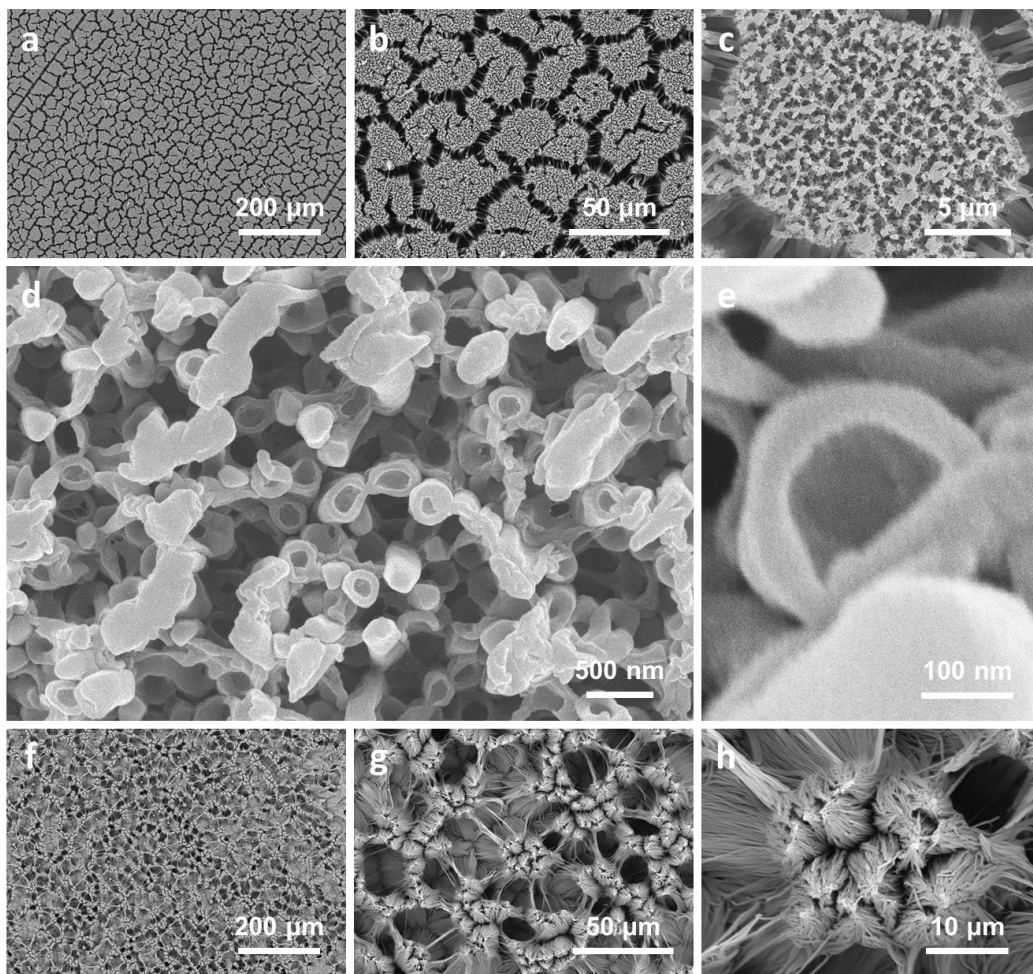


Fig. 3-6 SEM images of Nylon-11 nanostructures fabricated by the melt-infiltration method: (a ~ e)  $\alpha'$ -phase and (f ~ h)  $\delta'$ -phase obtained by slow-cooling and ice-quenching, respectively.

## 2) Solution-based template-wetting

As discussed in Chapter 2.5, template-wetting is a straightforward method for achieving polymer nanostructures.

In this work, Nylon-11 nanowires were fabricated by three different solution-based template-wetting methods: conventional template-wetting; gas-assisted nano-template infiltration (GANT); and thermally-assisted nano-template infiltration (TANI) method. Fig. 3-7 depicts the schematics of each template-wetting method with their processing conditions. As shown in the figure, the dominant factors for crystal structure controlling are gas-flow, solution concentration, vapour-environment, and additional heating. Further details of development and physical meaning of each of these processing parameters are given in Chapter 4 ~ 7.

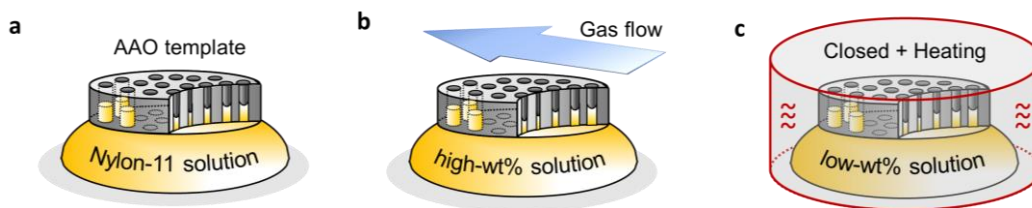


Fig. 3-7 Schematics of Nylon-11 nanowire growth mechanism for (a) conventional template-wetting method, (b) gas-assisted nano-template infiltration (GANT) method, and (c) thermally-assisted nano-template infiltration (TANI) method.

**Conventional template-wetting.** The AAO template was placed on top of 10 wt % Nylon-11 solution. This assembly was then left at room temperature with no additional gas-flow. As the formic acid naturally evaporated through the pores, the solution was drawn up through the pores via capillary forces, and Nylon-11 was able to crystallise into nanowires.

**GANT method.** The AAO template was placed on top of a drop of 17.5 wt % Nylon-11 solution in accordance with the conventional template wetting method. No additional protective layers were added, and the solution was not heated. To control the crystallisation rate of the solution, assisted gas-flow was introduced upon the AAO template using a portable mini fan placed immediately next to the floating template. The rate of assisted gas

was controlled by fan rotation speed and measured by an anemometer. The whole drying experiment proceeded under room temperature.

**TANI method.** 5 wt % Nylon-11 solution was dropped onto a cleaned petridish pre-heated at 40°C. In this method the AAO template was attached to a square glass before placing on top of the solution to limit the exposure of the top surface of the AAO template to the air, thus limiting the rate of formic acid evaporation. Also, a lid of petridish was placed over the sample to further reduce exposure to the surrounding air and to fill the environment using the vapour of formic acid. The sample was then placed on a hot plate (~ 80 °C).

For accurate characterisation of the nanowires, a thin Nylon-11 film formed below the AAO template during fabrication must be removed. To do so, excess material was scraped off using a razor blade. Next, formic acid was warmed on a hot plate to 80 °C and swabbed over the template bottom surfaces using a cotton bud. Once the thin Nylon-11 films had been removed, the nanowire filled template was washed in distilled water and dried at room temperature.

### 3.1.3 Aerosol-jet printing

We now discuss aerosol-jet printing (AJP) technique as the multi-layered nanocomposites fabrication route. To modify AJP for printing the nanocomposite, understanding the processing mechanism is essential. Therefore, this section provides a broad framework for AJP process. The operating principles are described with detailed atomization and aerodynamic focusing mechanisms. Then, the processing parameters for the AJP process are introduced with the example of process optimization for electrode printing. Details of advanced AJP technique for multi-layered nanocomposites is given in Chapter 8. Some part in here has been previously published and therefore has been adapted from that text.[3] Copyright permission and authors' contributions are given in Appendix A.

### 3.1.3.1 Operating principle

As an additive manufacturing process, three-dimensional (3D) printing technique is an emerging application area for functional nanomaterials, with widespread utility spanning sensors, flexible circuits, energy storage and harvesters, and biomedical applications.[169]–[171] In this field, AJP is a relatively recent method compared to another printing toolbox, such as extrusion-based printing (EXP) or inkjet printing (IJP) techniques.[172], [173] However, AJP offers a more versatile alternative to EXP or IJP, especially in terms of the selection of suitable materials for deposition. Because while EXP and IJP are limited to a narrow range of ink viscosities, AJP is capable of ink with a wide range of viscosities between 1 and 1000 cP, allowing variety of materials – from solution-based nano- and bio-materials to polymers – to be deposited over relatively large areas with high printing resolution ( $\sim 10 \mu\text{m}$ ).

A general schematic of the aerosol-jet process is shown in Fig. 3-8. According to the literature by Secor et al., the aerosol-jet printing process is classified by five steps: (i) atomising; (ii) transport; (iii) collimation; (iv) focusing; and (v) impaction.[174]

**(i) Atomising**

: Both ultrasonic and pneumatic atomisers are used to generate a fine mist (i.e. aerosol) of ink material. The size of aerosol droplets is typically 1 to 5  $\mu\text{m}$  in diameter.

**(ii) Transport**

: By a nitrogen carrier gas, the aerosol droplets are transported toward the deposition head (dep-head) through the plastic tubes. Due to the large-surface area of micron-sized droplets, there are rapid solvent evaporation and size reduction of the aerosol droplet when they contact with a dry carrier gas.[174] In addition, some droplets can be lost during aerosol transport process, because of gravitational settling or impingement on tube walls by diffusion.

**(iii) Collimation**

: Within the dep-head, the flow of aerosol is surrounded by a sheath gas.

**(iv) Focusing**

: When the aerosol and sheath gas passes through a deposition tip (nozzle) with the

opening of  $100 \sim 300 \mu\text{m}$ , the aerosol droplets are collimated due to the aerodynamic focusing.

(v) **Impaction**

: Finally, the aerosol droplets are reached to the substrate and deposited, maintaining velocity, focusing, and resolution.

Among various processes, we would like to discuss the mechanism of (i) atomising and (iv) focusing process in more detail because they are a unique process which define the distinct characteristic of AJP relative to other printing techniques.

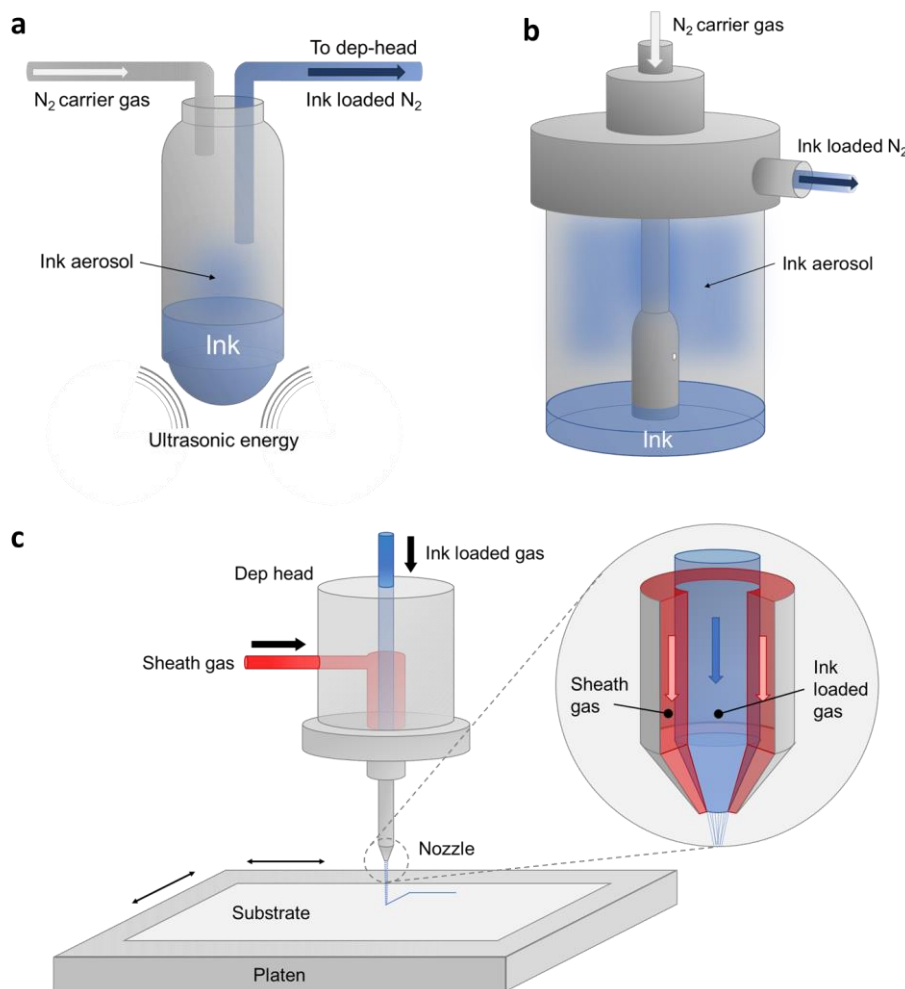


Fig. 3-8 Schematic of the aerosol-jet process: atomization by (a) ultrasonic atomizer and (b) pneumatic atomizer; (c) collimation, focusing and impaction by printing head. Fig. (a) and (c) are taken from the author's work from Ref. [3], reproduced with permission from IOP Publishing.

## 1) Atomising

In the AJP system, there are two different atomisers (ultrasonic and pneumatic atomiser), and they have different atomising mechanisms.[175]

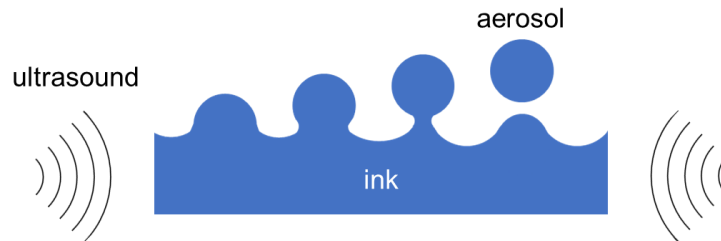


Fig. 3-9 Schematic of ultrasonic atomization mechanism.

In the case of the ultrasonic atomiser, capillary wave structure is induced at the ink surface via ultrasonication with MHz range frequency, creating fine aerosol droplets with a well-defined size distribution of 3 to 5  $\mu\text{m}$  (Fig. 3-9).[176], [177] The ultrasonication power is determined by the amount and viscosity of ink.[178] Therefore, considering maximum ultrasonication power in the system, materials with a viscosity in the range of 1 ~ 10 cP are appropriate for ultrasonic atomization. The size of the aerosol droplet is varied by the density, surface tension of ink and ultrasonication frequency.[178], [179] Solution with nanoscale particles is also able to be atomised, but the size of nanoparticles should be smaller than the final aerosol droplet size. According to the literature, nanoparticles and nanotubes with the size range of 10 nm to 500 nm were printed using the ultrasonic atomising system.

Pneumatic atomisers are extensively used in our daily life for spray and coating applications because fine mist can be achieved easily by air pressure and nozzle. Fig. 3-10 depicts the pneumatic atomisation, including atomisation and virtual impactor. When carrier gas is injected into the chamber through the upper hole, ink is also sucked up through the lower hole due to the pressure difference. Then the ink is sprayed by carrier gas at the nozzle and become fine aerosol with the size of 1 ~ 5  $\mu\text{m}$ . The size of the aerosol droplet is defined by nozzle design, gas velocity, liquid viscosity and surface tension.[180], [181] In contrast to ultrasonic atomization, a wide range of materials with a viscosity of 1 to 1000 cP are able to introduce by pneumatic atomiser because there is no limitation on processing

parameters, such as ultrasonication power. As a result, much bigger suspended particles can be atomised by pneumatic method relative to ultrasonic. The virtual impactor is used to remove excess atomisation gas or small molecules, condensing aerosol droplet stream.[182] However, due to the virtual impactor, the selection of inks with high vapour pressure is avoided because it would be dried during the process and printed as a powdery form. Therefore, low or medium vapour pressure solvent is appropriate for pneumatic atomization.[175]

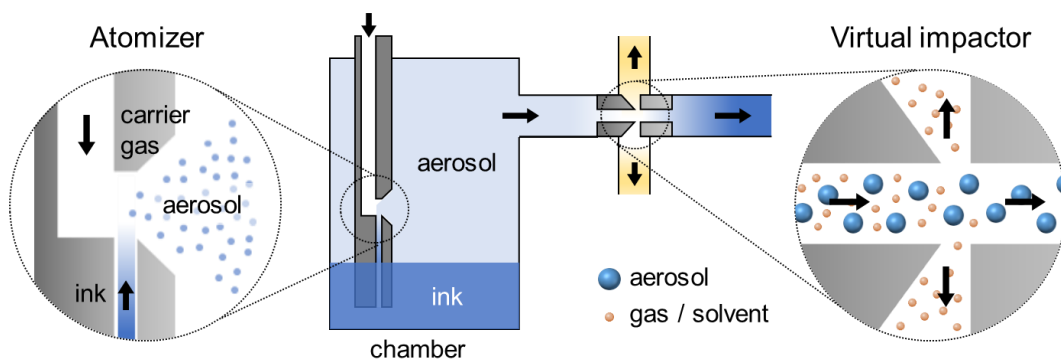


Fig. 3-10 Schematics of the pneumatic atomisation mechanism. Left and right circle show the magnified images of the atomiser nozzle and virtual impactor, respectively. Blue and orange spheres indicate aerosol droplets and gas (or solvent) molecules, respectively.

Considering the design of atomisers and atomisation mechanisms, relatively smaller amounts of material can be atomised by the ultrasonic system compared to the pneumatic atomiser. In addition, inks with high vapour pressure can also be used to ultrasonic atomised. In contrast, the pneumatic atomiser is appropriate to materials with high viscosity ( $> 10$  cP) and with the large size of suspended particles.

## 2) Focusing

When aerosol droplets are transported by a carrier gas, the aerosol gas-flow is surrounded by sheath gas-flow and collimated in the dep-head, generating a form of “jet” (or “beam”). This process is called “focusing”. Because the diameter of resulting aerosol-jet flow determines the printed line width, the focusing process is directly correlated with

the resolution of the aerosol printer. Binder et al. proposed the analytical model for aerosol-jet focusing.[183] There are two assumptions for the calculation. First, the aerosol and sheath gases are incompressible and laminar, which is described by the law of Hagan and Poiseuille. If the Reynolds number ( $Re$ ) is 800, the laminar flow can be sustained in the tube.[183] Next, both gases are not mixed and separated. The schematic of the flow profile at the nozzle is shown in Fig. 3-11. Both gases are axially symmetric, and the aerosol gas-flow is cylindrically surrounded by the sheath gas-flow.

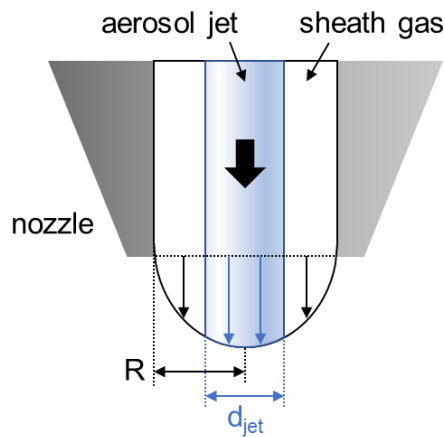


Fig. 3-11 Schematic of the aerosol flow profile at the printer nozzle.[183] The blue shade area displays the aerosol-jet flow.  $R$  and  $d_{jet}$  indicate the radius of the nozzle and aerosol-jet diameter, respectively.

Based on the assumptions, the flow profile  $U(r)$  is defined by

$$U(r) = v_a - v_s = \frac{2(Q_a + Q_s)}{\pi R^2} \times \left(1 - \frac{r^2}{R^2}\right) \quad (3-1)$$

where  $v_a$  is the velocity of aerosol-jet gas,  $v_s$  the velocity of the sheath gas-flow rate aerosol-jet flow rate,  $V_s$  the sheath gas-flow rate, and  $R$  the channel radius of the nozzle. By integrating Eq. (3-1), the aerosol-jet diameter  $d_{jet}$  can be calculated by

$$V_a = \int_0^{2\pi} \int_0^{d_{jet}/2} U(r) dr d\theta \quad (3-2)$$

$$d_{jet} = 2R \times \sqrt{1 - \sqrt{\frac{FR}{FR + 1}}} \quad (3-3)$$

where FR is the focus ratio ( $FR = Q_s / Q_a$ ).

Eq. (3-3) shows that the aerosol-jet diameter  $d_{jet}$  (= final printing width) only depends on the FR and size of the nozzle ( $R$ ), indicating that the printing resolution can be generalised by processing parameters regardless of kind of inks.

### 3.1.3.2 Processing parameters

Based on the ink atomising and aerosol focusing mechanism, the key processing parameters of AJP system can be summarised as follows: the aerosol-jet flow rate ( $Q_a$ ), the sheath gas-flow rate ( $Q_s$ ), the ( $R$ ), and the aerosol droplet size.[174] As discussed, these parameters determine the final resolution of the printer. However, to achieve the best quality of printed pattern, other processing parameters should also be optimised because they also affect morphology and uniformity. Goth et al. presented some initial investigations on the sensitivity of the process to some of the minor parameters.[184] Mahajan et al. subsequently carried out a more systematic study into the influence of minor parameters on the morphology and electrical properties of silver lines printed on silicon.[185] Thus, we summarise all the processing parameters with affecting factors (output) in Table 3-1. It must be noted that, while the importance of processing parameters, affecting factors are also deviated by properties of inks. Furthermore, the optimised condition for one ink cannot be generalised to other inks.

Table 3-1 Summary of processing parameters and affecting factors (output)

Group	Processing parameter	Output
key	aerosol-jet flow rate	resolution
	sheath gas-flow rate	
	channel radius of nozzle	
	aerosol droplet size	
others	atomiser power, ink temperature	droplet size distribution, aerosol density
	printing speed	thickness and width of printed line
	substrate temperature	drying speed, width of printed line
	tip height	width of printed line (overspray)

### 3.1.3.3 Methods

In this work, AJ200 AJP (Optomec Inc., New Mexico, USA) equipped with an ultrasonic and pneumatic atomiser was used to print conductive electrodes and also polymer-based nanocomposites. Several types of inks are prepared and introduced depending on the applications. A silver nanoparticle ink (Prelect TPS 50 G2, Clariant) was diluted 1:3 by volume with de-ionised water (ink:water), and it was usually atomised in the ultrasonic atomiser. During printing, a constant temperature (20 °C) of Ag ink was maintained using a water bath. 4 wt % P(VDF-TrFE) solution and 50 vol% polyamic acid (PAA) solution were prepared in N-Methyl-2-pyrrolidone (NMP), and they were atomised by the pneumatic atomiser.

Printing tips with a diameter of 150 µm and 250 µm were used for printing silver electrode and nanocomposite, respectively. The tip height of 3 mm was used throughout. The excitation current of ultrasonic atomiser was set to 0.6 mA. Printing speed and substrate temperature were constantly maintained: 1 mm s<sup>-1</sup> and 60 °C for the conductive electrode; and 10 mm s<sup>-1</sup> and 80°C for nanocomposite printing. A variety of substrates including silicon wafer (with native oxide), glass, and Kapton film (5 mils, DuPont) were used. All substrates were washed in acetone and dried with nitrogen gas prior to printing. No surface modification was carried out and a single pass was used for all prints. Post thermal annealing process (at 135 °C) was carried out immediately after printing using an oven (HeraTherm—Thermo Scientific). A Dektak profilometer (Veeco) was used to measure the resulting line profiles, with five profiles being recorded per sample.

### 3.1.3.4 Process optimisation for electrode printing

To print the silver nanoparticle electrode, the optimised printing conditions are investigated by using various combination of gas-flow rates. The gas-flow parameters were varied as part of the investigation included the sheath gas-flow rate ( $Q_s$ , 20 → 160 sccm) and aerosol-jet flow rate of ultrasonic atomiser ( $Q_a$ , 20 → 32 sccm).

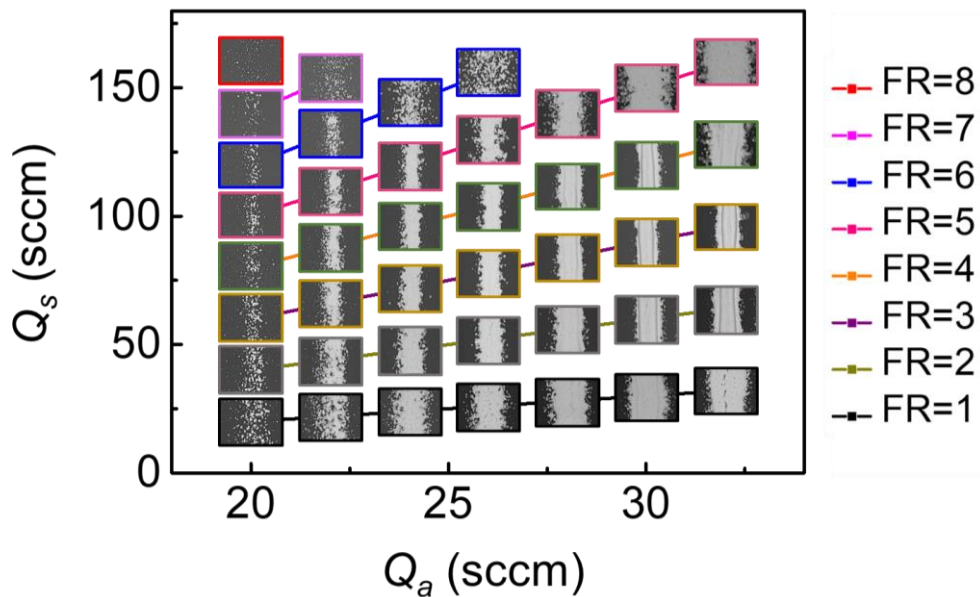


Fig. 3-12 The influence of two gas-flows on printed-line morphology. Lines printed at the same FR ( $= Q_s / Q_a$ ) are grouped together. A clear operability window can be seen for  $Q_a$  between 26 and 30 sccm, with FR between 2 and 4. Figure is taken from the author's work from Ref. [3], reproduced with permission from IOP Publishing.

The influence of the two gas-flow rates on the line morphology is demonstrated in Fig. 3-12. The focus ratio (FR) of each deposition is also highlighted with a different colour. It was found that a minimum  $V_a$  of around 25 sccm had to be reached in order to produce a continuous line. For each value of the  $V_a$ , the deposition could be seen to pass through an operational window as the FR was increased. Using a low FR produced lines that were broad and ill-defined. Increasing the FR improved the deposition, yielding lines with more distinct edges. Increasing the ratio further resulted in lines that were once again poorly-defined. In this way, an optimal window for deposition could be determined. Fig. 3-12

demonstrates that for this particular system (i.e. the combination of printer, ink, substrate, temperature and print speed), acceptable deposition occurs for  $V_a$  of between 26 and 30 sccm with FR between 2 and 4. Including the FR, other printer related factors, such as temperature, resistivity, flexibility, and printing speed, were also investigated and reported in our publication.[3]

## **3.2 Characterization**

This section provides a brief explanation of the characterisation and computational tools used throughout; polymer characterization, scanning probe microscopy, energy harvesting measurements, and modelling. Specific instrument details are also given.

### **3.2.1 Polymer characterisation**

In this section, polymer characterisation techniques are detailed; including scanning electron microscopy (SEM), X-ray diffraction (XRD), Fourier transform infrared (FT-IR) spectroscopy, and differential scanning calorimeter (DSC). We used SEM to investigate the surface morphology. XRD was used to study changes in the unit cell, while FT-IR was used to measure conformational changes. Using DSC, the thermal behaviour and crystallinity of polymer materials were studied.

#### **1) Scanning electron microscopy**

As a standard imaging technique, scanning electron microscopy (SEM) has been used for showing micrometre to nanometre-scale structures. Here, morphological analyses of materials were systematically studied by field-emission scanning electron microscopy (FE-SEM, FEI Nova NanoSEM)) with a beam intensity of 5 keV and desktop SEM (TM3030 Plus Tabletop Microscope, Hitachi) with accelerating voltage of 5 keV. A thin (< 10 nm) conductive layer of platinum (Pt) or palladium (Pd) were deposited on the sample

by using sputter coater (K575, EMITECH) at 40 mA for 20 s to prevent the charge accumulation during SEM imaging.

## 2) X-ray diffraction

The crystal structure of materials was characterised by X-ray diffraction (XRD) using a Bruker D8 diffractometer equipped with Lynx Eye position-sensitive detector (Cu  $K\alpha$  radiation,  $\lambda = 1.5418\text{\AA}$ ). Peak shift due to sample misalignment was adjusted by using a silicon substrate with a single crystal peak of  $32.96^\circ$  for mounting (Fig. 3-13a).

In the case of nanowires in AAO template, diffractograms of background AAO also needed to be considered. As shown in Fig. 3-13b, AAO template showed a broad amorphous pattern with the peak at  $27^\circ$  and two sharp peaks from the polymer supporting rings positioned outside of the AAO. Silicon peak at  $32.96^\circ$  was also observed as nanowires *within* AAO had to be attached on a silicon wafer to do the XRD measurement. Two additional peaks at  $13.5^\circ$  and  $17^\circ$  from support polymer ring did not overlap with diffraction patterns of Nylon or other polymers in this work, but they were removed by controlling the X-ray scan region.

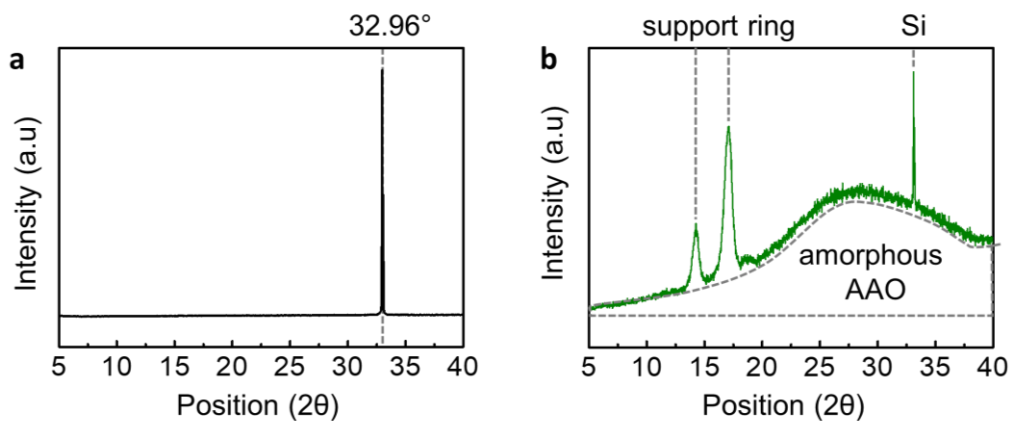


Fig. 3-13 Background XRD. (a) highly p-doped Si wafer displays only one distinct sharp peak at  $2\theta = 32.96^\circ$  within the scanning region from  $2\theta = 5 \sim 40^\circ$ . (b) AAO template shows a broad amorphous peak around  $2\theta = 28.5^\circ$ . Additional peaks of supported polymer rings are detected at  $2\theta = 14.2, 17.1^\circ$ . However, those peaks can be removed by controlling the X-ray scan area.

Differences in the XRD patterns for template-protected nanowires as compared to the freed nanowires suggest that the Nylon-11 nanowires have preferential crystal orientation. This is because, only lattice planes with scattering vectors ( $q$ ) normal to the sample surface produce diffraction peaks in Bragg-Brentano geometry. The template-freed nanowire sample can show all possible diffraction peaks because the nanowires are randomly oriented in the sample (Fig. 3-14a). In contrast, only family of peaks in the diffraction patterns are observed from the nanowires *within* AAO template. If we assume that crystals in the nanowires have unidirectional orientation, the direction of orientation can also be predicted based on the difference of diffractograms. Fig. 3-14b depicts the X-ray diffraction with different lattice directions. In the case of (200) plane, a Bragg-Brentano diffractometer produces a diffraction peak at a corresponding  $2\theta$  angle as Bragg's law is fulfilled. The (210) plane would diffract, however, only a background peak is observed because the lattice planes are not aligned with scattering vector ( $q$ ). This means that, if the sample displays a diffraction pattern with distinct peak corresponding to (200) plane, the orientation of (200) plane must be parallel to the sample surface.

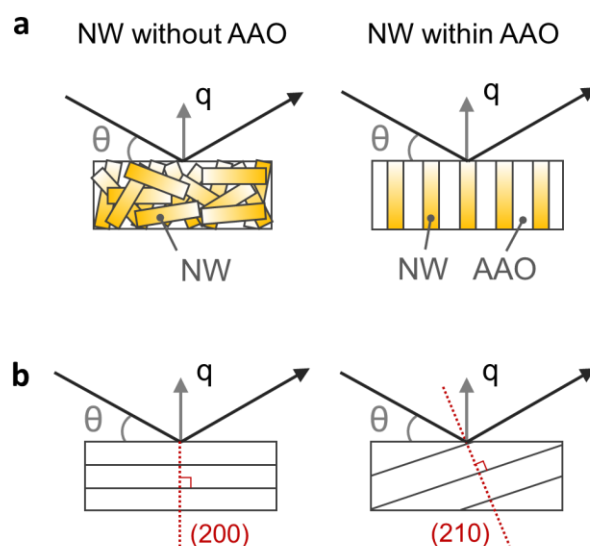


Fig. 3-14 X-ray diffraction mechanism in Bragg-Brentano geometry. (a) Schematics for the orientation of nanowire (left) without and (right) *within* a nanoporous template. Arrows display the direction of X-ray beam ( $\theta$ ) with a scattering vector ( $q$ ). (b) The direction of lattice planes and X-ray diffraction. Fig. (a) and (b) are taken from the author's work from Ref. [186], reproduced with permission from Royal Society of Chemistry.

### 3) Fourier transform infrared spectroscopy

Fourier transform infrared (FT-IR) spectroscopy measurements were carried out using a Bruker Tensor 27 IR spectrometer with attenuated total internal reflection attachment. Following a baseline measurement, the samples were placed on an IR transparent high refractive index crystal on which the IR beam is incident and pressure was applied from a small metal disk to ensure contact between the sample and the crystal.

FT-IR peak positions and their assignments of Nylon-11 are listed in Table 3-2. [187]–[189] The absorbance spectra of Nylon can be classified into four important regions. The region  $500 \sim 800 \text{ cm}^{-1}$  contains the amide V and VI bands. The  $1000 \sim 1400 \text{ cm}^{-1}$  region is characterised by the progression bands from the methylene segments. The amide I and II bands occur at the region  $1500 \sim 1700 \text{ cm}^{-1}$ , and the IR spectra around  $1640 \sim 1680 \text{ cm}^{-1}$  is assigned to amide I mode, which is conformationally related to dipole-dipole interactions.[189] As a result, deconvolution of amide I band can provide information regarding ordered and disordered hydrogen-bonded conformation. In the case of Nylon-11, the contribution of the band at  $1635 \text{ cm}^{-1}$  assigned to ordered hydrogen-bonded domain is distinct, and the contributions of non-hydrogen-bonded and disordered hydrogen-bonded domains are negligible. It means that the relative amount of crystalline region in the samples would be inferred based on the intensity difference between  $1635 \text{ cm}^{-1}$  peaks. Lastly, the  $3300 \text{ cm}^{-1}$  comprises the amide A band assigned to N-H stretching vibration and is sensitive to the strength of the hydrogen bond.[93]

Table 3-2 Region, assignments and peak positions (cm<sup>-1</sup>) of the infrared bands of Nylon-11

<b>region</b>	<b>assignments</b>	<b>peak position (cm<sup>-1</sup>)</b>
amide A	NH stretching	3309
	the overtone of amide I	3275
	combination of amide I and amide II	3197
CH <sub>2</sub> stretching	antisymmetric stretching	2923
	symmetric stretching	2852
amide I	non-H bonded (free)	1676
	H-bonded (disordered / amorphous)	1646
	H-bonded (ordered / crystalline)	1638
	unassigned	1623
amide II	H-bonded	1558
	H-bonded	1540
	free	1516
CH <sub>2</sub> scissoring	NH-vicinal CH <sub>2</sub> scissoring	1477
	CH <sub>2</sub> scissoring (in-phase)	1469
	CH <sub>2</sub> scissoring	1457
	CH <sub>2</sub> scissoring	1437
	CO-vicinal CH <sub>2</sub> scissoring	1419
amide III	amide III	1374
	CH <sub>2</sub> rocking	721

### 3) Differential scanning calorimeter

The thermal behaviour of polymeric materials was studied by differential scanning calorimeter (DSC). By using a Q2000 differential scanning calorimeter (TA Instruments), heating and cooling behaviours of polymer were measured at a rate of 5 °C/minute. All the samples were sealed into Tzero pans (TA Instruments) prior to the measurements.

Using the average data of the DSC peaks, the crystallinity was calculated by means of the equation:

$$\text{Crystallinity (\%)} = \frac{\Delta H_m}{\Delta H_m^0} \times 100 (\%) \quad (3-4)$$

where  $\Delta H_m$  and  $\Delta H_m^0$  are the equilibrium heat of fusion enthalpies of the samples and the perfect crystalline states, respectively.  $\Delta H_m$  is achieved from the area under the DSC melting peak. In the case of Nylon-11,  $\Delta H_m^0$  is around 189 J/g.[99]

#### 3.2.2 Scanning probe microscopy characterisation

Scanning probe microscopy (SPM) characterisation includes Kelvin probe force microscopy (KPFM), piezoresponse force microscopy (PFM), and quantitative nanomechanical property mapping (QNM). Here, all SPM measurements were conducted by a Bruker Multimode 8 with a Nanoscope V controller (Bruker). Antimony (n) doped Si tip (MESP-RC-V2, Bruker) with a nominal radius of ~ 35 nm, a resonant frequency of ~ 150 kHz, and nominal spring constant of 5 N m<sup>-1</sup> were used.

##### 1) Kelvin Probe Force Microscopy

Kelvin probe force microscopy (KPFM) has been used to quantify the work function ( $\phi$ ) of materials. Recently, it is also utilized to investigate the contact electrification at the nanoscale because it can measure the “surface potential” of materials.[32], [190]–[192]

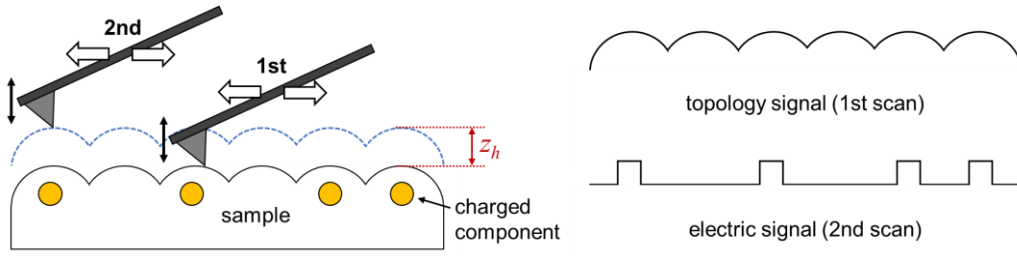


Fig. 3-15 Schematics for the operational mechanisms of Kelvin probe force microscopy (KPFM). (left) First topology scan in TappingMode™ and 2nd interleave scan in LiftMode™ with the lift scan height ( $z_h$ ). (right) Resulting topology and electrical signals during the 1st and 2nd scanning process.

As shown in Fig. 3-15, the topography of the sample is recorded by the mechanical vibration of the cantilever on the first trace and retrace scanning in TappingMode™.[193] (Since the cantilever is vibrating near its resonance frequency, the tuning process to find the resonance frequency of the AFM tip is necessary.) The cantilever is then lifted to the lift scan height ( $z_h$ ) and performed the second scan in LiftMode™ whilst maintaining a constant separation ( $z_h$ ) of the cantilever from the measured topography. (The  $z_h$  can be controlled manually and change the measured values of surface potential.) During the second scan, the mechanical vibration is turned off and an oscillating voltage ( $= V_{AC} \sin \omega t$ ) is applied directly to the tip, where  $V_{AC}$  is the alternating current (AC) voltage amplitude,  $\omega$  the resonant frequency of the cantilever, and  $t$  the time. If we assume that a conductive cantilever tip and a conductive sample form a capacitor structure, the energy ( $U$ ) between tip and sample is derived by parallel plate capacitor model:

$$U = \frac{1}{2} C (\Delta V)^2 \quad (3-5)$$

where  $C$  the local capacitance between the AFM tip and the sample,  $\Delta V$  the voltage difference between the two. Since the  $\Delta V$  consists of direct current (DC) and oscillator induced AC component,  $\Delta V$  can be described as follows:

$$\Delta V = \Delta V_{DC} + V_{AC} \sin \omega t \quad (3-6)$$

where  $\Delta V_{DC}$  includes applied DC voltage ( $V_{DC}$ ) from the feedback loop, work function differences ( $V_{CPD}$ ), surface charge effects, etc ( $V_{etc}$ ). The electrostatic force ( $F_{el}$ ) between tip and the sample can then be expressed as a function of the separation distance ( $z$ ):

$$F_{el} = \frac{1}{2} \frac{\partial C}{\partial z} (\Delta V)^2 \quad (3-7)$$

This means that the local surface potential can be achieved by varying the  $V_{DC}$  applied to the tip. Between tip and sample, if  $\Delta V$  is non-zero, the cantilever experiences  $F_{el}$ , and amplitude can be detected during vibration. However, if  $\Delta V$  become zero by adjusting  $V_{DC}$ , cantilever amplitude will be zero. As a result, the relatively weak but long-range electrostatic interactions can be measured, minimizing the influence of topography.[193]

In the same way, the work function ( $\phi$ ) of materials can also be calculated. In principle, when there is a contact between two different conductive materials, electron flow occurs from the material with lower work function ( $\phi_1$ ) to the material with higher work function ( $\phi_2$ ) to equalize the Fermi energy level ( $E_F$ ). If we assume that these two conductive materials are charged with equal and opposite surface charge on each side, a potential is developed between two materials like a parallel plate capacitor. Such potential is called the contact potential difference (CPD), which equals the work function difference ( $\phi_2 - \phi_1$ ) between the two materials. Therefore, voltage induced by CPD ( $V_{CPD}$ ) is given by

$$V_{CPD} = \frac{\phi_2 - \phi_1}{e} = \frac{\phi_{sample} - \phi_{tip}}{e} \quad (3-8)$$

where  $e$  is the elementary charge ( $= 1.60217662 \times 10^{-19}$  C). To measure  $\phi$  of a material,  $\phi$  of the AFM tip needs to be measured using a reference material. Using a MESP-RC-V2 tip, the surface potential of a reference gold (Au) film with  $\phi \sim 5.1$  eV was measured (Fig. 3-16). An average  $V_{CPD}$  of 462 mV is obtained, and  $\phi_{tip}$  of 5.84 eV is calculated. Now,  $\phi$  of samples can be measured by KPFM as long as the same tip and lift scan height ( $z_h$ ) are maintained.

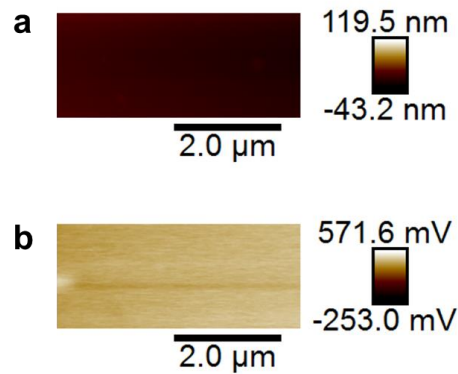


Fig. 3-16 KPFM characteristics of Au sample: (a) Topography and (b) surface potential images. The lift scan height, and tip velocity were 80 nm, 10  $\mu\text{m/s}$ , respectively. The average surface potential value of Au is 462 mV.

## 2) Piezoresponse force microscopy

Piezoresponse force microscopy (PFM) enables the visualization and manipulation of piezoelectric (or ferroelectric) domains. When AC bias of  $V_{AC} \sin \omega t$  is applied to the sample through the AFM tip (i.e. cantilever) in contact mode, the size of piezoelectric domain is changed due to the converse piezoelectric effect (Fig. 3-17a). The deflection of laser induced by displacement of the cantilever can be detected by the position sensitive photodetector (PSPD). A lock-in amplifier received the resulting signals from PSPD and demodulate it. The topography and piezoresponse, including the amplitude and phase of in-phase/out-of-phase deflection, are then measured simultaneously by z-feedback controller and lock-in amplifier, respectively.[193] The piezoelectric response and corresponding detection mechanism by PFM are illustrated in Fig. 3-17b, c. When electric field ( $E$ ) aligns parallel to the spontaneous polarization ( $P$ ) of piezoelectric material (in-phase), the cantilever is vertically lifted by  $d_{33}$  effect, changing in vertical deflection of laser. When  $E$  and  $P$  are orthogonal (out-of-phase), a shear movement of piezoelectric material is detected due to the  $d_{15}$  coefficient and causes a torsional bending of the cantilever changing in horizontal deflection of laser.

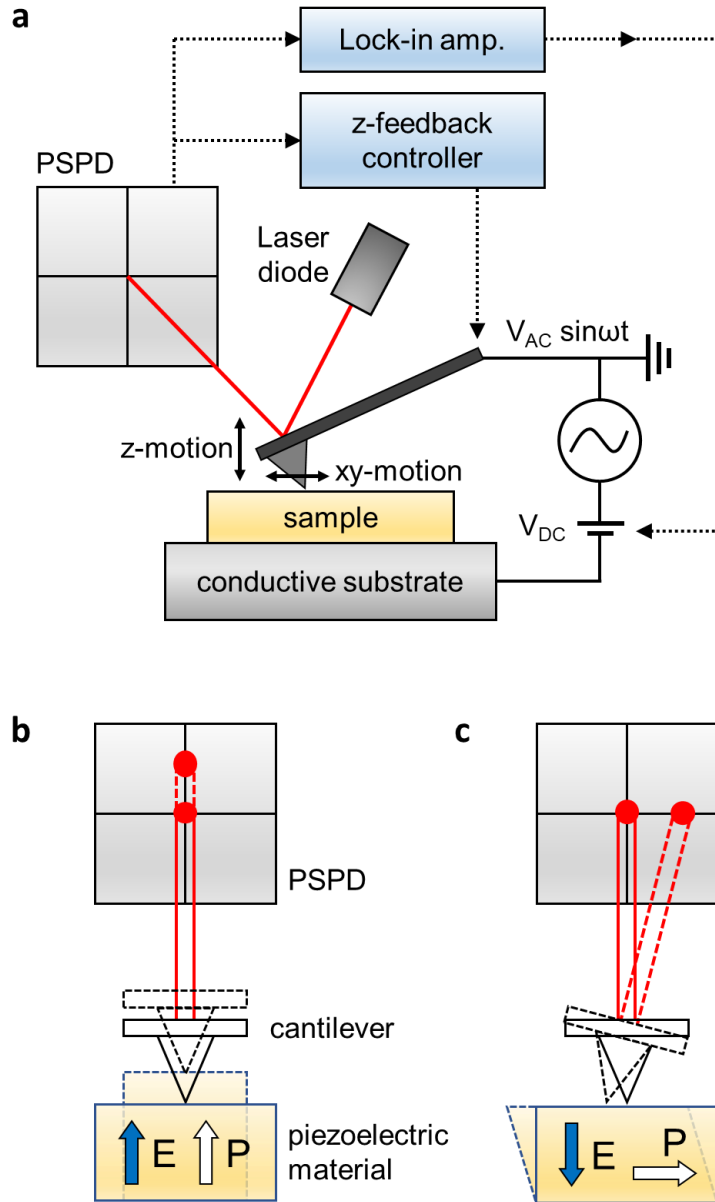


Fig. 3-17 Schematic representations of the operational mechanisms of piezoresponse force microscopy (PFM): (a) the contact mode PFM used, (b) vertical and (c) lateral displacement of piezoelectric materials (i.e. piezoresponse) with cantilever movement.  $E$  and  $P$  indicate applied electric field and internal polarization of piezoelectric material, respectively.

A DC bias is also able to be applied to the tip and changes the polarization of piezoelectric domains. The amplitude and direction of polarization of piezoelectric domains can be controlled by the signal (positive or negative) and amplitude of the DC voltage, respectively.

To calibrate the PFM, a periodically poled lithium niobate ( $\text{LiNbO}_3$ ) calibration sample (Bruker) was used. To reduce the electrostatic interaction between tip and sample, the surface potential of sample is measured preliminarily using KPFM. The measuring surface potential of the sample is then applied to the tip. By tuning the phase of a lock-in amplifier, the maximum in-phase piezoelectric signals can be achieved without out-of-phase component.[194], [195] It is noted that the slight increasing trend of PFM response amplitude can be also observed in non-piezoelectric material due to the internal voltage coupling of the PFM equipment.[194] The measured piezoresponse of non-piezoelectric material can be used to calibrate the signals from such coupling effect.

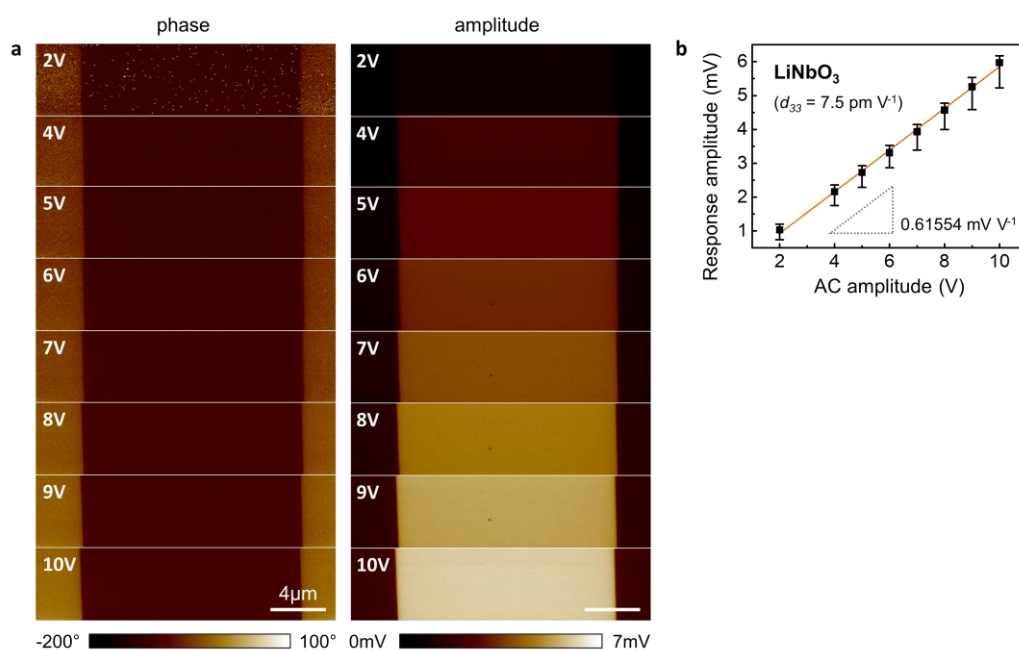


Fig. 3-18 PFM characteristics of calibration sample ( $\text{LiNbO}_3$ ). (a) Phase (left) and amplitude (right) mapping as a function of AC amplitude. (b) Piezoelectric response amplitude of  $\text{LiNbO}_3$  as a function of AC amplitude. Fig. (a) and (b) are taken from the author's work from Ref. [186], reproduced with permission from Royal Society of Chemistry.

A linearly increasing trend of vertical PFM response can be achieved by ramping the AC amplitude (Fig. 3-18). To account for the difference between the zero-to-peak applied voltage input and the RMS output of the lock-in amplifier, the PFM response amplitude needed to be corrected by a factor of  $\sqrt{2}$ . The slope of the resultant trend ( $\sim 0.62$  mV/V) and the piezoelectric coefficient of  $\text{LiNbO}_3$  ( $d_{33} = 7.5$  pm/V) allows us to calculate a vertical sensitivity of  $82 \mu\text{V/pm}$ .

### 3) Quantitative nanomechanical property mapping

Quantitative nanomechanical property mapping (QNM) was used to explore the mechanical properties of the different crystal structures in a film and a single nanowire.[196], [197] QNM, using an AFM operated in TappingMode™, can be used to simultaneously map sample topography, elastic modulus, adhesion, deformation, and dissipation with nanoscale resolution via the analysis of force-distance curves at every pixel of the scanned area.[198]–[200]

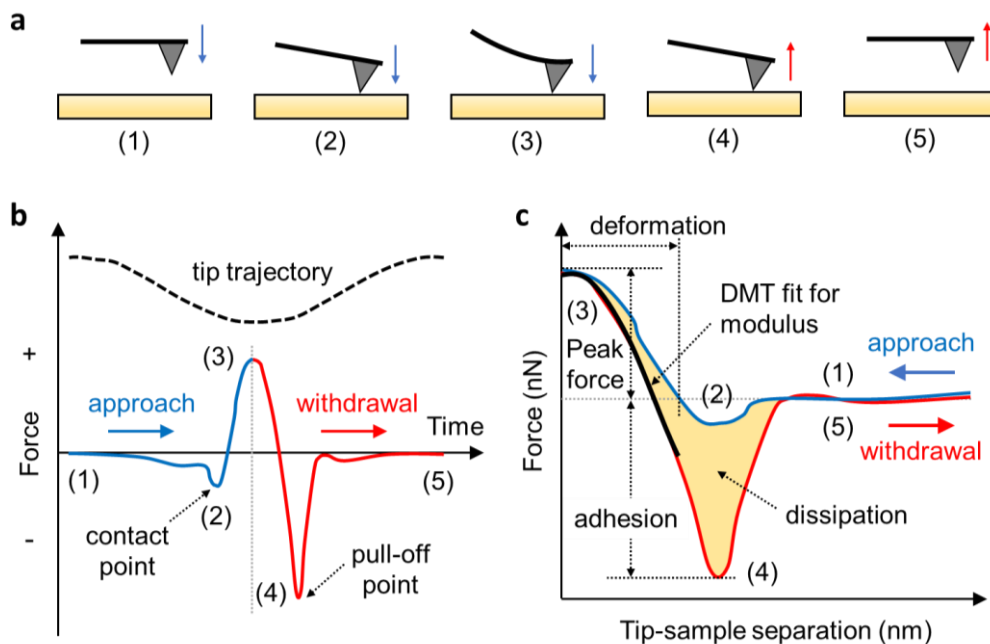


Fig. 3-19 Operation mechanism of QNM: (a) Schematics for approaching and withdrawing motion of AFM tip in TappingMode™; (b) plot of force (blue, red solid lines) and z-position of tip (dashed line) as a function of time; and (c) force-separation plot and resulting nanomechanical properties of sample.

Fig. 3-19a demonstrates the approaching and withdrawing motion of probe in TappingMode™. The changes in z-position (dashed line) and the measured force during the motion (red and blue solid lines) are plotted in Fig. 3-19b. At position (1), the force is very small or zero because the distance between tip and sample surface is far enough. When the tip approaches the surface, attractive force, such as van der Waals and electrostatics forces, pulls down the tip toward the surface until the tip contacts the surface (position 2). (This attraction is represented by the negative force.) Due to the downward motion of the tip by the system, the repulsion force between tip and sample then increases until the tip reaches its bottom-most position (position 3). The value of force at position (3) is defined as the “peak force”, and it is measured and kept constant by the feedback system. After position (3), the system forces tip to withdraw from the surface. The repulsive force then decreases and the adhesion increases. When the force reaches the minimum (at position 4), the tip is pulled-off from the surface. Like position (1), once the tip has fully pulled off the surface, there is no force between the tip and surface (position (5)). To calculate the nanomechanical properties, the force curve is converted to force vs. tip-sample separation curve (Fig. 3-19c). To calculate Young’s modulus, the withdrawal curve is fit using the Derjaguin–Muller–Toporov (DMT) model:[200], [201]

$$F - F_{adh} = \frac{4}{3}E^*\sqrt{R(d - d_0)^3} \quad (3-9)$$

where  $F - F_{adh}$  is the force on the tip relative to the adhesion force ( $F_{adh}$ ),  $E^*$  the reduced modulus,  $R$  the tip end radius, and  $d - d_0$  the deformation of the sample.  $E^*$  can be described by

$$E^* = \left[ \frac{1 - \nu_s^2}{E_s} + \frac{1 - \nu_{tip}^2}{E_{tip}} \right]^{-1} \quad (3-10)$$

where  $\nu_s$  is the Poisson’s ratio of the sample,  $E_s$  the Young’s modulus of the sample,  $\nu_{tip}$  the Poisson’s ratio of the tip, and  $E_{tip}$  the Young’s modulus of the tip. If we assume that  $E_{tip}$  is infinite, the  $E_s$  can be calculated using  $\nu_s$ . (In this work, the focus is on elastic modulus of materials, thus we opted not to deal with other nanomechanical properties, such as adhesion, deformation, and dissipation, in more detail in this section. The ways to acquire those properties are well-established in the literature.[200])

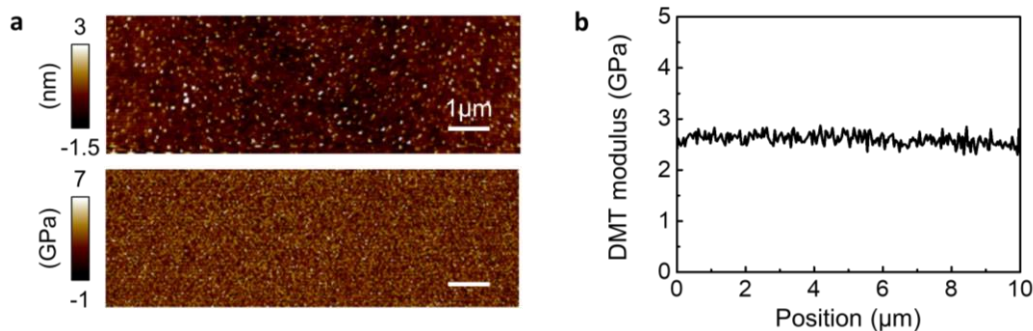


Fig. 3-20 QNM characteristics of the calibration sample (PS). (a) Topology (above) and DMT modulus (below) mapping of the surface of PS. (b) DMT modulus of PS as a function of position. Fig. (a) and (b) are taken from the author's work from Ref. [186], reproduced with permission from Royal Society of Chemistry.

QNM calibration was performed according to the manufacturer's (Bruker) instructions. First of all, the tip calibration (including deflection sensitivity measurement and thermal tune) was conducted using standard sapphire samples. Then, to calibrate the measuring condition, the DMT modulus of a Polystyrene (PS) film (Bruker) was recorded. Since the DMT value of a standard PS film is already known (2 ~ 3 GPa), we tuned parameters such as peak force amplitude and frequency to reach the specified DMT value. Fig. 3-20 shows QNM mapping of a standard PS sample. A DMT modulus of 2.6 GPa was achieved in PS reference film via calibrated scanning.

### 3.2.3 Electrical property characterization

#### 1) Dielectric constant

Dielectric permittivity measurement of polymer nanocomposites in this work was carried out by depositing nanocomposites on highly doped silicon wafer acting as the bottom electrode, and then sputtering Au electrodes on top of the sample with square mask with the size of  $(300 \mu\text{m})^2$ . The dielectric properties were recorded between frequencies of 100 and 100 kHz using an impedance analyser (4294A, Agilent Technologies) in the Cp–D (parallel capacitance – dissipation factor) mode. The dielectric constant is calculated using the capacitor equation  $C = (k \cdot \epsilon_0 \cdot A) / d$  where  $k$  is the dielectric constant,  $\epsilon_0$  the permittivity of vacuum ( $8.854 \times 10^{-12}$  F/m),  $A$  the active measurement area ( $= 90,000 \mu\text{m}^2$ ),

*d* the thickness of nanocomposite. The thickness of the film was measured by a Dektak profilometer (Veeco), with five profiles being recorded per sample.

## **2) Energy harvesting performance characterization**

To characterise energy harvesting performance, ~ 100 nm thick Au film was sputtered on either side (or bottom side) of sample for piezoelectric devices (or triboelectric devices). In the case of the piezoelectric device, a shadow mask was used to prevent Au from being deposited to the edge of the template, with a few mm being left around the edge to prevent the possibility of shorting the top and bottom Au electrodes. Thin copper wires were attached on these surfaces using conductive silver paint for electrical access to the Nylon-11 nanowires *within* the template. For the triboelectric generator, an Au-coated Teflon film was prepared as a counterpart substrate.

A vibration generating system was designed and constructed by Dr Richard Whiter from our group.[202] Briefly, magnetic shaker (LDS Systems V100) was connected to an amplifier (LDS Systems PA25E-CE) driven by a signal generator (Thurlby Thandor TG1304) to generate vibration motion based on a programmed signal in the signal generator.[202] Energy harvesting data in the form of output voltages and currents were collected by data acquisition modules. Two different modules were used to record the electrical data on a computer depending on the purpose; multimeter (Keithley 2002) for voltage and picoammeter (Keithley 6487) for current measurement. (Fig. 3-21)

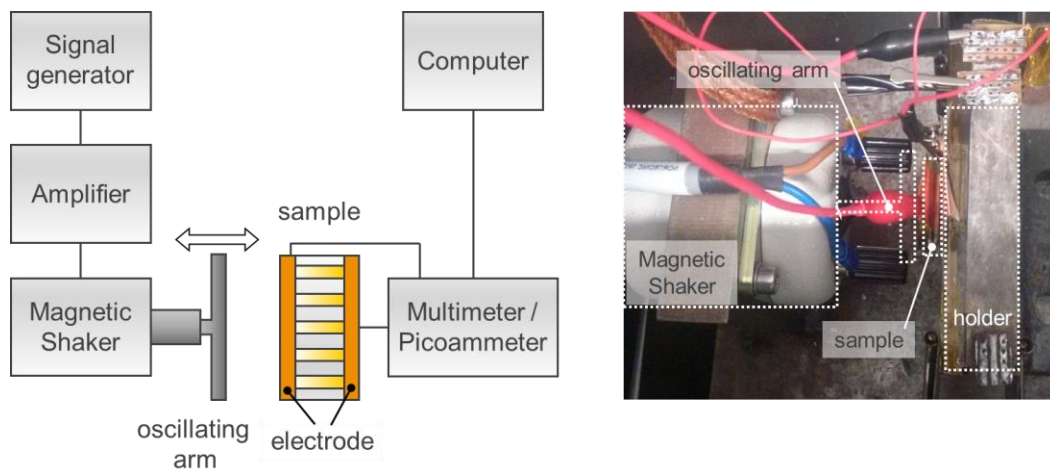


Fig. 3-21 Schematic diagram and photograph of energy harvesting setup.

### 3.2.4 Modelling

To verify and support the experimental result, finite element analysis (FEA) and molecular simulation were conducted using COMSOL Multiphysics 5.2 and Materials Studio 8.0, respectively.

#### 1) Finite element analysis

Using COMSOL Multiphysics software, the simulation of gas-flow dynamics in the GANT method (Chapter 5.2) was demonstrated based on three different effects: the turbulent flow of the assisted gas, heat transfer in all components, and the vaporisation of the solvent in the Nylon solution, while in the template pores. For the turbulent flow, we assumed that the gas-flow rate and pressure field are independent of the property of the used gas, such as moisture content level and temperature. Heat transfer in the model was considered to have two different aspects: conduction and convection. The heat transfer between the template wall and the solution is governed by conduction, while in the gas-flow, the heat transfer via convection and the effect of turbulent flow. The cooling effect during solvent evaporation needs to be considered as well based on the heat of vaporisation

( $H_{vap}$ ). To calculate the amount of vaporised solvent, the material transport equation is used with turbulent flow as a diffusion coefficient.

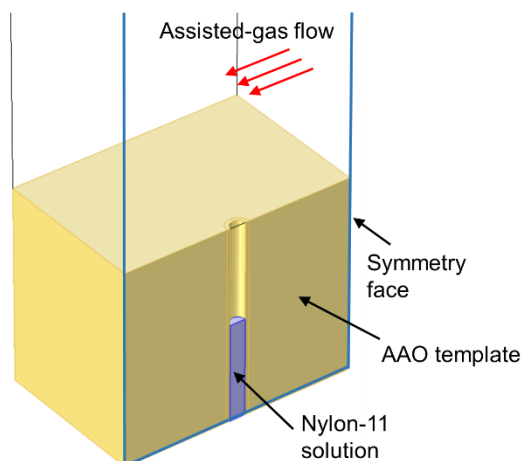


Fig. 3-22 The symmetry geometry used in the simulation. Fig. is taken from the author's work from Ref. [2], reproduced with permission from Royal Society of Chemistry.

The modelling geometry was built based on the experimental conditions. (Fig. 3-22) The inner diameter and thickness of the nanopore is 200 nm (measured from SEM images) and 100 nm, respectively. The height of the nanopore is assumed to be 5  $\mu\text{m}$  filled with 70  $^{\circ}\text{C}$  formic acid having  $H_{vap}$  of 23.1 kJ/mol. The assisted gas is air with an initial temperature of 20  $^{\circ}\text{C}$  and enters to the right side of the geometry. The inlet velocity of the turbulent flow was set by the gas-flow rate.

## 2) Molecular structure simulations

To investigate the molecular level configuration of Nylon-11, we created a refined crystal structure of both the  $\alpha$ -phase and the  $\delta'$ -phase using the Materials Studio 8.0 software package.[203] These simulations were carried out with help from Prof. James A. Elliot, and assisted by Findlay Williams.

The detailed molecular structure of Nylon-11 has never been explored before due to the large amorphous proportion and lack of clarity on the crystalline phase morphology.

Thus, we established the most likely molecular structure using Materials Studio 8.0. First, the rough atomic coordination of Nylon-11 was predicted based on the crystallographic information of another type of Nylons, such as  $\alpha$ -Nylon-6,  $\gamma$ -Nylon-77,  $\alpha$ -Nylon-66 and  $\alpha$ -Nylon-6,10. Next, a force field-based energy optimisation technique allowed us to find the most appropriate molecular geometry and bonding within the proposed unit cell parameters of Nylon-11. We then compared the calculated powder diffraction pattern of the optimised molecular structure to the experimental data in the literature.

The  $\alpha$ -phase Nylon-11 was established based on the  $\alpha$ -phase Nylon-6,10 study by Bunn and Garner.[204] The initial  $\alpha$ -Nylon-11 chain was extrapolated from an  $\alpha$ -Nylon-6,10 model, maintaining a tetrahedral bond angle of  $109^\circ$  between carbon atoms and a torsional angle of  $180^\circ$ . Regarding the chain conformation, we built the structure with fully extended anti-parallel molecular chains, which is the configuration suggested in the majority of Nylon-11 studies. [82]–[85], [90], [205] To determine the unit cell dimensions and the indices of reflections for the triclinic  $\alpha$ -phase Nylon-11, we compared the proposed unit cells in previous studies and took the parameters from the literature by Dosiere et al.[205] These unit cell parameters were then tweaked to achieve optimum matching with experimental data, as shown in Table 3-3.[89] With a satisfactory unit cell in place, the chain configuration was optimised using the Forcite molecular dynamics module. In the case of the most thermodynamically stable  $\alpha$ -phase, a condensed-phase optimised molecular potentials for atomistic simulation studies (COMPASS) force field was introduced in order to perform a geometrical optimisation which acknowledged the effect of electrostatic interactions with hydrogen bonding.[206]

Table 3-3 A comparison between the unit cell parameters determined by Dosiere et al., and the altered set used to match the simulated XRD pattern with the experimental patterns.

	<b>a (Å)</b>	<b>b (Å)</b>	<b>c (Å)</b>	<b><math>\alpha</math> (°)</b>	<b><math>\beta</math> (°)</b>	<b><math>\gamma</math> (°)</b>
<b>Reference (<math>\alpha</math>)</b> [205]	9.65	5.25	14.9	50.5	90.0	72.0
<b>Modelling (<math>\alpha</math>)</b>	9.75	5.15	15.1	51.5	90.0	71.0

The approach to the smectic pseudo-hexagonal  $\delta'$ -phase Nylon-11 model was different from that of the  $\alpha$ -phase, as literature on its structure is less common.[93] The

initial unit cell of  $\delta'$ -Nylon-11 was created using the atomic coordination of hexagonal  $\gamma$ -phase Nylon-77. The  $a$  and  $b$  parameters were kept the same for the Nylon-11 model and the  $c$  parameter was scaled according to the change in chain length between the -77 and -11 configurations. A geometrical optimisation was then conducted on the chain within the constraints of the derived unit cell. In the case of the  $\delta'$ -phase, it was appropriate to use the Universal force field[207] rather than COMPASS; this is because it is known that the direction of hydrogen bonding in  $\delta'$ -phase is random along the chain, so the simulation was set up to intentionally ignore electrostatic effects.

## Chapter 4

# **Nano-Piezoelectric Generator based on Nylon-11 Nanowires Grown by Template-Wetting Method**

In this work, Nylon-11 nanowires were fabricated, for the first time, using a conventional template-wetting method. Unlike the typical gravity-induced template wetting method for P(VDF-TrFE) nanowires,[202] herein, Nylon-11 nanowires were prepared by capillary wetting method, which was necessary in order to prevent fast drying of the infiltrated Nylon-11 solution, and which reproducibly yielded a large density of nanowires of narrow size distribution. In order to carry out further characterisation, the nanowires could be subsequently transferred to any substrate in the form of nanowire mats that resulted upon preferential dissolution of the AAO template in phosphoric acid. More importantly, the Nylon-11 nanowires were found to be self-poled and were incorporated as-grown into template-based nano-piezoelectric generators for energy harvesting with a wide temperature range of operation and excellent fatigue performance, without the requirement of poling via large external electric fields that are otherwise typically required for piezoelectric performance. A substantial amount of this work has been previously

published and therefore has been adapted from that text.[208] Copyright permission and authors' contributions are given in Appendix A.

## 4.1 Growth mechanism of Nylon-11 nanowire

As discussed in Chapter 2.6, in the case of typical gravity-induced template wetting, a polymer melt or solution is typically cast on to the top surface of the template. However, this method was found to be unsuitable for Nylon-11 nanowire formation because incomplete pore-infiltration of the Nylon-11 solution was found to result due to fast evaporation of the formic acid solvent. In addition, a thick film of Nylon-11 was obtained on the top of the template surface, preventing further soaking of the pores, and hence no nanowires were obtained using this method. Capillary wetting was therefore adopted as a viable alternative to ensure complete infiltration of the template pores, for the template-assisted fabrication of Nylon-11 nanowires. A schematic of the Nylon-11 nanowire growth process *within* the pores of an AAO template is shown in Fig. 4-1.

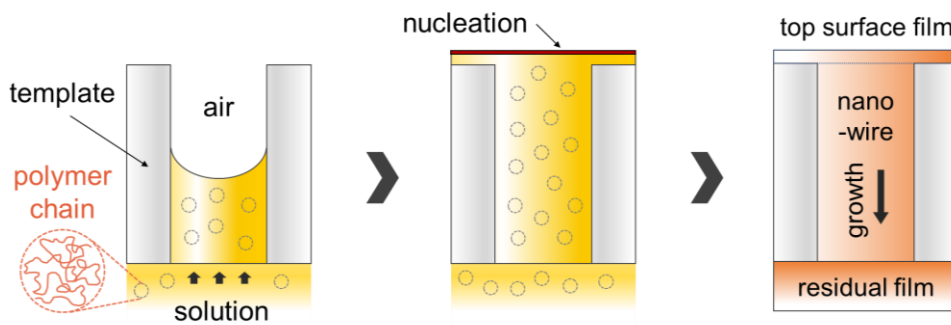


Fig. 4-1 Schematic of the growth mechanism of Nylon-11 nanowires by capillary infiltration within AAO template pore.

The Nylon-11 nanowire formation inside the AAO template is comprised of three steps: (i) Nylon-11 solution infiltration into the AAO template by capillary force, (ii) initiation of nucleation on the top surface of the solution due to the solvent evaporation, and (iii) crystal growth along the AAO template wall. It has been observed that when

templates were wetted with polymers at temperature slightly above their solidification temperatures,[142] the elevated temperature of the polymer solution enhanced the mobility of the molecules. The polymer in solution was found to infiltrate the pores as a liquid thread preceded by a meniscus during capillary wetting. Thus, in our fabrication process, a warm (~ 60 °C) formic acid solution of Nylon-11 was used to infiltrate the AAO template pores by the aid of capillary action. As the solution travelled through the pore channels, a thin Nylon-11 film is formed on the top surface of AAO template (Fig. 4-2). In addition, the thick powdery film with a thickness of ~ 122  $\mu\text{m}$ , originating from the Nylon-11 solution being infiltrated, also remained at the bottom of the template. These top and bottom films were loosely attached to the template surface and could be easily removed by mechanical polishing, leaving a nanowire-filled AAO template. Details of nanowire fabrication method are discussed in Chapter 3.1.2.

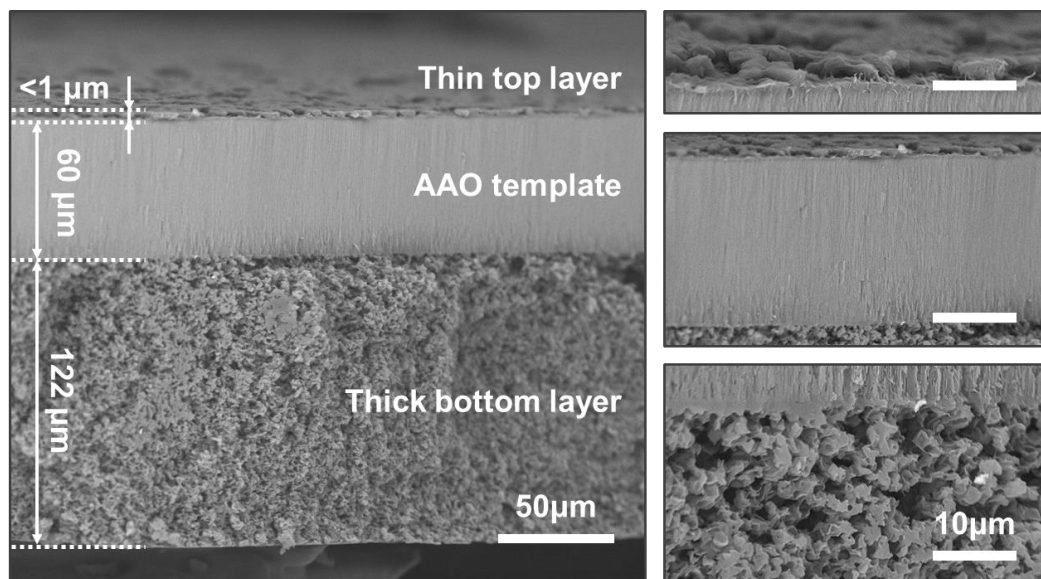


Fig. 4-2 Cross-section SEM images of Nylon-11 filed AAO template. Right images represent the magnified images of (top) top surface thin Nylon-11 film, (middle) nanowire-filled AAO template, and (bottom) bottom thick Nylon-11 film.

The proposed growth mechanism was verified through SEM imaging of the nanowires prepared by varying the starting Nylon-11 polymer concentration in the solution. On varying the wt % of Nylon-11 polymer in the solution, either continuous or beaded nanowires were obtained at high concentration (10 ~ 20 wt %) solution, or a mixture of

nanoparticles and nanowires were obtained at low concentration (2 and 5 wt %), as can be observed from the SEM images, taken after removal of the template, in Fig. 4-3. In the case of 2 wt % Nylon-11 in formic acid, no 1D nanowire growth was observed and only particulate deposition with a diameter similar to that of the pore channels resulted instead (Fig. 4-3a). With increasing concentration of the Nylon-11 solution, the percentage of nanowires increased, as observed for 5 wt % Nylon-11 sample, in which low aspect ratio (average length 4  $\mu\text{m}$  and diameter  $\sim$  250 nm) nanowires and a considerable (40  $\sim$  50 vol%) growth of Nylon-11 nanoparticles was obtained (Fig. 4-3b).

A minimum of 10 wt % was found to be an optimum concentration for obtaining high aspect-ratio Nylon-11 nanowires with an average length of  $\sim$  40  $\mu\text{m}$  (Fig. 4-3c) with significantly reduced beaded structure ( $<$  5 vol.%) in the sample (Fig. 4-3c, d and inset of Fig. 4-3d). Beyond this concentration, the length of the nanowires was found to decrease, as the viscosity of the solution increased with increasing concentration, thus inhibiting complete infiltration of the pore channels. Nylon-11 nanowires freed from the AAO template underwent noticeable stretching (indicated by arrows in Fig. 4-3d) alike Nylon-11 bulk, and sometimes appearing as nanoribbons.

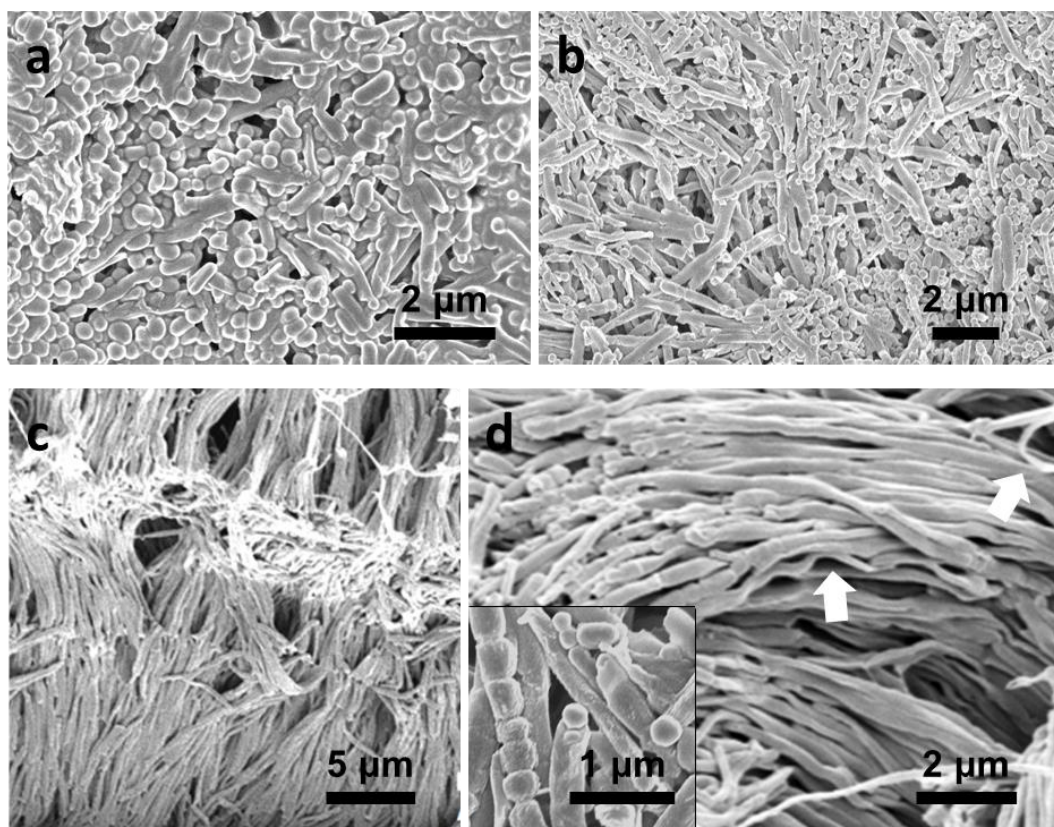


Fig. 4-3 Effect of concentration on the microstructure of Nylon-11 nanowires. Templates were completely removed to study the SEM images. (a) For 2 wt % Nylon-11 in formic acid no 1-dimensional growth and only particulate deposition of diameter as same that of the pore channels (~250 nm) was observed. (b) For 5 wt% Nylon-11 in formic acid, low aspect ratio (average length 4  $\mu\text{m}$  and diameter ~250 nm) nanowires and a considerable (40 ~ 50 vol %) growth of Nylon-11 nanoparticles were observed. (c) Aligned Nylon-11 nanowires obtained from 10 wt% solution. (d) Close-up view of the Nylon-11 nanowires arrays from 10 wt% solution showing tips of the nanowires consisting of Nylon-11 nanoparticles (inset). Fig. (a) ~ (d) are taken from the author's work from Ref. [208], reproduced with permission from John Wiley and Sons.

The average diameter of the freed nanowires measured from several SEM images was  $270 \pm 20$  nm, which is almost 45% larger than the nominal pore size of the AAO templates. Detailed SEM studies revealed that the Nylon-11 nanowires freed from the AAO template underwent noticeable stretching sometimes appearing as nanoribbons/nanotapes. The significant deformation of Nylon-11 nanowires without mechanical failure is suggestive of their soft and flexible nature and conforms to the mechanical characteristics of Nylon-11. Therefore, in order to measure the true diameter of Nylon-11 nanowires, AAO templates were only partially dissolved to expose the tips of Nylon-11 nanowires, from which an average diameter of 196 nm was measured (Fig. 4-4a). Dense long nanowire arrays freed from the template (inset of Fig. 4-4b) were also occasionally observed to roll as mats, assisted by the support of a thin Nylon-11 film (10 ~ 20 nm thick) present at the bottom, following cleaning and dissolution of the template as a result of joining of the soft nanowire bases (Fig. 4-4b).

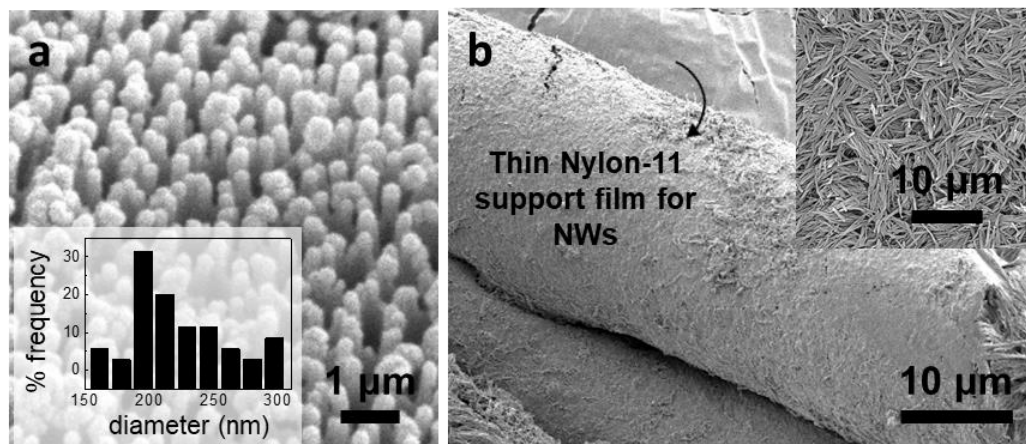


Fig. 4-4 SEM images of nanowires and nanowire mat. (a) Partially etched Nylon-11 filled AAO template reveals the tips of the nanowires and allows estimation of the diameter more accurately. The frequency of the distribution of the diameters of Nylon-11 nanowire is shown in the inset. (b) Flexible Nylon-11 nanowires form a dense mat which can be carefully transferred to any substrate and could roll without mechanical tearing. Inset shows the dense mat-like feature of the nanowires. Fig. (a) and (b) are taken from the author's work from Ref. [208], reproduced with permission from John Wiley and Sons.

## 4.2 Crystal structure of Nylon-11 nanowires grown by template-wetting

Detailed structural characterization was subsequently carried out by XRD. For Nylon-11 nanowires without AAO template (Fig. 4-5, orange), relatively sharp diffraction peak was observed at  $2\theta = 21.6^\circ$ , along with weak diffraction of  $2\theta = 6.2^\circ$  and  $22.8^\circ$ . Interestingly, these are unreported peak configuration. Although the  $2\theta = 21.6^\circ$  peak is reported as the main peak of pseudo-hexagonal phase,  $2\theta = 22.8^\circ$  has never been investigated. Therefore, in the case of Nylon-11 nanowires by conventional template wetting method, it is difficult to define accurate crystal structures.

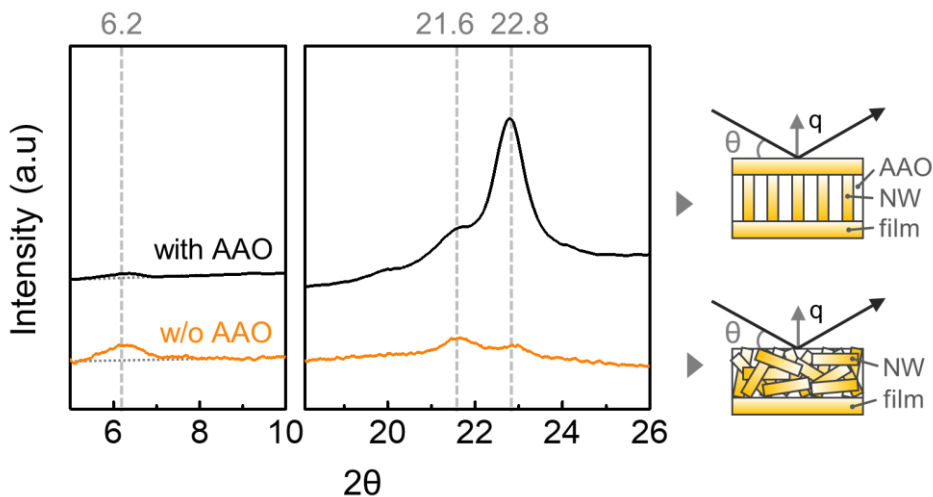


Fig. 4-5 XRD patterns of Nylon-11 nanowires synthesized by conventional template wetting process (black) before and (orange) after the template removal. Accompanying schematics display the morphology of sample and the direction of X-ray beam ( $\theta$ ) with a scattering vector ( $q$ ).

The relative intensity between  $2\theta = 21.6^\circ$  and  $22.8^\circ$  is changed in the Nylon-11 nanowire *within* AAO template (Fig. 4-5, black). In the case of Nylon-11 nanowires grown by conventional template-wetting, one recognizable diffraction peak was observed at  $2\theta = 22.8^\circ$  as compared to the XRD pattern of the corresponding template-freed nanowires. In addition, the intensity of the peak at  $2\theta = 6.2^\circ$  is also reduced. These results indicate that the crystals in the nanowires have a preferential orientation perpendicular to the lattice plane corresponding to  $2\theta = 22.8^\circ$  peak.

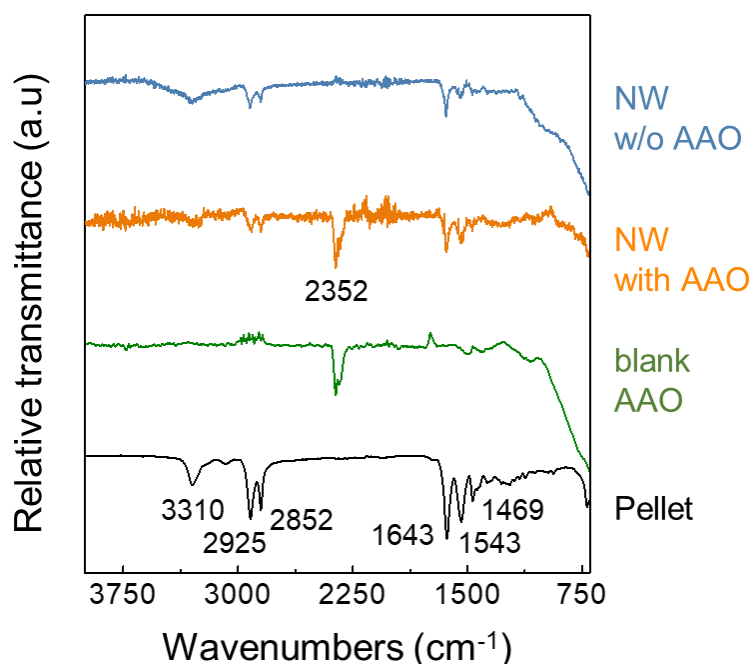


Fig. 4-6 Room temperature FT-IR spectra of Nylon-11 nanowires (blue) without and (orange) with AAO template. FT-IR spectra of (olive) blank AAO template and (black) commercial Nylon-11 pellets are also shown for reference. Fig. is taken from the author's work from Ref. [208], reproduced with permission from John Wiley and Sons.

Room-temperature FT-IR spectra of the template-protected and template-freed Nylon-11 nanowires are shown in Fig. 4-6, as compared to Nylon-11 pellets and a blank AAO template. Typically, in Nylon-11, the region  $500 \sim 800 \text{ cm}^{-1}$  comprises the amide V and VI bands, whereas, the  $1000 \sim 1400 \text{ cm}^{-1}$  zone is sensitive to the methylene segments. The region  $1500 \sim 1700 \text{ cm}^{-1}$  contains the amide I and II bands and is characteristic of N-H bending from ordered, disordered, and free N-H groups and C=O bonds. The regions typical to hydrogen bonding are from  $1600$  to  $1800 \text{ cm}^{-1}$  and from  $3000$  to  $3600 \text{ cm}^{-1}$ . [134] FT-IR of Nylon-11 pellets showed intense bands resulting from the absorption of active  $\text{H}_2\text{O}$ , CO and  $\text{CO}_2$  molecules. [188], [189] Stretching and bending of C=O and O-H units gave rise to strong FT-IR signals between  $1700 \sim 2300 \text{ cm}^{-1}$  and  $3200 \sim 3600 \text{ cm}^{-1}$ , thereby suppressing the bands from Nylon chains. Both the pellets and Nylon-11 nanowires showed sharp bands observable at  $1469$ ,  $1543$ , and  $1643 \text{ cm}^{-1}$  due to intense N-H stretching in amide groups. A strong transmittance band  $\sim 2352 \text{ cm}^{-1}$  in the nanowire sample was due to

absorbance of CO<sub>2</sub> molecules in the AAO template for the template-protected sample. A slight difference between the ratio of the bands at 2852 and 2925 cm<sup>-1</sup> was observed between Nylon-11 pellet and nanowires, which can be assigned to symmetric and antisymmetric CH<sub>2</sub> stretching, respectively.[187] The amide A band occurring at about 3310 cm<sup>-1</sup> in both Nylon-11 pellet and nanowires was due to the N-H stretching vibration that is sensitive to the strength of the hydrogen bond. A somewhat increased transmittance, as well as varying ratios in the transmittance bands in the Nylon-11 nanowires as compared to Nylon-11 pellets, suggests that the hydrogen bonds might break and the dipoles rotate to re-form bonds in a new direction due to the nanowire formation. However, no considerable difference was noticed in the band intensities in freed Nylon-11 nanowires suggesting that no dipole reorientation occurred upon freeing the nanowires.

### 4.3 Thermal behaviour of Nylon-11 nanowires

DSC measurements on Nylon-11 pellets, spin-cast Nylon-11 film, as well as template grown Nylon-11 nanowires are shown in Fig. 4-7. During the heating cycle, a single melting peak at  $T_m = 189.5$  °C was recorded for Nylon-11 pellets as well as spin-cast Nylon-11 film ( $T_m \sim 186$  °C). In contrast, in the case of template-protected nanowires (Fig. 4-7, orange), the melting peak split into two distinct peaks, at 183.9 °C and 186.9 °C, corresponding to typical melting points for  $\alpha$ - and  $\delta'$ - phases respectively.[209], [210] However, it does not indicate that Nylon-11 nanowires fabricated by the conventional template-wetting method are  $\alpha$ - or  $\delta'$ - phases. The denomination of the crystal structure of template-wetted nanowires will be discussed in Chapter 7 in more detail. For the template-freed nanowires, the doublet peaks shifted to a higher temperature at 186 °C and 189 °C, respectively. During the DSC cooling cycle (Fig. 4-7b), Nylon-11 nanowires (both template-protected and freed) recrystallized at a relatively higher temperature ( $\sim 167$  °C) as compared to the Nylon-11 film and pellets. The higher  $T_m$  observed in Nylon-11 nanowires suggest a possible use of Nylon-11 nanowires at a higher operational temperature as compared to other ferroelectric polymers.[6], [211]

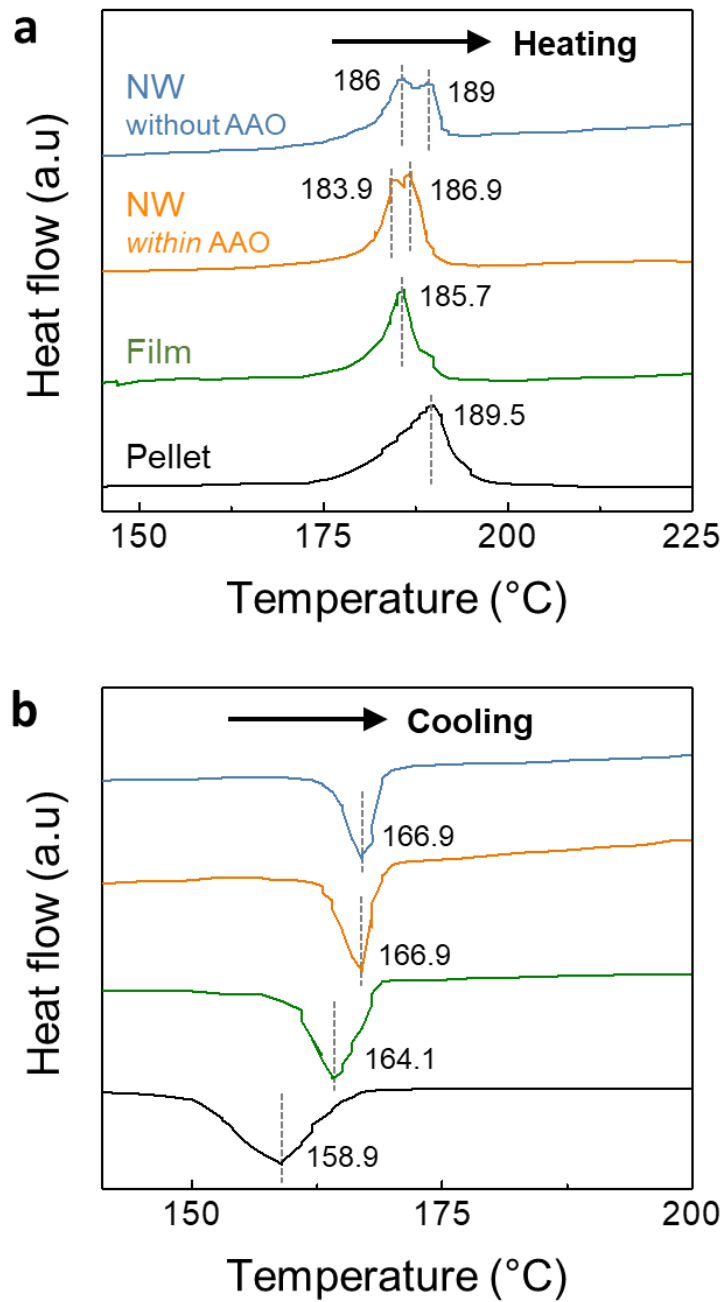


Fig. 4-7 DSC thermograms (a) heating and (b) cooling cycles of Nylon-11 nanowires before and after template dissolution in comparison with parent pellets and spin-coated film. Fig. (a) and (b) are taken from the author's work from Ref. [208], reproduced with permission from John Wiley and Sons.

## 4.4 Nanowire-based nano-piezoelectric generator

A nano-piezoelectric generator based on template-grown vertically aligned Nylon-11 nanowires was fabricated by sputter coating both sides of the template with gold for electrical access to the nanowires *within* AAO template. The electrical output was measured in response to periodic impacting perpendicular to the long axis of the nanowires, by an oscillating mechanical arm at a set frequency in an energy harvesting measurement setup (Details are given in Chapter 3.2).

Fig. 4-8a shows the schematic of the nano-piezoelectric generator structure and the impacting arrangement, where the generator sample is rigidly fixed at the mean position of the oscillating arm in order to generate maximum compressive force upon impacting. It is ensured that the Nylon-11 nanowire filled template is totally free of any residual film, and crack-free before Au electrodes are deposited on both sides of the template. The device structure is typical for template-based generators, allowing both mechanical and electrical access to the vertical array of nanowires *within* AAO template.[202], [212]–[215] Fig. 4-8b and c show the output open circuit voltage ( $V_{OC}$ ) and short-circuit current ( $I_{SC}$ ) respectively, measured in response to the periodic impacting at a frequency ( $f$ ) ranging from 5 to 20Hz and amplitude of 0.5 mm. Nano-piezoelectric generator output data taken at frequencies up to 150 Hz or at periodic impacting amplitude from 0.5 mm to 2.5 mm are shown in Fig. 4-9. The observed positive (and negative) peaks in  $V_{OC}$  and  $I_{SC}$  correspond to compression (and releasing) of the nano-piezoelectric generator. The peak-to-peak value of output increased with both increasing frequency as well as amplitude. This is because the impacting force of higher frequency and amplitude improve the piezoelectric response. We observed a peak  $V_{OC}$  of  $\sim 0.7$  V and a peak  $I_{SC}$  of  $\sim 60$  nA from the device when impacted at a frequency of 5 Hz and amplitude of 0.5 mm, akin to gentle finger tapping. This value is comparable to that reported from P(VDF-TrFE) nanowire-based NG reported earlier by our group.[202] The electrical output of the generator was measured across different resistors, as shown in Fig. 4-8d, and a peak in output power density of  $\sim 0.027$   $\mu\text{W cm}^{-2}$  was observed under impedance-matched conditions across a load resistance of  $\sim 10$  M $\Omega$  (Fig. 4-8e).

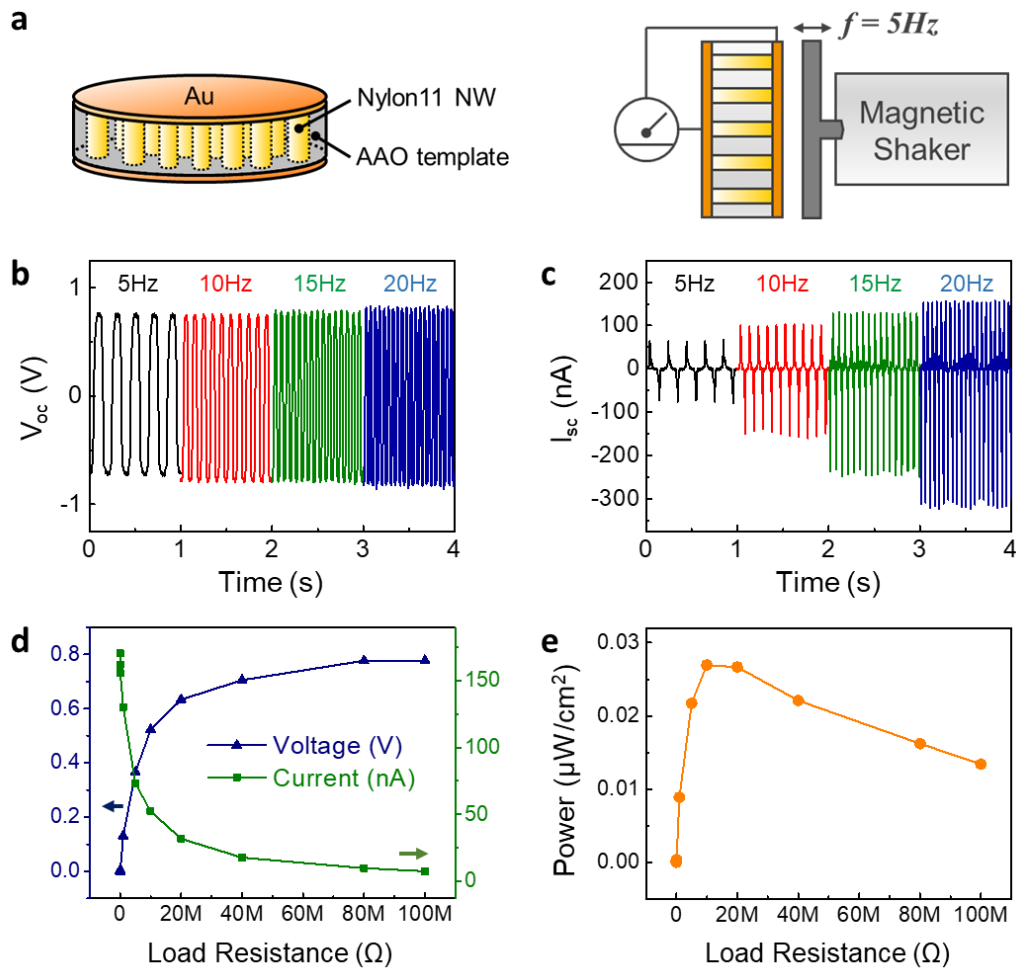


Fig. 4-8 Nylon-11 nanowire-based nano-piezoelectric generator. (a) Schematic showing the structure of the Nylon-11 nanowire-based nano-piezoelectric generator, where Au electrodes were deposited on both sides of the nanowire-filled AAO template. Piezoelectric output is generated in response to periodic impacting using a bespoke impacting setup by which the nanowires are subjected to periodic uniaxial compression and relaxation. (b) Open circuit voltage ( $V_{oc}$ ) and (c) short circuit current ( $I_{sc}$ ) output of the Nylon-11 nanowire-based generator, in response to periodic impacting for a range of frequencies between 5 and 20 Hz and a fixed amplitude of  $\sim 0.5$  mm. (d) (blue triangle) Voltage and (green square) current and (e) peak power density of a single device, measured across different load resistances. Fig. (a) ~ (e) are taken from the author's work from Ref. [208], reproduced with permission from John Wiley and Sons.

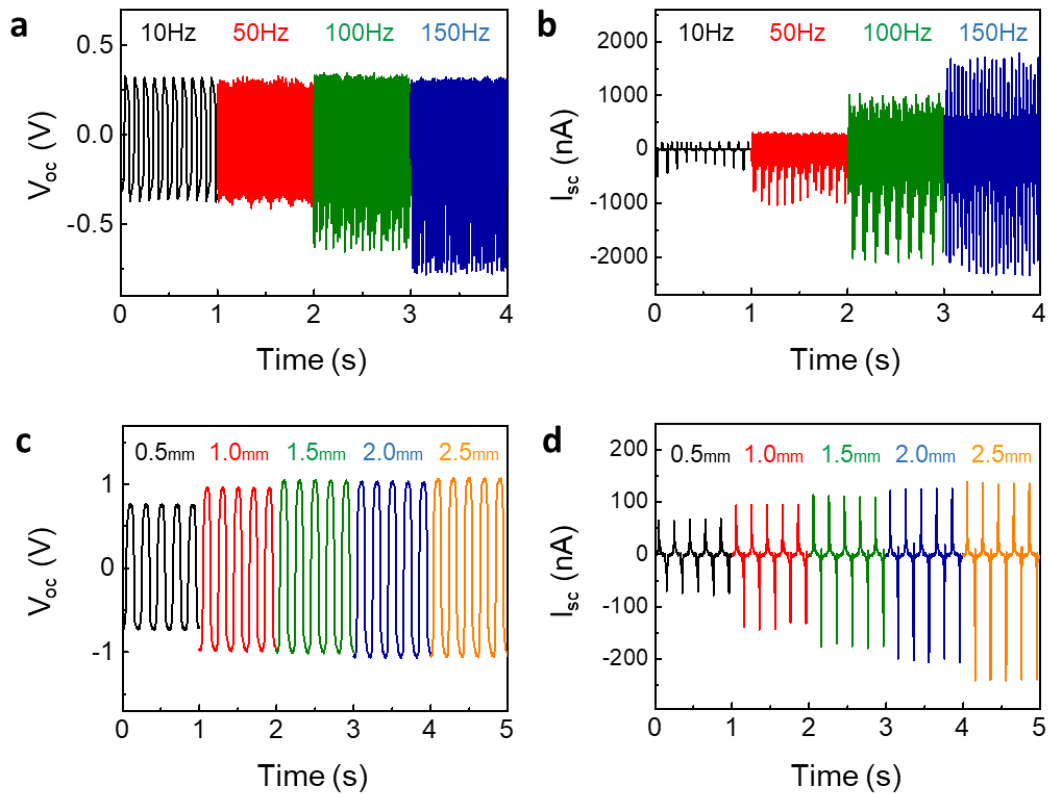


Fig. 4-9 Electrical output with various input signals. The open circuit voltage ( $V_{oc}$ ) and short circuit current ( $I_{sc}$ ) under the application of a periodic impacting force (a), (b) at fixed amplitude of  $\sim 0.5\text{mm}$  with various frequencies, and (c), (d) at a fixed frequency of 5 Hz with various amplitudes. Fig. (a) ~ (d) are taken from the author's work from Ref. [208], reproduced with permission from John Wiley and Sons.

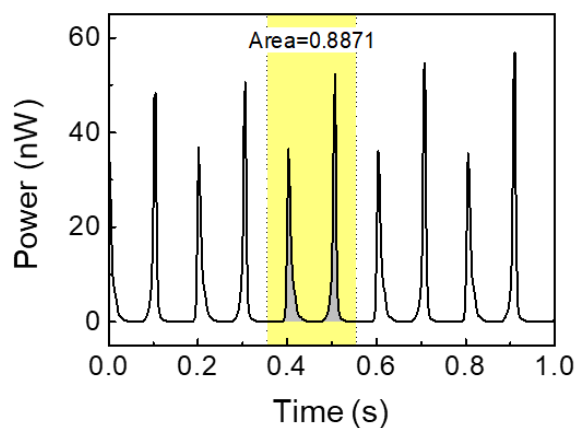


Fig. 4-10 The change of power according to the time under  $10\text{M}\Omega$  load resistance of device. Grey area indicates the integration of power in terms of one cycle time (0.2 s), calculating the value of 0.8871. Fig. is taken from the author's work from Ref. [208], reproduced with permission from John Wiley and Sons.

To achieve the device efficiency ( $\chi'$ ), [18] electrical energy output and input strain energy need to be calculated. (Detailed development processes are described in Appendix B5.) The electrical energy output from a device per cycle was approximated using power integration. Fig. 4-10 shows a plot of power variation in terms of time under 10 M $\Omega$  load resistance. Calculated electrical energy is  $9.07 \times 10^{-10}$  J when integrating and averaging over 20 cycles. The strain energy can be calculated as

$$\text{Strain Energy} = \frac{1}{2} A L \varepsilon^2 E \quad (4-1)$$

where  $A$  is the combined cross-sectional area of the nanowires *within* the device,  $L$  the original length of the nanowires (= 60  $\mu\text{m}$ ),  $\varepsilon$  the strain in the nanowires after deformation and  $E$  the Young's Modulus of Nylon-11 (= 1.5 GPa). [135] The strain energy is then calculated to be  $6.17 \times 10^{-8}$  J.  $\chi'$  is thus found to be 1.47%.

The mechanical-to-electrical energy conversion efficiency ( $\chi$ ), [18] of Nylon-11 nanowire is given by

$$\chi = \frac{\text{electrical work perfored by element}}{\text{net energy supplied to element}} \quad (4-2)$$

where  $T$  is the period of one cycle. This is found to be 11.55 % for an impedance-matched load.

High-temperature operation up to 150  $^{\circ}\text{C}$  was also demonstrated by impacting the Nylon-11 based nano-piezoelectric generator while it was mounted on a temperature-controlled heating stage (Fig. 4-11). The measured electrical output decrease with increasing temperature as indicated in Fig. 4-11b. This is possibly due to the changes of crystal structure. (The changes of crystal structure after thermal annealing process are given in Chapter 7.2 in more details.) However, while there is a slight decrease in the output at higher temperatures, comparing the P(VDF-TrFE) with  $T_m$  of 150  $^{\circ}\text{C}$ , the ability of the Nylon-11 generator to withstand such high temperatures is noteworthy and indicates its suitability for operation in high temperature vibration environments, for example, for energy harvesting applications in vibrating car engines and/or heavy machinery where temperatures typically reach  $\sim 150$   $^{\circ}\text{C}$ .

Finally, fatigue testing was carried out by continuously impacting the device for up to 15 h at 5 Hz ( $\sim 2.7 \times 10^5$  cycles). Fig. 4-12a shows that the Nylon-11 based nano-piezoelectric generator exhibited negligible change in  $V_{oc}$  over the entire period of continuous testing. Cross-sectional SEM images taken before and after fatigue testing are shown in Fig. 4-12b and c, indicating no significant change in the morphology of the nanowires and/or the AAO template.

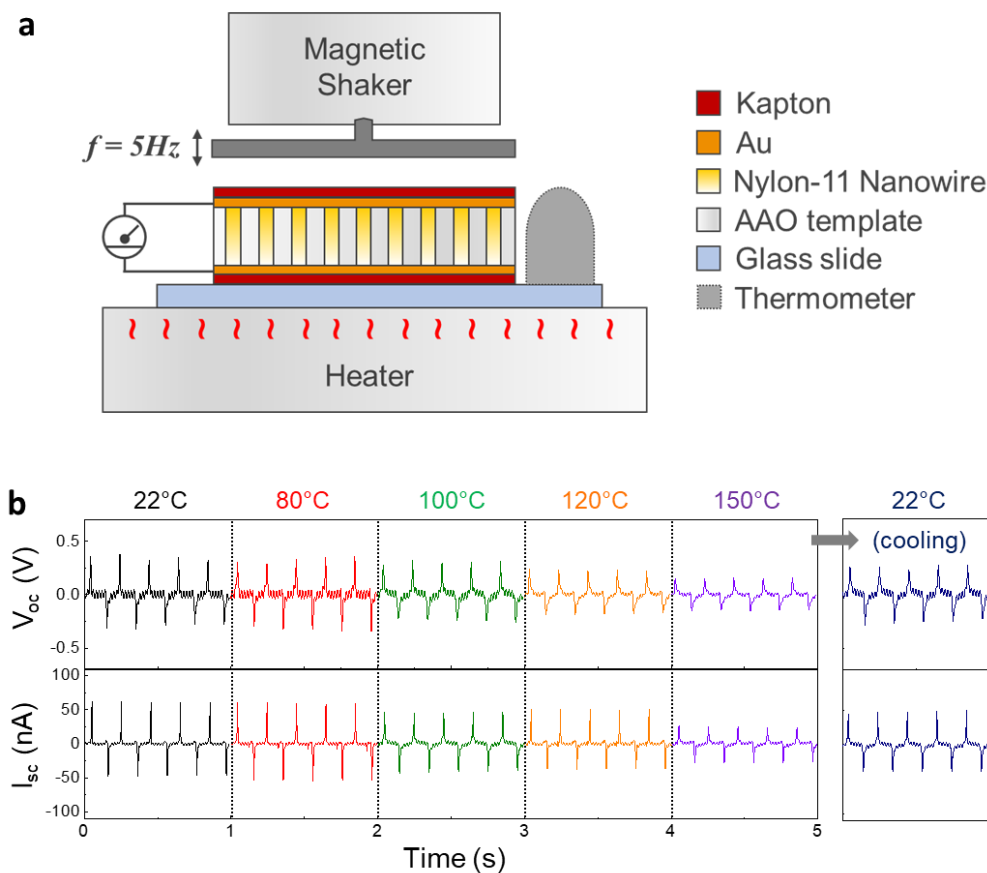


Fig. 4-11 High-temperature operation of Nylon-11 nanowire-based nano-piezoelectric device. (a) Schematic showing the nano-piezoelectric generator being impacted as it is directly mounted on a standard laboratory hotplate with a K-type thermocouple in close proximity to the device to monitor its temperature. Before recording the electrical output in response to impacting, care was taken to stabilize the temperature of the device by adjusting the hotplate temperature and waiting till the thermocouple reading was stable in time. (b) High-temperature electrical output data recorded at temperature ranging from room temperature (22 °C) to 150 °C. The nano-piezoelectric generator output data were also recorded upon cooling back to room temperature. Fig. (a) and (b) are taken from the author's work from Ref. [208], reproduced with permission from John Wiley and Sons.

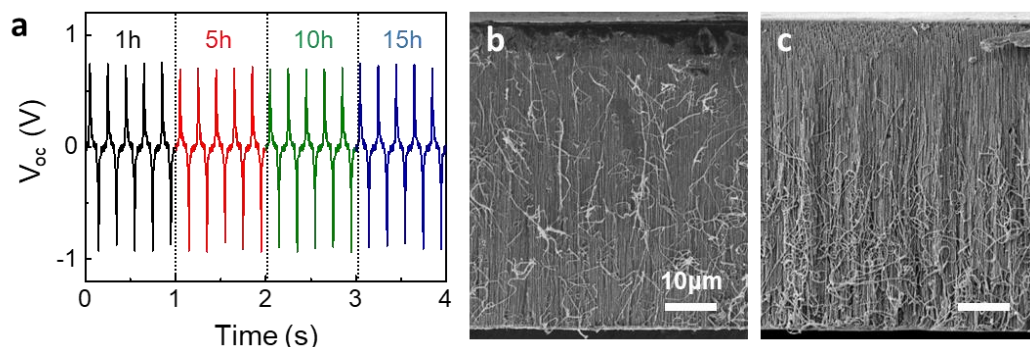


Fig. 4-12 Fatigue test results of nano-piezoelectric device. (a) Open-circuit voltage recorded over time in response to continuous impacting at a frequency of 5 Hz and amplitude of  $\sim 0.5$  mm on the same Nylon-11 nano-piezoelectric generator device for 15 h (270 k impacting cycles in total). Data were recorded after 1 h (18 k cycles), 5 h (90 k cycles), 10 h (180 k cycles), and 15 h (270 k cycles). Cross-sectional SEM images of the Nylon-11 nanowire-based generator (b) before and (c) after fatigue testing, showing unchanged device structure after 270 k impact cycles. Note that the template cleaving process resulted in some of the nanowires being pulled out of the pores. Fig. (a) ~ (c) are taken from the author's work from Ref. [208], reproduced with permission from John Wiley and Sons.

## 4.5 Conclusions

In conclusion, we have reported, for the first time, the fabrication of high-quality vertically aligned Nylon-11 nanowire arrays by conventional template-wetting method via capillary action inside AAO templates, which in contrast to parent pellets and film deposited by spin casting. The flexible and chemically resilient Nylon-11 nanowire arrays are easily transferable to other substrates as flexible mats, supported by very thin Nylon-11 film, thus allowing access to the nanowires outside the AAO template. The measured thermal response indicates that Nylon-11 nanowires may be useful in high-temperature piezoelectric applications as compared to other polymers such as PVDF and P(VDF-TrFE). The energy harvesting performance of a nano-piezoelectric generator based on the template-grown Nylon-11 nanowire arrays was investigated and revealed high energy conversion efficiency with stable operation over 15 hr of continuous impacting. The 'self-poled' nature of the Nylon-11 nanowires renders them particularly attractive for use in low-cost and simple energy generator designs as they require minimal post-processing steps.

## Chapter 5

# **$\delta'$ -phase Nylon-11 Nanowires Fabricated by Gas-Assisted Nano- Template Infiltration (GANT) method for Triboelectric Generators**

According to the literature, the properties of Nylon-11 significantly depends on the crystal structure. For example, the highest mechanical stiffness is observed in the  $\alpha$ -phase, while  $\delta'$ -phase exhibits ferroelectric behaviour (Details of crystal structures related properties are discussed in Chapter 2.4). In the previous chapter, even though we fabricated the Nylon-11 nanowires, we were unable to control the crystal structure. In addition, the crystallinity of nanowires, which is closely related to the mechanical and dielectric property of semi-crystalline polymers, was relatively low compared to Nylon-11 films.

In this chapter, we propose an alternative one-step, near room-temperature method, namely gas-flow assisted nano-template (GANT) infiltration method, for the fabrication of highly crystalline self-poled  $\delta'$ -phase Nylon-11 nanowires *within* nanoporous AAO templates, without any subsequent processing such as stretching and/or electrical poling

required. The gas-flow assisted method allows for controlled crystallisation rate that manifest as rapid solvent evaporation and an extreme temperature gradient within the nanopores of the template, as accurately predicted by finite-element simulations, resulting in the  $\delta'$ -phase crystal structure. Furthermore, the preferential crystal orientation originating from template-induced nano-confinement effects leads to self-polarization of the nanowires, increasing average crystallinity up to  $\sim 40\%$ . The self-poled  $\delta'$ -phase Nylon-11 nanowires show enhanced surface charge density when compared to melt-quenched films as observed by KPFM. Correspondingly, a triboelectric generator device based on GANT Nylon-11 nanowires showed a ten-fold increase in output power density compared to an aluminium-based device, when subjected to identical mechanical excitations. A substantial amount of this work has been previously published and therefore has been adapted from that text.[2] Copyright permission and authors' contributions are given in Appendix A.

## 5.1 Nylon-11 for triboelectric generators

As we discussed in Chapter 2.2, an investigation into Nylon as a potential tribo-positive candidate is essential to enhance triboelectric generator performance and extend the range of applications as Nylon is one of the very few synthetic materials on the tribo-positive side (Fig. 5-1). Furthermore, the induced spontaneous polarization in ferroelectric Nylon-11 could serve to enhance the performance of the triboelectric generator through inherent surface charge density modification. In order to maximize such spontaneous polarisation in Nylon-11, the material needs to possess a pseudo-hexagonal structure with randomly oriented hydrogen bonds, referred to as the " $\delta'$ -phase", where this structure allows for easy aligning of the dipole moment.[95], [96] This  $\delta'$ -phase, however, is typically achieved through extremely fast crystallisation that is required to avoid the formation of large domain size.[91], [97], [101], [188] As a result, most of the studies regarding the  $\delta'$ -phase Nylon-11 have been carried out on films grown via melt-quenching. Although several alternative techniques, such as spin coating[93], vapour deposition[111], electrospinning[112], thermal annealing[216], and adding carbon nanostructures[113], have been suggested, most of these reported approaches resulted in a lower crystallinity and/or still require harsh processing conditions, such as high temperature (290 °C) and high voltage (40 kV). Moreover, these methods involve further drawing and electrical poling

process to enhance the spontaneous polarisation of the Nylon-11 films.[103] By producing Nylon-11 nanowires using conventional template wetting method (Chapter 4), spontaneous polarization can be achieved via nano-confinement without stretching and/or poling process. However, greater control of the exact crystal structure through nano-confinement methods remains challenging, in part owing to the crystal growth initiation site.

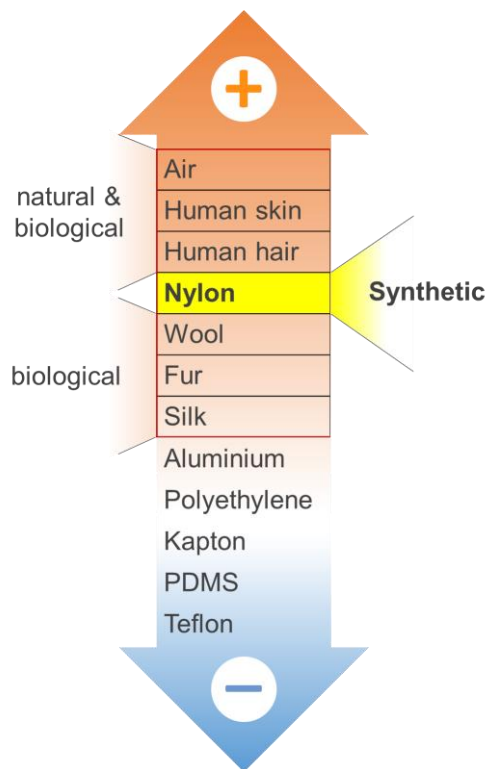


Fig. 5-1 Trieboelectric series of common materials with highlighted position of tribo-positive materials. Plus and minus sign indicate the materials' charge donating and accepting properties, respectively. Fig. is taken from the author's work from Ref. [2], reproduced with permission from Royal Society of Chemistry.

Here, we mitigate this problem by introducing an assisted gas-flow to the template-wetting technique. The assisted gas-flow enables precise control of the crystallisation rate of the Nylon-11 polymer solution while in the template pores, resulting in the required  $\delta'$ -phase crystal structure. We find that the presence of the  $\delta'$ -phase in Nylon-11 nanowires leads to enhanced spontaneous polarisation, and thus precise control of the crystalline phase through our method is beneficial for triboelectric energy harvesting performance.

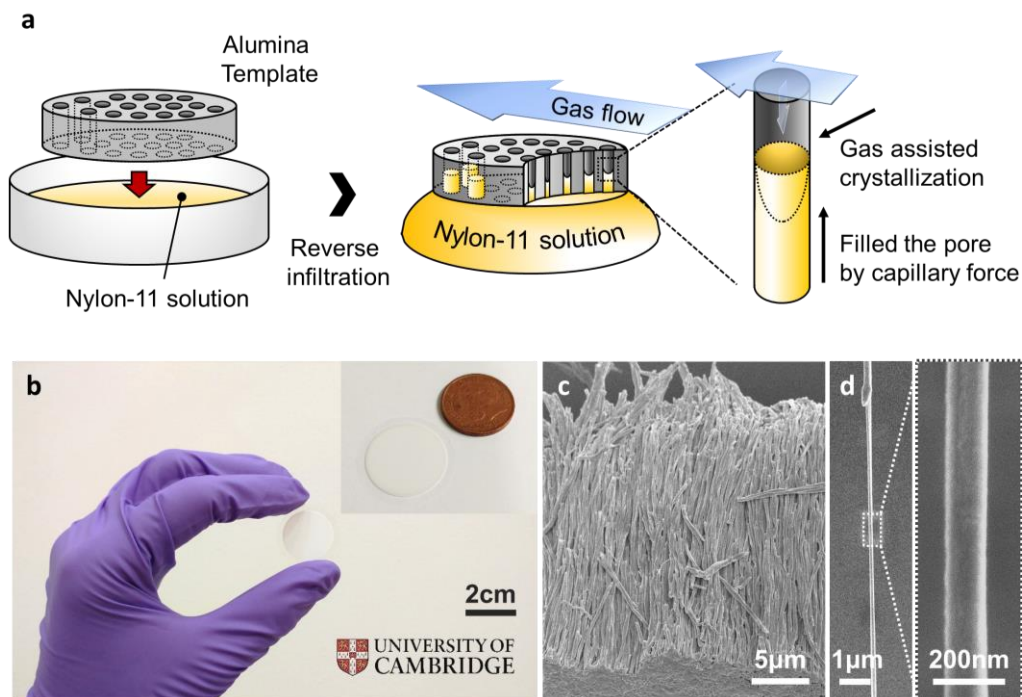


Fig. 5-2 (a) Schematic of the nanowire fabrication procedure. (b) Photographs of a fabricated nanowire-filled AAO template. The inset shows size comparison with a British one-pence coin. (c, d) SEM images of template-freed nanowires and a single strand of Nylon nanowire, respectively. Fig. (a) ~ (d) are taken from the author's work from Ref. [2], reproduced with permission from Royal Society of Chemistry.

The GANT fabrication procedure is schematically illustrated in Fig. 5-2a. To achieve  $\delta'$ -phase Nylon-11 nanowires, the AAO template was placed on top of a 17.5 wt % Nylon-11 solution in formic acid at 70 °C. At the same time, assisted gas-flow ( $\sim 3$  m/s) was introduced in a direction parallel to the template surface. (Detailed procedure has been described in Chapter 3.1.2). Fig. 5-2b shows a photograph of an AAO template (diameter  $\sim 2$  cm and thickness  $\sim 60$   $\mu\text{m}$ ) filled with Nylon-11 nanowires grown using the GANT method. High-resolution SEM imaging was carried out on the resulting nanowires. Well-aligned nanowire arrays were detected in samples after the template material was dissolved using mild acid (Fig. 5-2c, d). A single nanowire strand has uniform width and length of 200 nm and 60  $\mu\text{m}$  respectively, which are similar to the dimensions of the AAO template pore channels. In cross-sectional SEM images of a cleaved template, stretched and entangled Nylon-11 nanowire strands (white thread-like regions) were observed (Fig. 5-3).

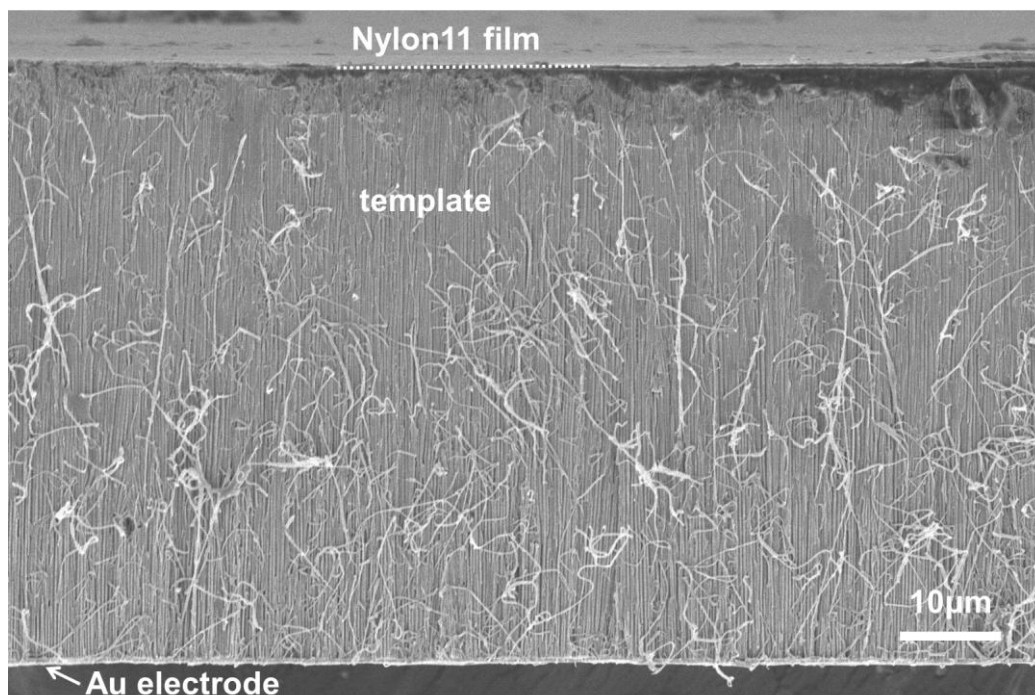


Fig. 5-3 Cross-section SEM image of a nanowire-filled AAO template. White threads indicate the Nylon-11 nanowires, which are stretched during the template breaking process. Fig. is taken from the author's work from Ref. [2], reproduced with permission from Royal Society of Chemistry.

## 5.2 Gas-flow assisted crystal structure control

Detailed crystal structural characterization was subsequently carried out by XRD. At room temperature, a melt-quenched film with pseudo-hexagonal  $\delta'$ -phase typically showed broader reflection peak at  $2\theta \sim 21.6^\circ$  corresponding to (hk0) plane, which represents merged planes of (100), (010), and (110).[89] However, without assisted gas-flow, Nylon-11 nanowires displayed a relatively strong peak at  $2\theta = 22.6^\circ$  with a very weak  $\delta'$ -phase peak ( $2\theta = 21.6^\circ$ ). This diffraction pattern is consistent with our previous result regarding the Nylon-11 nanowires manufactured by conventional template wetting method (Fig. 4-5). The GANT infiltration process allowed control of the crystal structure, wherein we were able to manipulate the rate of crystallisation by adjusting the speed of gas-flow. As shown in Fig. 5-4a (left panel), the relative peak intensity of the  $\delta'$ -phase gradually increased with increasing the rate of assisted gas-flow up to a gas-flow rate of  $\sim 3$  m/s, without any further increment thereafter. The relative changes in intensities between the peak at  $21.6^\circ$  and peak at  $22.6^\circ$  are depicted in Fig. 5-4a (right panel), where the variation

in average peak intensities is plotted as a function of gas-flow rate. This result indicates that the crystal structure of nano-confined Nylon-11 nanowires could be well-controlled using different gas-flow rate, leading to the formation of pseudo-hexagonal  $\delta'$ -phase Nylon-11 nanowires.

In order to compare the crystallography of the nanowires, melt quenched Nylon-11 films with  $\delta'$ -phase, were grown. Fig. 5-4b shows the XRD from both a melt-quenched film and nanowires in the AAO template. While the melt-quenched film showed a relatively broad  $\delta'$ -phase peak at  $2\theta_{\text{hk}0} = 21.6^\circ$ , the  $\delta'$ -phase nanowires that were grown using the GANT method exhibited a  $\delta'$ -phase peak with a smaller full width at half-maximum. It means that the nanowires have more organised (pseudo)-hexagonal lattice structure.[89] It is to be noted that the volume of nanowires was only about  $\sim 50\%$  of the film with the same size and thickness (Fig. 3-4) as the XRD data for nanowires was taken while the nanowires were still embedded in the AAO template. This indicated that the actual amount of crystalline region in the nanowire per unit area is larger than that of the melt-quenched film. These results suggest that even through the conventional melt-quenching method, the presence of large amorphous regions cannot be prevented in the films due to the thickness of the film and the low thermal conductivity of Nylon.[97] However, this problem is mitigated via the GANT method where the  $\delta'$ -phase in Nylon-11 nanowires is realised to a larger extent.

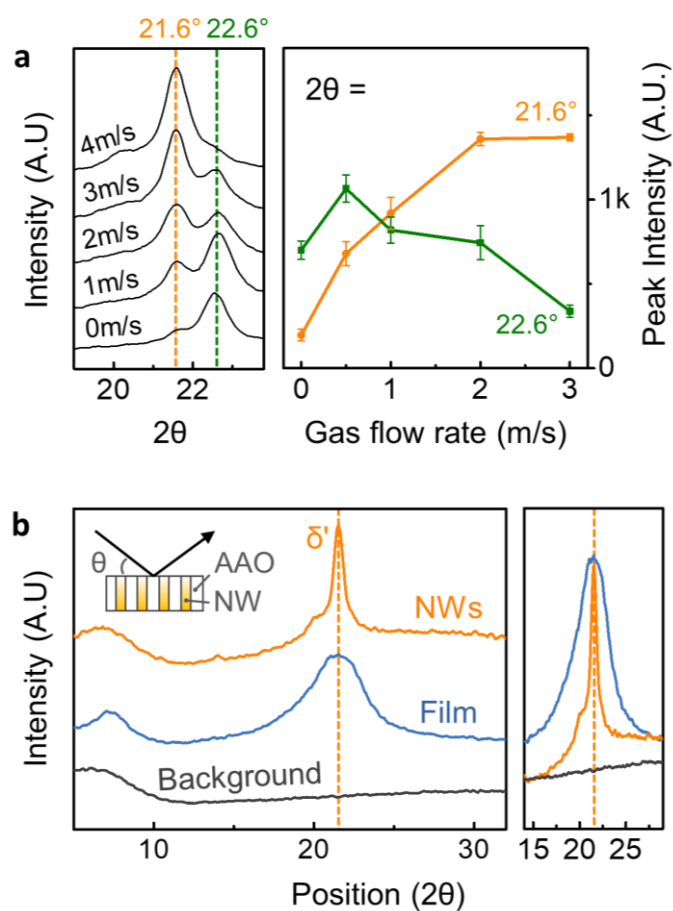


Fig. 5-4 (a) (left) XRD patterns of nanowire-filled templates crystallised at various assisted gas-flow rates. (right) Based on the normalised XRD patterns, the average intensity of the peak at  $21.6^\circ$  and  $22.6^\circ$  is plotted as a function of assisted gas-flow rate. (b) XRD patterns of a nanowire-filled template (orange), melt-quenched film (blue), and silicon background (grey). The right image shows the magnification of the  $\delta'$ -phase range. Fig. (a) and (b) are taken from the author's work from Ref. [2], reproduced with permission from Royal Society of Chemistry.

The crystallisation mechanism initiated by the GANT method was verified using finite element analysis using COMSOL Multiphysics as illustrated in Fig. 5-5 (Modelling details are discussed in Chapter 3.2.4). To further investigate the rapid crystallisation process, the effect of both solvent evaporation as well as temperature of the solution have been considered. In terms of solvent evaporation, our simulations revealed that through the assisted gas-flow, the artificially generated dry and cool turbulent air flow effectively encourages the evaporation of the solvent. Fig. 5-5a and b show the induced turbulent flow by the assisted gas within the nanopore channels, whose speed increased with increasing assisted gas-flow velocity (Fig. 5-5c). The velocity of the turbulent gas-flow, evaluated 10 nm above the surface of the solution, was 36  $\mu\text{m/s}$  for an assisted-gas velocity of 3.1 m/s. This is an extremely high flow rate considering the nanopore is  $\sim 200$  nm in diameter. As a result, nucleation can be initiated at the surface of the exposed solution by rapid solvent evaporation. In our computational model, we also considered the effect of solution cooling within the pore channel: both turbulent flow-induced evaporative cooling and conductive cooling via the nano-template walls. The overall cooling mechanism is demonstrated in Fig. 5-5d, e, taking into consideration the turbulent flow around the exposed Nylon-11 solution, as well as the heat transfer through the pore walls. As a result of this cooling, a temperature gradient is generated both on the top surface and the side of the Nylon-11 solution. Fig. 5-5f shows the significant temperature gradient produced by evaporative cooling (orange) and thermal conduction (blue) as a function of the distance from the top and side surfaces of the solution, respectively. The crystal growth direction can be inferred from these heat transfer simulation, as the growth of the crystalline region is most likely to occur in the direction of the largest temperature gradient (Fig. 5-6).

In addition, considering the crystal growth direction of the GANT method and due to the size of the nano-pores, the crystal growth length ( $\sim 100$  nm) can be limited, resulting in extremely rapid nucleation and growth. Hence fast crystallisation is achieved within the confines of the nanopores, even with mild external conditions, such as low gas-flow rate (3 m/s) and near-room temperature conditions.

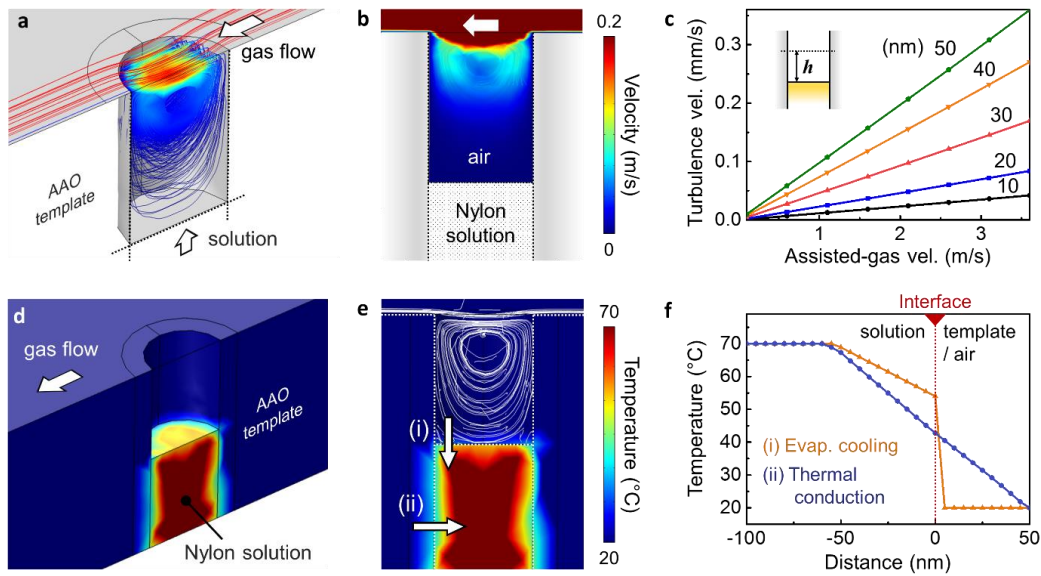


Fig. 5-5 Numerical simulation results of turbulence flow generated by assisted gas-flow (3.1 m/s): (a) 3D view and (b) xz-plane view. (c) Plot showing the relationship between the velocity of turbulent flow at different heights above the solution surface and assisted gas-flow rate. (d) Simulation result of heat transfer around the solution-filled nano-pore. (e) the xz-plane view of (d) with turbulent flow showing two dominant cooling mechanisms: (i) evaporative cooling and (ii) thermal conductive cooling. (f) The temperature gradient from the centre of the solution to the air (orange) and template wall (blue). The initial temperature of the Nylon solution and assisted gas were taken to be 70 °C and 20 °C, respectively. Fig. (a) ~ (f) are taken from the author's work from Ref. [2], reproduced with permission from Royal Society of Chemistry.

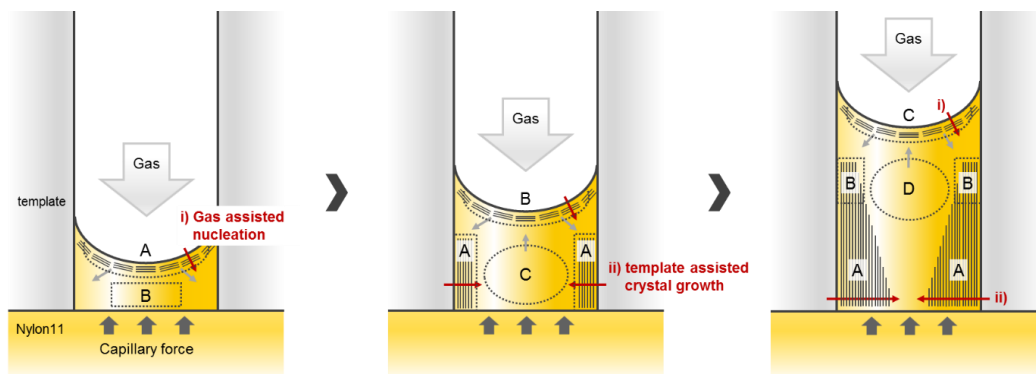


Fig. 5-6 Schematic of the polymer crystallisation process in the nano-dimensional pore of the GANT infiltration method. Fig. is taken from the author's work from Ref. [2], reproduced with permission from Royal Society of Chemistry.

### 5.3 Self-poled $\delta'$ -phase nanowires through GANT method

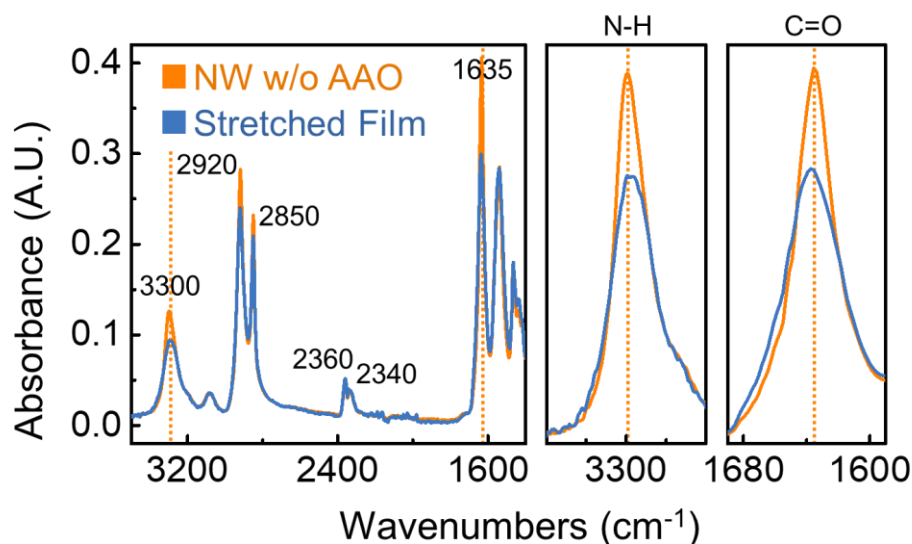


Fig. 5-7 FT-IR absorbance spectra for (orange) template-free nanowires and (blue) additionally stretched film. Fig. is taken from the author's work from Ref. [2], reproduced with permission from Royal Society of Chemistry.

The molecular bond structure of  $\delta'$ -phase nanowires was measured using room temperature FT-IR spectroscopy (Fig. 5-7). A template freed  $\delta'$ -phase nanowire mat[208] and stretched film were prepared to confirm the effect of nanoconfinement. According to the literature, FT-IR spectra of Nylon-11 have two important regions related to dipole alignment. The region 1500-1700 cm<sup>-1</sup> contains the amide I and II mode and is assigned to hydrogen-bonded or free amide group. The band at 3300 cm<sup>-1</sup> (amide A peak) is assigned to N-H stretching vibration and is sensitive to the hydrogen bond.[93], [187], [188] The region 1500-1700 cm<sup>-1</sup> is shown in Fig. 5-7 for both stretched film and nanowires, containing the amide I and amide II bands. In this region, two materials show similar intensity except for 1635 cm<sup>-1</sup> band because the conformation in the amorphous phase is expected to be the same.[93] The 2920 and 2850 cm<sup>-1</sup> bands of both materials are assigned to the antisymmetric and symmetric CH<sub>2</sub> stretching modes of the methylene groups, respectively. The significant differences in the absorption intensities of the N-H stretching modes at 3300 cm<sup>-1</sup> and C=O stretching modes at 1635 cm<sup>-1</sup> show direct evidence of

molecular ordering. Considering that the peak intensity of  $\delta'$ -phase nanowires is much higher than that of film, it would be inferred that the GANT method generates highly crystalline and well-ordered structures in  $\delta'$ -phase nanowires.

In order to investigate the direction of polarization and quantify the surface charge variations between Nylon-11 nanowires and melt-quenched films arising from the self-poled nature of the former, we employed KPFM, where the surface charge potential difference between the material and an AFM tip can be measured (Fig. 5-8). Melt-quenched Nylon-11 film showed a surface potential difference of 82 mV. In contrast, a higher surface potential (426 mV) was observed from the self-poled  $\delta'$ -phase nanowire-filled template. It is noted that the enhanced surface charge potential difference of self-poled nanowires demonstrates the relationship between polarisation and surface charge density. Our results indicate an “upward” direction of polarisation, which corresponds to the expected charge donating property.

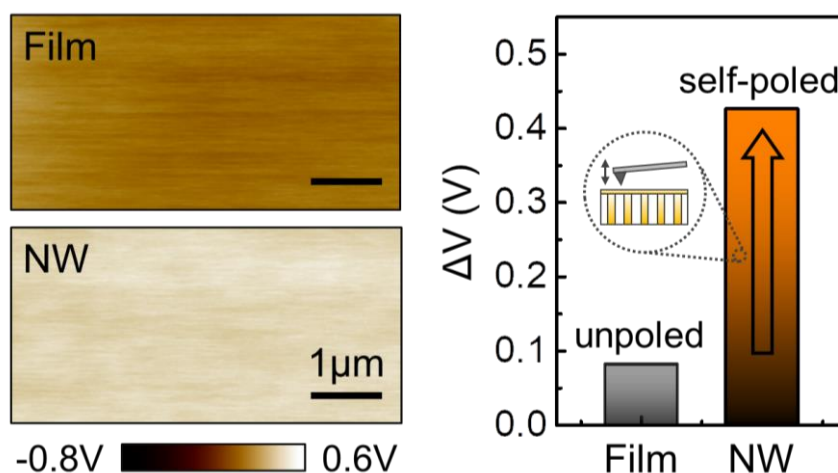


Fig. 5-8 (left) KPFM potential images of the melt-quenched Nylon-11 film and the top surface of the self-poled  $\delta'$ -phase nanowires filled template device. (right) The plot for the surface charge potential difference of each sample. The inset shows KPFM measured surface structure. Fig. is taken from the author's work from Ref. [2], reproduced with permission from Royal Society of Chemistry.

## 5.4 Nanowire-based triboelectric generators

A triboelectric generator was fabricated using self-poled  $\delta'$ -phase nanowires embedded within AAO template. The bottom side of AAO template was coated with gold (Au) electrodes ( $\sim 100$  nm), and an Au-coated Teflon film was prepared as a counterpart substrate. Al films and melt-quenched Nylon-11 film were also prepared to compare the device performance with the nanowire-based triboelectric generator (Fig. 5-9). The triboelectric generator shows the output in response to periodic impacting for a fixed frequency and amplitude of 5 Hz and  $\sim 0.5$  mm, respectively.

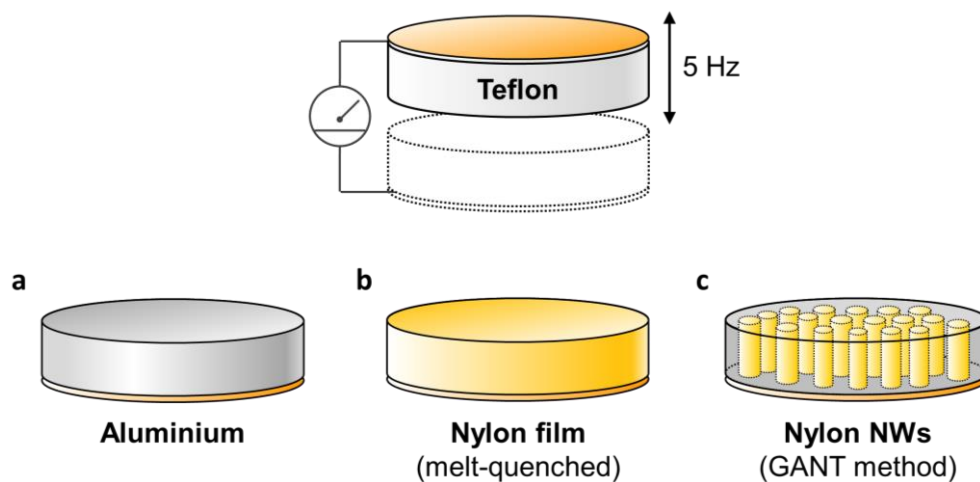


Fig. 5-9 Schematic of the structure of triboelectric generator consisted of tribo-negative material of Teflon and three different tribo-positive materials of (a) aluminium, (b) melt-quenched Nylon-11 film, and (c) Nylon-11 nanowires grown by GANT method.

Fig. 5-10a and b show the open-circuit voltage ( $V_{OC}$ ) and short-circuit current density ( $J_{SC}$ ) respectively, measured in response to the periodic impacting at a frequency ( $f$ ) of 5 Hz and amplitude of 0.5 mm in an energy harvesting setup that has been previously described.[202] The Al-based device showed a peak  $V_{OC}$  of  $\sim 40$  V and a peak  $J_{SC}$  of  $\sim 13$   $\text{mA}\cdot\text{m}^{-2}$ . Following the triboelectric series, higher device performance was observed from a melt-quenched Nylon-11 film based triboelectric generator with  $V_{OC}$  of  $\sim 62$  V and  $J_{SC}$  of  $\sim 21$   $\text{mA}\cdot\text{m}^{-2}$  than from the Al-based generator. The self-poled  $\delta'$ -phase nanowire based triboelectric generator displayed further enhanced output performance with a peak  $V_{OC}$  of  $\sim 110$  V and a peak  $J_{SC}$  of  $\sim 38$   $\text{mA}\cdot\text{m}^{-2}$  likely due to the self-poled nature of the nanowires.

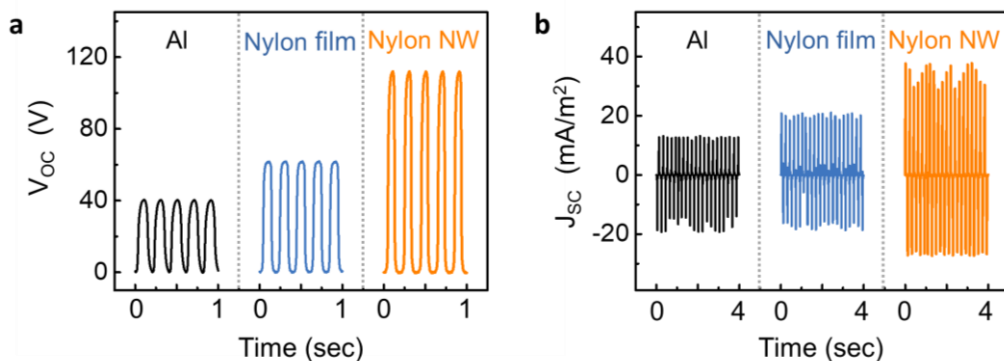


Fig. 5-10 Electrical output of GANT fabricated nanowire-based triboelectric device. (a) Open-circuit output voltages of triboelectric generators with different combinations of materials. The output voltage increases from  $\sim 40$  V in the device with Al to  $\sim 110$  V in the device with  $\delta'$ -phase Nylon nanowires. (b) Short-circuit output current densities of the same device as in (a). Fig. (a) and (b) are taken from the author's work from Ref. [2], reproduced with permission from Royal Society of Chemistry.

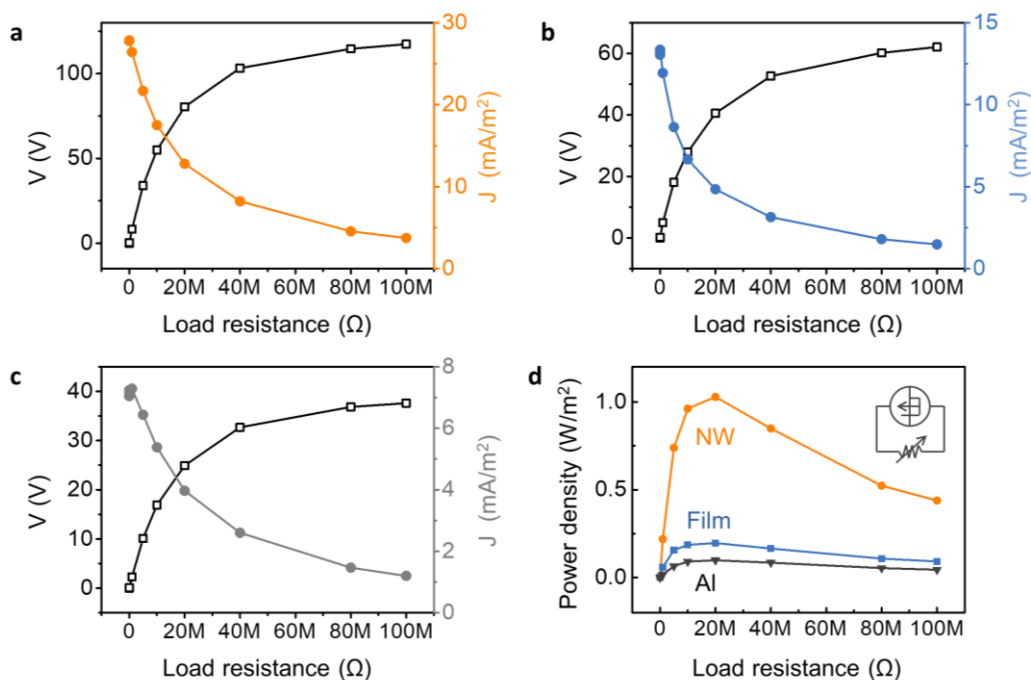


Fig. 5-11 Electrical output with load resistors and power of the device: (a) nanowire-filled template, (b) melt-quenched film and (c) Al-based triboelectric generators. (d) The power density of different triboelectric generators as a function of variable load resistance. The gradual increase and a decrease of voltage and current density across the various load resistors, respectively. The power density is calculated by the multiplication of current density squared and load resistance. Inset indicates the circuit structure. Fig. (a) ~ (d) are taken from the author's work from Ref. [2], reproduced with permission from Royal Society of Chemistry.

The electrical power output of the triboelectric generator was measured across different resistors. The peak output power density of  $1.03 \text{ W}\cdot\text{m}^{-2}$ ,  $0.19 \text{ W}\cdot\text{m}^{-2}$ , and  $0.099 \text{ W}\cdot\text{m}^{-2}$  were observed from the Nylon-11 nanowire, Nylon-11 (melt-quenched) film, and Al-based device respectively under impedance-matched conditions at a load resistance of  $\sim 20 \text{ M}\Omega$  (Fig. 5-11a-c).<sup>8</sup> The observed output power from nanowire-based triboelectric generator was  $\sim 6$  times and  $\sim 10$  times higher than those of a melt-quenched Nylon-11 film and Al based generator, respectively (Fig. 5-11d). Such remarkable improvement in the output performance of  $\delta'$ -phase nanowires can be rationalised as follows; the self-polarization of the nanowires gave rise to larger surface charge density, which resulted in more charge being transferred as compared to the film surface. It should be noted that the surface area of the nanowires is only  $\sim 50 \%$  as compared to the melt-quenched film. It indicates that polarisation in the nanowire effectively further enhances the surface charge density of the device.

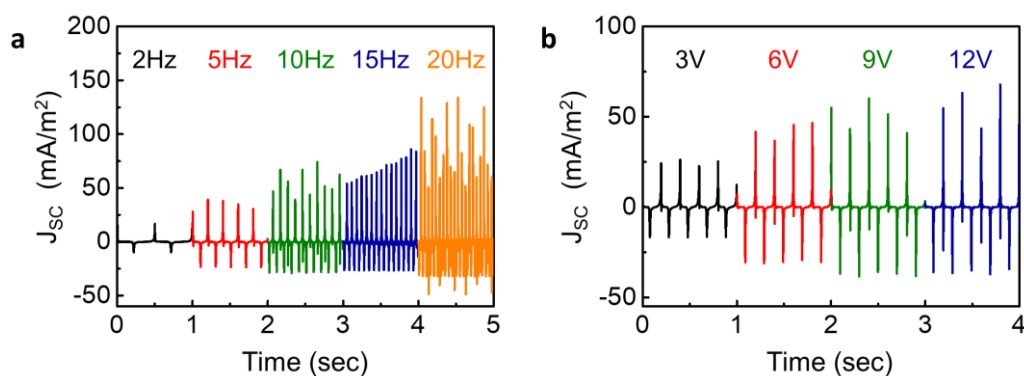


Fig. 5-12 Electrical output of the device under various input conditions. Short circuit current density of the nanowire device was measured under the application of a periodic impacting force (a) at variable frequency between 2 ~ 20 Hz with amplitude of 6 V and (b) at different amplitude between 3 ~ 12 V with frequency of 5 Hz. In our energy generator system, force amplitude of magnetic shaker can be controlled by applied voltage. Fig. (a) and (b) are taken from the author's work from Ref. [2], reproduced with permission from Royal Society of Chemistry.

<sup>8</sup> Hypothetically, if materials in triboelectric generators are true dielectric, the resistance of the load for the maximum coupling of the device circuit would be an infinite. In this aspect, the relatively low optimum resistance ( $20 \text{ M}\Omega$ ) indicates that materials in this experiment are not a good insulator and the device performance would be further improved by using materials with better dielectric properties.

Regarding the triboelectric generator performance, various input conditions including frequencies and amplitudes have been tested (Fig. 5-12). The  $J_{SC}$  was measured in response to the periodic impacting at a frequency ranging from 5 to 20 Hz with amplitude of 6 V. In addition, the amplitude was also varied from 3 V to 12 V within constant frequency of 5 Hz. As a result, it is clearly seen that the electrical output was found to increase with increasing impact frequencies and amplitudes. These performance enhancement at high frequency and high amplitude are attributed to the preventing of the charge loss and more conformal contact for more transferred charge, respectively.

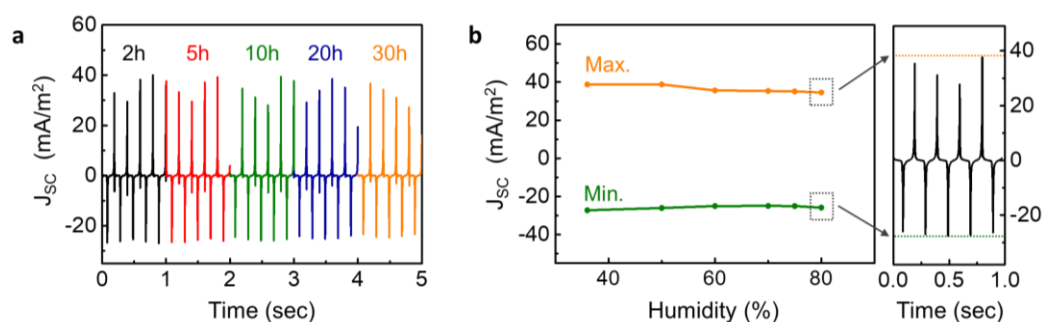


Fig. 5-13 Reliability test of the triboelectric device. (a) Fatigue testing: short circuit current density recorded over time in response to continuous impacting at a frequency of 5 Hz and amplitude of 6 V on the same Nylon-11 nanowire based triboelectric generator for 30 h (~ 540,000 cycles impacting cycles in total). Data were recorded after 2 h (18 k cycles), 5 h (90 k cycles), 10 h (180 k cycles), 20 h (360 k cycles), and 30 h (540 k cycles). (b) Triboelectric generator performance under various humidity condition. The maximum (orange) and minimum peak of short circuit density were collected at certain humidity. (right image) Fig. (a) and (b) are taken from the author's work from Ref. [2], reproduced with permission from Royal Society of Chemistry.

In addition, fatigue testing was carried out by continuously impacting the Nylon-11 nanowire-based device at 5 Hz and amplitude of 6V for up to 30 hours ( $\approx$  540,000 cycles). Fig. 5-13a shows that the  $\delta'$ -phase nanowire-based triboelectric generator exhibited a negligible change in  $J_{SC}$  over the entire period of continuous testing. Reliability tests under various humidity conditions were also carried out by impacting the  $\delta'$ -phase nanowire-based triboelectric generator device within a humidity-controlled box. (Fig. 5-13b) Although Nylon is known to be prone to degradation in the presence of moisture, the  $\delta'$ -phase nanowire-based triboelectric generator showed reliable output performance up

to high humidity condition ( $\sim 80\%$ ), indicating that the AAO template serves to encapsulate and protect the nanowires from environmental factors.

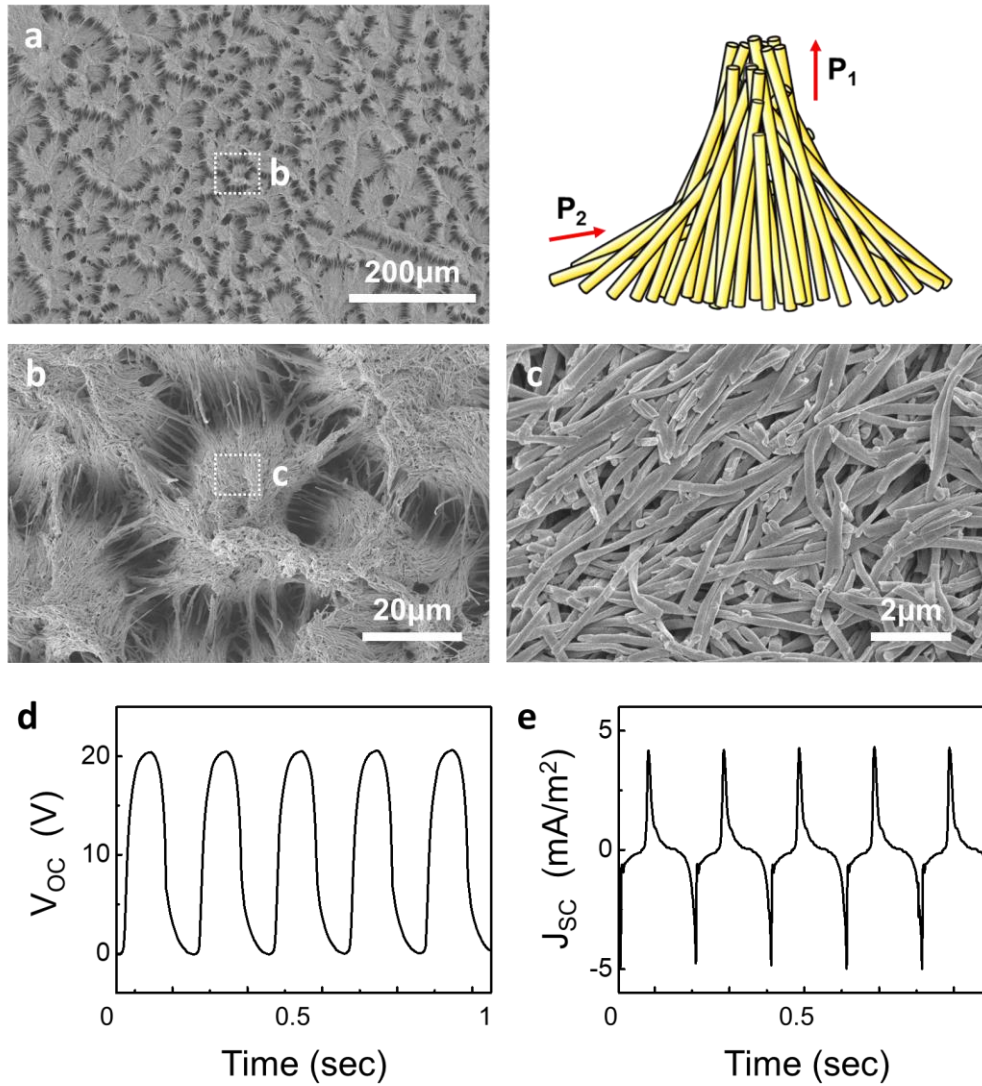


Fig. 5-14 Template-free nanowire-based triboelectric generator. (a)-(c) SEM images of a template freed nanowire mat. The inset illustrates the random direction of the spontaneous polarisation. (d) and (e) show the output performance of the nanowire mat based triboelectric generator. Fig. (a) ~ (e) are taken from the author's work from Ref. [2], reproduced with permission from Royal Society of Chemistry.

To further confirm the effect of self-polarization on triboelectric generator performance, we also measured the output performance of the template-freed  $\delta'$ -phase nanowire mat where the nanowires are lying on the substrate with randomly oriented polarisation directions (Fig. 5-14a-c). Interestingly, the template-freed nanowires mat based device generated suppressed output performance ( $V_{OC} = 20V$  and  $J_{SC} = 4.0 \text{ mA}\cdot\text{m}^{-2}$ ), even though it was thinner and had a larger effective surface area (Fig. 5-14d and e). Due to the randomly oriented polarisation in the nanowire mat, the generation of triboelectric charge was likely inhibited during the contact and separation process. These results support the orientation directed polarisation effects in the Nylon-11 nanowires while they are still aligned and embedded within the template.

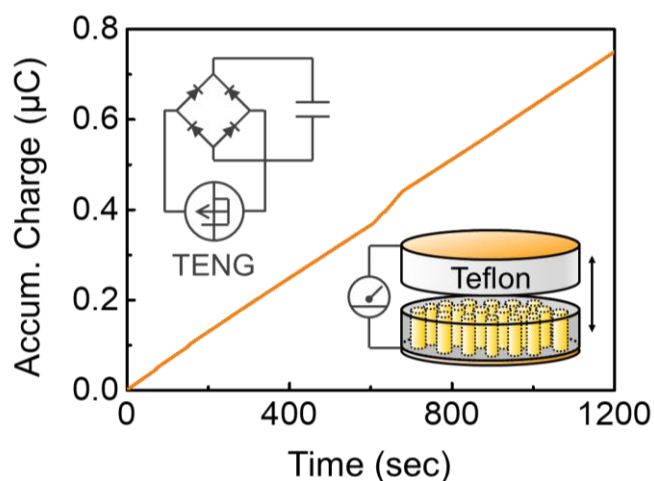


Fig. 5-15 Charge accumulation trend of the nanowire-based device with respect to time. Left top and right bottom insets show the circuit structure and schematic of the triboelectric generator. Fig. is taken from the author's work from Ref. [2], reproduced with permission from Royal Society of Chemistry.

To confirm the energy generated by the  $\delta'$ -phase nanowire-based on triboelectric generator, a  $470 \mu\text{F}$  capacitor was connected to the device using a full-wave bridge rectifying circuit (Fig. 5-15). The  $\delta'$ -phase Nylon-11 nanowire-based triboelectric generator under mechanical pressure at 5 Hz for about 20 minutes successfully charged the capacitor with a charging speed of  $\sim 38 \mu\text{C}\cdot\text{min}^{-1}$ . Notably, the accumulated charge increased with time, suggesting the Nylon nanowire-based triboelectric generator had excellent stability.

The electric power produced by the Nylon nanowire-based triboelectric generator was used to directly turn on several commercial light-emitting diodes (LEDs). During contact and separation with 5 Hz frequency, 36 white LEDs were driven by the produced output voltage without the need for external energy storage devices (Fig. 5-16).

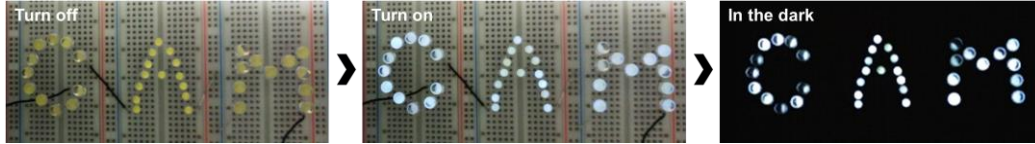


Fig. 5-16 LED lightning test for  $\delta'$ -phase Nylon-11 nanowire-based triboelectric generator. 36 white LEDs were parallelly connected with device. Fig. is taken from the author's work from Ref. [2], reproduced with permission from Royal Society of Chemistry.

We conducted analytical simulations using a finite element method (FEM) with COMSOL Multiphysics software to further confirm the effects of self-polarization on triboelectric potential. To confirm the working mechanism of the self-poled nanowire-based triboelectric generator, we carried out a theoretical analysis based on the Gauss theorem.[35], [47]

In the dielectric-to-dielectric contact-separation mode triboelectric generators (Fig. 2-4a), the electric potential difference ( $\Delta V$ ) between two electrodes can be given by

$$\begin{aligned}\Delta V &= E_1 t_1 + E_2 t_2 + E_{air} d \\ &= \left[ -\frac{Q}{S \varepsilon_0 \varepsilon_{r1}} t_1 \right] - \left[ \frac{Q}{S \varepsilon_0 \varepsilon_{r2}} t_2 \right] + \left[ \frac{S \sigma - Q}{S \varepsilon_0} d \right] \quad (5-1) \\ &= -\frac{Q}{S \varepsilon_0} \left( \frac{t_1}{\varepsilon_{r1}} + \frac{t_2}{\varepsilon_{r2}} + d \right) + \frac{\sigma d}{\varepsilon_0}\end{aligned}$$

where  $E$  is electric field strength,  $t_1$  and  $t_2$  are the thickness of the two surfaces,  $d$  is the distance between two different layers,  $Q$  is the value of transferred charge,  $S$  is the area of the electrode,  $\sigma$  is the triboelectric charge density,  $\varepsilon_0$  is the vacuum permittivity, and  $\varepsilon_{r1}$  and  $\varepsilon_{r2}$  are the relative permittivity (dielectric constant) of dielectric materials, respectively. In the conductor-to-dielectric structure,  $t_1/\varepsilon_{r1}$  can be ignored because the metal layer acts as triboelectric layer and electrode.

Under open-circuit conditions, the value of transferred charge ( $Q$ ) become zero since no charge is transferred between the two top and bottom electrodes. Thus, if we assume electric potential of the bottom electrode to be zero, the equation for the open-circuit voltage ( $V_{oc}$ ) can be calculated by

$$V_{oc} = \frac{\sigma d}{\epsilon_0} \quad (5-2)$$

Using experimentally determined  $V_{oc}$  of each triboelectric generator, we can obtain a theoretical triboelectric charge density ( $\sigma$ ).

$$\sigma = \frac{V_{oc}\epsilon_0}{d} \quad (5-3)$$

When  $d$  is maximum (0.5 mm) and  $\sigma$  of Al, the melt-quenched Nylon film, and the nanowire-filled template are 0.78, 1.06, and 1.95  $\mu\text{C m}^{-2}$ , respectively.

A COMSOL Multiphysics simulation demonstrated the triboelectric potential difference of three different structure triboelectric generators with Teflon as the top part and: (a) Al, (b) Nylon-11 film, and (c)  $\delta'$ -phase Nylon-11 nanowires in the template as the bottom parts (Fig. 5-17). We assumed that the length of the dielectric and electrodes are infinite because they are significantly larger than the thickness of the dielectric layer. The nanowire-filled AAO template structure was simplified in the simulation, considering the surface area of the nanowires ( $\sim 50\%$ ). Because of the charge density ( $\sigma$ ) difference, the nanowire sample shows the highest potential different between the top and bottom electrodes. In addition, the self-poled Nylon nanowire region exhibits relatively higher electric potential than the AAO template region. It indicates that further enhanced triboelectric performance of nanowire containing AAO template devices is mainly attributed to the self-polarization of the nanowires.

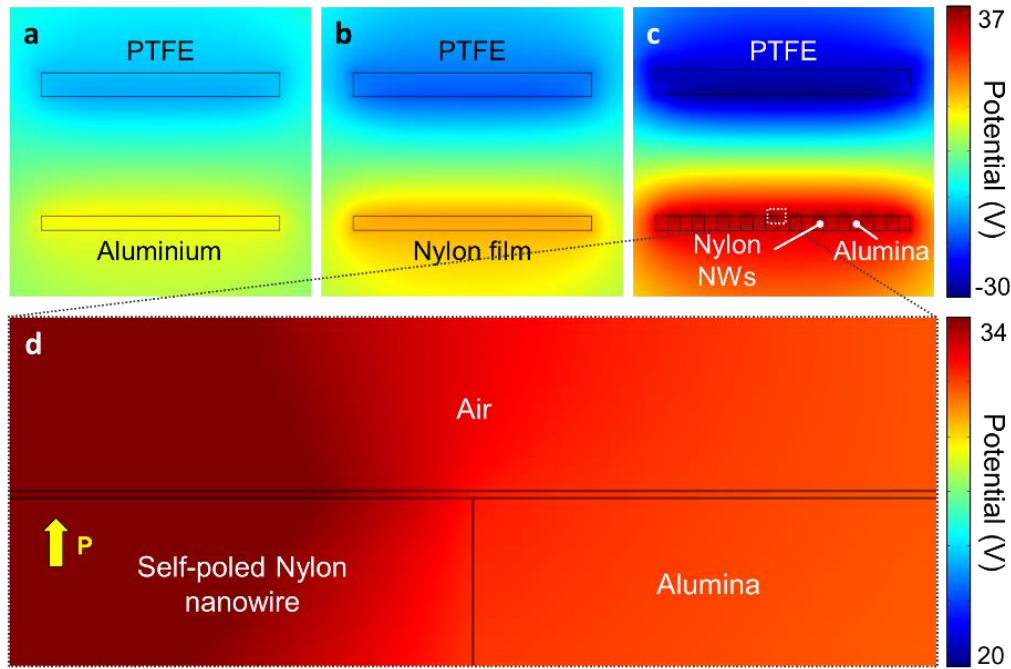


Fig. 5-17 Calculated electric potential distribution at different surface charge density: (a) Al, (b) Nylon-11 film, and (c)  $\delta'$ -phase Nylon-11 nanowires. Fig. (a) ~ (d) are taken from the author's work from Ref. [2], reproduced with permission from Royal Society of Chemistry.

The ideal electric potential of self-poled Nylon-11 nanowire-based triboelectric generators can be calculated based on the experimental result of spontaneous polarisation.[217] Under short-circuit conditions ( $V = 0$ ), the transferred charge ( $Q_{sc}$ ) are given by

$$Q_{sc} = \frac{S\sigma d\epsilon_{r1}\epsilon_{r2}}{t_1\epsilon_{r2} + d\epsilon_{r1}\epsilon_{r2} + t_2\epsilon_{r1}} \quad (5-4)$$

The value of  $Q_{sc}$  can therefore be varied as a function of  $d$ . When the generator is fully released ( $d = 0.5$  mm), the maximum transferred charge per unit area was theoretically calculated to be 0.65, 0.94, and 1.75  $\mu\text{C m}^{-2}$  for Al, melt-quenched Nylon film, and the nanowire-filled template, respectively. The transferred charge ( $Q_{sc}$ ) are also calculated using the integration of short-circuit current ( $I_{sc}$ ) (Fig. 5-18). The dimensions which used for the calculation are summarised in Table 5-1.

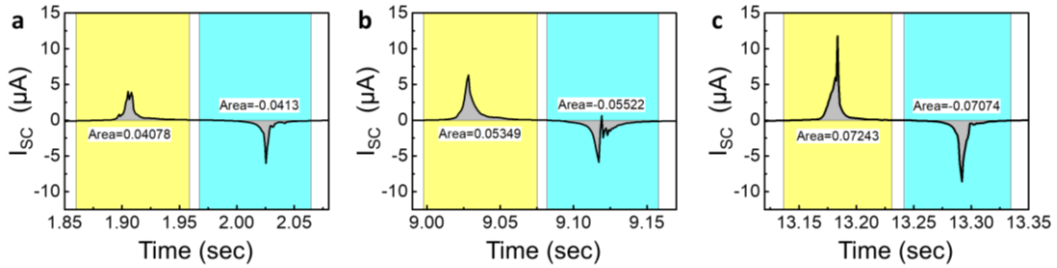


Fig. 5-18 The short circuit current ( $I_{sc}$ ) of various triboelectric generators: (a) Al, (b) melt-quenched Nylon-11 film, and (c)  $\delta'$ -phase Nylon-11 nanowire-based devices. The amount of transferred charge ( $Q_{sc}$ ) can be calculated by the integration of graph. Fig. (a) ~ (c) are taken from the author's work from Ref. [2], reproduced with permission from Royal Society of Chemistry.

Table 5-1 Dimensions of the triboelectric generator

Symbol	Meaning	Value	unit
$d$	max. separation distance	0.5	mm
$t_1$	thickness of PTFE	100	$\mu\text{m}$
$t_2$	thickness of Nylon film & AAO template	60	$\mu\text{m}$
$S$	surface area of the electrode	3.14	$\text{cm}^2$
$V_{OC,Al}$	$V_{OC}$ of Al-based device	40	V
$V_{OC,film}$	$V_{OC}$ of melt-quenched film-based device	60	V
$V_{OC,NW}$	$V_{OC}$ of $\delta'$ -phase NW-based device	110	V
$\epsilon_0$	vacuum permittivity	8.85E-12	$\text{F m}^{-1}$
$\epsilon_{r, film}$	relative permittivity of Nylon-11 film[208], [218]	3.7	
$\epsilon_{r, AAO}$	relative permittivity of AAO template	9	
$\epsilon_{r, NW}$	relative permittivity of oriented Nylon[208], [218]	4.5	
$\epsilon_{r, PTFE}$	relative permittivity of PTFE	2.1	
$P_r$	spontaneous polarization of Nylon-11[217]	55	$\text{mC m}^{-2}$

## 5.5 Conclusions

To summarise, we have demonstrated for the first time, a novel and facile GANT infiltration method for the fabrication of highly oriented, self-poled  $\delta'$ -phase Nylon-11 nanowires, as a rarely synthesised tribo-positive material. Assisted gas-flow controlled the crystallisation speed, resulting in the  $\delta'$ -phase crystal structure. Preferential crystal orientation originates from the nanoconfinement effect in the template, resulting in self-poling of the Nylon-11 nanowires with an increased average crystallinity of up to  $\sim 40\%$ . When self-poled Nylon-11 nanowires were combined with counterpart tribo-negative surfaces, such as Teflon, the resulting output power was observed to be  $\sim 6$  times and  $\sim 10$  times higher than those of melt-quenched Nylon-11 film- and Al-based triboelectric generator, respectively. The output power generated by the Nylon-11 nanowire-based device was high enough to drive commercial electronic components such as LEDs and capacitors without external power sources. The work provides a new strategy to develop highly crystalline and self-poled Nylon in a facile and robust manner, thus providing a means to realise a much-needed synthetic tribo-positive material with enhanced surface charge density for use in a high-performance triboelectric generator. The patent application has been filed based on this new technology.

## Chapter 6

# **$\alpha$ -phase Nylon-11 Nanowires Fabricated by Thermally-Assisted Nano-Template Infiltration (TANI) Method for Triboelectric Generators**

Spontaneous polarization (or remanent polarization) in a ferroelectric polymer is the polarization which remains when an applied electric field is reduced to zero, and it is one of the most important characteristics which determines the performance of charge-based energy harvesting devices. The intensity and stability of spontaneous polarization are attributed to the molecular structure of the ferroelectric polymer. Therefore, identifying material with a stable, well-packed molecular structure is crucial to further improve the performance of energy harvesting devices, as well as widening the range of possible applications.

Among various crystal structures of Nylon-11, spontaneous polarization has only been achieved in the metastable  $\delta'$ -phase with relatively sparse chain packing and random hydrogen bonds, here the spontaneous polarization realized by electrical poling of the

ferroelectric polymer.[96], [108], [110] In the case of the thermodynamically stable  $\alpha$ -phase, although it exhibits the highest crystallinity with outstanding thermal stability based on denser molecular packing and well-ordered hydrogen bonds, it has been known that it is not possible to achieve dipole alignment via electric poling.[219], [220] This is because tightly packed hydrogen bonds in the  $\alpha$ -phase restrain the dipole rotation up to the point of electrical breakdown, and this is why  $\alpha$ -phase has been known as a ‘polar’ but ‘non-ferroelectric’ phase.[103], [106]

In this work, we have developed  $\alpha$ -phase Nylon-11 nanowires which exhibit an exceptionally strong and thermally stable spontaneous polarization using a thermally-assisted nano-template infiltration (TANI) method. Through nanoconfined molecular self-assembly, the definitive dipole alignment of  $\alpha$ -phase Nylon-11 nanowires has been achieved for the first time without any external electrical poling. To demonstrate the formation of well-aligned  $\alpha$ -phase nanowires, we performed sophisticated analysis of XRD patterns with and without the supporting template and confirmed it by molecular simulations. The remarkably high surface potential of the self-poled  $\alpha$ -phase nanowires, corresponding to high-intensity spontaneous polarization, was measured directly by KPFM, indicating that the  $P_r$  of non-ferroelectric  $\alpha$ -phase is much higher than that of the ferroelectric  $\delta'$ -phase nanowires. The robust thermal stability of the spontaneous polarization in  $\alpha$ -phase nanowires is also confirmed by surface potential changes before and after thermal annealing. As a practical trial, we introduced  $\alpha$ -phase Nylon-11 nanowires into a triboelectric generator. The device exhibited a 4-fold and 34-fold increase in output power density compared to a  $\delta'$ -phase nanowire-based device and a conventional aluminium-based device under the same mechanical excitation. A substantial amount of this work is under reviewing process, to be published. The authors’ contributions are given in Appendix A.

## 6.1 Ideal remanent polarization calculation

To compare the chain and hydrogen bonds configuration, we have conducted molecular simulations using a program called Materials Studio 8.0.[203] (Details of simulation process are given in Chapter 3.2.4). As a semi-crystalline polymer, Nylon-11

has at least four crystal structures referred to as the triclinic  $\alpha$  and  $\alpha'$ , monoclinic  $\beta$ , pseudo hexagonal  $\gamma$ ,  $\delta$  and  $\delta'$ . [78], [89] As mentioned, the pseudo-hexagonal phases (such as  $\delta'$ -phase) display ferroelectric properties due to sparse chain packing and random hydrogen bonding. As Fig. 6-1a and b illustrate, the un-poled  $\delta'$ -phase has randomly oriented Nylon-11 chains within a pseudo-hexagonal unit cell, resulting in the cancellation of dipole moments. [89] Additional mechanical drawing and subsequent electric poling process allow chains to rotate such that the amide groups point in the same direction, resulting in net dipole moment (Fig. 6-1c, d). In contrast, the  $\alpha$ -phase can adopt a well-aligned molecular structure in the triclinic unit-cell without stretching and/or high voltage poling (Fig. 6-1e, f). This is because the hydrogen bonds are organised into well-defined sheets held together by van der Waals interactions, with the amide groups of adjacent chains located at about the same height along the chain axis. [89] As a result, the dipole moment perpendicular to the chain axis, points along a single direction. (This is the reason why  $\alpha$ -phase is ‘polar’.) However, it must be noted that such unidirectional dipole moments of  $\alpha$ -phase are limited to a localized crystalline region, and the directions of such crystalline regions are randomly determined during the crystallisation process. Furthermore, it is also impossible to align every dipole in the  $\alpha$ -phase sample due to the restraints on dipole rotation up to the electrical breakdown. As a result, the net polarization of pristine  $\alpha$ -phase (bulk) sample is much smaller than that of electrically poled  $\delta'$ -phase sample.

So how high can the spontaneous polarization be, when dipoles in a bulk  $\alpha$ -phase are fully aligned? To evaluate the maximum spontaneous polarization in Nylon-11, we estimate the “ideal”  $P_r$  values of perfectly aligned  $\delta'$ -phase and  $\alpha$ -phase. To a first-order approximation, the  $P_r$  scales with the dipole moment and the crystallinity. [77], [221] Using molecular simulation, the dipole moment for individual molecules can be measured by assigning charge to the atoms. As a minimum repeating unit, the dipole moments per one unit cell values of  $88 \times 10^{-30}$  C m and  $101 \times 10^{-30}$  C m are obtained in a pseudo-hexagonal  $\delta'$ -phase and triclinic  $\alpha$ -phase respectively. In the case of  $\delta'$ -phase, assuming a crystallinity of about 40 %, the calculated  $P_r$  is  $3.2 \mu\text{C cm}^{-2}$ ; this is in good agreement with the experimentally determined value of about  $2.5 \mu\text{C cm}^{-2}$ . [101] In contrast,  $\alpha$ -phase with the same crystallinity shows the  $P_r$  of  $7.5 \mu\text{C cm}^{-2}$ , meaning that fully aligned  $\alpha$ -phase would have much greater spontaneous polarization than that of electrically poled  $\delta'$ -phase. This is because the fully stretched chain structure in the  $\alpha$ -phase maximizes the dipole moment per

monomer unit.[221] In addition, considering the crystal structure, the distance between adjacent molecules in the triclinic  $\alpha$  cell is much smaller than that in pseudo-hexagonal  $\delta'$ -phase. Lastly, from a realistic point of view, well-defined hydrogen-bonded sheets in  $\alpha$ -phase would enable more aligned and stable dipole configuration.

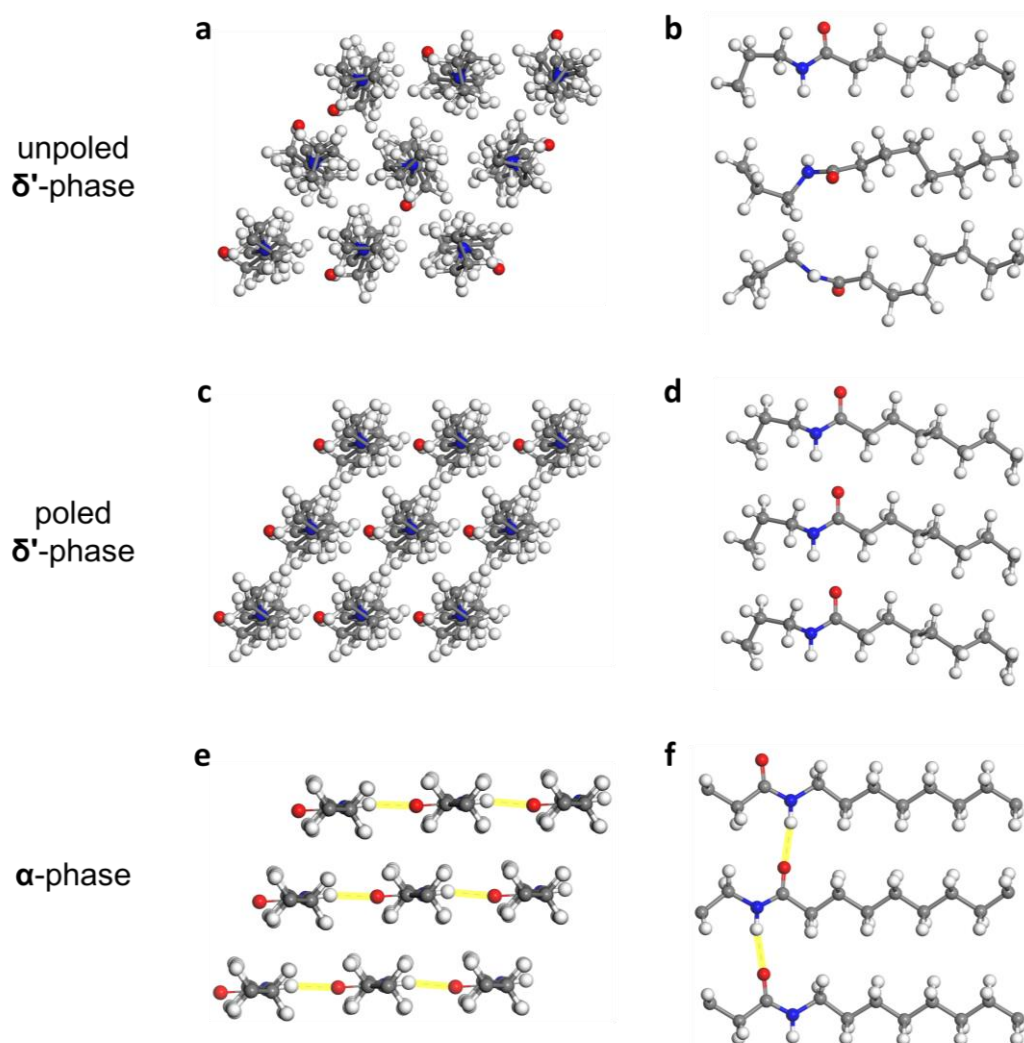


Fig. 6-1 Molecular structure and chain packing of Nylon-11. (a, b) Schematics show packing of Nylon-11 monomeric chains in unpoled  $\delta'$ -phase viewed along the c axis and b axis respectively. All molecules lie in a random orientation. (c, d) The crystal structures and molecular packing of the poled  $\delta'$ -phase. All the oxygen atoms point the same direction. (e, f) Crystal structure of  $\alpha$ -phase. Because  $\alpha$  is the most thermodynamically stable phase, the molecules are fully stretched with trans configuration and aligned with the hydrogen bonding sheet. The yellow lines indicate intermolecular hydrogen bonding. Grey spheres represent carbon atoms, red spheres oxygen atoms, blue spheres nitrogen atoms, and white spheres hydrogen atoms.

## 6.2 Thermally-assisted crystal structure control

To align the dipoles in  $\alpha$ -phase Nylon-11 nanowires, we introduced a nano-confinement method, such as nano-template wetting, because this technique enables the self-polarization of polymer nanowires during the crystallisation process without an additional high-voltage poling process.[202], [208] However, due to the difficulties of process optimisation, most nanowires manufactured via a conventional template-wetting process show poor crystallinity, resulting in a lower  $P_r$  than that of electrically poled films.[186] Furthermore, despite a large amount of related research over the past decade, controlling the polymer crystal structure in the nano-sized pore remains challenging. As a result, nanowires with the most stable phase of polymer, including  $\alpha$ -phase Nylon-11, have never been demonstrated.

To solve these problems, we developed the TANI method, which allows us to finely tune the crystallisation process in the nanopores. We note that the critical factor influencing phase control of Nylon-11 is the speed of crystallisation.[81], [92]–[94], [222] In particular, in the case of the highly ordered and thermodynamically stable  $\alpha$ -phase, slow crystallisation with sufficient driving force for molecular configurational flexibility is crucial. Therefore, to reduce the crystallisation rate and increase the chain mobility, we have controlled the vapour environment, solution concentration, and temperature. (Details of the experimental process are discussed in Chapter 3.1).

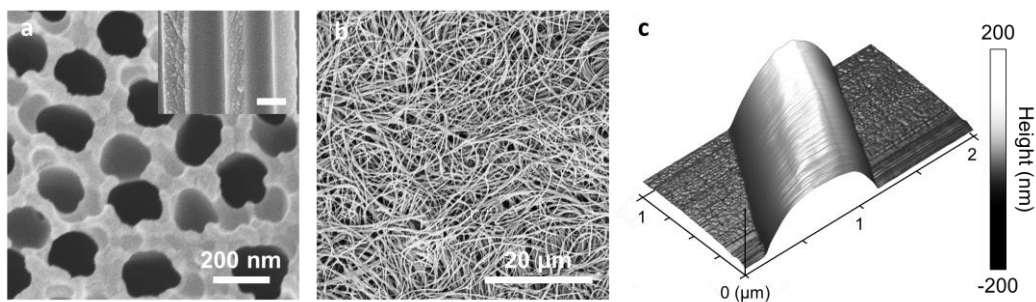


Fig. 6-2 Morphology of nano-template and resulting polymer nanowires. a. SEM image of the nano-template surface with 200 nm pores. Inset shows the template cross-section. Scale bar indicates 200 nm. b. SEM image of template-free nanowires, indicating that each nanowire has a uniform width of 200 nm, which is similar to the dimensions of the nano-template pore channels. c. AFM topography image of a single nanowire strand showing that a highly dense and smooth surface (without grain boundaries) can be obtained by the TANI process.

Fig. 6-2a shows the SEM images of an AAO nano-porous template. The top surface and cross-section images indicate that the pore size is around 200 nm. The morphology of the nanowires manufactured by TANI method is displayed in Fig. 6-2b, c. Long chain-shaped nanowires with uniform width (200 nm) and length (60  $\mu\text{m}$ ) were detected after the AAO was dissolved using mild acid. These nanowire dimensions are similar to that of the nano-template pore channels. The surface morphology of the nanowire can be measured by AFM. Compared to the Nylon-11 film, the nanowires show a uniform and smooth surface topography without grain boundaries (Fig. 3-2).

Detailed crystal structure characterization was carried out by XRD. Typically, the nanowires fabricated by conventional nano-template wetting method generated diffraction patterns with weak intensity of peaks at  $2\theta = 21.6^\circ$  and  $22.8^\circ$  (Fig. 6-3, left panel, black line).[208] In contrast, it is reported that an  $\alpha$ -phase Nylon-11 film shows two distinct peaks at  $2\theta = 20^\circ$ ,  $24.2^\circ$ , and one small peak at  $7.8^\circ$ . [89] This result confirms that the  $\alpha$ -phase Nylon-11 with desirable crystallinity cannot be obtained by typical nanoconfinement method. To achieve the  $\alpha$ -phase nanowires, we subjected Nylon-11 solution to crystallization in a closed heating system. In this system, the solvent vapour environment effectively suppressed the evaporation speed in the nanopores, resulting in slow crystallisation. Furthermore, additional heating allowed us to increase the chain mobility which is required for molecular alignment. Fig. 6-3 (left panel, red lines) shows that  $\alpha$ -phase nanowires were achieved by this TANI method, and that the peak intensities increased with temperature. To investigate the optimised processing conditions for highly crystalline  $\alpha$ -phase nanowires, we deliberately varied the temperature and solution concentration, measuring the crystallite size ( $D_p$ ). First,  $D_p$  gradually increases with temperature, indicating that the additional heating increases the driving force for molecular reorientation and ordering (Fig. 6-3, right up panel). The  $D_p$  is also affected by the concentration of solution. A dilute solution allows larger crystals to be formed because of the increased free volume of polymer chains. These results indicate that the desirable, highly crystalline  $\alpha$ -phase nanowires can be achieved by the TANI process at high-temperature and in low concentration.

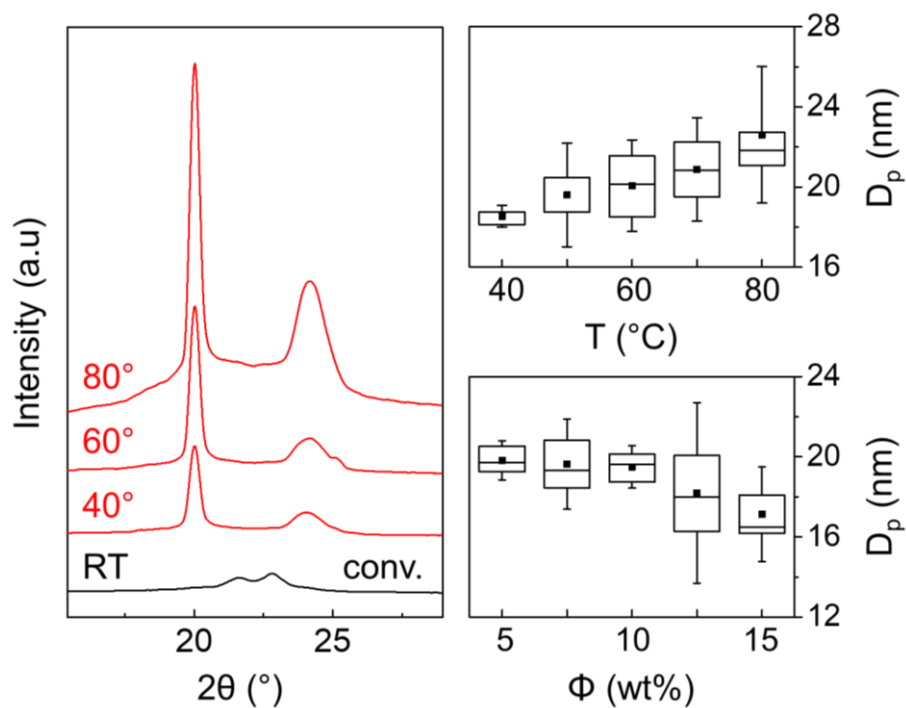


Fig. 6-3 (left) XRD patterns of nanowires crystallised at various temperatures. Phase changes can be observed between (black) the conventional room temperature template wetting method and (red) the TANI method with different temperature. (right) Based on the diffraction analysis, the size of crystals ( $D_p$ ) is plotted as a function of (above) temperature and (below) solution concentration. '■' indicate mean  $D_p$  value at certain condition. The middle line, top and bottom boundaries in the box indicate the median, 75 % and 25 % values, respectively.

Fig. 6-4 compares the diffraction pattern of the  $\alpha$ -phase nanowires with that of film. The diffraction pattern of template-freed nanowires (red) displays identical peak positions with the triclinic  $\alpha$ -phase film (black). Notably, the diffractogram of the nanowire sample shows much sharper peaks of (200), (210/010) planes with a smaller full width at half-maximum (FWHM) and smaller amorphous region ( $2\theta = \sim 21.6^\circ$ ) than those of  $\alpha$ -phase film. Furthermore, the  $\alpha$ -phase nanowires have much higher crystallinity ( $\chi = 50\%$ ) with larger  $D_p$  ( $23.4 \pm 2.05$  nm) than those of film ( $\chi = 41\%$ ,  $D_p = 16 \pm 1.52$  nm). These results suggest that the TANI method generated highly crystalline  $\alpha$ -phase nanowires with larger crystal sizes compared to the  $\alpha$ -phase film. The origin of higher crystallinity is corroborated using FT-IR measurements. (Detailed peak positions and their assignments are listed in Chapter 3.2.1) In Fig. 6-5, much higher IR peak intensity at both N-H stretching and amide I regions was observed from the  $\alpha$ -phase nanowires. Considering that the N-H stretching ( $3300\text{ cm}^{-1}$ ) and the amide I ( $1635\text{ cm}^{-1}$ ) bands reflect the overall distribution of hydrogen-bonded strengths and local ordering of hydrogen bonds respectively,[96], [188], [189] it can be inferred that the TANI method enables well-ordered crystal growth based on the formation of hydrogen bonds.

The direction of molecular orientation is verified by detailed XRD analysis of the nanowires *within* the nano-porous AAO template. In principle, a single crystal sample in a Bragg-Brentano diffractometer would produce only one family of lattice planes with scattering vectors ( $q$ ) normal to the sample surface in the diffraction pattern. Despite the  $\alpha$ -phase nanowires are not representing single crystals, the discrepancy in the diffractograms between the vertically aligned nanowires and randomly positioned nanowires indicates a highly ordered nanowire crystal structure with preferential chain alignment. In the case of nanowires *within* the AAO template (Fig. 6-4, orange), only one distinct diffraction peak at  $2\theta_{(200)} = 20^\circ$  was observed. In other words, the (001) and (210/010) planes would diffract at  $2\theta = 7.8^\circ$  and  $24.2^\circ$ , but only minimal diffractions were obtained because those peaks are not represented in the Bragg-Brentano geometry. This means that the nanowires manufactured by controlled nano-template wetting process have preferential crystal orientation with the molecular chain axis perpendicular to the nanowire length direction, consistent with previous reports.[137], [158], [159]

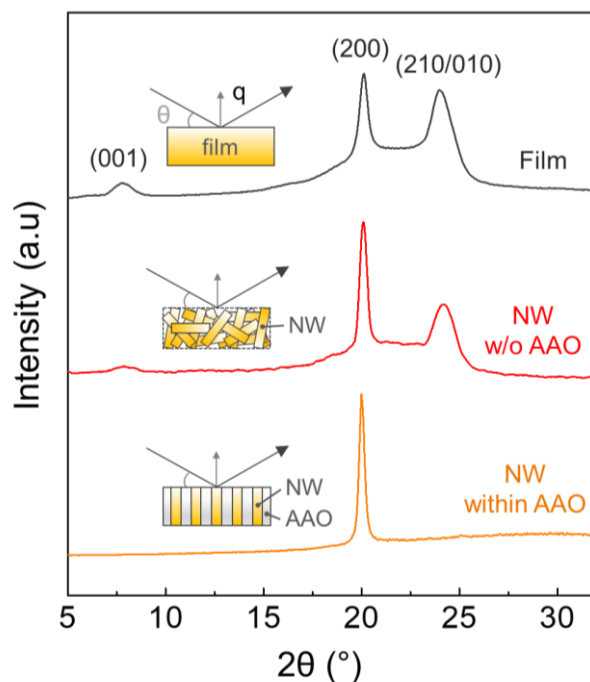


Fig. 6-4 XRD patterns of (black)  $\alpha$ -phase Nylon-11 film and nanowires (red) without and (orange) *within* a nano-porous AAO template. Inset schematics display the morphology of sample and the direction of X-ray beam ( $\theta$ ) with a scattering vector ( $q$ ). The TANI method results in identical peak positions for both film and nanowire; the nanoconfinement effect results in nanowires with sharper main peaks and smaller amorphous region, indicating a more ordered and bigger crystalline region. The discrepancies between patterns obtained from the nanowire without and *within* the AAO template shows the preferential crystal orientation in the nanowires.

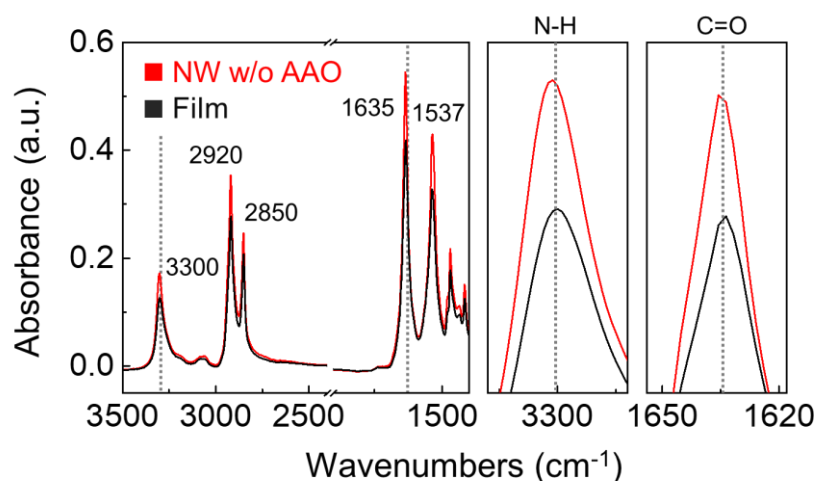


Fig. 6-5 FT-IR absorbance spectra of  $\alpha$ -phase (red) template-freed nanowires and (black) film. Middle and right graphs indicate the infrared spectra near N-H stretching (3300  $\text{cm}^{-1}$ ) and amide I (1635  $\text{cm}^{-1}$ ) modes, respectively.

The molecular simulation results validate the determinations of  $D_p$  and preferential orientation in  $\alpha$ -phase nanowires (Analytical details are discussed in Chapter 3.2.1). With the assumption of an ideal (or unlimited)  $D_p$  and random orientation, the simulated powder diffraction pattern displays the highest peak at  $2\theta_{(210/010)} = 24.2^\circ$  with the second highest peak at  $2\theta_{(200)} = 20^\circ$  (Fig. 6-6, top). However, introducing the experimentally achieved  $D_p$  values changes the order of the highest peaks and broadens the diffraction pattern (Fig. 6-6, middle). Considering the broad diffraction peak ( $2\theta = 21.6^\circ$ ) of amorphous region in the  $\alpha$ -phase, the simulated result is well matched with the experimentally achieved diffraction patterns. Lastly, preferred orientation correction based on the Rietveld-Toraya equation results in a diffractogram with remarkably high and sharp peak at  $2\theta_{(200)} = 20^\circ$ , showing a good agreement with that of nanowires *within* AAO template (The contribution of AAO template to the diffraction pattern is discussed in Chapter 3.1.2). These agreements of relative peak intensity and FWHM between calculated and experimental results confirm that the relatively large crystals in the  $\alpha$ -phase nanowires are preferentially aligned perpendicular to the b axis.

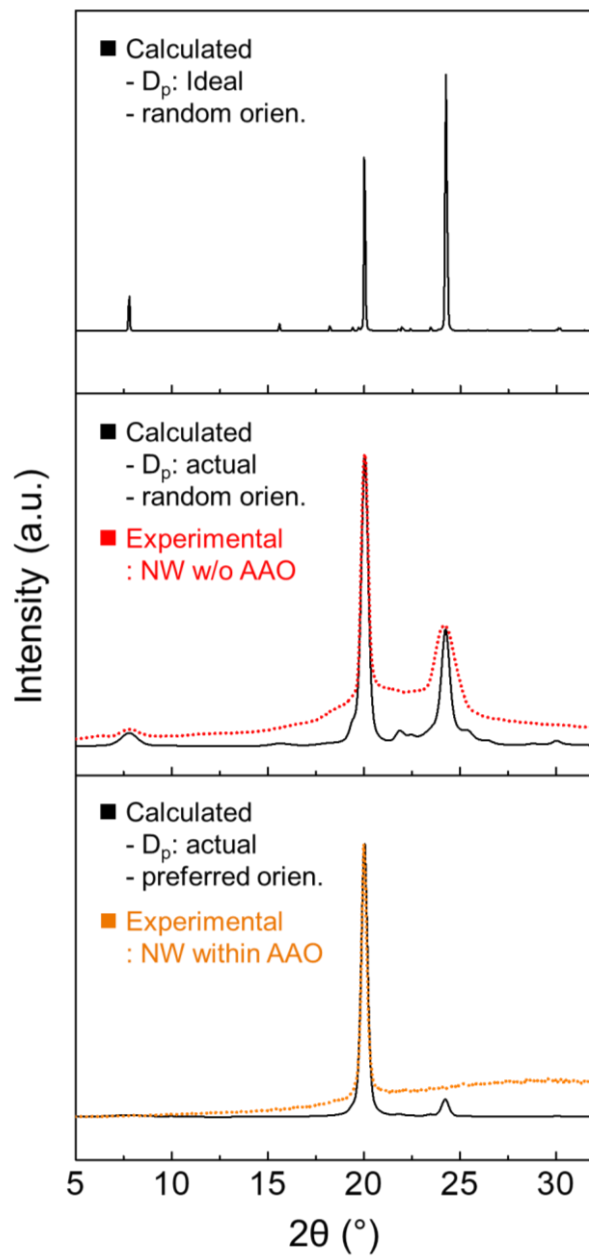


Fig. 6-6 Comparison of calculated and experimentally achieved XRD patterns. (black) The calculated XRD patterns for  $\alpha$ -phase Nylon-11 with the assumption of ideal/real  $D_p$  and random/preferred orientation. They are in good agreement with the experimentally observed spectra of (red dot) nanowires without template and (orange dot) nanowires *within* template.

### 6.3 Spontaneous polarization in $\alpha$ -phase nanowires

It is believed that the spontaneous polarization in Nylon-11 results mainly from dipole alignment, because the  $P_r$  value is close to zero as the dipole density approaches zero in oriented and poled Nylon-11.[223], [224] This indicates that the preferred chain orientation arising from the nanoconfinement effect can generate spontaneous polarization (called self-polarization), and the intensity of spontaneous polarization has a close relationship with the degree of molecular alignment.

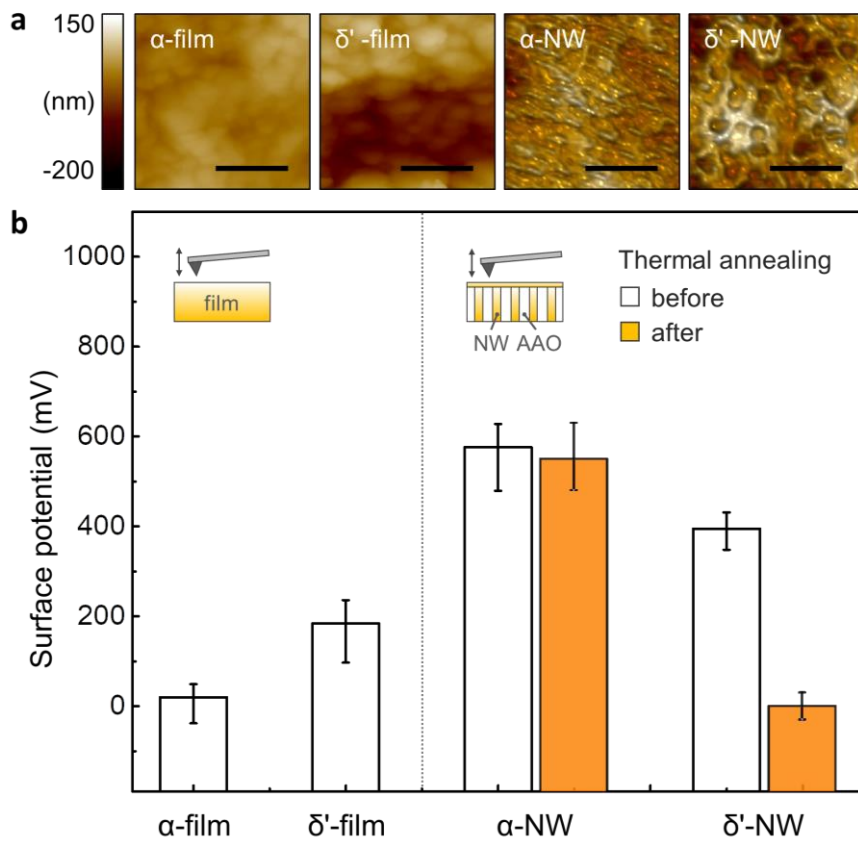


Fig. 6-7 KPFM analysis. a. AFM topography images of  $\alpha$ -phase,  $\delta'$ -phase Nylon-11 films and nanowires. The surface of nanowire sample is covered by merged nanowire tips. Scale bar indicates 1  $\mu\text{m}$ . b. Plots of the surface potential of various films and nanowires. Thermal stability of nanowire samples was also investigated by surface potential measurement (white bar) before and (orange bar) after thermal annealing at 165  $^{\circ}\text{C}$ . Inset schematics indicate the way to measure the surface potential using KPFM.

To investigate the intensity of spontaneous polarization, a full set of surface potential analysis was conducted by KPFM. Although the  $P_r$  of ferroelectric materials has been observed by polarization-electric field (P-E) hysteresis loops, the  $P_r$  of ‘non-ferroelectric’ materials cannot be measured in this way as they do not show such hysteresis behaviour. In contrast, KPFM can measure the material’s surface potential, and such surface potential includes the contribution of work function difference and surface charge induced by mechanical rubbing or ferroelectric polarization.[59], [190], [191] Thus KPFM analysis provides a reliable method for showing the difference in  $P_r$ . Fig. 6-7a displays the top surface morphology of film and nanowire samples. Although the nanowires are embedded in the AAO template, the surface potential can be measured because the top surfaces are covered by a thin film consisting of merged nanowire tips. In principle, the almost similar surface potential should be achieved in materials with the same crystal structures. However, when we compare the surface potential of Nylon-11 films and nanowires, the nanowires show much higher values than the films with the same crystal structures (Fig. 6-7b). The  $\alpha$ -phase nanowire sample displays more positive surface potential (576 mV) compared to  $\alpha$ -phase film sample (20 mV). In addition, a much higher surface potential is observed in  $\delta'$ -phase nanowires (395 mV) than equivalent films (184 mV). These results indicate that the nanoconfinement effect effectively aligned the dipoles and generated self-polarization in the nanowires.[2] It must be noted that the surface potential of the ‘non-ferroelectric’  $\alpha$ -phase nanowire is much higher than that of ‘ferroelectric’  $\delta'$ -phase nanowires. This is in good agreement with our  $P_r$  calculation results from molecular simulations, indicating that the dipoles in  $\alpha$ -phase nanowire are not only well-aligned but also better packed than those in the  $\delta'$ -phase nanowires. Thermal stability tests confirm the effect of chain ordering and hydrogen bonding on the changes of dipole orientation. After a thermal annealing process at 165 °C, the surface potential of the  $\delta'$ -phase nanowires dropped from 395 mV to 0 mV, while  $\alpha$ -phase nanowires maintained their surface potential within the error range (Fig. 6-7b, orange bar). This is because the molecular configuration and resulting self-polarization of metastable  $\delta'$ -phase was manipulated and disappeared by thermal energy, respectively. [89] However, the  $\alpha$ -phase nanowires sustained their surface potential as well as corresponding self-polarization at high temperature due to the strongly hydrogen bonded, well-ordered and highly packed molecular structures. The change in X-ray diffractogram after annealing confirms the

thermal stability of molecular configuration and induced polarization. As shown in Fig. 6-8a, in the case of  $\delta'$ -phase nanowires, the intensity of  $21.6^\circ$  peak corresponding to (hk0) plane of  $\delta'$ -phase decrease after thermal annealing, while the intensity of peak at  $20.4^\circ$  increase. In contrast, the peak positions and intensities in diffractograms of  $\alpha$ -phase nanowires before and after  $165^\circ\text{C}$  annealing are almost the same (Fig. 6-8b), indicating that  $\alpha$ -phase crystal structure and resulting spontaneous polarization in nanowires are thermally stable. In summary, these surface potential results imply that the non-ferroelectric  $\alpha$ -phase nanowires exhibit strong spontaneous polarization and good thermal stability relative to ferroelectric  $\delta'$ -phase.

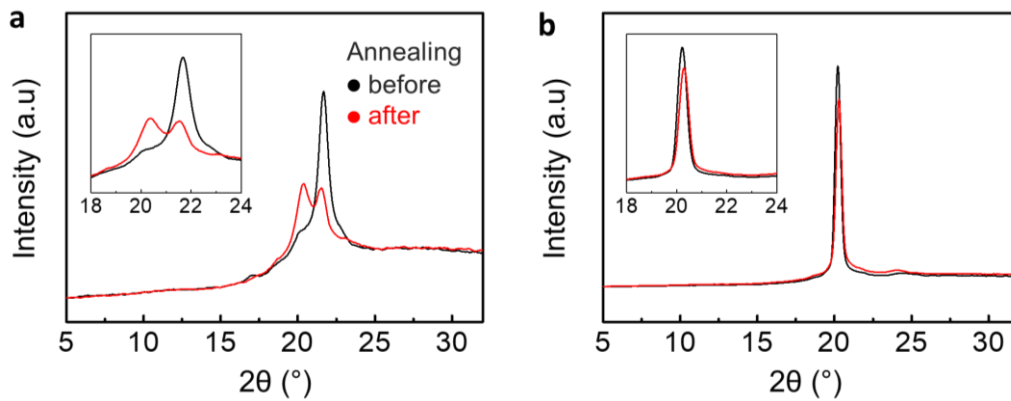


Fig. 6-8 Comparison of XRD patterns (black) before and (red) after thermal annealing at  $165^\circ\text{C}$ : (a)  $\delta'$ -phase and (b)  $\alpha$ -phase of Nylon-11 nanowires *within* AAO template. Inset displays the magnified area from  $2\theta$  of  $18^\circ$  to  $2\theta$  of  $24^\circ$ .

In order to verify the spontaneous polarization-based charge accumulation ability, we measured the changes in surface potential before and after mechanical rubbing (Fig. 6-9). Charge transfer occurs during the contact of two materials with different work functions, and the friction of the AFM tip on the surface of the material induces such an effect.[190] Furthermore, the  $P_r$  in the ferroelectric polymer affects the amount of transferred charge during the rubbing process because the direction of polarization and the degree of dipole orientation together change the charge affinity on the surface.[60] We measured the surface potential of pristine  $\alpha$  and  $\delta'$ -phase nanowire samples and rubbed the middle part of the scanned area using contact mode AFM (Fig. 6-9a, c). As a result, the  $\alpha$ -phase nanowires showed a surface potential change of 180 mV compared to the unrubbed area, while the  $\delta'$ -phase displayed corresponding to a charge of 20 mV (Fig. 6-9b, d).

Therefore, more charge were transferred and accumulated on the  $\alpha$ -phase nanowires than on the  $\delta'$ -phase nanowires during rubbing via AFM tip. Comparison with the  $\alpha$ -phase film also confirms that the increased charge transfer can be attributed to the polarization in the nanowires (Fig. 6-9e, f). These results show that dipoles in the ‘non-ferroelectric’  $\alpha$ -phase nanowires are aligned, and the intensity is much higher than that of ‘ferroelectric’  $\delta'$ -phase.

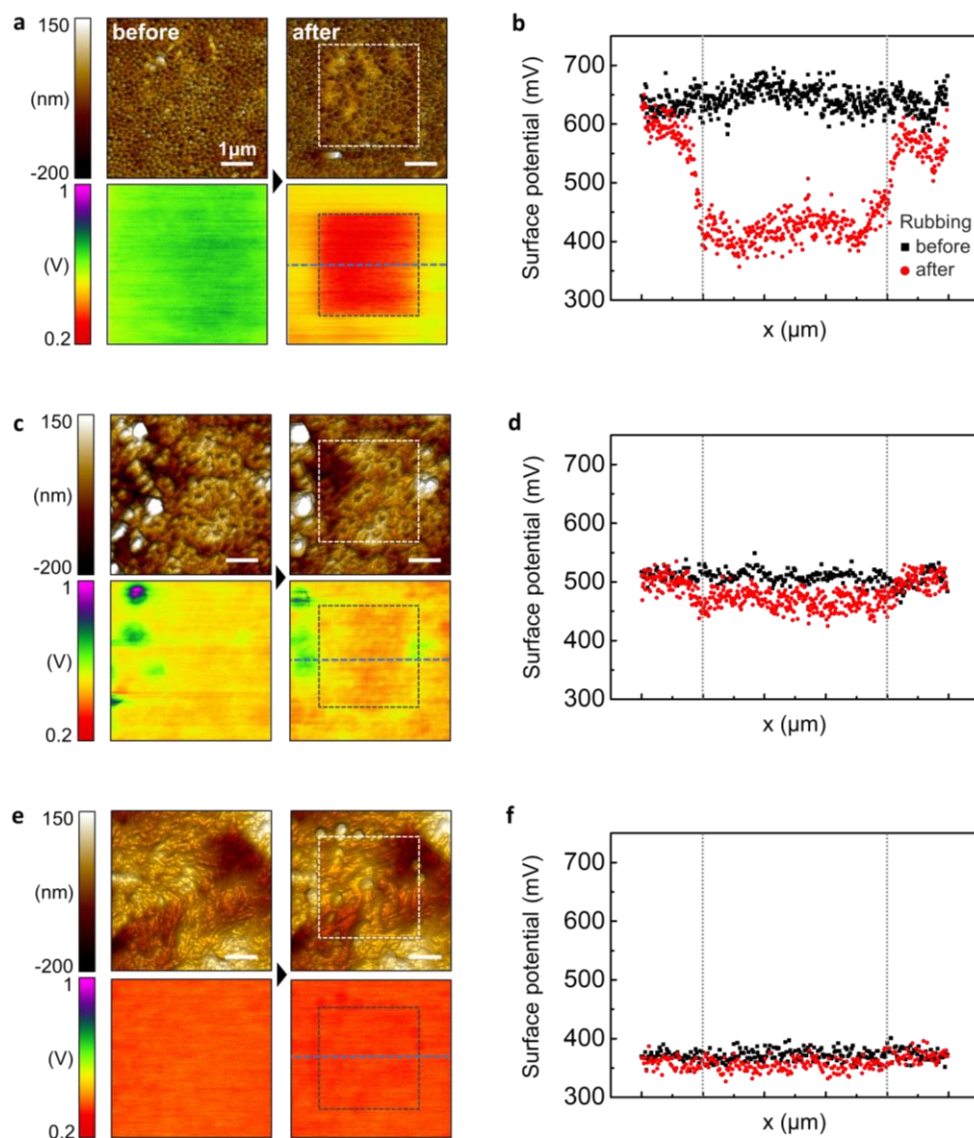


Fig. 6-9 Charge accumulation capability of (a, b)  $\alpha$ -phase, (c, d)  $\delta'$ -phase nanowires, and (e, f)  $\alpha$ -phase film before and after rubbing process. (a, c, e) AFM topography and surface potential images (left) before and (right) after rubbing process. Dot squares indicates rubbing area. Scale bar indicates 1  $\mu\text{m}$ . Blue dot line indicates the data acquisition position for plotting. (b, d, f) Surface potential changes (black square) before and (red circle) after rubbing process.

## 6.4 Nanowire-based triboelectric generators

Based on  $\alpha$ -phase Nylon-11 nanowires, we developed a contact-separation mode triboelectric generator with the size of  $3.14 \text{ cm}^2$ . An Al film and  $\delta'$ -phase nanowire-based device were also prepared to compare the device performances.

Fig. 6-10a shows the  $J_{SC}$  measured in response to the periodic impacting at a frequency of 5 Hz and amplitude of 0.5 mm in an energy harvesting setup that has been previously described (Chapter 3.2.3). The Al-based triboelectric generator showed a peak  $J_{SC}$  of  $\sim 13 \text{ mA}\cdot\text{m}^{-2}$ . Due to the better charge affinity and self-polarization effect, higher performance was observed from a  $\delta'$ -phase nanowire-based device with  $J_{SC}$  of  $\sim 38 \text{ mA}\cdot\text{m}^{-2}$  than from the Al-based generator, in a good agreement with our previous results regarding  $\delta'$ -phase nanowire-based triboelectric generator (Chapter 5). The self-poled  $\alpha$ -phase nanowire-based triboelectric generator displayed further enhanced output with a peak  $J_{SC}$  of  $\sim 74 \text{ mA}\cdot\text{m}^{-2}$  likely due to the more ordered and aligned polarization. The electrical power output of the triboelectric generators was measured across different resistors. The peak output power density of  $3.38 \text{ W}\cdot\text{m}^{-2}$ ,  $1.03 \text{ W}\cdot\text{m}^{-2}$ , and  $0.099 \text{ W}\cdot\text{m}^{-2}$  were observed from  $\alpha$ -phase nanowire,  $\delta'$ -phase nanowire, and Al-based devices respectively under impedance-matched conditions at a load resistance of  $\sim 5 \text{ M}\Omega$ ,  $20 \text{ M}\Omega$ , and  $20 \text{ M}\Omega$  respectively (Fig. 6-10b, c). The observed output power from  $\alpha$ -phase nanowire-based triboelectric generator was  $\sim 3$  times and  $\sim 34$  times higher than those of  $\delta'$ -phase nanowire and Al-based device, respectively. Considering that the surface area of the nanowires in the device surface was only  $\sim 50 \%$  that of the Al film, this result indicates that the spontaneous polarisation in the  $\alpha$ -phase nanowire effectively further enhances the surface charge density of the device. Furthermore, an output power comparison between  $\alpha$ -phase and  $\delta'$ -phase nanowire-based devices illustrates that the much higher  $P_r$  in closely packed and aligned molecular structure of  $\alpha$ -phase contributed to the enhancement of device performance, in good agreement with the results of modelling and surface potential analysis.

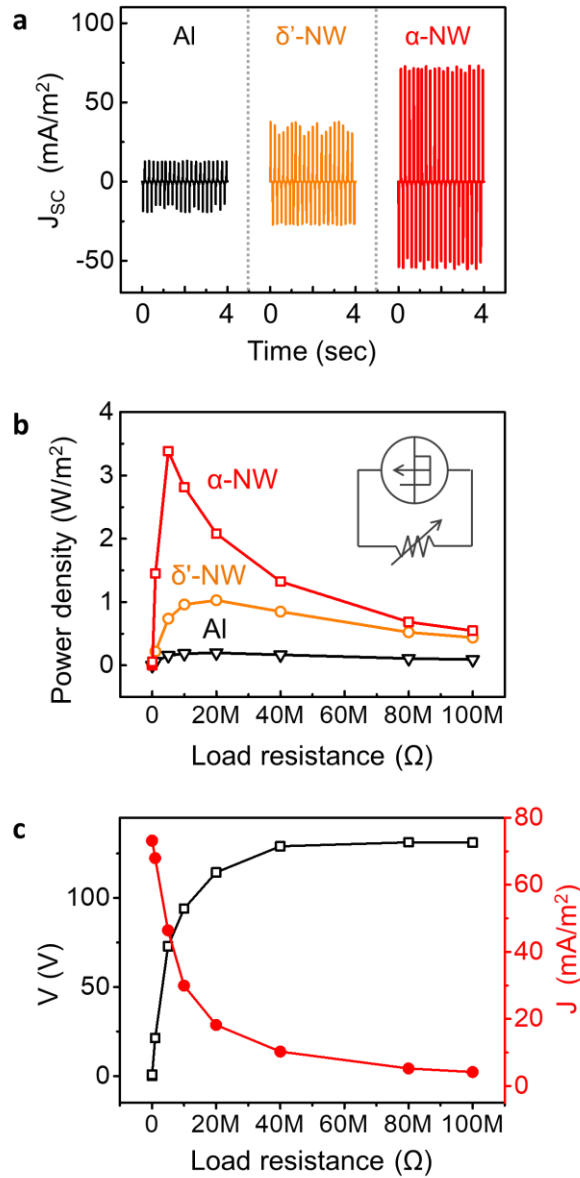


Fig. 6-10 Triboelectric generator device performance. (a) Short-circuit output current densities of triboelectric generators with different combinations of materials: (black) Al, (orange)  $\delta'$ -phase nanowire, and (red)  $\alpha$ -phase nanowire. (b) The power density of the same devices as a function of variable load resistance. The power density is calculated by the multiplication of current density squared and load resistance. (c) The gradual increase and a decrease of voltage and current density across the various load resistors, respectively. Various input condition.

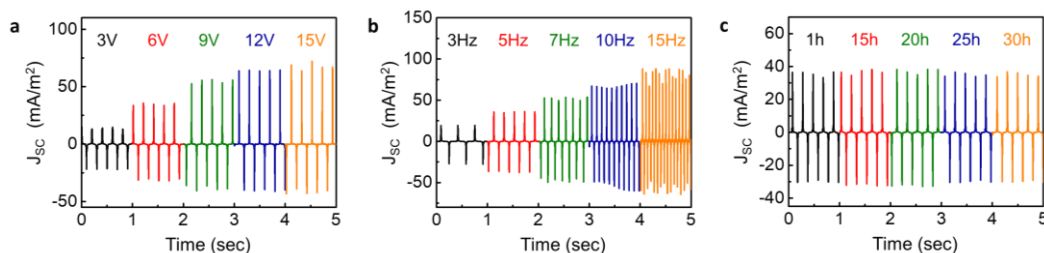


Fig. 6-11 Electrical output of the device under various input condition. (a, b) Short circuit current density of the  $\alpha$ -phase nanowire device was measured under the application of a periodic impacting force between 3 ~ 15 V with constant frequency of 5 Hz and a variable frequency between 3 ~ 15 Hz with amplitude of 6 V. In our energy generator system, force amplitude of magnetic shaker can be controlled by applied voltage. (c) Short circuit current density recorded over time in response to continuous impacting at a frequency of 5 Hz and amplitude of 6 V on the same Nylon-11 nanowire-based triboelectric generator for 30 h (~ 540,000 cycles impacting cycles in total). Data were recorded after 1 h (18 k cycles), 15 h (270 k cycles), 20 h (360 k cycles), 25 h (450 k cycles), and 30 h (540 k cycles).

The electrical output was found to increase with increasing impact amplitude and frequencies as expected (Fig. 6-11a, b). In addition, the  $\alpha$ -phase nanowire-based triboelectric generator exhibited a negligible change in output current density over the entire period of fatigue testing ( $\approx$  540,000 cycles), demonstrating the high mechanical stability of the spontaneous polarization in  $\alpha$ -phase nanowires and the robustness of the nanowire-based device itself (Fig. 6-11c). It must be noted that the mechanical stiffness of  $\alpha$ -phase nanowires is much higher than that of the  $\delta'$ -phase nanowires because of the well-ordered hydrogen bonding. (The mechanical properties of Nylon-11 nanowires will be discussed in Chapter 7). Although no abrasion was observed during the fatigue test in either the  $\alpha$  or  $\delta'$ -phase nanowires, such a stiffness difference implies that the  $\alpha$ -phase nanowire is more appropriate for use in friction-based triboelectric generators.

## 6.5 Conclusions

Nylon-11 nanowires with unprecedented intensity and thermal stability of spontaneous polarization have been fabricated for the first time using the TANI method. Through the nanoconfinement effect,  $\alpha$ -phase Nylon-11 nanowires with preferential crystal orientation were achieved. The crystal structure, molecular alignment and crystallite size of self-poled  $\alpha$ - and  $\delta'$ -phase nanowires were corroborated by XRD and molecular

simulation. The intensity and thermal stability of spontaneous polarization were indirectly investigated by the changes of surface potential in KPFM measurements. We also introduced the resulting nanowires into triboelectric generators to prove that non-ferroelectric  $\alpha$ -phase nanowires with higher surface potential outperform ferroelectric  $\delta'$ -phase nanowires. Consequently, we have verified that, due to the ordered crystal structures and higher molecular packing density, the net dipole moment of self-poled 'non-ferroelectric'  $\alpha$ -phase Nylon-11 can be much higher than that of self-poled 'ferroelectric'  $\delta'$ -phase. Furthermore, the strong hydrogen-bonding (which has previously been considered as a serious disadvantage for the polarization of Nylon-11) actually serves to enhance the stability of the molecular structure, resulting in a constant spontaneous polarization up to near the melting temperature.

## Chapter 7

# **Phase Tunable Nanoconfined Polymer Crystallisation Method for Nylon-11 Nanowires : A Comparative Study**

Polymorphism, defined as the existence of several crystalline structures in material, is of particular interest in ferroelectric (or piezoelectric) polymers as functional properties may vary dramatically across different crystal phases. As a result, the relationship between the crystalline phase and properties of polymers, such as PVDF and odd-numbered Nylon, has been studied extensively.[103], [225], [226] However, the majority of research to date has been conducted on films or on bulk materials.[1], [77], [227] In the case of one-dimensional nanowire structures, even though they have many attractive advantages such as a preferential molecular orientation and large surface area, only a limited number of phases and their properties have been realised and studied because appropriate fabrication method capable of manipulating crystal structures of nanowires have not been developed.[2], [202], [208] Therefore, in-depth studies regarding conventional nanofabrication method and properties of polymer nanowires are crucial for expanding our

knowledge of structure-property relationships, as well as widening the range of possible applications.

In this chapter, we investigate the crystallisation mechanism in the template-wetting method and suggest three distinct combinations of processing conditions for different phases of Nylon-11 nanowires. The crystallographic, and electromechanical characteristics, as well as thermal behaviour of resulting nanowires are then collected and compared. A substantial amount of this work has been previously published and therefore has been adapted from that text.[186] Copyright permission and authors' contributions are given in Appendix A.

## **7.1 Nanowire growth mechanism**

### **7.1.1 Evaporation-driven crystallisation**

The typical way to obtain bulk or film of Nylon-11 samples is by “temperature-driven” crystallisation.<sup>9</sup> This method results in increased chain mobility at high temperatures, regardless of melt or solution processing, and subsequent decreases in chain mobility with decreasing temperature.[142] Melt and ice quenching for  $\delta'$ -phase film and precipitation of Nylon-11 solution in 1,4-butanediol with gradual cooling for the  $\alpha$ -phase powder are examples of this temperature-driven method.[88] This means that the heating or cooling rate is a key variable that can be altered to influence Nylon-11 crystallisation, and therefore the resultant crystal structure. However, a highly crystalline Nylon-11 sample cannot be achieved via such temperature-driven approach because the polymer molecules do not have sufficient mobility for the crystal size to grow during the crystallisation (cooling) process. This is because, during gradual cooling with a constant cooling rate, it is not possible to provide the sample with the sufficient amount of thermal energy for crystal ordering after a certain point of time (Fig. 7-1a). As a result, Nylon-11 samples fabricated by typical temperature-driven crystallisation have relatively low crystallinity.

---

<sup>9</sup> Temperature driven crystallisation: In the case of polymer solution, more polymer can be dissolved at high temperature than at lower temperature. If this polymer solution were to be cooled down, a crystallized polymer can be achieved by precipitation, and such method can be defined as temperature driven crystallisation.

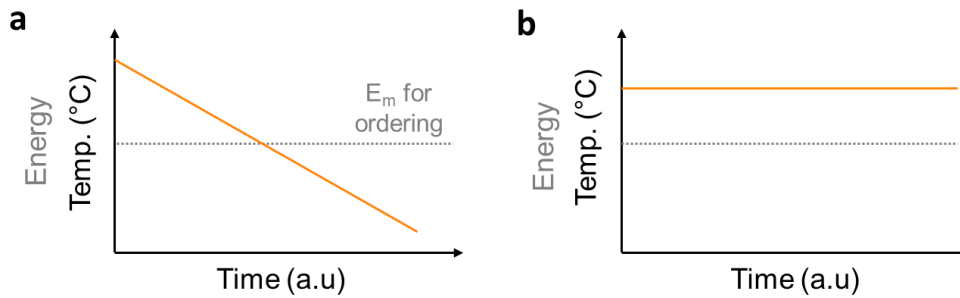


Fig. 7-1 Changes in temperature as a function of time in (a) temperature- and (b) evaporation-driven crystallisation method. Grey dot line indicates the minimum energy ( $E_m$ ) for polymer crystal ordering.

Thus, to increase the crystallinity, we used a crystallisation method that is “evaporation-driven”. This method increases the chain mobility by using a good solvent, and crystallisation then proceeds, driven by the evaporation of that solvent. Therefore, the solvent should be relatively volatile (i.e. having a high vapour pressure) and have good compatibility with the polymer material used. In the case of Nylon-11, among the good solvents, formic acid is the most appropriate due to its rapid evaporation rate (heat of vaporization =  $+23.1 \text{ kJ mol}^{-1}$  as compared to  $+31.3 \text{ kJ mol}^{-1}$  for acetone,  $+40.66 \text{ kJ mol}^{-1}$  for water).[228] The advantage of this evaporation-driven crystallisation is that the temperature-induced chain mobility can be maintained through the process, resulting in much higher sample crystallinities (Fig. 7-1b)

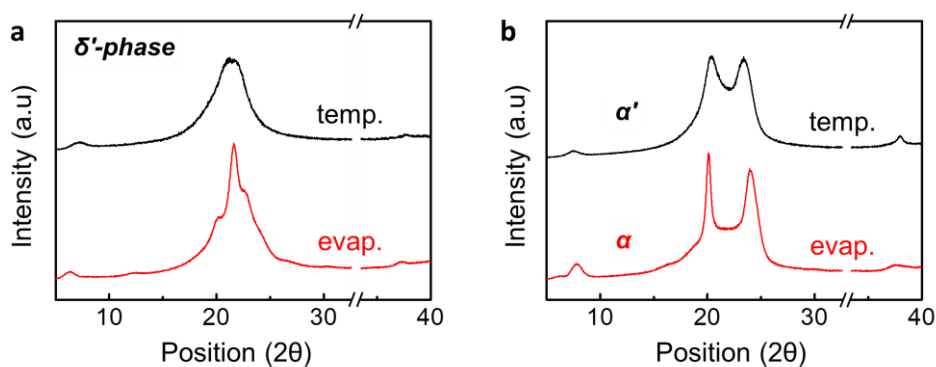


Fig. 7-2 XRD patterns of Nylon-11 films fabricated by (black) temperature-driven and (red) evaporation-driven methods: (a)  $\delta'$ -phase and (b)  $\alpha'$ - and  $\alpha$ -phase samples.

To compare the temperature- and evaporation-driven crystallisation methods, Nylon-11 samples were fabricated using both crystallisation methods. Fig. 7-2 shows XRD patterns of Nylon-11 samples fabricated by both temperature-driven and evaporation driven crystallisation method. According to the literature, the (001) and (hk0) planes of pseudo-hexagonal  $\delta'$ -phase Nylon-11 correspond to the diffraction peaks at  $2\theta = 6.2^\circ$  and  $21.6^\circ$ , respectively.[89] This confirms that both temperature- and evaporation-driven crystallisation generated  $\delta'$ -phase films (Fig. 7-2a). In the case of  $\alpha$ -phase, it is difficult to compare the effect of different crystallisation methods directly as  $\alpha$ -phase cannot be achieved from polymer melt. As shown in Fig. 7-2b, the film made by temperature-driven crystallisation method (melt and slow cooling) gives rise to the diffractograms corresponding to  $\alpha'$ -phase, which is a defective  $\alpha$ -phase. In contrast, evaporation-driven method successfully produced a triclinic  $\alpha$ -phase film with three reflections located at  $2\theta = 7.8^\circ$ ,  $20^\circ$ , and  $24.2^\circ$ , corresponding to the (001), (200), and (210/010) planes, respectively.[89] Although the exact comparison is difficult in the case of  $\alpha$ -phase, the result of  $\delta'$ -phase film shows that both crystallisation methods can control the crystal structure of Nylon-11. In addition, the shape of the diffraction peaks produced by each method is different; the evaporation-driven samples exhibit much sharper peaks with smaller FWHM and much smaller amorphous regions, indicating that evaporation-driven crystallisation resulted in higher crystallinity. The degree of crystallinity obtained by DSC analysis supports this result. In the case of  $\delta'$ -phase Nylon-11, the average crystallinity of solution-processed film (38 %) is much higher than that of melt-quenched film (29 %). The average crystallinity of solution-processed  $\alpha$ -phase film is around 48 %, which is much higher than that of any reported  $\alpha$ -phase powder fabricated by temperature-driven crystallisation method, such as precipitation in 1,4-butanediol,[89] confirming that evaporation-driven method does generate a highly crystalline Nylon-11 film.

For this evaporation-driven crystallisation method, we must now consider which variables can be altered to influence the Nylon-11 crystal structure in the resultant sample. As discussed, two different variables can be manipulated in the evaporation-driven crystallisation method: temperature and evaporation rate. Since these two variables are inter-related, the processing conditions have to be designed carefully. For instance, if we increase the temperature, the evaporation rate will also increase, as the evaporation rate is a function of temperature. However, by introducing additional gas-flow or enclosing the

sample in a solvent vapour-rich atmosphere, the evaporation rate can independently increase or decrease, respectively. Then, four different processing conditions based on the combinations of the two variables can be made as follows (Table 7-1).

Table 7-1 Four processing conditions for evaporation driven crystallisation.

No.	Symbol	Name	Processing condition
i	ToEo	HT fast evaporation	with add. heating and gas-flow
ii	ToEx	HT natural evaporation	with add. heating and without add. gas-flow
iii	TxEo	RT fast evaporation	without add. heating and with add. gas-flow
Iv	TxEx	RT natural evaporation	without add. heating and without gas-flow

To verify the validity of these conditions, corresponding Nylon-11 films were fabricated, and the XRD patterns of the resulting films are shown in Fig. 7-3. (Diffraction peak positions of each sample are summarised in Table 7-2). The diffraction patterns of high temperature (HT) fast evaporation (i, ToEo) and the HT natural evaporation (ii, ToEx) samples corresponds with  $\alpha$ -phase Nylon-11. In contrast, the room temperature (RT) fast evaporation (iii, TxEo) and RT natural evaporation (iv, TxEx) samples showed similar diffractograms to  $\delta'$ -Nylon-11. Interestingly, the crystal structure of Nylon-11 was changed from  $\delta'$ - to  $\alpha$ -phase by “additional heating”, despite the crystallisation being governed by evaporation. Considering that the  $\alpha$ -phase is the thermodynamically stable phase, this result indicates that the additional heating is an essential prerequisite for  $\alpha$ -phase formation. In other words, room temperature does not provide sufficient energy to chain for synthesizing well-ordered crystal structures.

In terms of the influence of evaporation rate, comparison of two RT condition samples (iii and iv) does not display any significant changes. When we compare the film (i) and (ii), an additional diffraction peak at  $2\theta$  of  $21.5^\circ$ , which corresponds to the  $\delta'$ -phase, is observed in (ii, HT fast evaporation), indicating that fast evaporation generated a  $\delta'$ -phase region in the sample.

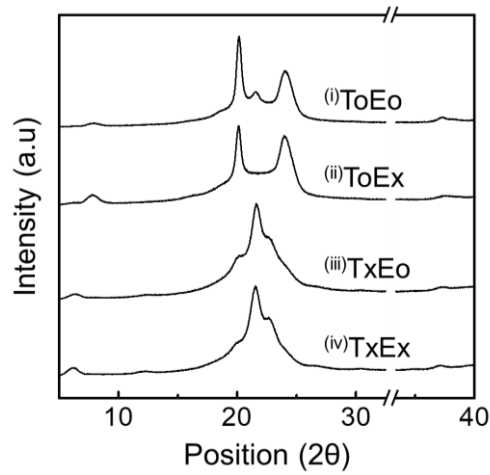


Fig. 7-3 XRD patterns of Nylon-11 films fabricated by evaporation-driven crystallisation. T and E indicate temperature and evaporation. (Resulting diffraction peak positions are summarised in Table 7-2)

Table 7-2 Indices of crystallographic planes of Nylon-11 films fabricated by different processing conditions of evaporation-driven crystallisation methods. Red dot indicates the diffraction peak induced by additional air-flow

$2\theta$ (°)	$d$ (Å)	Temp.	O	O	X	X
		Evap.	O	X	O	X
6.2	14.24				●	●
7.8	11.32		●	●		
20.2	4.40		●	●	●	●
21.5	4.12		●		●	●
22.6	3.93				●	●
24.0	3.70		●	●		
37.2	2.41		●	●	●	●

### 7.1.2 Capillary-infiltration

The next question is as follows: is it possible to synthesize the polymer nanowires via evaporation-driven method, and is it possible to apply the advantages of the evaporation-driven crystallisation method, such as higher crystallinity and phase tunability, to the resulting one-dimensional polymer nanowire structures? As discussed in Chapter 2.6, template-wetting is a well-known method to produce nanostructured polymers with preferential crystal orientation, and both polymer melt and solution can be used in this method. Due to the wetting mechanism, drop-casting of polymer melt or polymer solution onto the upper surface of the AAO template is sufficient to synthesize nano-cylindrical structures. In terms of crystallisation mechanisms, polymer melt- and solution-based template wetting correspond to temperature- and evaporation-driven crystallisation methods, respectively. One interesting aspect of most of the nanowires reported in the literature is the degree of crystallinity. Regardless of crystallisation method, resulting nanowires typically showed much lower crystallinity than that of film or bulk materials.[151], [155], [160], [162] Another interesting aspect of the literature is that even when the processing conditions are varied, it is still difficult to control the crystal structures of the generated nanowires.[155], [229]

We attribute the reason of such limitations to the “wetting direction”. In general, the polymer melt or solution used is dropped “onto” the AAO template, and the infiltration is along the direction of gravity. (Thus, we called it as a “gravity-infiltration” method.) However, it is also possible to infiltrate the solution (or melt) into the nano-pores from the opposite direction to gravity by capillary infiltration, thus it called “capillary-infiltration” method. As shown in Fig. 7-4a, in the case of gravity-infiltration, the evaporation rate of the solvent in the nanopores cannot be manipulated as both sides of the AAO template is blocked by the solution droplet on the top surface and the substrate at the bottom. When the polymer solution reaches the substrate, the evaporation- and temperature-driven crystallisation (nucleation and growth) are initiated from the top and bottom surfaces, respectively. This leads to another problem as a single nanowire results from two different crystallisation mechanisms. In contrast, in the case of capillary-infiltration method, the AAO template is placed on a droplet of solution, which infiltrates “upwards” into the nanopores by capillary action (Fig. 7-4b). As a result, the capillary-infiltration method

enables exposing the solution surface to external airflow, and the evaporation rate can be manipulated during the template-filling process. If the speed of solution infiltration is slow enough, this method could make a noticeable difference to the crystallisation rate, and therefore the resultant crystal structure, as the sufficient time to control the evaporation of the solution *within* the nanopores can be attained. When the solution fills and reaches the top surface of the nanopores, the same evaporation- and temperature-driven crystallisation processes occur. However, in the case of capillary-infiltration method, the contribution of temperature-driven crystallisation from the bottom substrate can be reduced substantially by applying a large amount of solution or increasing the temperature of substrate. As a result, the polymer crystallisation process is governed by the evaporation-driven mechanism only. To summarize the comparison of methodologies, the capillary-infiltration method allows control of the rate of evaporation, and therefore crystallisation can be controlled to a much greater extent than in the gravity-infiltration method.

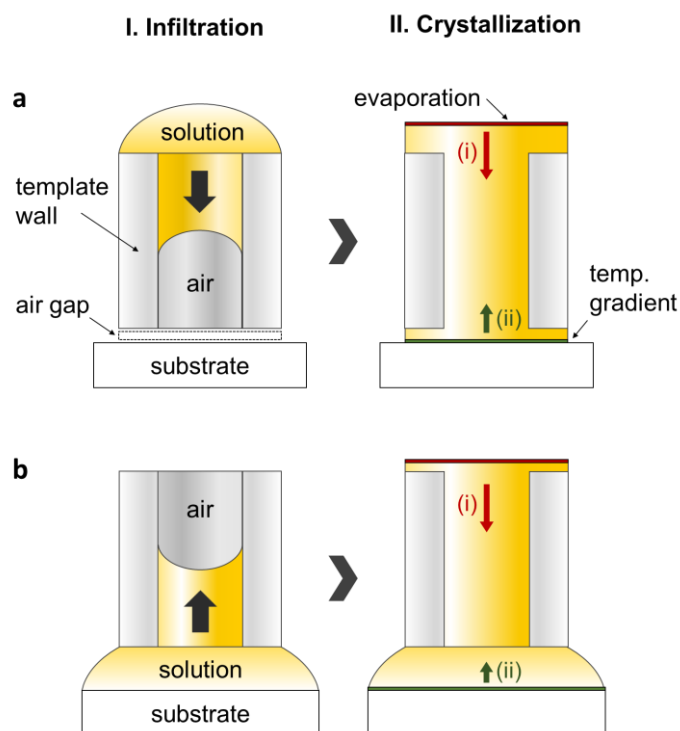


Fig. 7-4 Schematics of two different template-wetting methods. (a) gravity-infiltration method and (b) capillary-infiltration method. Grey arrows indicate the solution infiltration direction. Red and green arrows indicate the direction of (i) evaporation- and (ii) temperature-driven crystallisation.

### 7.1.3 Processing parameters for crystallisation in the nanopores

As discussed, Nylon-11 film fabrication from solution is governed by evaporation-driven crystallisation, indicating that the temperature and evaporation rate are critical variables for crystallisation. In the case of capillary-infiltration template-wetting method, one more processing parameter should be considered to control the crystallisation, which is the “concentration” of the polymer solution. The concentration is a significant parameter in three respects. Firstly, it affects the speed of crystallisation because the concentration is directly correlated with the distance between polymer chains in the solution. In evaporation-driven crystallisation, the crystallisation is initiated when the polymer chains meet and get entangled together (Fig. 7-5). Thus, the crystallisation speed of dilute solution is very slow because all the solvent between polymer chains has to evaporate. In contrast, a concentrated solution takes a much shorter period of time to crystallize.

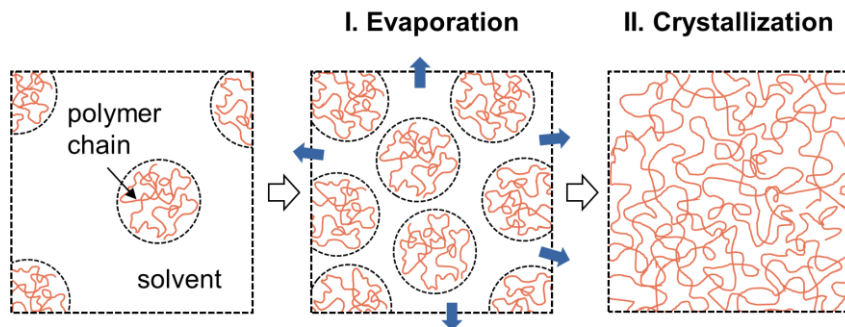


Fig. 7-5 Schematic representation of evaporation-driven crystallisation of dilute solution. Blue arrows indicate the evaporation of the solvent.

Second, the final length of the polymer nanowire is determined by the concentration of the solution. It is reported that the maximum height ( $h$ ) of the polymer solution which can reach via capillary infiltration is inversely proportional to the concentration of the solution, given by Jurin’s law defined as:

$$h = \frac{2\gamma(\cos \theta)}{\rho gr} \quad (7-1)$$

where  $\gamma$  is the surface tension of the polymer solution,  $\theta$  the contact angle of the meniscus at the pore wall,  $\rho$  the concentration of the polymer solution,  $g$  gravity, and  $r$  the radius of the nanopore.[230] However, in the case of 10 wt % Nylon-11 based experiment with AAO template [where  $\gamma = 0.033 \sim 0.043 \text{ N m}^{-1}$ ,  $\theta = 75^\circ \sim 82^\circ$ ,  $\rho = 1.01 \sim 1.03 \text{ g cm}^{-3}$ , and  $r = 125 \text{ nm}$  (pore diameter  $\sim 250 \text{ nm}$ ), respectively], the calculated maximum height ( $\sim 2.2 \times 10^7 \mu\text{m}$ ) that the Nylon-11 solution can reach via capillary force is much higher than the length of the pore channels (thickness of the template  $\sim 60 \mu\text{m}$ ). Therefore, the effect of concentration on nanowire length is not of significance in the methodology presented. Last, the concentration of solution affects the capillary filling rate in nanopores. According to the literature, the rate ( $dh/dt$ ) of the flow of polymer solution in the nanopore can be estimated by

$$\frac{dh}{dt} = \frac{R\gamma \cos \theta}{4\mu h} \quad (7-2)$$

where  $t$  is the time,  $R$  the hydraulic radius (the ratio between the volume of the liquid in the capillary section and the area of solid and liquid interface;  $R$  is one-half the radius of nanopore  $r$ ), and  $\mu$  the viscosity of the polymer solution.[142], [148] Because  $\mu$  in turn depends on the concentration of the polymer solution, the filling rate is also controlled by the concentration of the solution.

Using three processing parameters – temperature, evaporation rate, and concentration of solution –, we have designed capillary-infiltration based template-wetting processes for highly crystalline Nylon-11 nanowires. Processing temperature is tuned using a hot-plate from RT to the boiling point of formic acid ( $\sim 100 \text{ }^\circ\text{C}$ ). Fast evaporation rate can be achieved by generating a gas-flow using an additional fan. Also, solvent-vapour rich atmosphere via loosely sealed system enabled us to reduce the effective evaporation rate due to the volatility of formic acid. The concentration of Nylon-11 solution was varied from 5 to 20 wt %. All Nylon-11 solution was synthesised at  $60 \text{ }^\circ\text{C}$  to increase the supersaturation concentration. To define the changes of crystal structures in Nylon-11 nanowires, we measure the XRD pattern of samples *within* and without an AAO template. (Experimental details are given in Chapter 3.1.2)

First of all, to serve as a reference, we fabricated nanowires using 10 wt % solution at room temperature. The solution and AAO template were exposed to the surrounding air without additional gas-flow.

As shown in Fig. 7-6a (black), diffractions at  $2\theta = 6.2^\circ$ ,  $21.6^\circ$ , and  $22.8^\circ$  were achieved when reference Nylon-11 nanowires were *within* an AAO template. According to the literature, the diffraction peak at  $2\theta = 21.6^\circ$  corresponds to the  $(hkl)$  plane of pseudo-hexagonal  $\delta'$ -phase Nylon-11 but the  $22.8^\circ$  peak has not been previously reported. Thus, it is difficult to define the exact crystal structure of these reference nanowires. Upon removal of the AAO template, the nanowires were divided into two samples, the relative peak intensity between peaks at  $21.6^\circ$  and  $22.8^\circ$  was observed to vary consistently between the samples. This difference can likely be attributed to two different crystallisation mechanisms acting within each nanowire. Although the evaporation-driven crystallisation is dominant in this capillary-infiltration template-wetting method, additional temperature-driven crystallisation can also occur at the interface between solution and substrate due to the temperature difference (Fig. 7-4b). SEM images of planes towards the top and bottom surfaces of the AAO template show that the length of resulting nanowires is shorter than the length of the nanopores due to the separation of the two parts (Fig. 7-6c ii and iii). Fig. 7-6c (i) and (iv) displays top and bottom films of this sample. Small spheres of diameter approximately  $5\ \mu\text{m}$  on the bottom surface in Fig. 7-6c (iv) originates from the removal process of the thick bottom film. These results imply the importance of process optimisation to achieve nanowires with uniform morphology and crystal structure.

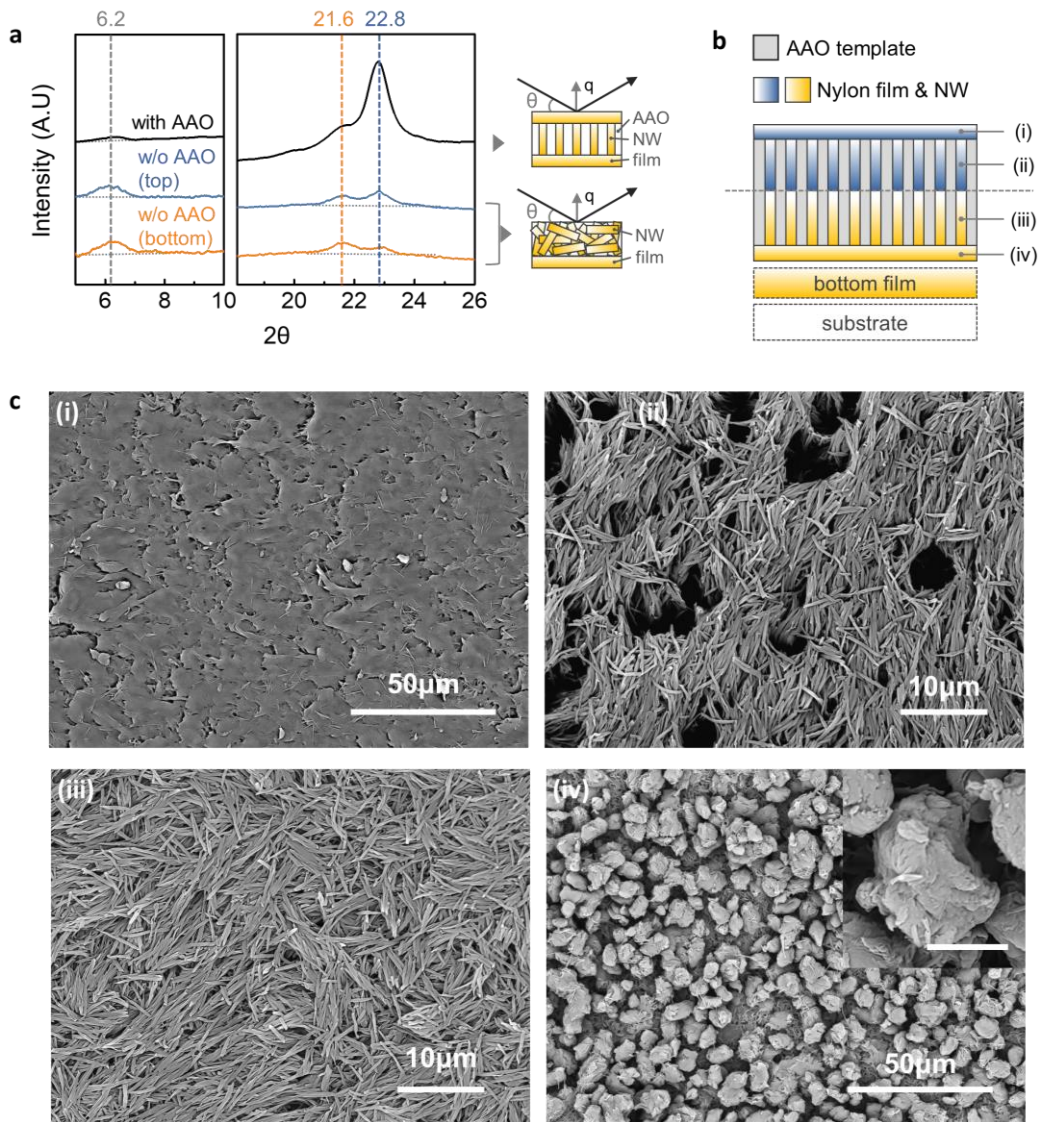


Fig. 7-6 Characteristics of reference Nylon-11 nanowires. (a) XRD analysis of reference Nylon-11 nanowires (black) *within* and (blue, orange) without AAO template. Inset schematics display the morphology of sample and the direction of X-ray beam ( $\theta$ ) with a scattering vector ( $q$ ). (b) Schematic image of Nylon-11 nanowires fabricated by reference condition. The resulting nanowires are divided into two parts (blue and orange) due to different crystallisation mechanism. (c) SEM images of part of reference nanowires. (i) ~ (iv) correspond to the location in the schematic (b). Scale bar in the inset of (iv) indicates 5  $\mu\text{m}$ .

Based on these reference sample results, the processing conditions – solution wt %, temperature, and additional gas-flow rate – were altered, and the changes in resulting diffractograms are observed (Fig. 7-7). (All XRD analysis was conducted using nanowires *within* the AAO template). Firstly, the influence of solution concentration (wt %) was examined at room temperature (Fig. 7-7a). The crystallisation process proceeded under standard atmospheric conditions (flow rate  $\sim 0$  m/s), and the intensity of peaks  $2\theta = 21.6^\circ$  and  $22.6^\circ$  was observed to increase with increasing wt %. However, the gradient of the  $21.6^\circ$  peak is much greater than that of the  $22.6^\circ$  peak. Considering that the method to achieve the metastable  $\delta'$ -phase with a dominant peak at  $2\theta = 21.6^\circ$  is melt-quenching, this result means that reduction of the distance between polymer chains by increasing solution concentration induced fast crystallisation and promoted the  $\delta'$ -phase formation.

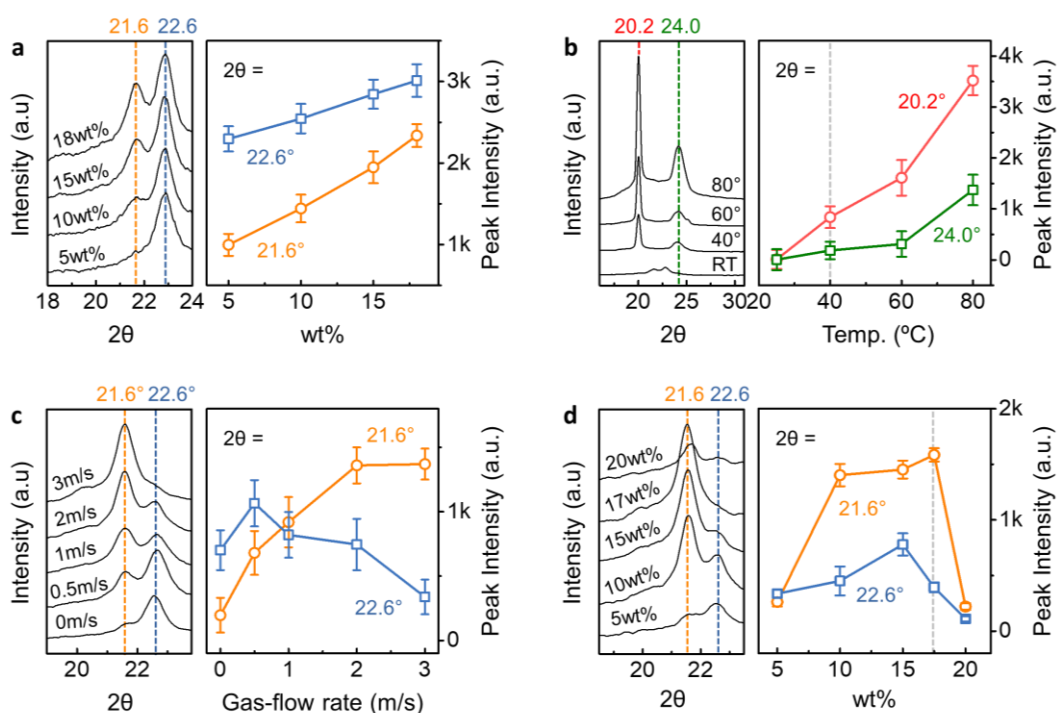


Fig. 7-7 Changes in XRD patterns with different processing conditions: (a) RT solution concentration (wt %) variation in standard atmospheric conditions (flow rate  $\sim 0$  m/s); (b) temperature variation of 10wt % solution in solvent vapour rich atmosphere; (c) gas-flow variation of 10 wt % solution at RT; and (d) RT solution wt % variation with gas-flow (3m/s). Fig. (c) is taken from the author's work from Ref. [2], reproduced with permission from Royal Society of Chemistry.

Secondly, the effect of changing the processing temperature was examined (Fig. 7-7b). To reduce the variation in evaporation rate at different temperatures, the experiment was conducted in a closed system filled with a solvent vapour-rich atmosphere, and the concentration of solutions are fixed to 10 wt %. Interestingly, the crystal structure of Nylon-11 nanowires is affected even by mild heating ( $\sim 40^\circ\text{C}$ ), indicating that this temperature is sufficient to increase the chain mobility to that which is required for molecular alignment. In addition, the intensity of  $\alpha$ -phase peaks further increased with increasing temperature due to temperature-induced crystal ordering. This result is in a good agreement with the experimental results of Nylon-11 film (Fig. 7-2), indicating that the temperature is key to changing the crystal structure of Nylon-11 nanowires.

Finally, the impact of the additional gas-flow was also explored (Fig. 7-7c). Based on the processing conditions for the reference sample (10 wt % solution and room temperature), we introduced gas-flow across the upper surface of the AAO template, which was varied in order to control the evaporation rate of the solution. The previously unreported peak at  $22.6^\circ$  can be reduced in the XRD spectra of samples made under additional gas-flow conditions. Simultaneously, the intensity of the  $\delta'$ -phase peak at  $21.6^\circ$  was increased by increasing gas-flow, meaning that the gas-flow increased the evaporation rate and resulted in fast crystallisation in the nanopores. To further boost the crystallisation speed, we manipulated the wt % of the solution, while maintaining the gas-flow at a rate of 3 m/s (Fig. 7-7d). (All experiments were conducted at RT.) As a result, the intensity of  $\delta'$ -phase peak at  $21.6^\circ$  was further increased (relative to the peak intensity shown in Fig. 7-7c), while the peak at  $22.6^\circ$  further decreased. This can be explained as a reduction in the number of solvent molecules between the polymer chains, compounded with gas-flow induced fast evaporation. Therefore, both processing conditions can be applied simultaneously to maximize the crystallisation rate. The optimal wt % value was found experimentally to be 17.5 wt %. A solution of 20 wt % may further improved results, however, due to the viscosity of the solution it was not possible to fill the AAO nanopores to their entirety via capillary action alone. All of these results suggest that we can tune the crystal structure of Nylon-11 nanowires using the capillary-infiltration template-wetting method with evaporation-driven crystallisation.

#### 7.1.4 Three different methods to control the crystal structure of Nylon-11 nanowires

Various crystal phases can be realised in single Nylon-11 nanowires simultaneously because the processing parameters are inter-related. It is then difficult to figure out the property differences associated with the crystal structures. Thus, based on the results of previous section, optimized combinations of processing parameters for definite  $\delta'$ - and  $\alpha$ -phase Nylon-11 nanowires are defined (Table 7-3). Then we named these methods based on their optimized conditions: gas-assisted nano-template infiltration (GANT), and thermally-assisted nano-template infiltration (TANI) method. As a reference, processing conditions for conventional template-wetting method are also included.

Table 7-3 Optimum processing conditions for each method: conventional template-wetting, GANT, and TANI methods.

	Concentration (%)	Temp. (°C)	gas-flow rate (m/s)
Conventional	10	RT	0
GANT	17.5	RT	3
TANI	5	80	0 (closed system)

Three processing conditions and corresponding nanowire growth mechanisms are illustrated in Fig. 7-8. The reference nanowires were fabricated by using 10 wt % Nylon-11 solution in the conventional method which is in the middle of concentration ranges explored in other methods (Fig. 7-8a). The solution infiltrates the AAO template at room temperature and is crystallized under standard atmospheric conditions without additional gas-flow. The nucleation is initiated from the top surface of the solution because of the solvent evaporation. The crystals grow in the downward direction. As a typical capillary-infiltration method, thin top surface film and thick bottom film remain after finishing all processes. To generate metastable  $\delta'$ -phase nanowires, a maximum concentration of Nylon-11 solution of 17.5 wt % was used with additional gas-flow (3 m/s) at room temperature using the GANT method (Fig. 7-8b). This more concentrated solution resulted in fast crystallisation and very slow infiltration due to the close distance between polymer chains and high viscosity, respectively. Such fast crystallisation and slow capillary-infiltration gave rise to initiation of the nucleation *within* the nanopores.

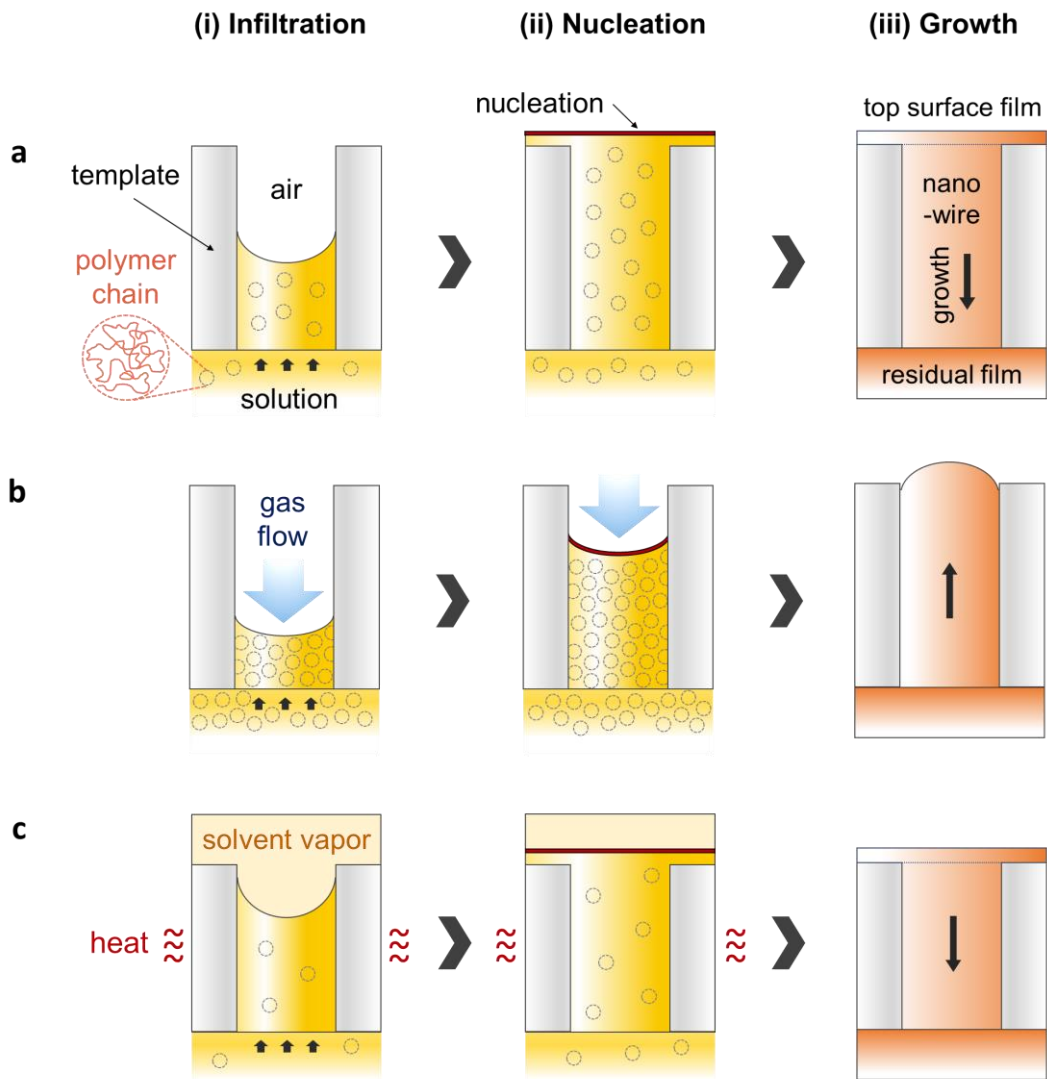


Fig. 7-8 Schematics of Nylon-11 nanowire growth mechanism for (a) conventional template wetting method, (b) GANT, and (c) TANI method.

Additional gas-flow further promoted fast crystallisation via an increased evaporation rate. Lastly, the thermodynamically stable  $\alpha$ -phase Nylon-11 nanowires were synthesized in a loosely sealed petri-dish with heating via the TANI method (Fig. 7-8c). The loosely closed system facilitated a formic acid atmosphere, resulting in the suppression of crystallisation rate. Furthermore, a very diluted solution (5 wt %) was used to reduce the crystallisation rate. Sufficient driving force to form ordered crystal structures can be introduced by additional heating ( $\sim 80$  °C). As discussed, although temperature and evaporation rate are inter-related, the loosely sealed nanowire growth system allowed us to reduce the evaporation rate at high temperature. In this system, the nucleation is initiated from the top surface and propagated to the downward direction akin to conventional template-wetting. However, due to very slow evaporation rate and high temperature, the resulting crystal structures are different.

Three different crystal structures of Nylon-11 nanowires were identified and compared by XRD analysis (Fig. 7-9a).  $\alpha$ -phase nanowires (orange) were characterized by three reflections located at  $2\theta = 7.8^\circ$ ,  $20^\circ$ , and  $24.2^\circ$ . These peak positions correspond to the (001), (200), and (210/010) planes of the reported triclinic  $\alpha$ -phase Nylon-11 film respectively.[89] This means that the slow crystallisation and driving force induced by the heating process generated nanowires with the most thermodynamically stable crystal structure. In the case of  $\delta'$ -phase nanowires (blue), the diffractograms exhibited two diffraction peaks at  $2\theta = 6.2^\circ$  and  $21.6^\circ$ , corresponding to the (001) and (hk0) planes of pseudo-hexagonal  $\delta'$ -phase Nylon-11 respectively.[2], [89] This suggests that additional gas-flow during template-wetting significantly increased the rate of crystallisation, resulting in a metastable crystal structure. In comparison to the  $\alpha$ - and  $\delta'$ -phase nanowires, the diffractogram intensity of nanowires grown by conventional template-wetting (black) is significantly lower. This indicates that both TANI and GANT methods produced highly crystalline nanowires.

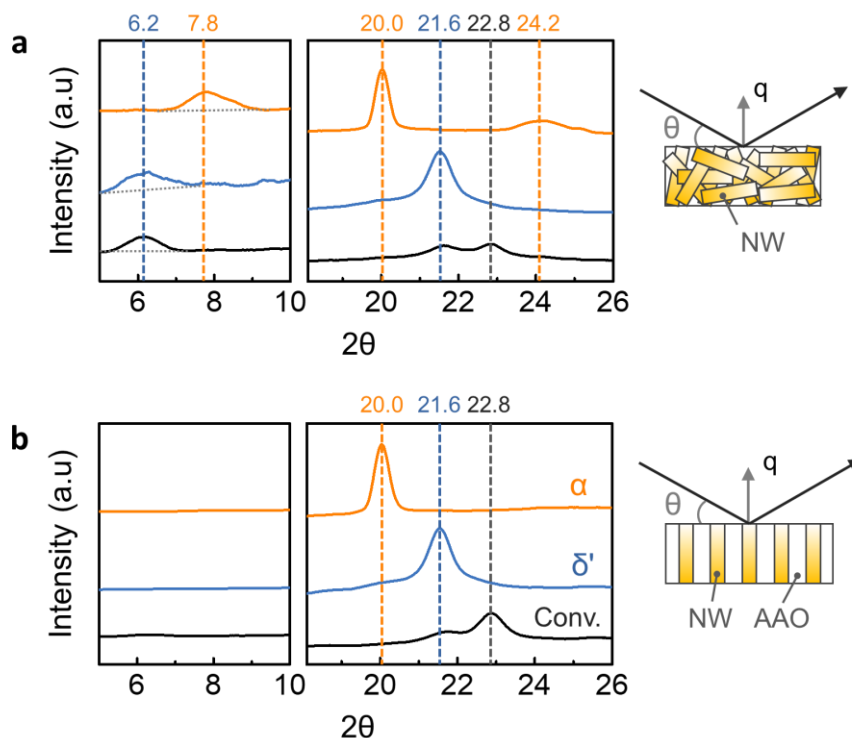


Fig. 7-9 XRD patterns of Nylon-11 nanowires (a) without and (b) with a nanoporous AAO template:  $\alpha$ -phase nanowires (orange);  $\delta'$ -phase nanowires (blue); and nanowires by conventional method (black). Fig. (a) and (b) are taken from the author's work from Ref. [186], reproduced with permission from Royal Society of Chemistry.

We further verified the direction of molecular orientation of each sample by XRD investigation of nanowires *within* the AAO template (Fig. 7-9b). In Bragg-Brentano geometry, only lattice planes with scattering vectors ( $q$ ) normal to the sample surface produce diffraction peaks. The discrepancy in the diffraction patterns between the vertically aligned nanowires *within* the template and randomly positioned nanowires therefore reveals the preferential chain orientation in the nanowires. (Details are discussed in Chapter 3.2.1) When we conducted the XRD measurement on the nanowires in the AAO template, the  $\alpha$ -phase nanowires (orange) only showed one distinct sharp peak at  $2\theta = 20.0^\circ$  corresponding to the (001) plane, indicating that the chain axis was perpendicular to the nanowire growth direction.[137], [158], [159] In the case of the  $\delta'$ -phase nanowires (blue), a single diffraction peak was observed at  $2\theta = 21.5^\circ$ . The absence of an (001) peak indicates that the  $\delta'$ -phase nanowires also had a chain direction perpendicular to the template wall. It must be noted that the  $\delta'$ -phase nanowires have a preferential crystal orientation, despite

the fact that they were fabricated by fast crystallisation process, where the resulting polymer shows no preferred orientation. This is because the crystallisation process occurred *within* the nanopores. Although the speed of crystallisation is much faster than other methods, nanowires show a preferential crystal orientation as long as the crystals grew *within* the nanopores.[162] For the case of Nylon-11 nanowires grown by conventional template-wetting, one recognizable diffraction peak was observed at  $2\theta = 22.8^\circ$  as compared to the XRD pattern of the corresponding template-freed nanowires. Although there is insufficient data regarding the peak position of reference nanowires (black), the preferential chain orientation in these nanowires could still be inferred through the differences in the diffractograms.

Based on the XRD peak information, we calculated the size of crystals using the Scherrer equation:  $D_p = (0.94 \times \lambda) / (\beta \cos \theta)$ , where  $D_p$  is average crystallite size,  $\beta$  is line broadening in radians,  $\theta$  is Bragg angle, and  $\lambda$  is X-ray wavelength (= 0.15418 for Cu K- $\alpha$ ). As a result, the  $\alpha$ -phase nanowires show the biggest crystal size of  $21 \pm 2.1$  nm, while  $11 \pm 1.3$  nm and  $10 \pm 1.1$  nm were observed from  $\delta'$ -phase and conventionally grown nanowires, respectively (Fig. 7-10 and Table 7-4). These size discrepancies reconfirm the validity of our processing conditions. The large crystal size of  $\alpha$ -phase nanowires is attributed to the slow crystallisation speed with sufficient chain mobility from additional heating. In contrast, fast crystallisation in the gas-flow assisted method inhibited the growth of crystals, resulting in relatively small size of  $\delta'$ -phase crystals.

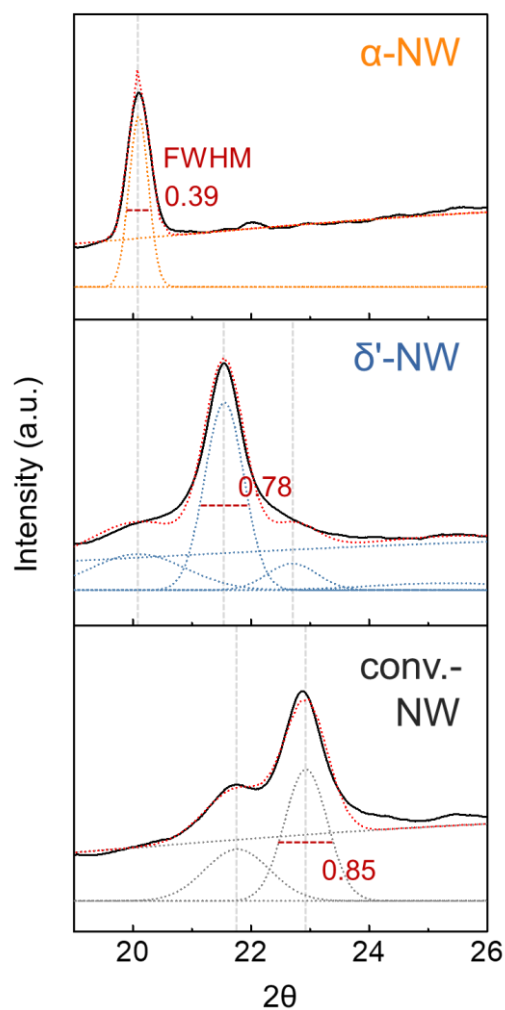


Fig. 7-10 XRD peak analysis of Nylon-11 nanowires with different crystal structures. Fig. is taken from the author's work from Ref. [186], reproduced with permission from Royal Society of Chemistry.

Table 7-4 Summary of XRD peak analysis: FWHM and calculated  $D_p$  for each phase and peak positions. (Accuracy  $\pm 3$  nm)

Phase	$2\theta$ (°)	FWHM	$D_p$ (nm)
$\alpha$	20.10	0.39	21.62
$\delta'$	21.55	0.78	10.83
	20.09	1.89	4.45
	22.70	1	8.47
Conv.	22.93	0.85	9.96
	21.76	1.28	6.56

## 7.2 Thermal behaviour

### 7.2.1 DSC analysis

DSC analysis was carried out to determine the thermal and structural properties of Nylon-11 nanowires, from which the melting temperature ( $T_m$ ) and the melt crystallisation temperature ( $T_c$ ) were recorded (Fig. 7-11 and Fig. 7-12). (All of the original DSC curves are given in Appendix B6). To investigate the nanoconfinement effect of nanowires, as-received Nylon-11 films were also prepared. During the heating cycle, a single melting peak at 190 °C was observed in the  $\alpha$ -phase (orange) and melt-quenched  $\delta'$ -phase films (grey), in a good agreement with reported values.[89] However, when  $\delta'$ -phase films were fabricated via solution-based method (blue), the a dominant melting peak was observed at 187 °C with a minor melting peak at 191 °C. Furthermore, the crystallinity of solution-processed  $\delta'$ -phase films was improved (38 %) compared to that of melt-quenched films (29 %), indicating that solution-based method generated highly crystalline phase even the similar diffractograms were exhibited (Fig. 7-3b). In the case of nanowires *within* AAO, the  $\alpha$ -phase showed the melting peak at 189 °C that is 1 °C lower than that of films. The  $\delta'$ -phase nanowire also displayed decreased melting peaks at 185 °C and 189 °C, and the difference between the two melting peaks became more distinct. The  $T_m$  depression found in the nanowires in the AAO template would be explained by the Gibbs-Thomson equation[150], [231]:

$$\Delta T_m = T_m - T_m(d) = \frac{4 \sigma_{sl} T_m}{d \Delta H_f \rho_s} \quad (7-3)$$

where  $\Delta T_m$  is the melting point depression,  $T_m$  the normal (bulk) melting point,  $T_m(d)$  the melting point of cylindrical nanocrystals with diameter  $d$ ,  $\sigma_{sl}$  the surface tension of the solid-liquid interface,  $\Delta H_f$  the bulk enthalpy of fusion (per g of material), and  $\rho_s$  the concentration of the solid.[150] This equation is well-matched with the  $T_m$  suppression of 1 ~ 2 °C observed in the nanowires relative to films because  $\Delta T_m$  is inversely proportional to  $d$ . When the nanowires are freed from the AAO template, the melting behaviour of  $\alpha$ -phase nanowires transited to bimodal melting, maintain the dominant  $T_m$  at 189 °C. Furthermore, the position of dominant melting peak of  $\delta'$ -phase nanowires is altered from

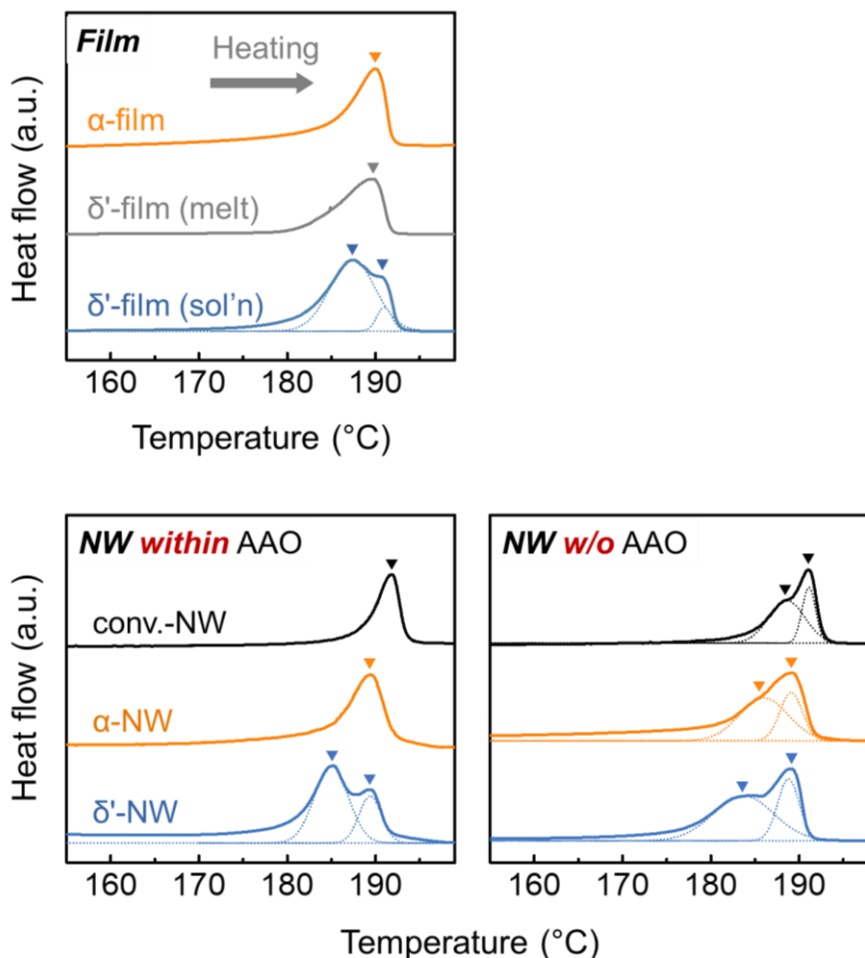


Fig. 7-11 DSC thermograms obtained during the first heating for Nylon-11 films and nanowires. Four different crystal structures of films and nanowires were investigated: (orange)  $\alpha$ -, (grey) melt-quenched  $\delta'$ -, and (blue) solution-based  $\delta'$ -phase films and nanowires. (black) un-reported phase from nanowires fabricated by conventional template-wetting.

185 °C to 189 °C. The melting behaviour of nanowires fabricated by conventional template wetting method was also manipulated with the similar trend to  $\alpha$ -phase nanowires. According to the literature, several sources can be responsible for multiple melting peaks[232]: 1) recrystallisation during melting; 2) multiple crystalline phases exist simultaneously; 3) phase transition occurring during heating; and 4) removal of defects or improvement of ordering in the crystal structures by annealing effect. In the case of Nylon-11 nanowires without AAO, it is possible to experience recrystallisation during the melting process. This is because when nanowires are in the template, the thermal behaviour is restricted by the template wall. The crystal perfection possibly changes during template

dissolving process. Interestingly, the  $T_m$  of nanowires (*within* the AAO) fabricated by conventional template wetting method was achieved at 191 °C that is much higher than that of  $\alpha$ - and  $\delta'$ -nanowires. Furthermore, the crystallinity of this un-reported phase of Nylon-11 is 40 %, which is much higher than that of  $\delta'$ -phase nanowires (38 %), meaning that nanowires fabricated by conventional template wetting has also stable and highly crystalline phase.

During the cooling cycle, films and template-freed nanowires with the same phases exhibited the similar crystallisation behaviour (Fig. 7-12 and Table 7-5). The  $T_c$  of  $\alpha$ -phase film and nanowires are found near 165 °C, and solution-based  $\delta'$ -phase film and nanowires displayed a  $T_c$  at around 164 °C. The difference of the  $T_c$  between  $\alpha$ - and  $\delta'$ -phase possibly arises due to the residual ordering in the polymer melts. In contrast, *within* the template, the Nylon-11 showed different crystallisation behaviour with relatively weak and broad crystallisation peak at around 156 °C. This is because homogeneous nucleation occurred in the nano-sized pores. As discussed by Lutkenhaus et al.[149], heterogeneous nucleation is typified by a sharp crystallisation peak upon cooling in DSC, which we observe here for Nylon-11 films and template-freed nanowires. A broad and supercooled crystallisation transition are attributed to the homogeneous nucleation where there are a few defects to initiate crystal growth. It must be noted that, in the case of PVDF or P(VDF-TrFE), such homogenous nucleation was only observed when they were confined in very small size of pores (< 50 nm).[149] (For bulk or crystallisation in bigger pores (~ 200 nm), P(VDF-TrFE) presented the sharp crystallisation peak corresponding to heterogeneous nucleation.) This is because the size of nanostructures should be smaller than the natural average distance between heterogeneous nucleation centres to achieve the complete confinement.[137], [138] In contrast, in the case of Nylon-11, homogeneous nucleation is observed in 200 nm pores, indicating that the distance between nucleation centres of Nylon-11 is much bigger than that of PVDF and its copolymers. Above all, this means that the complete confinement of Nylon-11 can be achieved via 200 nm AAO template. The  $T_m$ ,  $T_c$ , and degree of crystallinity ( $\chi$ ) of various phases of films and nanowires are summarised in Table 7-5.

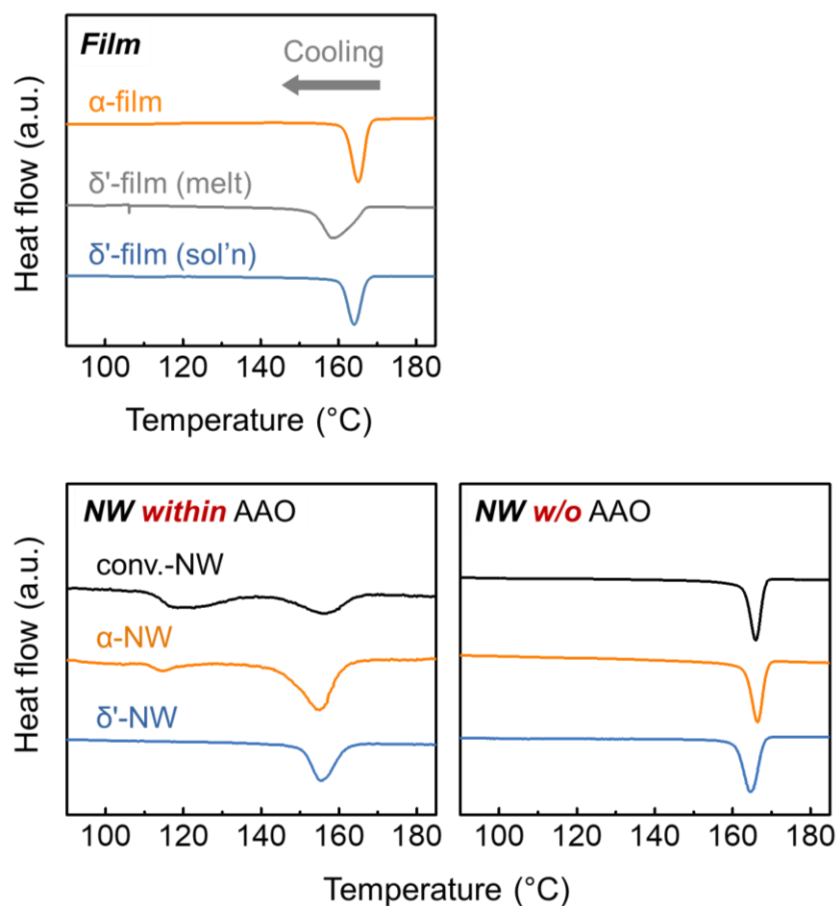


Fig. 7-12 DSC thermograms obtained during the cooling for Nylon-11 films and nanowires. Four different crystal structures of films and nanowires were investigated: (orange)  $\alpha$ -, (grey) melt-quenched  $\delta'$ -, and (blue) solution-based  $\delta'$ -phase films and nanowires. (black) un-reported phase from nanowires fabricated by conventional template-wetting.

Table 7-5 The  $T_m$ ,  $T_c$ , and  $\chi$  of various phases of Nylon-11 films and nanowires observed by DSC measurement. The bold character in the temperature values indicate the dominant peak. The  $\chi$  of nanowires were measured only from the template-freed samples.

	phase	$T_m$ (°C)	$T_c$ (°C)	$\chi$ (%)
<b>Film</b>	$\alpha$	190	165	48
	$\delta'$ (melt-quenched)	190	158	29
	$\delta'$ (solution-based)	<b>187</b> , 191	164	38
<b>NW</b> (within AAO)	unknown	191	<b>157</b> , 119	
	$\alpha$	189	<b>155</b> , 114	
	$\delta'$	<b>184</b> , 189	155	
<b>NW</b> (without AAO)	unknown	187, <b>191</b>	166	40
	$\alpha$	185, <b>189</b>	166	48
	$\delta'$	185, <b>189</b>	163	38

### 7.2.2 X-ray diffractograms

To measure the thermal stability of Nylon-11 nanowires, X-ray diffractograms before and after 165 °C annealing of samples are compared. Three different samples with nanowires grown by conventional template-wetting,  $\delta'$ -phase nanowires, and  $\alpha$ -phase nanowires were prepared. XRD measurement was conducted on the nanowires *within* an AAO template. In the case of nanowires grown by conventional template-wetting, the intensity of dominant peak at 22.8° was significantly reduced after annealing (Fig. 7-13a). Considering that the nanowire has a preferential chain orientation and corresponding plane is the main direction of orientation perpendicular to the nanowire growth direction, this result implies that the preferential orientation in nanowire is removed, changing the molecular configuration. In addition, this suggests that the phase of nanowire grown by conventional template-wetting is also a thermally unstable phase. The molecular configuration of  $\delta'$ -phase nanowires was also changed after thermal annealing. The intensity of 21.6° peak corresponding to (hk0) plane of  $\delta'$ -phase decrease after thermal annealing, while the intensity of peak at 20.4° increase, indicating that the preferential orientation is also disappeared similar to nanowires grown by conventional template-wetting (Fig. 7-13b). However, it must be noted that the thermal behaviour of  $\delta'$ -phase nanowire is definitely different with that of  $\delta'$ -phase film. According to the literature, crystal structure of pseudo-hexagonal  $\delta'$ -phase film is transformed to triclinic  $\alpha'$ -phase after 165°C annealing because of molecular stabilization during the annealing.[89] As discussed in Chapter 2.4,  $\alpha'$ -phase has two distinct peaks at 20.4° and 23.4° (Fig. 3-1) without 21.6° peak. Whereas,  $\delta'$ -phase nanowire still has a 21.6° peak with similar intensity to 20.4°, indicating that  $\delta'$ -phase crystals are remaining after the thermal annealing possibly due to the relatively large crystallinity of  $\delta'$ -phase nanowires than  $\delta'$ -phase films. Lastly, in the case of  $\alpha$ -phase nanowire, the peak positions and intensities in diffractograms before and after 165°C annealing are almost the same (Fig. 7-13c). This means that  $\alpha$ -phase nanowires can preserve their crystal structures at very high temperature due to strong hydrogen bonding and ordered crystal structures.

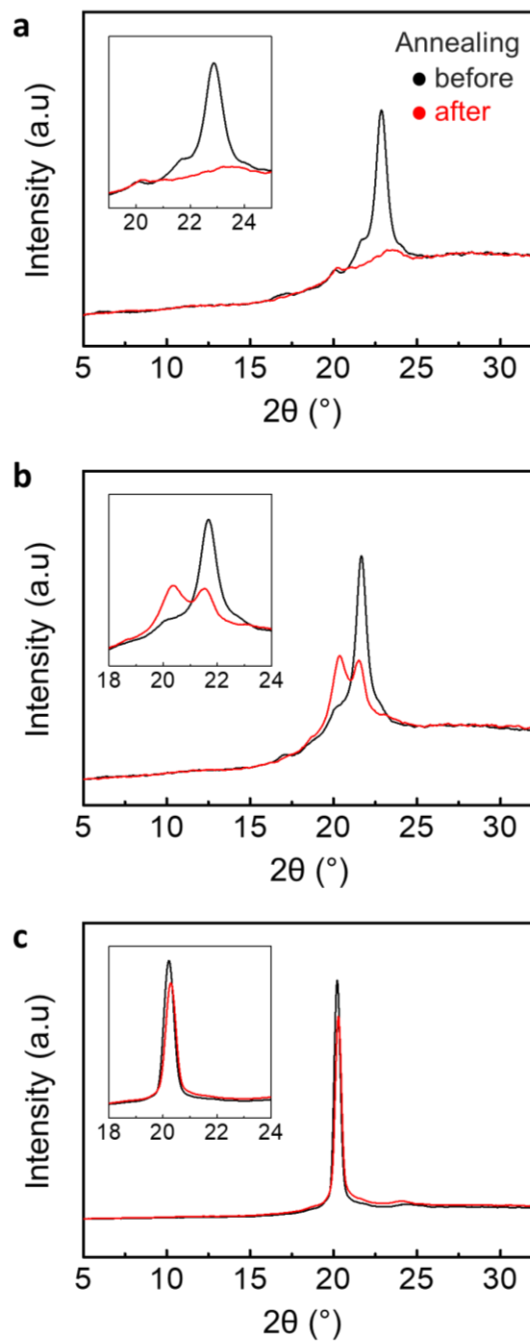


Fig. 7-13 Comparison of XRD patterns of nanowires *within* AAO template (black) before and (red) after thermal annealing at 165 °C: (a) nanowires grown by conventional template-wetting, (b)  $\delta'$ -phase nanowires and (c)  $\alpha$ -phase nanowires. Inset displays the magnified area.

## 7.3 Electromechanical characteristics

### 7.3.1 Mechanical stiffness of Nylon-11 single nanowire

Fig. 7-14 shows the height changes across identical nanowires of different Nylon-11 crystal structures mounted on a silicon substrate, while height-correlated trends were presented in the corresponding DMT modulus mapping mode.[201] However, since the nanowire modulus is not a function of its thickness, the topography-related modulus was assumed to have resulted from tip-nanowire interaction.[196], [197] Therefore, a reliable DMT modulus could be achieved by recording the measurement at the top of the nanowire.

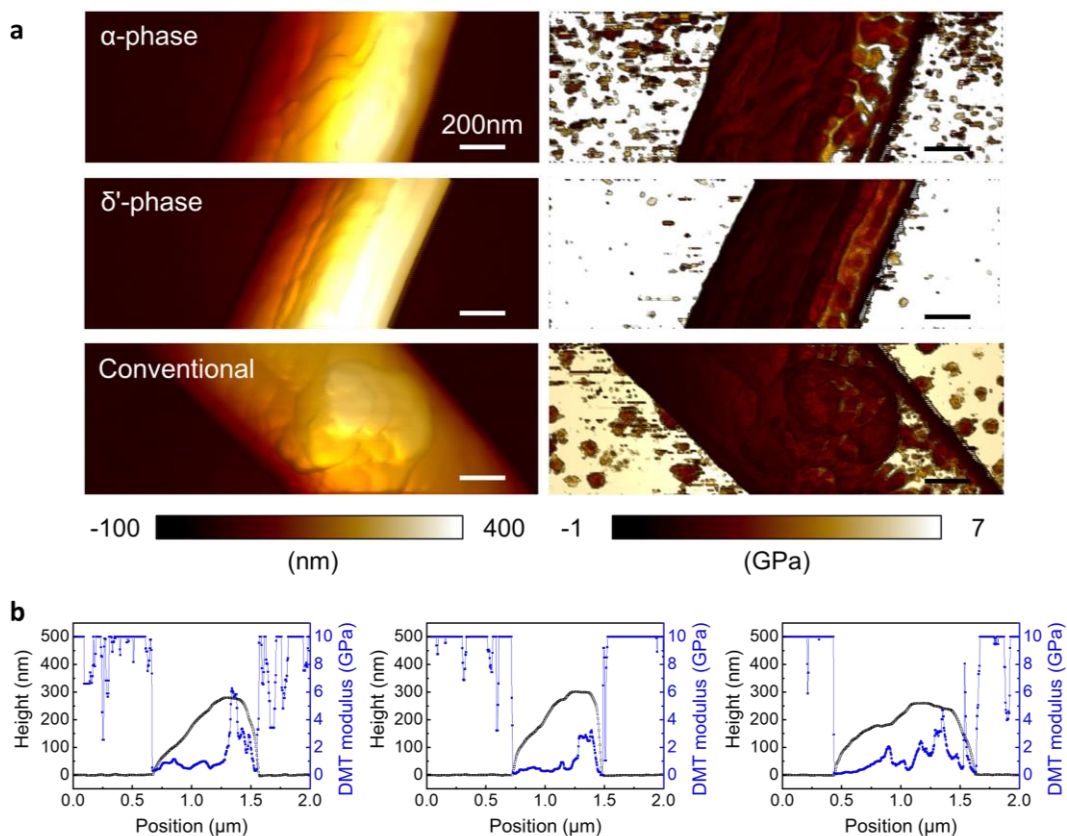


Fig. 7-14 QNM characteristics of various nanowire phases. (a) Topology (left) and DMT modulus (right) mapping of  $\alpha$ -phase,  $\delta'$ -phase and conventional nanowires. (b) Average DMT modulus along the whole width of each nanowire. Fig. (a) and (b) are taken from the author's work from Ref. [186], reproduced with permission from Royal Society of Chemistry.

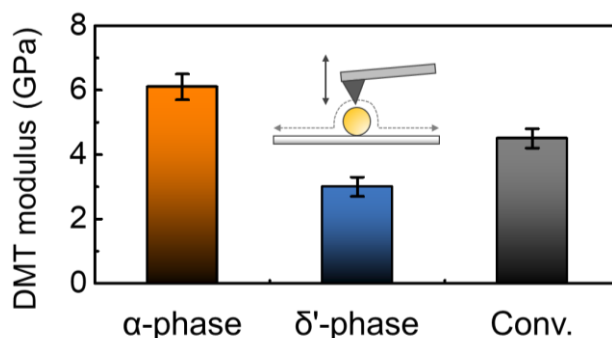


Fig. 7-15 Average DMT modulus of  $\alpha$ -phase (orange),  $\delta'$ -phase (blue) and conventional (black) nanowires. Fig. is taken from the author's work from Ref. [186], reproduced with permission from Royal Society of Chemistry.

In Fig. 7-15, the  $\alpha$ -phase nanowire (orange) showed the highest modulus (6.1 GPa), which is double that of  $\delta'$ -phase nanowire (blue, 3 GPa). Nanowires prepared through the conventional template-wetting method (black) exhibited an intermediate modulus of 4.5 GPa. The difference in respective moduli of the different nanowire samples can be explained by the corresponding crystal structures. Firstly, the stiffness of the  $\alpha$ -phase nanowires can be attributed to the crystal structure of  $\alpha$ -phase Nylon-11 and the relatively big crystal size. Since the polymer chains have sufficient time to align and stack up during crystallisation,  $\alpha$ -phase Nylon-11 typically contains highly packed crystal structures with hydrogen bonding sheets. Furthermore, due to the same reason, as discussed, the size of crystal in  $\alpha$ -phase nanowires is much larger than others. As a result,  $\alpha$ -phase displays good mechanical stiffness because the mechanical property of semi-crystalline polymer is attributed to the crystalline region dominantly.[103], [106], [233] In contrast, the  $\delta'$ -phase exhibits suppressed hydrogen bonding and crystal growth due to fast-crystallisation.[103], [106] This means that the positive contribution of hydrogen bonding to crystal structure is relatively small in the  $\delta'$ -phase nanowire, resulting in much lower DMT modulus. For the case of nanowires prepared via a conventional template-wetting method, the modulus can be explained through the processing conditions. The only difference between the  $\alpha$ -phase growth method and conventional template-wetting method is the growth temperature, which is related to the driving force for chain alignment. The latter therefore has sufficient time to crystallize but does not have enough energy to produce a more ordered and bigger crystal structure, resulting in the comparatively lower modulus than  $\alpha$ -phase nanowires.

It should be noted that the DMT model is not generally suitable for the analysis of cylinder indentation,[201] and an acceptable model for this particular problem does not exist to the best of our knowledge. To address this issue, we have performed finite-element simulations of nano-indentation on nanowires and thin films (Fig. 7-16).

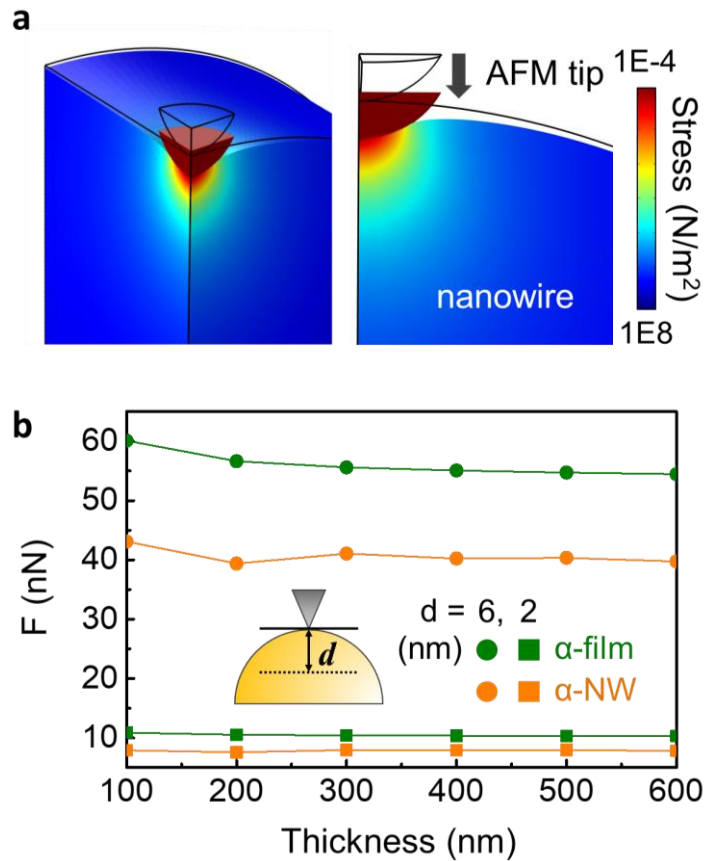


Fig. 7-16 Numerical simulation results of nano-indentation: (a) cross-sectional view of a 6 nm indentation of a nanowire using a 25 nm AFM tip. (b) Indentation force change as a function of thickness of the film (green) and the nanowire (orange). The simulation was conducted using deformation depth ( $d$ ) of 6 nm (circle) and 2 nm (square). Fig. (a) and (b) are taken from the author's work from Ref. [186], reproduced with permission from Royal Society of Chemistry.

The indentation force due to the AFM tip on both the nanowires and the films was characterized by changing the sample deformation depth ( $d$ ) and sample thickness. It can be seen that, as the film becomes thinner, the required force to deform the film increases. In the case of the nanowire, however, this effect is reduced and is almost constant due to the suppressed circumferential clamping of a nanowire.[196], [197] In addition, the film

requires a much higher force for a given deformation than a nanowire, which is more pronounced for larger deformation (6 nm, circle). These results show that nanowires are inherently softer than films of the same intrinsic mechanical properties, and that they are less affected by the substrate upon reduction of thickness. It also suggests that the DMT model underestimates Young's modulus of nanowire samples. Despite this, in our QNM experiments, we found that the  $\alpha$ -phase nanowire exhibited much higher DMT modulus (6.1 GPa) than that of  $\alpha$ -phase film (2.5 GPa) (Fig. 7-17), even when the deformation range was similar to that of the simulation (Fig. 7-18). Our results indicate that due to a large amount of hydrogen bonding and well-aligned crystal structure in the nanowire,  $\alpha$ -phase nanowires were found to exhibit much higher mechanical strength than the corresponding film.

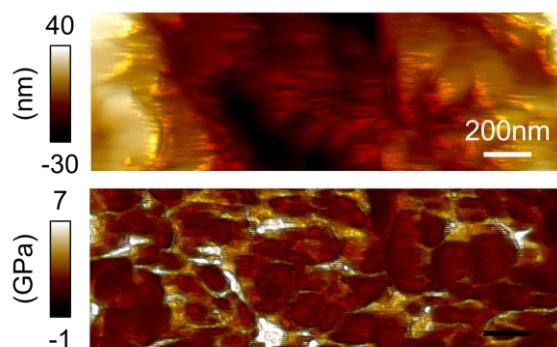


Fig. 7-17 QNM characteristics of  $\alpha$ -phase Nylon-11 film: Height (above) and DMT modulus (below) maps are illustrated. Fig. is taken from the author's work from Ref. [186], reproduced with permission from Royal Society of Chemistry.

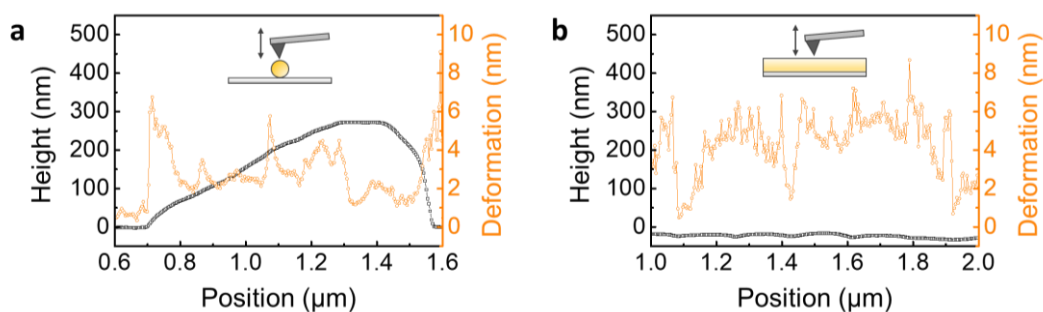


Fig. 7-18 QNM characteristics of (a) an  $\alpha$ -phase Nylon-11 nanowire and (b) an  $\alpha$ -phase Nylon-11 film: The plots indicate height (black) and deformation (orange). Fig. (a) and (b) are taken from the author's work from Ref. [186], reproduced with permission from Royal Society of Chemistry.

### 7.3.2 Piezoelectric response of nanowire arrays

In addition to the mechanical properties, the piezoelectric response of the three different nanowire phases was characterized by PFM (Fig. 7-19).[195], [197] It is noted that, in the case of nanoconfined Nylon-11 nanowires, the additional poling process for PFM analysis is not necessary as self-polarization occurs through preferential molecular orientation.[2], [208] With the polarisation direction being parallel to the nanopore axis, the PFM measurement was performed at the top surface of the nanowires filled AAO template.[159], [161] As shown in Fig. 7-20a, the top surface of AAO template contains the tips of the  $\delta'$ -phase nanowires, resulting in an oscillating piezo-response with the application of AC bias between the tip and sample. The average deflection amplitude resulting from the piezoelectric response changed as a function of AC bias, as plotted in Fig. 7-20c, d. The piezoelectric amplitude of  $\delta'$ -phase nanowires was proportional to the AC bias with a slope of  $0.264 \text{ mV V}^{-1}$ , which suggests that  $\delta'$ -phase nanowire is piezoelectric (piezoelectric coefficient,  $d_{33} = 3.22 \text{ pm V}^{-1}$ ). In contrast,  $\alpha$ -phase and conventionally grown nanowires do not display significant piezoelectric response (Fig. 7-19, Fig. 7-21, and Fig. 7-22).

It is known that, among various phases of Nylon-11,  $\delta'$  is the crystal structure which exhibits the highest piezoelectric response.<sup>3,24,28-31</sup> However, in the “film” shape of  $\delta'$ -phase, piezoelectric response can be observed only after drawing and/or electric poling process. The  $\delta'$ -phase nanowires, however, show a distinct piezoelectric response without high voltage poling process due to the nanoconfinement effect, attributed to self-poling in these nanowires due to the growth process.[2], [202], [211] On the contrary, in the case of the  $\alpha$ -phase nanowires, even though they exhibited a preferential crystal orientation along the nanowire axis, no significant piezo-response was observed (Fig. 7-21). This suggests that strong hydrogen bonding in the  $\alpha$ -phase nanowires not only enhanced the nanomechanical properties, but also suppressed the response to an external electric field. This observation is in agreement with reported results from Nylon-11 film of similar crystalline structure.[95], [103], [106]

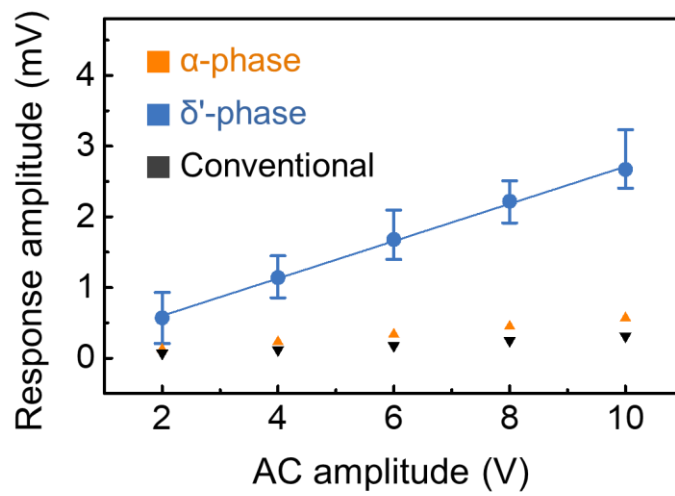


Fig. 7-19 Piezoelectric response amplitude of  $\alpha$ -phase (orange),  $\delta'$ -phase (blue) and conventional (black) nanowires as a function of AC amplitude. Fig. is taken from the author's work from Ref. [186], reproduced with permission from Royal Society of Chemistry.

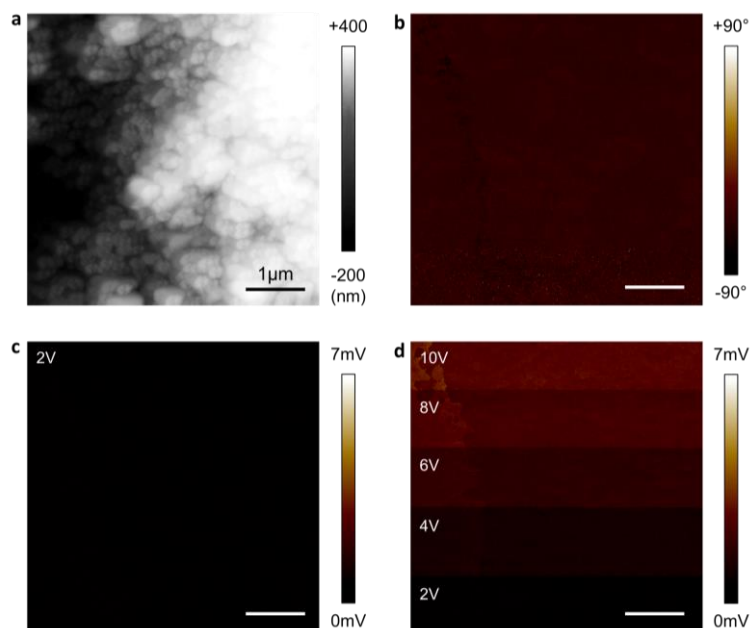


Fig. 7-20 PFM characteristics of top surface of AAO template filled with  $\delta'$ -phase nanowires. (a) Height, (b) phase mapping, (c) piezo-response amplitude at AC amplitude of 2V and (d) piezo-response amplitude at various AC amplitude. Fig. (a) ~ (d) are taken from the author's work from Ref. [186], reproduced with permission from Royal Society of Chemistry.

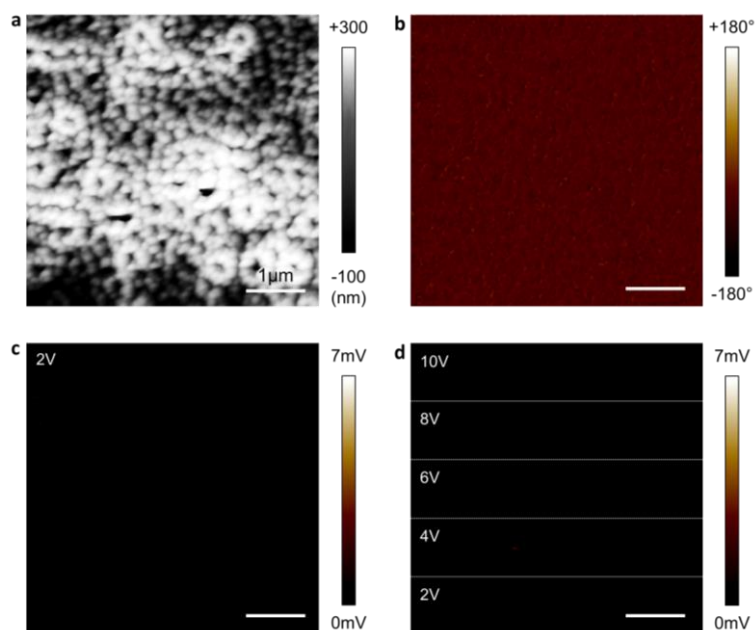


Fig. 7-21 PFM characteristics of top surface of AAO template filled with  $\alpha$ -phase nanowires. (a) Height, (b) phase mapping, (c) piezo-response amplitude at AC amplitude of 2V and (d) piezo-response amplitude at various AC amplitude. Fig. (a) ~ (d) are taken from the author's work from Ref. [186], reproduced with permission from Royal Society of Chemistry.

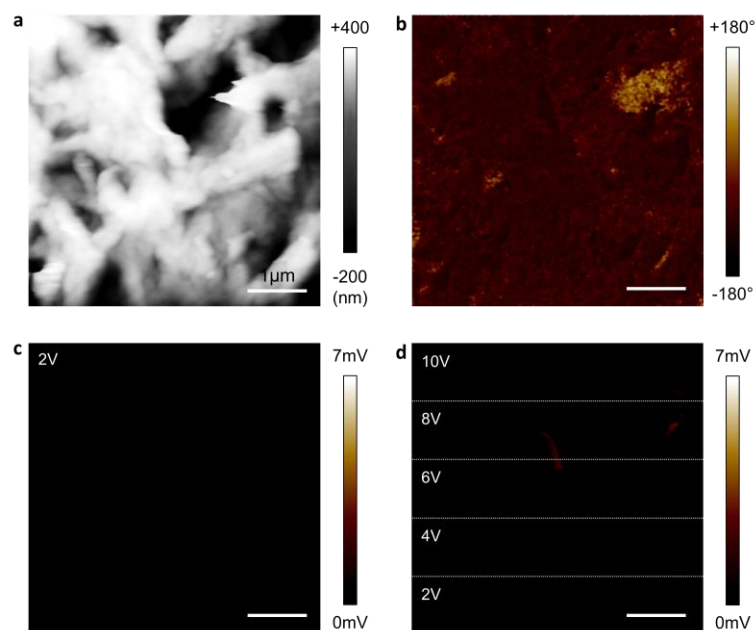


Fig. 7-22 PFM characteristics of top surface of AAO template filled with conventionally grown nanowires. (a) Height, (b) phase mapping, (c) piezo-response amplitude at AC amplitude of 2V and (d) piezo-response amplitude at various AC amplitude. Fig. (a) ~ (d) are taken from the author's work from Ref. [186], reproduced with permission from Royal Society of Chemistry.

## 7.4 Conclusions

In this chapter, different crystallisation mechanisms of Nylon-11 nanowire fabricated by template-wetting method was discussed in great detail. Beyond typical temperature-driven crystallisation and gravity-infiltration template-wetting, the potential of evaporation-driven crystallisation and capillary infiltration template-wetting method was presented. Various combinations of three processing parameters – temperature, gas-flow rate, and concentration of solution – enables us to tune the crystallisation condition. As a result,  $\alpha$ - and  $\delta'$ -phase Nylon-11 nanowires with much higher crystallinity than that of films can be achieved. XRD analysis confirmed the resulting crystal structures, size of crystals and preferential orientation in nanowires. Thermal behaviour showed that Nylon-11 nanowires were fabricated by homogeneous nucleation and complete wetting *within* 200 nm nanopores. The electromechanical characteristics display the property of three types of nanowire samples with different crystallography.  $\alpha$ -phase nanowires showed the highest Young's modulus but did not exhibit significant piezoelectric behaviour. In contrast, a distinct piezoelectric response was achieved from the relatively soft  $\delta'$ -phase nanowires. A similar trend in the variation of properties across the different crystal phases was observed in Nylon-11 films. However, compared to the properties of films with the same crystal structure, the modulus of  $\alpha$ -phase nanowires and the piezoelectric response of  $\delta'$ -phase nanowires was larger. These results suggest that the nanoconfinement effect leads to enhancement of the electromechanical properties of each crystal structure based on molecular level optimisation.

## Chapter 8

# Multi-layered Nanocomposites by Dual Aerosol-Jet Printing Method for Energy Applications

In this chapter, we show that an advanced aerosol-jet printing technique can provide facile access to multi-layered nanocomposites. The ideal dispersion of nano-insertions is achieved via independent atomization of polymer and ink containing the nano-insertions. Multi-layered structures of the thermoplastic polymer-based nanocomposite are accomplished without a cross-linking agent, thereby unlimited combinations of multi-layered nanocomposites are possible. The resultant nanocomposites exhibit high dielectric constant and low dielectric loss, with outstanding reliability over the whole printed region. Preliminary single-layered nanocomposite-based triboelectric energy harvesting measurement shows that there was an improvement of output performance compared to a neat polymer-based device, but further work is needed to achieve reliable results, including the influence of materials and layer combinations.

## 8.1 Route to nanocomposites with ideal dispersion

We believe that the origin of the long-standing problems related to nanocomposite dispersion is not due to the materials, but method. Typically, materials are “pre-mixed” to fabricate nanocomposites. In other words, the mixing of polymer and nano-insertions is a prerequisite in conventional nanocomposite fabrication methods.

As discussed in Chapter 3.1.3, aerosol-jet printing is a relatively new additive manufacturing technique that enables large area and high-resolution printing of materials with a wide range of ink viscosities between 1 and 1000 cP.[3], [169]–[171] The aerosol-jet printing technique enables atomizing ink to a fine mist, or aerosol, and printing them by using a carrier gas to jet this aerosol towards a substrate.[3], [174] Thus, both polymer solution and nanomaterial dispersed solution are atomized and printed separately by pneumatic and ultrasonic atomizer without pre-mixing of polymer matrix and nano-insertions. *A priori*, the aerosol-jet printing technique could also be used to print nanocomposites. For example, nanocomposites of bismuth telluride ( $\text{Bi}_2\text{Te}_3$ ) or antimony telluride ( $\text{Sb}_2\text{Te}_3$ ) nanocrystals with poly(3,4-ethylenedioxythiophene) polystyrene sulfonate (PEDOT:PSS) matrix[236] has already been obtained by using aerosol-jet printer in our group. However, previous studies only present the possibilities of aerosol-jet printed nanocomposites without evaluating the properties associated with the degree of dispersion and multi-layered structures.

In this work, two different polymer solutions of 4 wt % P(VDF-TrFE) and 50 vol% poly(amic acid) in N-Methyl-2-pyrrolidone (NMP), and two different nanomaterials dispersed solution of silver (Ag) nanoparticle and copper (Cu) nanoparticles are prepared. The proper atomizer for materials is determined by solution viscosity and properties of base solvent. Two aerosol streams become one by the Y-shape connector, but materials are not mixed in the connector and transporting tubes because materials remain as aerosols (Fig. 8-1). The aerosol stream is focused by the deposition head (dep-head) up to the printing resolution and deposited on various substrates, such as glass, PI film, PET film, and silicon wafer, with the assistance of nitrogen gas. The substrate is heated to increase the degree of dispersion, and the setting temperature is changed depending on the solvent. The thickness of the printed nanocomposites can be manipulated by changing the number of printed layers. After printing, the samples are cured in an oven. In the case of P(VDF-TrFE) based nanocomposite, to increase the crystallinity, the printed nanocomposite was annealed for

2h at 135 °C, which appears above its Curie temperature (118 °C) but below its melting temperature (150 °C).

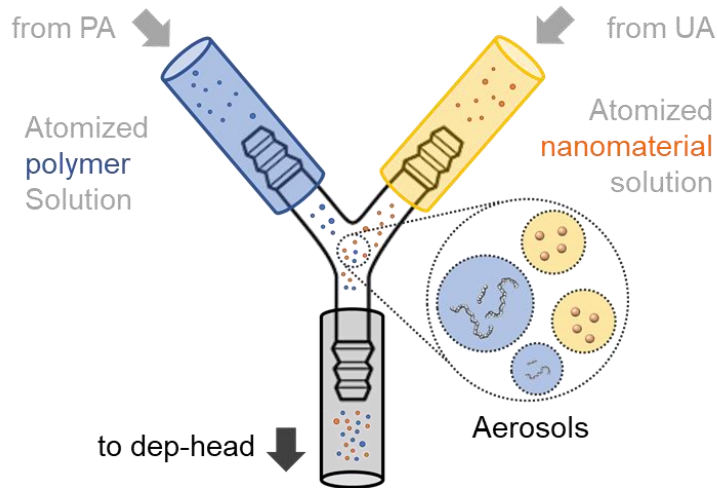


Fig. 8-1 Schematic of Y-shape connector for aerosol-jet printed nanocomposite.

## 8.2 Nanoparticle dispersion in aerosol-jet printed nanocomposite

Fine tuning of the ratio between the printing amount of polymer and nanomaterials is enabled because the aerosol deposition is controlled by nitrogen gas-flow regulator. Table 8-1 shows the sheath, pneumatic atomizer (PA), and ultrasonic atomizer (UA) flow rate corresponding to the overall focusing, amount of polymer aerosol, and nanomaterials, respectively. Sample 1 corresponds to 100 % polymer, and the number of nanoparticles in the polymer matrix gradually increases with number of samples, while the amount of polymer matrix is maintained. The variation of the number of nanoparticles in polymer matrix is investigated by studying XRD patterns of the printed nanocomposite.

As a reference, PI/Ag nanoparticle nanocomposite was printed using aerosol-jet printing technique because the optimized printing conditions for printing each of these materials are well-established in our group. The diffractograms of aerosol-jet printed PI/Ag nanoparticles nanocomposites are displayed in Fig. 8-2. Since PI is an amorphous polymer,

only the peaks at  $38.2^\circ$  and  $44.4^\circ$  corresponding to the first and second ordered diffraction of Ag nanoparticles are obtained from all samples. From Sample no. 1 to 8, the peak intensity of Ag nanoparticles are gradually increased with increasing UA flow rate. Interestingly, in the case of Sample No. 2, despite Ag nanoparticles being printed, the intensity of the first order Ag peak is significantly small and hence indistinguishable, indicating that realizing nanocomposites with extremely small number of nanoparticles is enabled by the aerosol-jet printer.

Table 8-1 Setting values of sheath, pneumatic atomizer (PA), and ultrasonic atomizer (UA) gas-flow rate for nanocomposite printing. Gas-flow rates are quoted in standard cubic centimetres per minute (sccm).

Sample No.	1	2	3	4	5	6	7	8
Sheath (sccm)	0.41	0.42	0.43	0.45	0.48	0.50	0.52	0.53
PA (sccm)	3.70	3.82	3.86	3.88	3.92	3.95	3.99	4.01
UA (sccm)	0.63	1.33	1.47	1.56	1.64	1.72	1.79	1.87

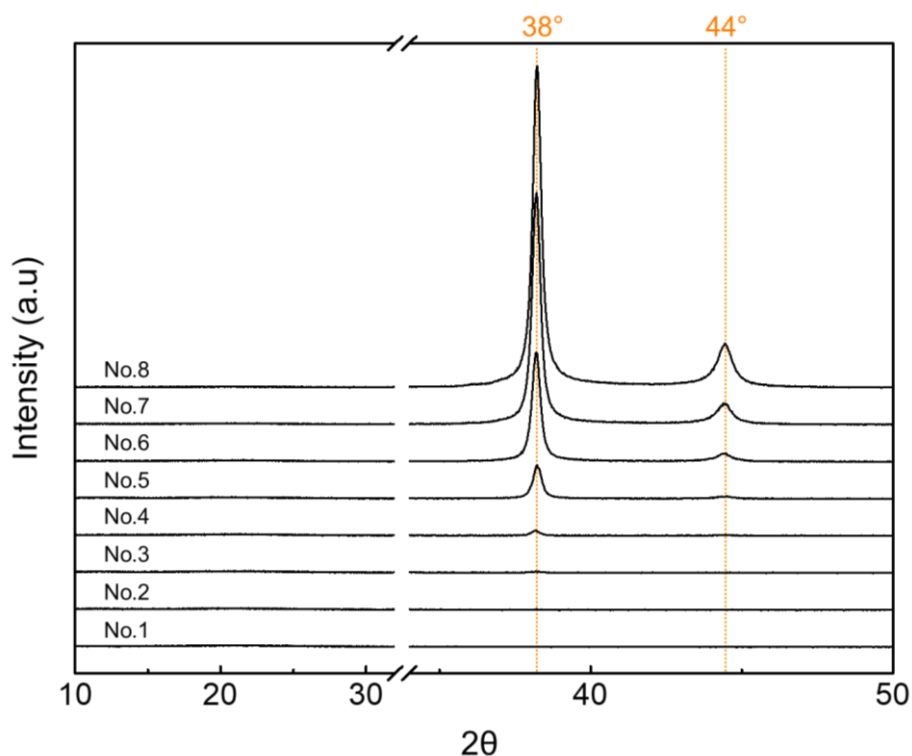


Fig. 8-2 XRD patterns of aerosol printed PI/Ag NPs nanocomposite. Orange dot lines at  $38^\circ$  and  $44^\circ$  correspond to the diffractions first and second ordered peak of Ag NPs, respectively.

The surface morphology of aerosol-jet printed PI/Ag nanoparticles nanocomposites were imaged by SEM. To verify the number of Ag nanoparticles in PI matrix, SEM scanning was conducted without coating of conductive metals. As a result, conductive Ag nanoparticles can be distinguished clearly by brightness difference in the SEM images. Fig. 8-3a shows a gradual increase of the number of Ag nanoparticles in the PI matrix with increasing UA flow rate. The SEM image of 100 % PI printed line displays contrast gradient according to the height without Ag nanoparticles (Fig. 8-3b). In contrast, the Ag nanoparticles can be detected on the printed PI line in the magnified image of Sample No.3 (Fig. 8-3c), indicating that both polymer and nanomaterials were well-deposited on the substrate. It must be noted that all nanoparticles with average size of 100 nm are deposited as a single particle in the printed line. This result means that aerosol-jet printing method enables fine dispersion of Ag nanoparticles in PI matrix.

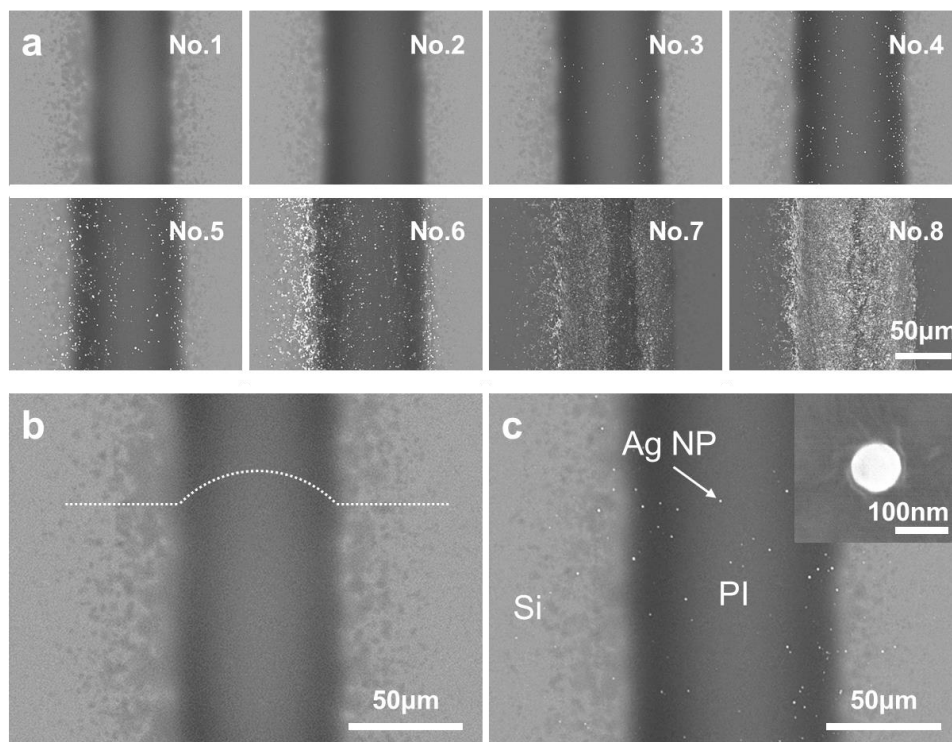


Fig. 8-3 Microstructure of aerosol printed PI/Ag NPs nanocomposite. (a) Changes in surface morphology of Sample No.1 to No.8. Magnified image of sample (b) No.1 and (c) No.3. Inset of (c) indicate the single Ag NP in the PI matrix. White dot indicate the conductive Ag NP.

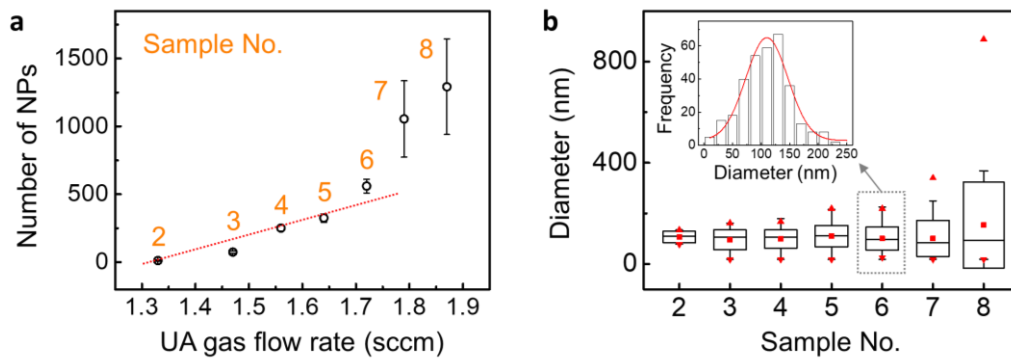


Fig. 8-4 SEM image analysis data for the calculation of degree of dispersion. (a) Relationship between UA gas-flow rate and number of Ag nanoparticles. (b) Diameter of Ag nanoparticles in each SEM image of sample. ‘■’, ‘▲’, and ‘▼’ indicate mean, 99 %, and 1 % value, respectively. The middle line, top and bottom boundaries in the box indicate the median, plus and minus standard deviation value. Inset shows the Ag NPs diameter distribution (column) and Gaussian fitting plot (red line).

The degree of dispersion of Ag nanoparticles in the PI matrix is investigated by SEM image analysis. The nanoparticle size analysis was conducted using samples No. 2 to No. 7. The number of Ag nanoparticles in the PI matrix is linearly proportional to the UA gas-flow rate from 1.33 sccm to 1.72 sccm (Fig. 8-4a), indicating that the aerosol-jet printer can finely control the number of deposited Ag nanoparticles. Above the 1.72 sccm, the error ratio increased significantly due to the unclear contrast difference between polymer and nanoparticle. Changes in diameter are shown in Fig. 8-4b. The diameter of Ag nanoparticle shows normal distribution function (Fig. 8-4b, inset). Interestingly, the average nanoparticle diameter of all samples are almost similar, while the standard deviation and the size of upper 99 % nanoparticle increase with increasing sample number because the number of deposited nanoparticles increases. This means that the nanoparticles are well-dispersed in the samples, and the degree of dispersion can be maintained even in the high-concentration condition. The increasing trend of the upper 99 % size indicates agglomeration of nanoparticles. Because the distance between nanoparticles is reduced gradually with increasing deposited amount, some nanoparticles merge to form larger particles, resulting in electrically conductive path at high concentration.

Different combinations of nanocomposites have also been fabricated. Instead of PI, P(VDF-TrFE) has been introduced as a polymer matrix because it is one of the widely used energy harvesting materials. For the comparison, P(VDF-TrFE) was printed with the same

Ag nanoparticles. Although 4 wt % P(VDF-TrFE) solution has lower viscosity than polyamic acid (PAA) solution, the PA gas-flow rate does not need to be adjusted because of wide processing window of PA. Similar to the PI/Ag nanoparticle composite, XRD analysis shows gradual increase of first and second order Ag diffraction peak (Fig. 8-5). In addition,  $\beta$ -phase P(VDF-TrFE) diffraction peak at  $20^\circ$  was also obtained in all samples because P(VDF-TrFE) is a semi-crystalline polymer. SEM images also display not only the changes in deposited nanoparticle numbers with increasing UA flow rate but also almost perfect degree of dispersion (Fig. 8-6). Furthermore, based on P(VDF-TrFE) matrix, different nanoparticles, such as Cu nanoparticles and graphene oxide (GO), were also applied. Although the nanoparticles were printed from pristine solutions without adding any other surfactant for polymer matrix, almost perfect dispersion of nanoparticle in polymer matrix has been achieved reliably. These results indicate that aerosol-jet printing technique enables the realization of well-dispersed nanocomposites independent of the compatibility between polymer matrix and inorganic nanoparticles.

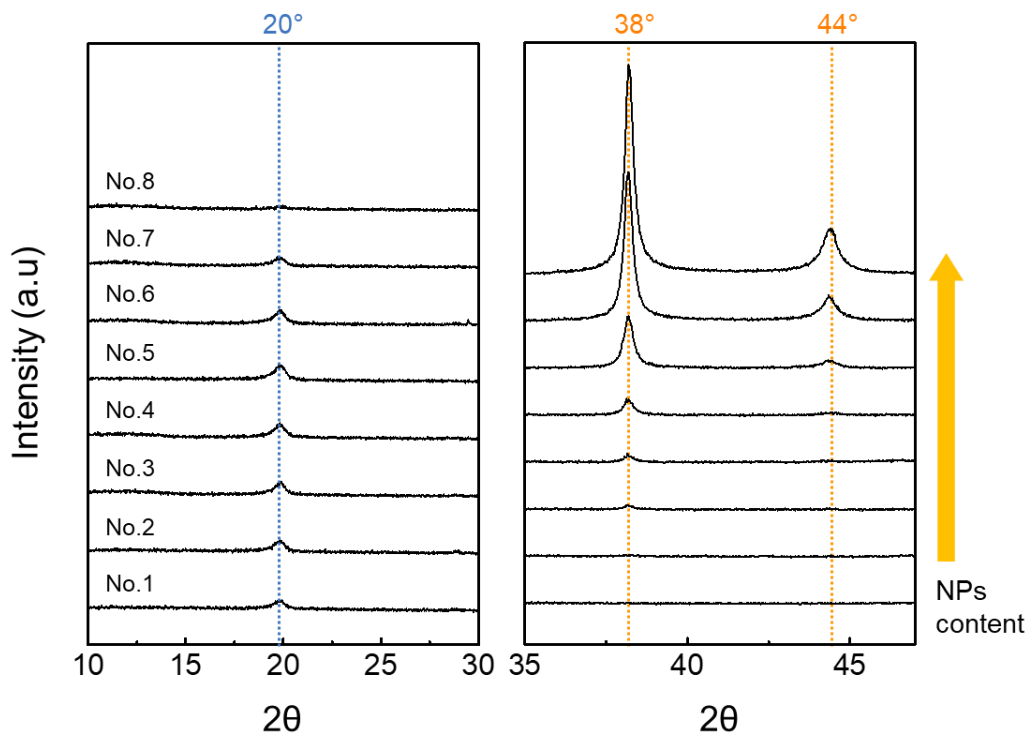


Fig. 8-5 XRD patterns of aerosol-jet printed P(VDF-TrFE)/Ag NPs nanocomposite. Blue dots ( $20^\circ$ ) and orange dots ( $38^\circ$ ,  $44^\circ$ ) lines correspond to the diffractions of P(VDF-TrFE)  $\beta$ -phase crystal, Ag NPs first and second ordered peaks, respectively.

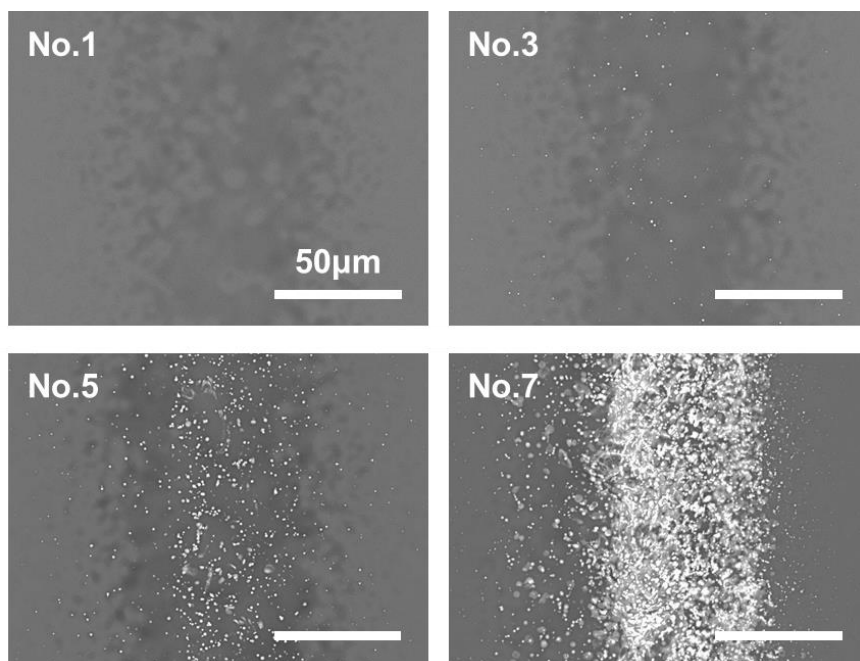


Fig. 8-6 SEM images of aerosol-jet printed P(VDF-TrFE)/Ag NPs nanocomposite.

Film type nanocomposite samples were prepared by overlapping printed lines side by side. Since the deposited polymer matrix is in a highly viscous solution state, printed nanocomposite lines could be merged spontaneously without formation of boundaries, while the nanoparticles did not agglomerate due to the viscosity of polymer matrix. As a result, the degree of dispersion in the single printed lines could also be preserved in large-area films. The SEM images of P(VDF-TrFE)/Ag nanoparticle nanocomposite shows well-dispersed Ag nanoparticles in the film without aggregation (Fig. 8-7). The thickness of a single-layered nanocomposite film is about 100 nm, and the total thickness of the film can be controlled by the number of printed layers spanning thickness scales from few hundreds of nanometres to millimetres.

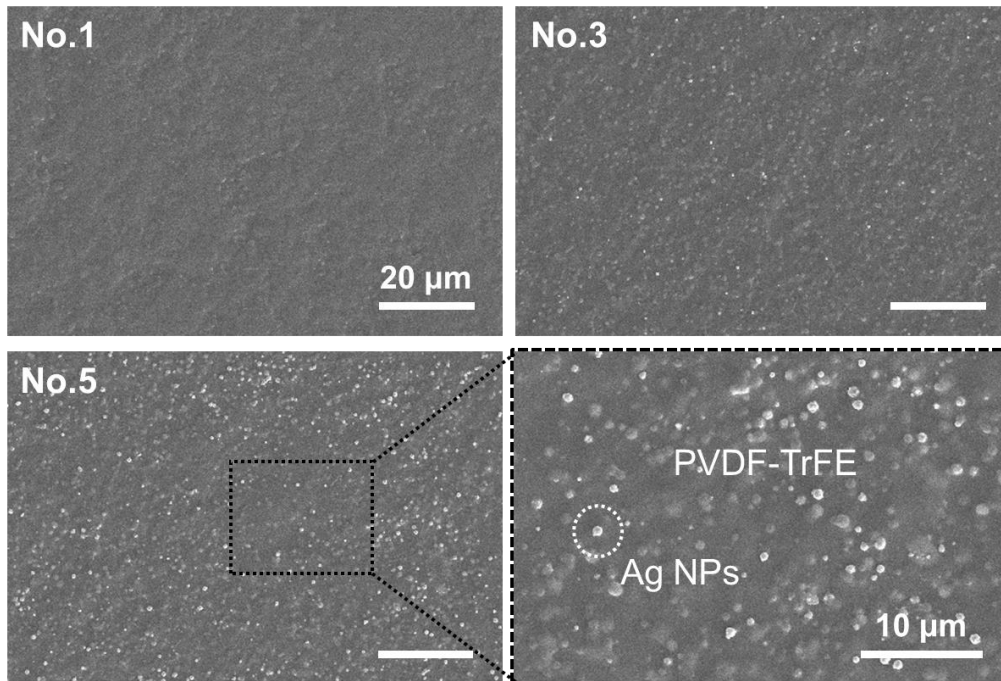


Fig. 8-7 SEM images of aerosol-jet printed film-typed P(VDF-TrFE)/Ag nanoparticle nanocomposite. The film was prepared by overwrapping lines side by side.

### 8.3 Dielectric properties of multi-layered nanocomposite

The dielectric constants of the single-layered aerosol-jet printed P(VDF-TrFE)/Ag nanoparticle nanocomposite with various nanoparticle concentration were measured at room temperature using an impedance analyser. The dielectric constant ( $\epsilon'$ ) of the nanocomposite is almost constant in the ranges from  $10^2$  to  $10^3$  Hz and gradually decrease with increasing scan frequency (Fig. 8-8a). The 100 % P(VDF-TrFE) sample shows  $\epsilon'$  of 14 and loss tangent of 0.02 at 1kHz. In the case of nanocomposite sample No. 2, 2-fold increase of average  $\epsilon'$  value (28) was observed with similar level of tangent loss (Fig. 8-8b). It must be noted that the differences in variation of  $\epsilon'$  as a function of frequency measured at six different positions with active area of  $\sim 0.1 \text{ mm}^2$  is significantly small compared to that of nanocomposites fabricated by other methods (Fig. 8-8, inset).[65], [66] This indicates that the aerosol-jet printing technique enables not only excellent dispersion, but also uniform distribution of nanoparticles in the polymer matrix (Fig. 2-12). Although the average  $\epsilon'$  value gradually increased with increasing UA flow rate, the fluctuation of loss

tangent at low-frequency range become severe from sample No. 4 (Fig. 8-8d). The overall variation of average  $\epsilon'$  is similar to conventional nanocomposite, but the size of our error bars is much smaller than others (Fig. 8-8e). Above a certain amount of Ag nanoparticles corresponding to UA flow rate of 1.75 sccm, the average  $\epsilon'$  value and loss tangent both exponentially increase, indicating that an electrical current path has been produced above the percolation threshold.

Although the  $\epsilon'$  value of P(VDF-TrFE) can be enhanced by adding Ag nanoparticles from 14 to 42 with relatively low loss tangent (Fig. 8-8a, b), further improvement in  $\epsilon'$  is accompanied by high loss tangent and lower breakdown strength (Fig. 8-8c, d). To increase the  $\epsilon'$  and breakdown strength simultaneously, we fabricated multi-layered nanocomposites. As shown in Fig. 8-9a, two different combinations of multi-layered nanocomposites were prepared with a reference 100 % P(VDF-TrFE) polymer dielectric. In the case of multi-layered nanocomposite (A), nanocomposite sample No. 7 with high dielectric constant and high loss tangent was inserted in the middle of P(VDF-TrFE) layers with low dielectric constant and low loss tangent. Then the P(VDF-TrFE) layers were replaced by nanocomposite sample No. 2 in multi-layered nanocomposite (B). As a result, the multi-layered nanocomposite (A) and (B) show  $\epsilon'$  of  $\sim 74$  and  $\sim 220$  at 1 kHz scan frequency with similar level of low loss tangent as pure P(VDF-TrFE) sample, respectively (Fig. 8-9b, c). These values are 5-times and 16-times higher than  $\epsilon'$  of P(VDF-TrFE), and the corresponding low loss tangent values cannot be achieved in single layer nanocomposite. In addition, despite P(VDF-TrFE) being a thermoplastic polymer, multi-layered nanocomposite structures can be realised via 4 wt % P(VDF-TrFE) solution without cross-linking agent spanning thickness scales from nanometres to millimetres. Lastly, the combination of layered structures and types of materials can be freely changed depending on the target applications. These indicate that aerosol-jet printing technique enhanced the processing window of multi-layered nanocomposites considerably.

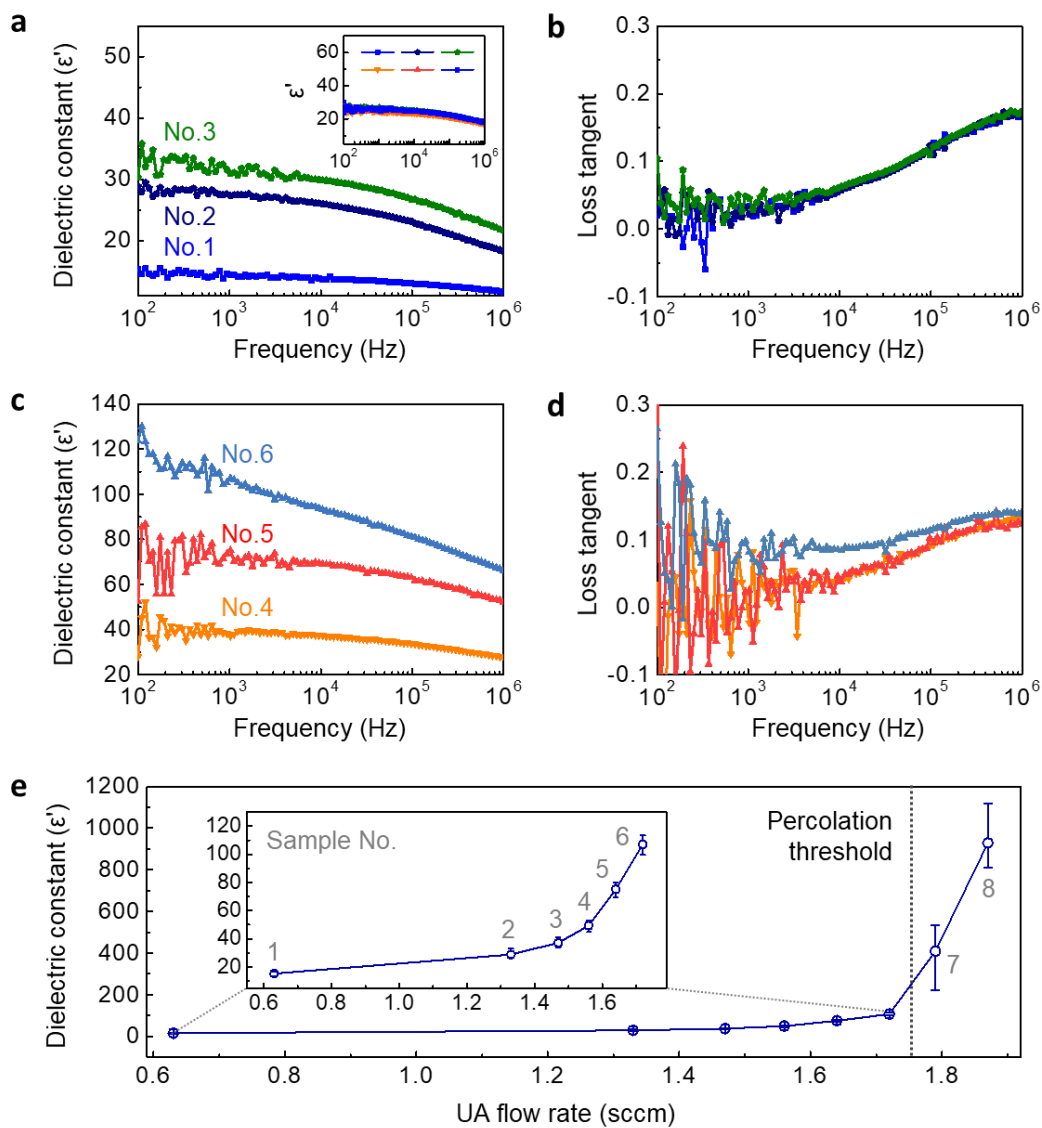


Fig. 8-8 Room temperature dielectric properties of P(VDF-TrFE)/Ag nanoparticles nanocomposite. (a, c) Dielectric constant and (b,d) loss tangent of nanocomposite with various Ag concentration as a function of scan frequency. Inset in (a) indicates the variation in dielectric constant measuring at six different positions in the sample No.2. (e) Average dielectric constant of nanocomposite as a function of the UA flow rate measured at 1 kHz.

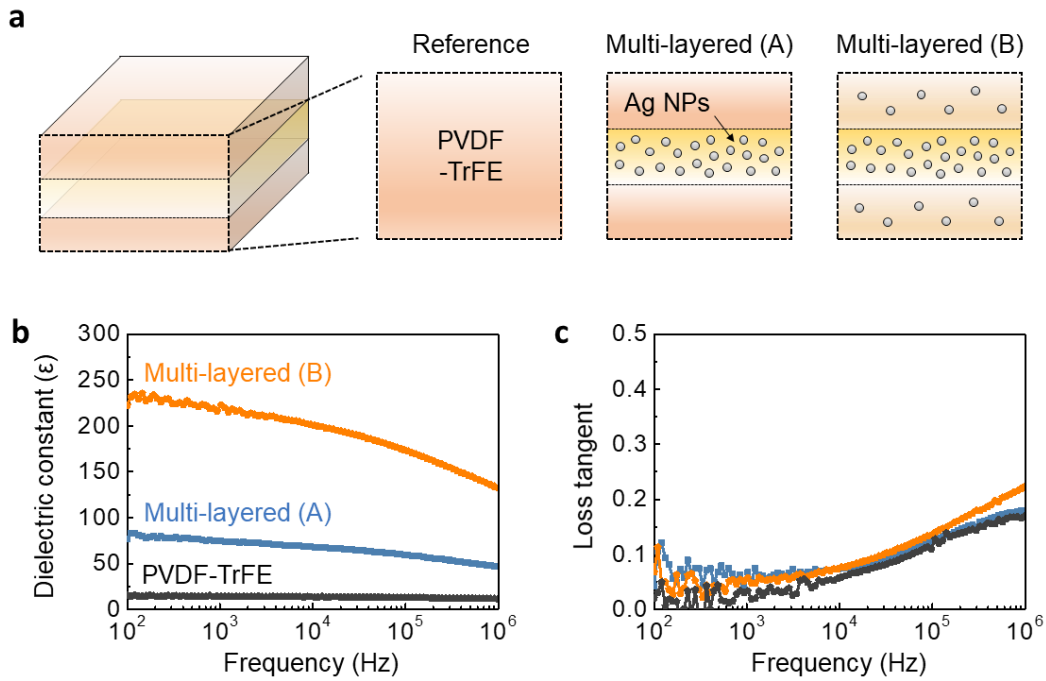


Fig. 8-9 Design and properties of multi-layered P(VDF-TrFE)/Ag nanoparticles nanocomposite. (a) Schematics of nanocomposite design for two different multi-layered structures and reference 100 % P(VDF-TrFE) sample. (b) Dielectric constant and (c) loss tangent of nanocomposite as a function of scan frequency.

## 8.4 Multi-layered nanocomposite-based triboelectric generator

The multi-layered nanocomposite-based triboelectric generator devices tested in this section were all preliminary attempts to show the influence of nanoparticles on device performance. To develop a contact-separation mode triboelectric generator, we deposited P(VDF-TrFE)/Ag nanocomposite with various Ag concentration by aerosol-jet printing technique on polyethylene terephthalate (PET) charge storage layer (Fig. 8-10a). An Al film was prepared as a counterpart triboelectric material. Fig. 8-10b shows the short circuit current ( $I_{SC}$ ) measured in response to the periodic impacting at a frequency of 5 Hz and amplitude of 0.5 mm in an energy harvesting setup that has been previously described (Chapter 3.2.3). The 100% P(VDF-TrFE)-based triboelectric generator showed a peak  $I_{SC}$  of  $\sim 10.5 \mu\text{A}$ . Due to the improved  $\epsilon'$  by adding Ag nanoparticles, higher  $I_{SC}$  was observed from P(VDF-TrFE)/Ag nanocomposite sample No. 2 than from the 100% P(VDF-TrFE)-based generator. However, although the  $\epsilon'$  increased with increasing sample numbers due

to the processing condition, the output  $I_{SC}$  of device was formed to decrease linearly with sample number. This may possibly be due to the exposure of Ag nanoparticles on the contact surface. During the contact electrification process, Ag nanoparticles on the surface may reduce the amount of triboelectric charge because the direct pairing of Ag nanoparticles and Al film gives rise to much smaller charge transfer compared to the pairing of P(VDF-TrFE) and Al film. Therefore, it was difficult to conclude the accurate influence of the nanoparticles themselves due to interrelationship among many variables, and a limited number of working devices.

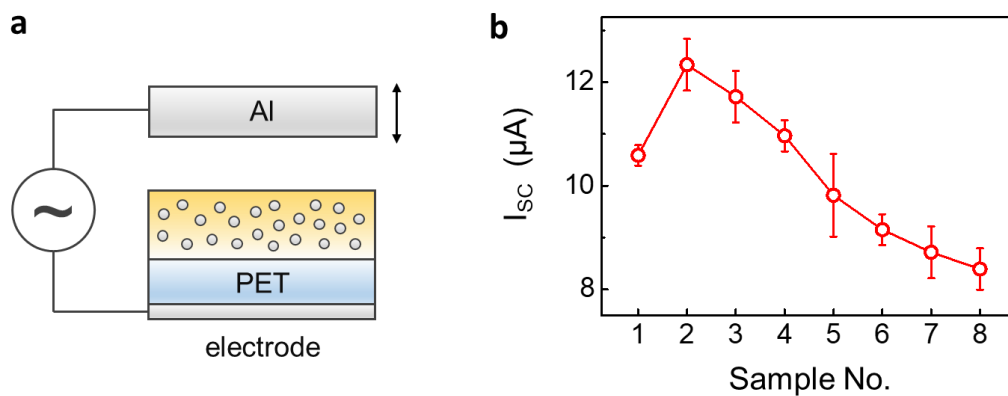


Fig. 8-10 Aerosol-jet printed nanocomposite-based triboelectric generator. (a) Schematic for triboelectric generator setup. PET and Al were introduced as a charge storage layer and counter electrode, respectively. (b)  $I_{SC}$  of each sample with different Ag concentrations.

## 8.5 Conclusions

In this chapter, we demonstrate that multi-layered nanocomposites, with an unlimited selection of polymers and ideal dispersion of nano-insertions, can be easily fabricated by a novel aerosol-jet printing technique. The ideal dispersion of nanomaterials in polymer matrix is achieved via independent atomization and confirmed by SEM-based image analysis. Due to the unique deposition which does not require pre-mixing, aerosol-jet printing technique enables the nanocomposites with various combinations of materials without adding additional process surfactant. With increasing UA flow rate corresponding to the amount of Ag nanoparticles, the average dielectric constant gradually increased similar to the trend seen in conventional nanocomposite, but the size of error bar in our

measurements is much smaller due to the uniform distribution of nanoparticles. Multi-layered thermoplastic polymer-based nanocomposites were accomplished without a cross-linking agent, resulting in high dielectric constant with low loss tangent. Preliminary single-layered nanocomposite-based triboelectric energy harvesting measurements showed that there is an improvement of output performance compared to a neat polymer-based device, but further tests are required before arriving at any conclusions about these devices.

## Chapter 9

# Conclusions and Future Work

In this thesis, we have developed novel functional polymeric nanomaterials, including nanowires and nanocomposites, for application in energy harvesting devices. First, template-wetting method has been adopted and modified to realise polymer nanowires, with a view to improve scalability and performance. Because the functional properties of ferroelectric polymers can be improved at the nanoscale, and vary depending on crystal structure, the nanowire growth methods and appropriate crystallisation mechanisms for various crystal structures are central to the work reported in this thesis. The focus is on Nylon-11 in particular, as its ferroelectric properties and hydrogen bonding are well-suited for both robust piezoelectric and triboelectric energy harvesting. Subsequently, advanced aerosol-jet printing technique is presented for realisation of multi-layered polymer-based nanocomposites. Although polymer-based nanocomposites and multi-layered structures have already been suggested separately to improve the performance of triboelectric energy harvesting devices, poor dispersion of nano-insertions in polymer matrices and limited variety of available polymers are still challenging. Therefore, optimum processing conditions for a novel non-mixable dual aerosol-jet printing technique and image analysis to measure the degree of nanoparticle dispersion are

demonstrated. The dielectric properties and energy harvesting capability of these nanocomposites are also investigated.

In Chapter 4, high-quality vertically aligned Nylon-11 nanowire arrays were fabricated via a template-wetting method for the first time. These nanowires were shown to exhibit self-polarization by exploiting the nanoconfinement effect, rendering them attractive for use in low-cost and simple energy generator designs as they require minimal post-processing steps. The measured thermal response indicated that such Nylon-11 nanowires might be useful in high-temperature piezoelectric applications as compared to other polymers such as PVDF and P(VDF-TrFE). High energy conversion efficiency with stable operation over 15 hr of continuous impacting was observed from a nano-piezoelectric generator based on the as-grown template-grown Nylon-11 nanowire arrays.

In Chapter 5, to further enhance the energy harvesting capability of Nylon-11 nanowires, a novel and facile gas-flow assisted nano-template (GANT) infiltration method was proposed. The fast crystallisation conditions resulting from the GANT method not only leads to self-polarization of the ferroelectric  $\delta'$ -phase nanowires but also increased average crystallinity of up to  $\sim 40\%$ . This evaporation-driven crystallisation mechanism was verified using finite element analysis. As a tribo-positive material, the self-poled Nylon-11 nanowires combined with counterpart tribo-negative Teflon surfaces showed  $\sim 6$  times and  $\sim 10$  times higher output power than those of melt-quenched Nylon-11 film and Al-based triboelectric device, respectively.

In Chapter 6, thermodynamically stable  $\alpha$ -phase Nylon-11 nanowires were investigated. Notably, definitive dipole alignment of  $\alpha$ -phase nanowires was shown to have been achieved for the first time via a novel thermally assisted nano-template infiltration (TANI) method, resulting in exceptionally strong and thermally stable spontaneous polarization, as confirmed by molecular structure simulations. The intensity and thermal stability of spontaneous polarization were indirectly investigated by the changes of surface potential in KPFM measurements. We also introduced the resulting nanowires into triboelectric generators to prove that non-ferroelectric  $\alpha$ -phase nanowires with higher surface potential outperform ferroelectric  $\delta'$ -phase nanowires. As a result, the output power density of an  $\alpha$ -phase nanowire-based device was shown to be enhanced by 340 % compared to a  $\delta'$ -phase nanowire-based device under the same mechanical excitation.

Consequently, we have verified that, due to the ordered crystal structures and higher molecular packing density, the net dipole moment of self-poled ‘non-ferroelectric’  $\alpha$ -phase Nylon-11 can be much higher than that of self-poled ‘ferroelectric’  $\delta'$ -phase. Furthermore, the strong hydrogen-bonding (which has previously been considered as a serious disadvantage for the polarization of Nylon-11) actually served to enhance the stability of the molecular structure, resulting in a constant spontaneous polarization up to near the melting temperature.

In Chapter 7, the crystallisation mechanism of Nylon-11 nanowire in template-wetting method was discussed in more detail. Based on the typical temperature-driven crystallisation and gravity-infiltration template-wetting, the potential of evaporation-driven crystallisation and capillary infiltration template-wetting method was presented. In addition, the crystallisation mechanism of three different template-wetting methods; conventional template wetting, GANT and TANI methods, was defined. XRD analysis confirmed that all the resulting nanowires had preferential crystal orientation, and  $\alpha$ -phase nanowire had the largest size of crystals with thermodynamically stable crystal structures. Thermal behaviour showed that homogeneous nucleation and complete wetting occurred during the crystallisation *within* 200 nm nanopores of the templates used. The nanoscale electromechanical characteristics showed that the  $\alpha$ -phase nanowires showed the highest Young’s modulus but did not exhibit significant piezoelectric behaviour. In contrast, a distinct piezoelectric response was achieved from the relatively soft  $\delta'$ -phase nanowires. Additionally, compared to the properties of films with the same crystal structure, the modulus of  $\alpha$ -phase nanowires and the piezoelectric response of  $\delta'$ -phase nanowires was larger. These results suggest that the nanoconfinement effect led to enhancement of the electromechanical properties of each crystal structure based on molecular level optimisation.

In Chapter 8, multi-layered nanocomposites were fabricated via modified aerosol-jet printing technique. The ideal dispersion of nanomaterials in polymer matrix was achieved via independent atomization and confirmed by SEM-based image analysis. Due to the non-mixable process, nanocomposites with various combinations of materials were enabled without additional processing or surfactant. The aerosol-jet printed nanocomposite showed a similar but more reliable relationship between dielectric constant and the number

of Ag nanoparticles compared to that of conventional nanocomposites in the literature. This result indicates that nanoparticles were uniformly distributed in polymer matrix. Stacking of thermoplastic polymer-based nanocomposites were accomplished without cross-linking agent, resulting in high dielectric constant with low loss tangent. Preliminary single-layered nanocomposite-based triboelectric energy harvesting measurement showed that there was an improvement of output performance compared to a neat polymer-based device, but further tests are required before arriving at any conclusions about the devices.

In terms of developed nanowire fabrication methods, all techniques can be applied to other functional polymeric materials, while exploiting the benefits of nanoconfinement. In particular, investigating the crystal structures and piezoelectric (and ferroelectric) properties of PVDF nanowires would be an interesting topic.

It would be also interesting to demonstrate the difference between melt-quenched  $\delta'$ -phase film and GANT fabricated  $\delta'$ -phase nanowires in terms of molecular configuration and piezoelectricity. This would provide information about the origin of piezoelectricity in ferroelectric polymers.[237] In other words, contribution of amorphous and crystalline region to the piezoelectric response could be investigated in more detail using these samples. As characterisation tools, Transmission Electron Microscopy (TEM) with Selected Area Electron Diffraction (SAED) and Small Angle X-ray Scattering (SAXS) could be used to reveal the properties of crystalline region and the crystal structure, respectively.

From an energy harvesting application perspective,  $\delta'$ -phase nanowires grown by GANT method would be a candidate for nano-piezoelectric energy harvesting devices because of its high piezoelectricity. The freestanding nanowire on a conducting grid and PFM characterization method would reveal the transverse piezoelectric expansion of  $\delta'$ -phase nanowires. Furthermore, thermal behaviour of  $\delta'$ -phase nanowires would be an interesting topic to explore because  $\delta'$ -phase nanowires show different crystal structure transition compared to conventional  $\delta'$ -phase film. This would provide information about the  $\delta$ -phase Nylon-11.

In terms of polymer crystallisation in nanopores, there have been reports regarding the relationship between the size of nanopores template and resulting crystal structure of polymer nanostructures (Chapter 2.6.4). Therefore, investigating the pore size effect in the

novel template-wetting processes developed here, including GANT and TANI methods, might be an interesting route to demonstrate more accurate polymer crystallization mechanism in the nanostructures.

The dual aerosol-jet printing technique would be applied to other applications, such as energy storage devices. In particular, the output performance of supercapacitors and battery devices would be enhanced by the excellent dispersion and uniform distribution of nano-insertions. Furthermore, all-in-one energy device with energy harvesting and storage could also be realised via aerosol-jet printing technique.

# Appendix A

## Authors' Contribution & Copyright Permission

### A.1 Authors' contribution

[1] Wang, T.; Farajollahi, M.; Choi, Y. S.; Lin, I.; Marshall, J. E.; Thompson, N. M.; Kar-Narayan S.; Madden, J. D. W.; Smoukov, S. K. "Electroactive Polymers for Sensing," *Interface Focus* 2016, 20160026.

: T.W., M.F., Y.S.C., I.T.L., J.E.M. and N.M.T. wrote the manuscript with input from all the authors. S.K.S., J.D.W.M., S.K.N. and T.W. conceived the initial goal of the review, with the final goal determined by all the authors. S.K.S., J.D.W.M. and S.K.N. supervised the review construction. M.F. and T.W. reviewed the ionic EAPs part; Y.S.C., I.T.L., J.E.M. and N.M.T. contributed the electronic EAPs part. All authors gave final approval for publication.

[2] Choi, Y. S.; Jing, Q.; Datta, A.; Boughey, C.; Kar-Narayan S. "A Triboelectric Generator Based on Self-poled Nylon-11 Nanowires Fabricated by Gas-flow Assisted Template Wetting," *Energy and Environmental Science* 2017, 10, 2180.

: Y.S.C. fabricated the materials and devices and carried out the experimental work and computational modelling. S.K.-N. designed and guided the experimental work. A.D. provided guidance on the fabrication aspects while Q.J. provided guidance on the modelling aspects of the paper as well as device design. C.B. helped with the energy harvesting measurements. Y.S.C. and S.K.-N. co-wrote the paper.

[3] Smith, M.; Choi, Y. S.; Boughey, C.; Kar-Narayan S. "Controlling and Assessing the Quality of Aerosol Jet Printed Features for Large Area and Flexible Electronics," *Flexible and Printed Electronics* 2017, 2, 015004.

: M.S., Y.S.C., and B.C. fabricated the samples and performed the measurements reported. S.K.-N. designed and guided the experimental work. M.S., Y.S.C., B.C. and S.K.-N. cowrote the paper.

[208] Datta, A.; Choi, Y. S.; Chalmers, E.; Ou, C.; Kar-Narayan S. “Piezoelectric Nylon-11 Nanowire Arrays Grown by Template Wetting for Vibrational Energy Harvesting Applications,” *Advanced Functional Materials* 2017, 27, 1604262.

: A.D., Y.S.C., and E.C. fabricated the samples and A.D., Y.S.C., E.C., and C.O. performed the measurements reported. A.D. and S.K.-N. designed and guided the experimental work. A.D., Y.S.C., and S.K.-N. cowrote the paper.

[186] Choi, Y. S.; Kim, S. K.; Williams, F.; Calahorra, Y.; Elliot, J. A.; Kar-Narayan S. “The Effect of Crystal Structure on the Electromechanical Properties of Piezoelectric Nylon-11 Nanowires,” *Chemical Communications* 2018, 54, 5863.

: Y.S.C. fabricated the materials and carried out the experimental work and computational modelling. S.K.-N. designed and guided the experimental work. J.A.E. and C.F. provided guidance on the modelling aspects of the paper. F.W. helped with the material fabrication and modelling. S.K.K. helped with the AFM measurements. Y.S.C. and S.K.-N. co-wrote the paper. All authors discussed the results and commented on the paper.

## **A.2 Copyright permission**

### 1) University guideline

Candidates for the PhD by Special Regulations and, with the approval of the relevant Degree Committee, candidates for the PhD (by general regulations) may submit a dissertation consisting of a number of previously published papers. In these cases, the dissertation must also contain a substantial introductory summary statement summarising rationale; placing the work in the context of the wider field of study; clarifying the extent to which works represent a consistent body of research, and the original contribution to knowledge they make; and providing clear detail on the exact contribution of the student to each included paper. It would not be necessary for any published work to be re-written prior to inclusion in a dissertation. The amount of published material to include is up to each candidate, however with the exception of candidates for the PhD by Special Regulations the included publications must refer to research carried out as part of a candidate’s degree.

2) Permission to include material written by this author where copyright has been assigned to a publisher.

- Ref [2] and [186]

(<http://www.rsc.org/journals-books-databases/journal-authors-reviewers/licences-copyright-permissions/#deposition-sharing>)

Author reusing their own work published by the Royal Society of Chemistry

You do not need to request permission to reuse your own figures, diagrams, etc, that were originally published in a Royal Society of Chemistry publication. However, permission should be requested for the use of the whole article or chapter except if reusing it in a thesis. If you are including an article or book chapter published by us in your thesis please ensure that your co-authors are aware of this.

Reuse of material that was published originally by the Royal Society of Chemistry must be accompanied by the appropriate acknowledgement of the publication. The form of the acknowledgement is dependent on the journal in which it was published originally, as detailed in 'Acknowledgements'.

- Ref [3]

(<https://publishingsupport.iopscience.iop.org/permissions-faqs/>)

Upon transfer of copyright, IOP and/or the copyright owner grants back to authors a number of rights. These include the right to include the Final Published Version of the article in your research thesis or dissertation. Please include citation details and, for online use, a link to the Version of Record. IOP's permission will be required for commercial use of an article published as part of your thesis. IOP does not allow ProQuest to publish or sell the article as part of your dissertation.

- Ref [1]

Subject: FW: [Request] permission to include published work within my thesis  
Date: 2018-06-13 15:58  
From: Publishing <publishing@royalsociety.org>  
To: "yc394@cam.ac.uk" <yc394@cam.ac.uk>

Hello

Yes that will be absolutely fine.

Kind regards,

Debbie

-----Original Message-----

From: Y. Choi [mailto:yc394@cam.ac.uk]

Sent: 06 June 2018 20:09

To: Publishing <publishing@royalsociety.org>

Subject: [Request] permission to include published work within my thesis

To whom it may concern,

I am the author of the following work published by The Royal Society Publishing:

[Wang T, Farajollahi M, Choi YS, Lin I-T, Marshall JE, Thompson NM, Kar-Narayan S, Madden JDW, Smoukov SK. 2016 Electroactive polymers for sensing. Interface Focus 6: 20160026. <http://dx.doi.org/10.1098/rsfs.2016.0026>] [1]

I wish to include this work within the electronic version of my thesis, which I am required to deposit in University of Cambridge's online repository (<https://www.repository.cam.ac.uk/>). The repository is non-commercial and openly available to all.

I would be grateful if you could advise if this will be acceptable.

Thank you for your time and attention.

Sincerely,  
Yeonsik

--  
Yeonsik Choi

PhD student  
Department of Materials Science & Metallurgy University of Cambridge  
27 Charles Babbage Road  
Cambridge CB3 0FS  
UK.

This email is sent on behalf of The Royal Society, 6-9 Carlton House Terrace, London SW1Y 5AG, United Kingdom. The contents of this email and any attachments are intended for the confidential use of the named recipient(s) only. They may be legally privileged and should not be communicated to or relied upon by any person without our express written consent. If you are not an addressee (or you have received this mail in error) please notify us immediately by email to: [it.admin@royalsociety.org](mailto:it.admin@royalsociety.org), and confirm the deletion of this email and attachments immediately. You should carry out your own virus check before opening any attachment. The Royal Society accepts no liability for any loss or damage which may be caused by software viruses or interception or interruption of this email. Please see our privacy policy [2] for details of how any personal data we collect from you, or that you provide to us, will be processed by us.

Registered charity no. 207043

The views or opinions are solely those of the author of this email, and do not represent those of The Royal Society unless specifically stated.

- Ref [208]

**JOHN WILEY AND SONS LICENSE  
TERMS AND CONDITIONS**

Jun 06, 2018

---

This Agreement between Mr. Yeonsik Choi ("You") and John Wiley and Sons ("John Wiley and Sons") consists of your license details and the terms and conditions provided by John Wiley and Sons and Copyright Clearance Center.

License Number	4363220671707
License date	Jun 06, 2018
Licensed Content Publisher	John Wiley and Sons
Licensed Content Publication	Advanced Functional Materials
Licensed Content Title	Piezoelectric Nylon-11 Nanowire Arrays Grown by Template Wetting for Vibrational Energy Harvesting Applications
Licensed Content Author	Anuja Datta, Yeon Sik Choi, Evie Chalmers, et al
Licensed Content Date	Nov 11, 2016
Licensed Content Volume	27
Licensed Content Issue	2
Licensed Content Pages	10
Type of use	Dissertation/Thesis
Requestor type	Author of this Wiley article
Format	Electronic
Portion	Full article
Will you be translating?	No
Title of your thesis / dissertation	Novel Functional Polymeric Nanomaterials for Energy Harvesting Application
Expected completion date	Oct 2018
Expected size (number of pages)	150
Requestor Location	Mr. Yeonsik Choi D16, Forster Court, 7 Charles Babbage Road,  Cambridge, UK CB3 0FY United Kingdom Attn: Mr. Yeonsik Choi
Publisher Tax ID	EU826007151
Total	0.00 GBP
Terms and Conditions	

**TERMS AND CONDITIONS**

This copyrighted material is owned by or exclusively licensed to John Wiley & Sons, Inc. or one of its group companies (each a "Wiley Company") or handled on behalf of a society with which a Wiley Company has exclusive publishing rights in relation to a particular work (collectively "WILEY"). By clicking "accept" in connection with completing this licensing transaction, you agree that the following terms and conditions apply to this transaction (along with the billing and payment terms and conditions established by the Copyright Clearance Center Inc., ("CCC's Billing and Payment terms and conditions"), at the time that you opened your RightsLink account (these are available at any time at <http://myaccount.copyright.com>).

# Appendix B

## Supporting information

### B.1 Gaussian theorem

#### 1) Definition of the charge

A “Charge” can be defined as the physical property of matter that causes it to experience a force when placed in an electromagnetic field (Fig. B1-1). In other words, positive charge (charge1) creates the electric field ( $\vec{E}$ ) and another charge (charge 2) in such electric field can feel the force ( $\vec{F}_e$ ).

$$\vec{F}_e = \vec{E} Q_2$$

where  $Q_2$  is the quantity of the electric charge of charge 2.

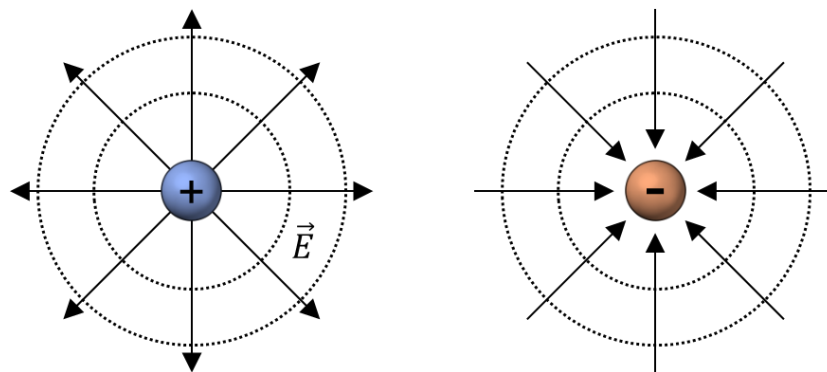


Fig. B1-1. Schematics for positive and negative charge and corresponding electric field.

#### 2) Gaussian theorem in parallel plate model

Gaussian theorem is then defined by

$$D = \varepsilon E$$

for homogeneous, isotropic, nondispersive and liner material, where  $\varepsilon$  is the permittivity. If we assume that charge are place on the infinite plate, the direction of  $\vec{E}$  of charge in the plate is perpendicular to the plate. Since  $D$  is ( $Q / \text{surface area of plate}$ ) in parallel plate model,  $E$  is expressed by

$$E = \frac{Q}{A \varepsilon} = \frac{\sigma A}{A \varepsilon} = \frac{\sigma}{\varepsilon}$$

where  $\sigma$  is the surface charge density, and  $A$  is the surface area of plate.

## B.2 Piezoelectric generator performance

1) In short-circuit condition, where  $V = 0$  and  $E$  is constant, the Eq. (2-3) become

$$D = dT$$

where  $D = Q_{\text{free}}/\text{Area}$  for parallel plate capacitor, and  $T = \text{Force} / \text{Area}$ . Therefore,

$$\frac{Q}{A} = d \frac{F}{A}$$

where  $Q$  is the free charges on the surface,  $A$  the surface area, and  $F$  the force. Considering the shape of the material in Fig. 2-2a, in 33 mode (i.e. parallel expansion),

$$\frac{Q}{ab} = d_{33} \frac{F}{ab}$$

$$Q = d_{33} F$$

In 31 mode (i.e. transverse expansion) in Fig. 2-2b,

$$\frac{Q}{ab} = d_{31} \frac{F}{bc}$$

$$Q = \frac{a}{c} d_{31} F$$

2) In the piezoelectric system,  $E$  is defined by

$$E = -gT + \beta^T D$$

In open-circuit condition, where  $Q = 0$  and  $D$  is constant, above equation become

$$E = -gT$$

The electric field ( $E$ ), which is the force per unit charge, can be defined by  $E = \text{Voltage} / \text{thickness of dielectric}$  for parallel plate capacitor because  $E \times \text{thickness}$  is required work moving a positive charge from the bottom of the dielectric material to the top surface, and it is a definition of voltage (V). Then,

$$\frac{V}{\text{thickness}} = g \frac{F}{A}$$

Considering the shape of the material in Fig. 2-2a, in 33 mode,

$$\frac{V}{c} = g_{33} \frac{F}{ab}$$

$$V = \frac{c}{ab} g_{33} F$$

In 31 mode (Fig. 2-2b),

$$\frac{V}{c} = g_{31} \frac{F}{bc}$$

$$V = \frac{1}{b} g_{31} F$$

### **B.3 Distance dependent electric-field model**

According to the Gaussian theorem, electric field ( $E$ ) can be derived as follows

$$D = \varepsilon E$$

$$\frac{Q}{A} = \varepsilon E$$

$$E = \frac{Q}{\epsilon A}$$

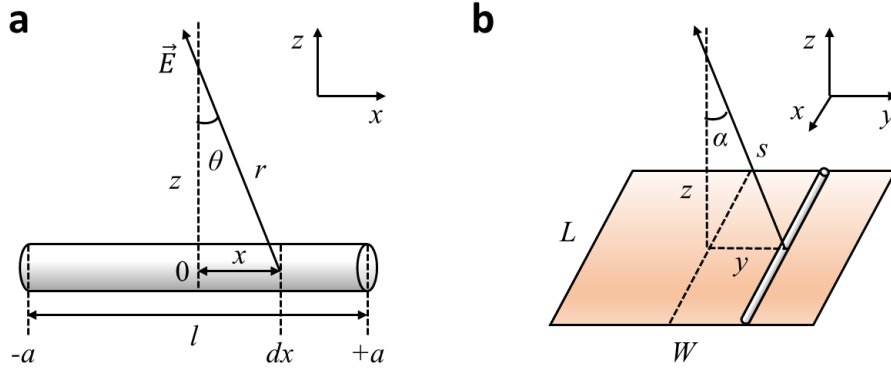


Fig. B3-1. Schematics for electric field calculation above the mid-point of a uniformly charged (a) line and (b) sheet. [40]

Considering a single charge is in the space (Fig. B3-1a),[40]

$$E = \frac{Q}{\epsilon A} = \frac{Q}{\epsilon (4\pi r^2)} = \frac{Q}{\epsilon 4\pi (z^2 + x^2)}$$

If the charge is on the line segment  $dx$ , the contribution to the electric field is described as

$$dE = \frac{\sigma dx}{4\pi\epsilon(z^2 + x^2)}$$

where  $\sigma$  is the charge density. The component of the electric field along  $z$  axis ( $dE_z$ ) is then given by

$$dE_z = dE \cos \theta = dE \frac{z}{r} = dE \frac{z}{\sqrt{z^2 + x^2}} = \frac{\sigma z}{4\pi\epsilon} \frac{dx}{(x^2 + z^2)^{3/2}}$$

The integration along the length of the line can be calculated by

$$E_z = \int_{-a}^a dE \cos \theta dx = \frac{\sigma z}{4\pi\epsilon} \left[ \frac{x}{z^2 \sqrt{x^2 + z^2}} \right]_{-a}^a = \frac{\sigma dx}{4\pi\epsilon z} \frac{l}{\left(\left(\frac{l}{2}\right)^2 + z^2\right)^{1/2}}$$

where  $l = 2a$ . Based on Fig. B3-1b,  $E_z$  can be extended to a uniformly charged plane, which is a collection of lines along y axis. The overall electric field above the midpoint along the z axis can be calculated by

$$E_{z,plane} = \iiint E_z \cos \alpha \, dx \, dy \, dz$$

## B.4 Crystal perfection index

A crystal perfection index (CPI) of the triclinic structure of Nylon-11 is defined by

$$CPI = \frac{\left(\frac{d_{200}}{d_{210/010}}\right) - 1}{\Omega} \quad (0-1)$$

where the factor  $\Omega$  is a constant.[89]

## B.5 Piezoelectric device – efficiency calculation

The way to calculate the device efficiency ( $\chi'$ ) and mechanical-to-electrical energy conversion efficiency ( $\chi$ ) are described in [18], [202] as follows:

$$\chi' = \frac{\text{output}}{\text{input}} = \frac{\text{electrical energy}}{\text{strain energy}}$$

$$\chi = \frac{\text{electrical work perfored by element}}{\text{net energy supplied to element}}$$

1) Electrical energy: It can be integrated from the resulted device *Power* under 10M $\Omega$  load resistance.

$$= \int IVdt \sim 0.907 \text{ nJ} = 9.07 \times 10^{-10} \text{ J (per one cycle)}$$

2) Strain energy

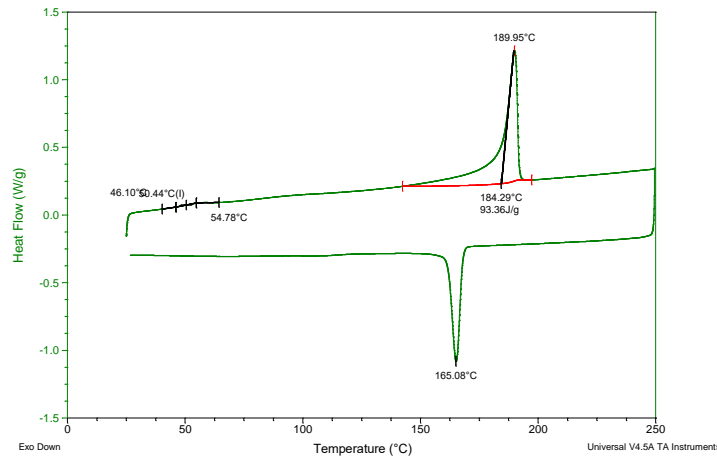
$$= \frac{1}{2} A L \varepsilon^2 E$$

where  $A$  is the effective working area,  $L$  the thickness of the device (i.e. length of the nanowires = 60  $\mu\text{m}$ ),  $\epsilon$  the dielectric permittivity, and  $E$  the Young's modulus ( $= 1.5 \text{ GPa} = 1.5 \times 10^9 \text{ N/m}^2$ ). Considering that strain ( $\epsilon$ ) and stress ( $\sigma$ ) are defined as  $\sigma/E$  and  $V_p/(g_{31} \cdot L)$  respectively, where  $V_p$  is the peak output voltage ( $= 0.95 \text{ V}$ ),  $g_{31}$  the piezoelectric voltage coefficient ( $= 50 \text{ mVm/N}$ ), the calculated  $\epsilon$  and  $\sigma$  are  $9.34 \times 10^{-5}$  and  $1.40 \times 10^5 \text{ N/m}^2$ , respectively. Considering the  $A$  of  $1.57 \times 10^{-4} \text{ m}^2$  for the AAO template with diameter of 2 cm and experimentally achieved  $\epsilon$  of 35.4 pF/m, strain energy of  $6.17 \times 10^{-8} \text{ J}$  (per one cycle) can be achieved.

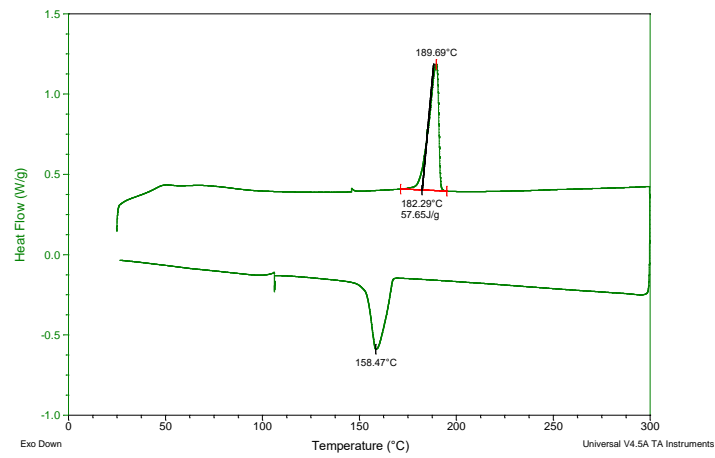
## B.6 DSC graphs – Nylon-11 samples

It must be noted that, in Fig. 7-11 and Fig. 7-12, the DSC graphs which has the closest value with the average  $T_m$  and  $T_c$  of more than 10 samples are given.

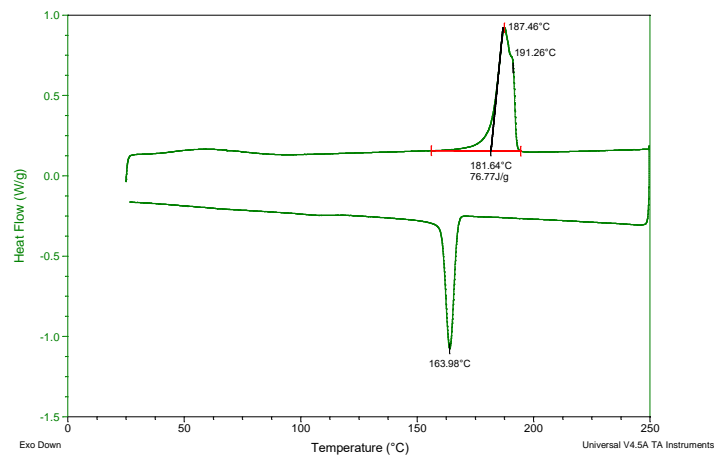
### 1) $\alpha$ -phase Film



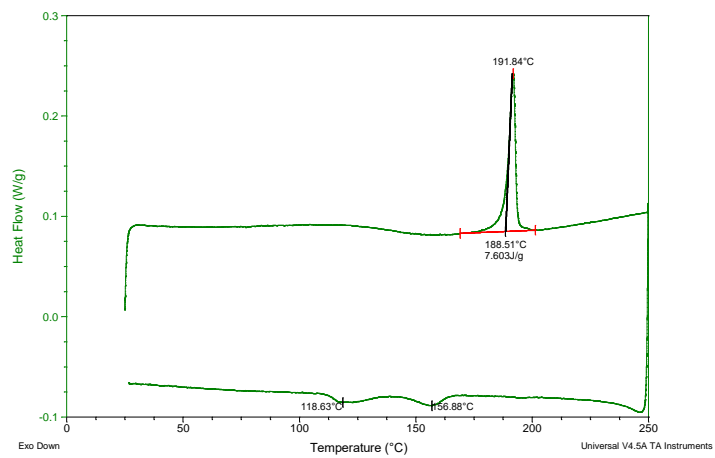
2)  $\delta'$ -phase film (melt-quenched)



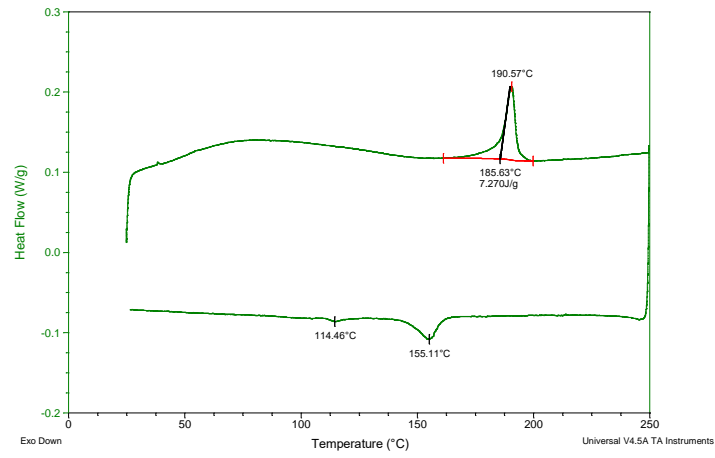
3)  $\delta'$ -phase film (solution processed)



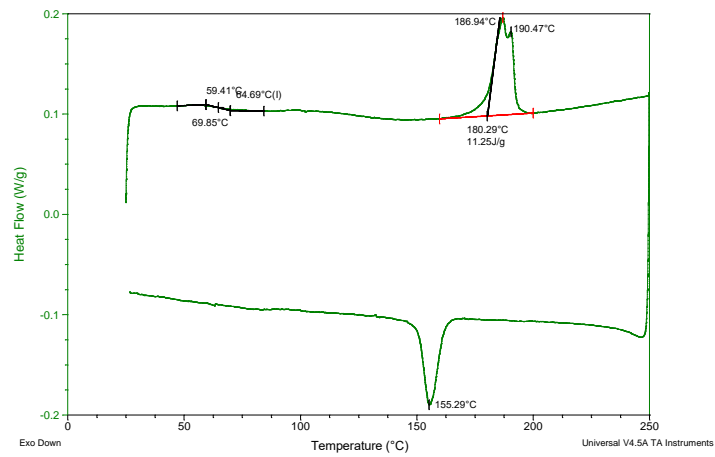
4) Nanowires fabricated by conventional template-wetting (*within* AAO)



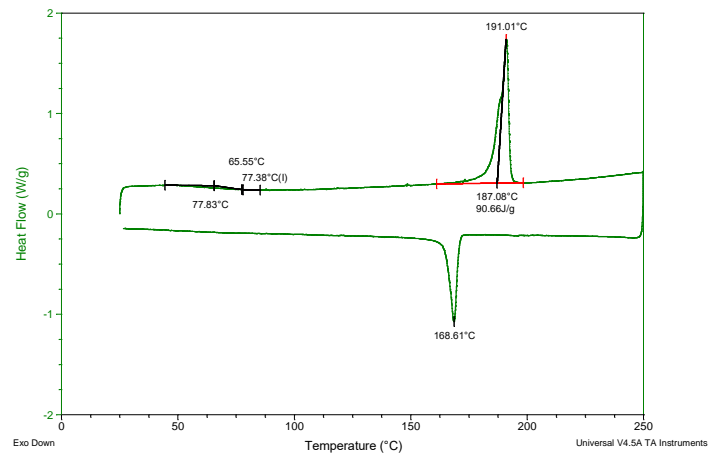
5)  $\alpha$ -phase nanowires (*within AAO*)



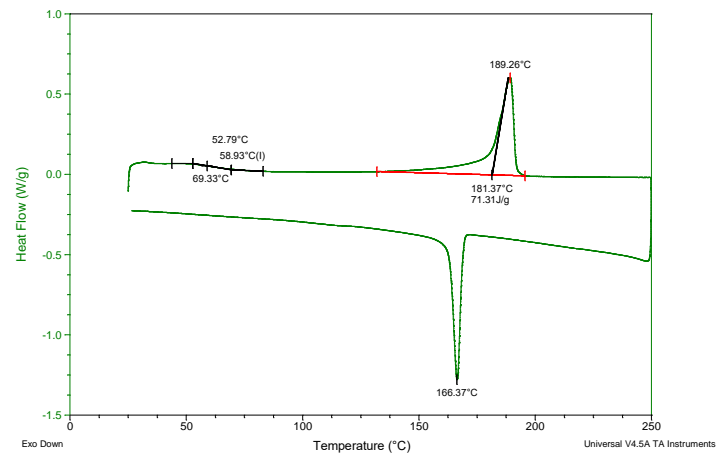
6)  $\delta'$ -phase nanowires (*within AAO*)



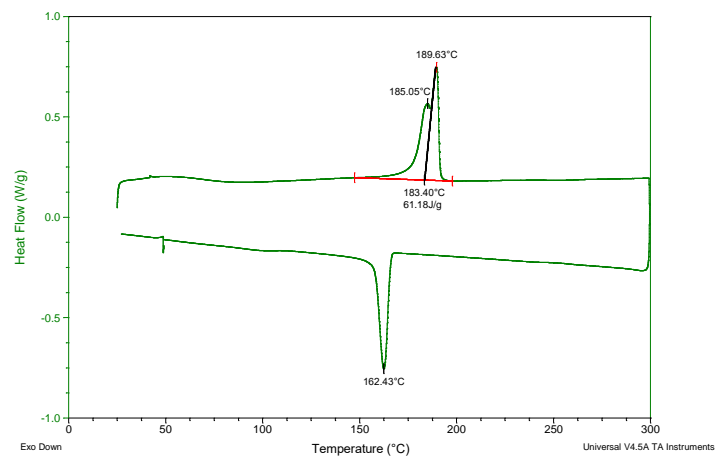
7) Nanowires fabricated by conventional template-wetting (*without AAO*)



8)  $\alpha$ -phase nanowires (*without* AAO)



9)  $\delta'$ -phase nanowires (*without* AAO)



# Bibliography

- [1] T. Wang *et al.*, “Electroactive polymers for sensing,” *Interface Focus*, vol. 6, pp. 1–19, 2016.
- [2] Y. S. Choi, Q. Jing, A. Datta, C. Boughey, and S. Kar-Narayan, “A triboelectric generator based on self-poled Nylon-11 nanowires fabricated by gas-flow assisted template wetting,” *Energy Environ. Sci.*, vol. 10, pp. 2180–2189, 2017.
- [3] M. Smith, Y. S. Choi, C. Boughey, and S. Kar-Narayan, “Controlling and assessing the quality of aerosol jet printed features for large area and flexible electronics,” *Flex. Print. Electron.*, vol. 2, p. 015004, 2017.
- [4] Y. S. Choi, “Nano-confined Polymer Materials for Energy Harvesting Devices,” University of Cambridge, Cambridge, 2016.
- [5] S. Katzir, “The Discovery of the Piezoelectric Effect,” *Arch. Hist. Exact Sci.*, vol. 57, no. 1, pp. 61–91, 2003.
- [6] S. Crossley, R. A. Whiter, and S. Kar-Narayan, “Polymer-based nanopiezoelectric generators for energy harvesting applications,” *Mater. Sci. Technol.*, vol. 30, pp. 1613–1624, 2014.
- [7] K.-F. Lei, Y.-Z. Hsieh, Y.-Y. Chiu, and M.-H. Wu, “The Structure Design of Piezoelectric Poly(vinylidene Fluoride) (PVDF) Polymer-Based Sensor Patch for the Respiration Monitoring under Dynamic Walking Conditions,” *Sensors*, vol. 15, no. 8, pp. 18801–18812, 2015.
- [8] Y. Tajitsu, “Sensing Complicated Motion of Human Body Using Piezoelectric Chiral Polymer Fiber,” *Ferroelectrics*, vol. 480, no. 1, pp. 32–38, 2015.
- [9] S. Trolier-McKinstry, “Crystal Chemistry of Piezoelectric Materials,” in *Piezoelectric and Acoustic Materials for Transducer Applications*, A. Safari and E. K. Akdougan, Eds. Boston, MA: Springer US, 2008, pp. 39–56.
- [10] J. S. Harrison and Z. Ounaies, “Piezoelectric Polymers,” *Encycl. Polym. Sci. Technol.*, vol. 3, 2001.
- [11] M. E. Lines and A. M. Glass, *Principles and Applications of Ferroelectrics and Related Materials*. Oxford: Oxford University Press, 2001.
- [12] Z. L. Wang, “Piezoelectric Nanogenerators Based on Zinc Oxide Nanowire Arrays,” *Science (80-. )*, vol. 312, no. 5771, pp. 242–246, 2006.
- [13] K. Il Park *et al.*, “Flexible nanocomposite generator made of BaTiO<sub>3</sub> nanoparticles and graphitic carbons,” *Adv. Mater.*, vol. 24, no. 22, pp. 2999–3004, 2012.
- [14] Y. Hu, L. Lin, Y. Zhang, and Z. L. Wang, “Replacing a battery by a nanogenerator with 20 V output,” *Adv. Mater.*, vol. 24, no. 1, pp. 110–114, 2012.

- [15] T. T. Pham *et al.*, “Reliable operation of a nanogenerator under ultraviolet light via engineering piezoelectric potential,” *Energy Environ. Sci.*, vol. 6, no. 3, pp. 841–846, 2013.
- [16] A. I. Kingon and S. Srinivasan, “Lead zirconate titanate thin films directly on copper electrodes for ferroelectric, dielectric and piezoelectric applications,” *Nat. Mater.*, vol. 4, no. 3, pp. 233–237, 2005.
- [17] J. M. Wu, C. Xu, Y. Zhang, and Z. L. Wang, “Lead-Free Nanogenerator Made from Single ZnSnO<sub>3</sub> Microbelt,” *ACS Nano*, vol. 6, no. 5, pp. 4335–4340, 2012.
- [18] S. Crossley and S. Kar-Narayan, “Energy harvesting performance of piezoelectric ceramic and polymer nanowires,” *Nanotechnology*, vol. 26, no. 34, p. 344001, 2015.
- [19] B. Lin and V. Giurgiutiu, “Modeling and testing of PZT and PVDF piezoelectric wafer active sensors,” *Smart Mater. Struct.*, vol. 15, no. 4, pp. 1085–1093, 2006.
- [20] C. R. Bowen, H. a. Kim, P. M. Weaver, and S. Dunn, “Piezoelectric and ferroelectric materials and structures for energy harvesting applications,” *Energy Environ. Sci.*, vol. 7, no. 1, pp. 25–44, 2014.
- [21] L. Seminara, M. Capurro, P. Cirillo, G. Cannata, and M. Valle, “Electromechanical characterization of piezoelectric PVDF polymer films for tactile sensors in robotics applications,” *Sensors Actuators, A Phys.*, vol. 169, no. 1, pp. 49–58, 2011.
- [22] Z. L. Wang, “Trielectrostatic Nanogenerators as New Energy Technology for Self-Powered Chemical Sensors,” *ACS Nano*, vol. 7, no. 11, pp. 9533–9557, 2013.
- [23] Z. L. Wang, J. Chen, and L. Lin, “Progress in triboelectric nanogenerators as a new energy technology and self-powered sensors,” *Energy Environ. Sci.*, vol. 8, no. 8, pp. 2250–2282, 2015.
- [24] S. Matsusaka, H. Maruyama, T. Matsuyama, and M. Ghadiri, “Trielectrostatic charging of powders: A review,” *Chem. Eng. Sci.*, vol. 65, no. 22, pp. 5781–5807, 2010.
- [25] R. G. Horn and D. T. Smith, “Contact Electrification and Adhesion Between Dissimilar Materials,” *Science (80-. )*, vol. 256, no. 5055, pp. 632–364, 1992.
- [26] R. G. Horn, D. T. Smith, and A. Grabbe, “Contact electrification induced by monolayer modification of a surface and relation to acid-base interactions,” *Nature*, vol. 366, no. 6454, pp. 442–443, 1993.
- [27] C. Liu and A. J. Bard, “Electrostatic electrochemistry at insulators,” *Nat. Mater.*, vol. 7, no. 6, pp. 505–509, 2008.
- [28] B. Baytekin, H. T. Baytekin, and B. A. Grzybowski, “What really drives chemical reactions on contact charged surfaces?,” *J. Am. Chem. Soc.*, vol. 134, no. 17, pp. 7223–7226, 2012.
- [29] M. Markevitch *et al.*, “Control of Surface Charges by Radicals as a Principle of Antistatic Polymers Protecting Electronic Circuitry,” *Science (80-. )*, vol. 341, pp. 1368–1371, 2013.

- [30] C. Xu *et al.*, “On the Electron-Transfer Mechanism in the Contact-Electrification Effect,” *Adv. Mater.*, p. 1706790, 2018.
- [31] L. S. McCarty and G. M. Whitesides, “Electrostatic charging due to separation of ions at interfaces: Contact electrification of ionic electrets,” *Angew. Chemie - Int. Ed.*, vol. 47, no. 12, pp. 2188–2207, 2008.
- [32] H. T. Baytekin, A. Z. Patashinski, M. Branicki, B. Baytekin, S. Soh, and B. A. Grzybowski, “The Mosaic of Surface Charge in Contact Electrification,” *Science (80-. )*, vol. 333, no. 6040, pp. 308–312, 2011.
- [33] J. Henniker, “Triboelectricity in Polymers,” *Nature*, vol. 196, p. 474, 1962.
- [34] Z. L. Wang, “Triboelectric nanogenerators as new energy technology for self-powered systems and as active mechanical and chemical sensors,” *ACS Nano*, vol. 7, no. 11, pp. 9533–9557, 2013.
- [35] S. Niu *et al.*, “Theoretical study of contact-mode triboelectric nanogenerators as an effective power source,” *Energy Environ. Sci.*, vol. 6, no. 12, p. 3576, 2013.
- [36] S. Wang, L. Lin, Y. Xie, Q. Jing, S. Niu, and Z. L. Wang, “Sliding-triboelectric nanogenerators based on in-plane charge-separation mechanism,” *Nano Lett.*, vol. 13, no. 5, pp. 2226–2233, 2013.
- [37] S. Niu *et al.*, “Theoretical Investigation and Structural Optimization of Single-Electrode Triboelectric Nanogenerators,” *Adv. Funct. Mater.*, vol. 24, pp. 3332–3340, 2014.
- [38] S. Niu *et al.*, “Theory of freestanding triboelectric -layer-based nanogenerators,” *Nano Energy*, vol. 12, pp. 760–774, 2015.
- [39] Y. Zi, S. Niu, J. Wang, Z. Wen, W. Tang, and Z. L. Wang, “Standards and figure-of-merits for quantifying the performance of triboelectric nanogenerators,” *Nat. Commun.*, no. May, p. 8376, 2015.
- [40] R. D. I. G. Dharmasena *et al.*, “Triboelectric nanogenerators: Providing a fundamental framework,” *Energy Environ. Sci.*, vol. 10, no. 8, pp. 1801–1811, 2017.
- [41] R. D. I. G. Dharmasena, K. D. G. I. Jayawardena, C. A. Mills, R. A. Dorey, and S. R. P. Silva, “A unified theoretical model for Triboelectric Nanogenerators,” *Nano Energy*, vol. 48, pp. 391–400, 2018.
- [42] J. Peng, S. D. Kang, and G. J. Snyder, “Optimization principles and the figure of merit for triboelectric generators,” *Sci. Adv.*, vol. 3, no. 12, pp. 1–7, 2017.
- [43] N. Cui *et al.*, “Dynamic Behavior of the Triboelectric Charges and Structural Optimization of the Friction Layer for a Triboelectric Nanogenerator,” *ACS Nano*, vol. 10, no. 6, pp. 6131–6138, 2016.
- [44] D. W. Kim, J. H. Lee, I. You, J. K. Kim, and U. Jeong, “Adding a stretchable deep-trap interlayer for high-performance stretchable triboelectric nanogenerators,” *Nano Energy*, vol. 50, pp. 192–200, 2018.
- [45] F. R. Fan, L. Lin, G. Zhu, W. Wu, R. Zhang, and Z. L. Wang, “Transparent

- triboelectric nanogenerators and self-powered pressure sensors based on micropatterned plastic films,” *Nano Lett.*, vol. 12, no. 6, pp. 3109–3114, 2012.
- [46] S. Wang, L. Lin, and Z. L. Wang, “Nanoscale triboelectric-effect-enabled energy conversion for sustainably powering portable electronics,” *Nano Lett.*, vol. 12, no. 12, pp. 6339–46, 2012.
- [47] G. Zhu *et al.*, “Triboelectric-generator-driven pulse electrodeposition for micropatterning,” *Nano Lett.*, vol. 12, no. 9, pp. 4960–4965, 2012.
- [48] C. K. Jeong *et al.*, “Topographically-Designed Triboelectric Nanogenerator via Block Copolymer Self-Assembly,” *Nano Lett.*, vol. 14, no. 12, pp. 7031–7038, 2014.
- [49] S. S. Kim, J. H. Lee, R. Hinchet, K. Kim, and S. Kim, “Shape memory polymer-based self-healing triboelectric nanogenerator,” *Energy Environ. Sci.*, vol. 8, pp. 3605–3613, 2015.
- [50] K. Y. Lee *et al.*, “Fully Packaged Self-Powered Triboelectric Pressure Sensor Using Hemispheres-Array,” *Adv. Energy Mater.*, vol. 6, no. 11, p. 1502566, 2016.
- [51] S. Wang *et al.*, “Maximum surface charge density for triboelectric nanogenerators achieved by ionized-air injection: Methodology and theoretical understanding,” *Adv. Mater.*, vol. 26, no. 39, pp. 6720–6728, 2014.
- [52] S. Shin, Y. H. Kwon, Y. Kim, J. Jung, M. H. Lee, and J. Nah, “Triboelectric Charging Sequence Induced by Surface Functionalization as a Method to Fabricate High Performance Triboelectric Generators,” *ACS Nano*, vol. 9, no. 4, pp. 4621–4627, 2015.
- [53] G. Song *et al.*, “Molecularly Engineered Surface Triboelectric Nanogenerator by Self-Assembled Monolayers (METS),” *Chem. Mater.*, vol. 27, pp. 4749–4755, 2015.
- [54] S. H. Shin *et al.*, “Formation of Triboelectric Series via Atomic-Level Surface Functionalization for Triboelectric Energy Harvesting,” *ACS Nano*, vol. 11, no. 6, pp. 6131–6138, 2017.
- [55] Y. Feng, Y. Zheng, S. Ma, and D. Wang, “High output polypropylene nanowire array triboelectric nanogenerator through surface structural control and chemical modification,” *Nano Energy*, vol. 19, pp. 48–57, 2016.
- [56] Y. H. Kwon, S.-H. Shin, J.-Y. Jung, and J. Nah, “Scalable and enhanced triboelectric output power generation by surface functionalized nanoimprint patterns,” *Nanotechnology*, vol. 27, no. 20, pp. 1–7, 2016.
- [57] H. Ryu *et al.*, “High-Performance Triboelectric Nanogenerators Based on Solid Polymer Electrolytes with Asymmetric Pairing of Ions,” *Adv. Energy Mater.*, vol. 7, no. 17, p. 1700289, 2017.
- [58] P. Bai *et al.*, “Dipole-moment-induced effect on contact electrification for triboelectric nanogenerators,” *Nano Res.*, vol. 7, no. 7, pp. 990–997, 2014.

- [59] J.-H. Lee *et al.*, “Control of Skin Potential by Triboelectrification with Ferroelectric Polymers,” *Adv. Mater.*, vol. 27, pp. 5553–5558, 2015.
- [60] K. Y. Lee *et al.*, “Controllable Charge Transfer by Ferroelectric Polarization Mediated Triboelectricity,” *Adv. Funct. Mater.*, vol. 26, no. 18, pp. 3067–3073, 2016.
- [61] W. Seung *et al.*, “Boosting Power-Generating Performance of Triboelectric Nanogenerators via Artificial Control of Ferroelectric Polarization and Dielectric Properties,” *Adv. Energy Mater.*, p. 1600988, 2016.
- [62] Y. Yang, H. Zhang, J. Chen, S. Lee, T. C. Hou, and Z. L. Wang, “Simultaneously harvesting mechanical and chemical energies by a hybrid cell for self-powered biosensors and personal electronics,” *Energy Environ. Sci.*, vol. 6, no. 6, pp. 1744–1749, 2013.
- [63] G. Q. Gu *et al.*, “Antibacterial Composite Film-Based Triboelectric Nanogenerator for Harvesting Walking Energy,” *ACS Appl. Mater. Interfaces*, vol. 9, no. 13, pp. 11882–11888, 2017.
- [64] X. He, H. Guo, X. Yue, J. Gao, Y. Xi, and C. Hu, “Improving energy conversion efficiency for triboelectric nanogenerator with capacitor structure by maximizing surface charge density,” *Nanoscale*, vol. 7, no. 5, pp. 1896–1903, 2015.
- [65] Prateek, V. K. Thakur, and R. K. Gupta, “Recent Progress on Ferroelectric Polymer-Based Nanocomposites for High Energy Density Capacitors: Synthesis, Dielectric Properties, and Future Aspects,” *Chem. Rev.*, vol. 116, no. 7, pp. 4260–4317, 2016.
- [66] Z.-M. Dang, J.-K. Yuan, S.-H. Yao, and R.-J. Liao, “Flexible Nanodielectric Materials with High Permittivity for Power Energy Storage,” *Adv. Mater.*, vol. 25, no. 44, pp. 6334–6365, 2013.
- [67] J. Chen *et al.*, “Enhancing Performance of Triboelectric Nanogenerator by Filling High Dielectric Nanoparticles into Sponge PDMS Film,” *ACS Appl. Mater. Interfaces*, vol. 8, no. 1, pp. 736–744, 2016.
- [68] J. W. Lee *et al.*, “Robust nanogenerators based on graft copolymers via control of dielectrics for remarkable output power enhancement,” *Sci. Adv.*, vol. 3, no. 5, pp. 1–10, 2017.
- [69] W. W. Shen, H. B. Mu, G. J. Zhang, J. B. Deng, and D. M. Tu, “Identification of electron and hole trap based on isothermal surface potential decay model,” *J. Appl. Phys.*, vol. 113, no. 8, p. 083706, 2013.
- [70] G. Chen and Z. Xu, “Charge trapping and detrapping in polymeric materials,” *J. Appl. Phys.*, vol. 106, no. 12, p. 123707, 2009.
- [71] J. Li, F. Zhou, D. Min, S. Li, and R. Xia, “The energy distribution of trapped charges in polymers based on isothermal surface potential decay model,” *IEEE Trans. Dielectr. Electr. Insul.*, vol. 22, no. 3, pp. 1723–1732, 2015.
- [72] Y. Feng, Y. Zheng, G. Zhang, D. Wang, F. Zhou, and W. Liu, “A new protocol toward high output TENG with polyimide as charge storage layer,” *Nano Energy*,

vol. 38, pp. 467–476, 2017.

- [73] T. Takada, H. Kikuchi, H. Miyake, Y. Tanaka, and M. Yoshida, “Determination of Charge-trapping Sites in Saturated and Aromatic Polymers by Quantum Chemical Calculation,” *IEEE Trans. Dielectr. Electr. Insul.*, vol. 22, no. 2, pp. 1240–1249, 2014.
- [74] C. Wu, T. W. Kim, and H. Y. Choi, “Reduced graphene-oxide acting as electron-trapping sites in the friction layer for giant triboelectric enhancement,” *Nano Energy*, vol. 32, pp. 542–550, 2017.
- [75] C. Wu *et al.*, “Enhanced Triboelectric Nanogenerators Based on MoS<sub>2</sub> Monolayer Nanocomposites Acting as Electron-Acceptor Layers,” *ACS Nano*, vol. 11, no. 8, pp. 8356–8363, 2017.
- [76] H. W. Park *et al.*, “Electron blocking layer-based interfacial design for highly-enhanced triboelectric nanogenerators,” *Nano Energy*, vol. 50, pp. 9–15, 2018.
- [77] M. Li *et al.*, “Revisiting the  $\delta$ -phase of poly(vinylidene fluoride) for solution-processed ferroelectric thin films,” *Nat. Mater.*, vol. 12, no. 5, pp. 433–438, 2013.
- [78] H. S. Nalwa, *Ferroelectric Polymers: Chemistry, Physics, and Applications*. New York: Marcel Dekker, Inc., 1995.
- [79] D. Mao, B. E. Gnade, and M. A. Quevedo-Lopez, “Ferroelectric Properties and Polarization Switching Kinetic of Poly (vinylidene fluoride-trifluoroethylene) Copolymer,” in *Ferroelectrics*, M. Lallart, Ed. Rijeka: IntechOpen, 2011.
- [80] H. J. Kim *et al.*, “Silk Nanofiber-Networked Bio-Triboelectric Generator: Silk Bio-TEG,” *Adv. Energy Mater.*, vol. 6, no. 8, p. 1502329, 2016.
- [81] a. Kawaguchi, I. Tokimitsu, Y. Fujiwara, M. Tabuchi, and K. Monobe, “Polymorphism in lamellar single crystals of Nylon 11,” *J. Macromol. Sci. Part B Phys.*, vol. 20, no. March 2015, pp. 1–20, 1981.
- [82] S. Rhee and J. L. White, “Crystalline structure and morphology of biaxially oriented polyamide-11 films,” *J. Polym. Sci. Part B Polym. Phys.*, vol. 40, no. 23, pp. 2624–2640, 2002.
- [83] H. Search, C. Journals, A. Contact, M. Iopscience, and I. P. Address, “Investigation of Nylon " texture " by X-ray diffraction,” *Br. J. Appl. Phys.*, vol. 10, pp. 225–230, 1959.
- [84] G. H. E. Roguet, S. Tence-Girault, S. Castagnet, J.C. Grandidier, “Micromechanisms Involved in the Atypical Tensile Behavior Observed in Polyamide 11 at High Temperature,” *J. Polym. Sci. Part B Polym. Phys.*, vol. 45, pp. 3046–3059, 2007.
- [85] W.P. Slichter, “Crystal structures in polyamides made from  $\omega$ -amino acids,” *J. Polym. Sci. Part A Polym. Chem.*, vol. 36, pp. 259–266, 1959.
- [86] R. Aelion, “Preparation and structure of some new types of polyamides,” *Ann. Chim. Appl*, vol. 3, pp. 5–61, 1948.

- [87] S. Dasgupta, W. B. Hammond, and W. A. Goddard, "Crystal structures and properties of nylon polymers from theory," *J. Am. Chem. Soc.*, vol. 118, no. 49, pp. 12291–12301, 1996.
- [88] K.G. Kim, B.A. Newman, and J.I. Scheinbeim, "Temperature dependence of the crystal structures of nylon 11," *J. Polym. Sci. Part B Polym. Phys.*, vol. 23, pp. 2477–2482, 1985.
- [89] J. Pepin, V. Miri, and J. M. Lefebvre, "New Insights into the Brill Transition in Polyamide 11 and Polyamide 6," *Macromolecules*, vol. 49, no. 2, pp. 564–573, 2016.
- [90] B. A. Newman, T. P. Sham, K. D. Pae, B. A. Newman, T. P. Sham, and K. D. Pae, "A high - pressure x - ray study of Nylon 11 A high-pressure x-ray study of Nylon 11," *J. Appl. Phys.*, vol. 48, no. 10, pp. 4092–4098, 1977.
- [91] Q. Zhang, Z. Mo, H. Zhang, S. Liu, and S. Z. D. Cheng, "Crystal transitions of Nylon 11 under drawing and annealing," *Polymer (Guildf.)*, vol. 42, no. 13, pp. 5543–5547, 2001.
- [92] Tadahiro Sasaki, "Notes on the polymorphism in nylon 11," *J. Polym. Sci. Part C Polym. Lett.*, vol. 3, pp. 557–560, 1965.
- [93] S. S. Nair, C. Ramesh, and K. Tashiro, "Crystalline phases in nylon-11: Studies using HTWAXS and HTFTIR," *Macromolecules*, vol. 39, no. 8, pp. 2841–2848, 2006.
- [94] E. Balizer, J. Fedderly, D. Haught, B. Dickens, and A. S. Dereggi, "FTIR and X-ray study of polymorphs of Nylon 11 and relation to ferroelectricity," *J. Polym. Sci. Part B Polym. Phys.*, vol. 32, pp. 365–369, 1994.
- [95] J. I. Scheinbeim, "Piezoelectricity in  $\gamma$ -form Nylon 11," *J. Appl. Phys.*, vol. 52, no. 10, pp. 5939–5942, 1981.
- [96] J. I. Scheinbeim, J. W. Lee, and B. A. Newman, "Ferroelectric polarization mechanisms in nylon 11," *Macromolecules*, vol. 25, no. 14, pp. 3729–3732, 1992.
- [97] Z. Zhang, M. H. Litt, and L. Zhu, "Unified Understanding of Ferroelectricity in n-Nylons: Is the Polar Crystalline Structure a Prerequisite?," *Macromolecules*, vol. 49, pp. 3070–3082, 2016.
- [98] S. Gogolewski, "Effect of annealing on thermal properties and crystalline structure of polyamides. Nylon 11 (polyundecaneamide)," *Colloid Polym. Sci.*, vol. 257, no. 8, pp. 811–819, 1979.
- [99] Q. Zhang, Z. Mo, S. Liu, and H. Zhang, "Influence of annealing on structure of Nylon 11," *Macromolecules*, vol. 33, no. 16, pp. 5999–6005, 2000.
- [100] H. Pressure, "High pressure melting and crystallisation of Nylon-11," *J. Mater. Sci.*, vol. 20, pp. 1753–1762, 1985.
- [101] S. L. Wu, J. I. Scheinbeim, and B. A. Newman, "Ferroelectricity and piezoelectricity of nylon 11 films with different draw ratios," *J. Polym. Sci. Part B-Polymer Phys.*, vol. 37, no. 19, pp. 2737–2746, 1999.

- [102] J. O. Fernandez, G. M. Swallowe, and S. F. Lee, "Crystallisation of Nylon 11 under compressive high strain rates," *J. Appl. Polym. Sci.*, vol. 80, no. 11, pp. 2031–2038, 2001.
- [103] B. A. Newman, P. Chen, K. D. Pae, and J. I. Scheinbeim, "Piezoelectricity in nylon 11," *J. Appl. Phys.*, vol. 51, no. 10, pp. 5161–5164, 1980.
- [104] M. H. Litt, C. H. Hsu, and P. Basu, "Pyroelectricity and piezoelectricity in nylon 11," *J. Appl. Phys.*, vol. 48, no. 6, pp. 2208–2212, 1977.
- [105] S. C. Mathur, J. I. Scheinbeim, B. A. Newman, C. Mathur, J. I. Scheinbeim, and B. A. Newman, "Piezoelectric properties and ferroelectric hysteresis effects in uniaxially stretched nylon - 11 films," *J. Appl. Phys.*, vol. 59, no. 9, p. 2419, 1984.
- [106] G. Wu, O. Yano, and T. Soen, "Dielectric-and-Piezoelectric-Properties-of-Nylon-9-and-Nylon-11," *Polymer Journal*, vol. 18, no. 1. pp. 51–61, 1986.
- [107] Y. Takase, J. W. Lee, J. I. Scheinbeim, and B. A. Newman, "High-temperature characteristics of nylon-11 and nylon-7 piezoelectrics," *Macromolecules*, vol. 24, pp. 6644–6652, 1991.
- [108] J. W. Lee, Y. Takase, B. a Newman, and J. I. Scheinbeim, "Ferroelectric polarization switching in nylon-11," *J. Polym. Sci. Part B-Polymer Phys.*, vol. 29, no. 3, pp. 273–277, 1991.
- [109] J. W. Lee, Y. Takase, B. A. Newman, and J. I. Scheinbeim, "Effect of annealing on the ferroelectric behavior of nylon-11 and nylon-7," *J. Polym. Sci. Part B-Polymer Phys.*, vol. 29, no. 3, pp. 279–286, 1991.
- [110] Y. Takahashi, M. Shimomura, M. Kutani, and T. Furukawa, "Ferroelectric switching characteristics and crystal structure of nylon 11," *Polymer Journal*, vol. 29, no. 3. pp. 234–239, 1997.
- [111] K. Meurisch, B. Gojdka, T. Strunskus, V. Zaporojtchenko, and F. Faupel, "Vapour phase deposition of highly crystalline self-poled piezoelectric nylon-11," *J. Phys. D. Appl. Phys.*, vol. 45, p. 055304, 2012.
- [112] M. Dhanalakshmi and J. P. Jog, "Preparation and characterization of electrospun fibers of Nylon 11," *Express Polym. Lett.*, vol. 2, no. 8, pp. 540–545, 2008.
- [113] G. Mago, D. M. Kalyon, and F. T. Fisher, "Nanocomposites of polyamide-11 and carbon nanostructures: Development of microstructure and ultimate properties following solution processing," *J. Polym. Sci. Part B Polym. Phys.*, vol. 49, no. 18, pp. 1311–1321, 2011.
- [114] S. Stankovich *et al.*, "Graphene-based composite materials," *Nature*, vol. 442, no. 7100, pp. 282–286, 2006.
- [115] Q. Li *et al.*, "Flexible high-temperature dielectric materials from polymer nanocomposites," *Nature*, vol. 523, no. 7562, pp. 576–579, 2015.
- [116] T. Ramanathan *et al.*, "Functionalized graphene sheets for polymer nanocomposites," *Nat. Nanotechnol.*, vol. 3, no. 6, pp. 327–331, 2008.

- [117] G. Zhang, Y. Li, S. Tang, R. D. Thompson, and L. Zhu, "The Role of Field Electron Emission in Polypropylene/Aluminum Nanodielectrics Under High Electric Fields," *ACS Appl. Mater. Interfaces*, vol. 9, no. 11, pp. 10106–10119, 2017.
- [118] P. Hu *et al.*, "Topological-structure modulated polymer nanocomposites exhibiting highly enhanced dielectric strength and energy density," *Adv. Funct. Mater.*, vol. 24, no. 21, pp. 3172–3178, 2014.
- [119] J. Y. Oh *et al.*, "Effect of microstructure and morphological properties of carbon nanotubes on the length reduction during melt processing," *Compos. Sci. Technol.*, vol. 112, pp. 42–49, 2015.
- [120] S. K. Kumar, N. Jouault, B. Benicewicz, and T. Neely, "Nanocomposites with polymer grafted nanoparticles," *Macromolecules*, vol. 46, no. 9, pp. 3199–3214, 2013.
- [121] Q. Li *et al.*, "Sandwich-structured polymer nanocomposites with high energy density and great charge–discharge efficiency at elevated temperatures," *Proc. Natl. Acad. Sci.*, vol. 113, no. 36, pp. 9995–10000, 2016.
- [122] Y. Wang, J. Cui, Q. Yuan, Y. Niu, Y. Bai, and H. Wang, "Significantly Enhanced Breakdown Strength and Energy Density in Sandwich-Structured Barium Titanate/Poly(vinylidene fluoride) Nanocomposites," *Adv. Mater.*, vol. 27, no. 42, pp. 6658–6663, 2015.
- [123] C. R. Martin, "Nanomaterials: A membrane-based synthetic approach," *Science (80-. )*, vol. 266, no. 5193, pp. 1961–1966, 1994.
- [124] G. Nimtz, P. Marquardt, D. Stauffer, and W. Weiss, "Raoult's Law and the Melting Point Depression in Mesoscopic Systems," *Science (80-. )*, vol. 242, no. 4886, pp. 1671–1672, 1998.
- [125] R. V. Parthasarathy and C. R. Martin, "Synthesis of polymeric microcapsule arrays and their use for enzyme immobilization," *Nature*, vol. 369, pp. 298–301, 1994.
- [126] Z. Cai and C. R. Martin, "Electronically Conductive Polymer Fibers with Mesoscopic Diameters Show Enhanced Electronic Conductivities," *J. Am. Chem. Soc.*, vol. 111, no. 11, pp. 4138–4139, 1989.
- [127] Z. Cai, J. Lei, W. Liang, V. Menon, and C. R. Martin, "Molecular and Supermolecular Origins of Enhanced Electronic Conductivity in Template-Synthesized Polyheterocyclic Fibrils. 1. Supermolecular Effects," *Chem. Mater.*, vol. 3, no. 5, pp. 960–967, 1991.
- [128] D. J. Quiram, R. A. Register, G. R. Marchand, and D. H. Adamson, "Chain orientation in block copolymers exhibiting cylindrically confined crystallisation," *Macromolecules*, vol. 31, no. 15, pp. 4891–4898, 1998.
- [129] V. M. Cepak and C. R. Martin, "Preparation of polymeric micro- and nanostructures using a template-based deposition method," *Chem. Mater.*, vol. 11, no. 5, pp. 1363–1367, 1999.
- [130] L. Zhu *et al.*, "Crystallisation temperature-dependent crystal orientations within

- nanoscale confined lamellae of a self-assembled crystalline - Amorphous diblock copolymer,” *J. Am. Chem. Soc.*, vol. 122, no. 25, pp. 5957–5967, 2000.
- [131] Y. L. Loo, R. A. Register, A. J. Ryan, and G. T. Dee, “Polymer crystallisation confined in one, two, or three dimensions,” *Macromolecules*, vol. 34, no. 26, pp. 8968–8977, 2001.
- [132] M. Steinhart *et al.*, “Polymer nanotubes by wetting of ordered porous templates,” *Science (80-. )*, vol. 296, no. 5575, p. 1997, 2002.
- [133] V. Cauda, G. Canavese, and S. Stassi, “Nanostructured piezoelectric polymers,” *J. Appl. Polym. Sci.*, vol. 132, no. 13, pp. 1–14, 2015.
- [134] J. S. Stephens, D. B. Chase, and J. F. Rabolt, “Effect of the electrospinning process on polymer crystallisation chain conformation in nylon-6 and nylon-12,” *Macromolecules*, vol. 37, no. 3, pp. 877–881, 2004.
- [135] C. Chang, V. H. Tran, J. Wang, Y. K. Fuh, and L. Lin, “Direct-write piezoelectric polymeric nanogenerator with high energy conversion efficiency,” *Nano Lett.*, vol. 10, no. 2, pp. 726–731, 2010.
- [136] L. Persano *et al.*, “High performance piezoelectric devices based on aligned arrays of nanofibers of poly(vinylidene fluoride-co-trifluoroethylene),” *Nat. Commun.*, vol. 4, pp. 1610–1633, 2013.
- [137] Z. Hu, G. Baralia, V. Bayot, J. F. Gohy, and A. M. Jonas, “Nanoscale control of polymer crystallisation by nanoimprint lithography,” *Nano Lett.*, vol. 5, no. 9, pp. 1738–1743, 2005.
- [138] Z. Hu, M. Tian, B. Nysten, and A. M. Jonas, “Regular arrays of highly ordered ferroelectric polymer nanostructures for non-volatile low-voltage memories,” *Nat. Mater.*, vol. 8, no. 1, pp. 62–67, 2009.
- [139] Y. Liu, D. N. Weiss, and J. Li, “Rapid nanoimprinting and excellent piezoresponse of polymeric ferroelectric nanostructures,” *ACS Nano*, vol. 4, no. 1, pp. 83–90, 2010.
- [140] P. G. de Gennes, “Wetting: statics and dynamics,” *Rev. Mod. Phys.*, vol. 57, no. 3, pp. 827–863, Jul. 1985.
- [141] T. Young, “III. An essay on the cohesion of fluids,” *Philos. Trans. R. Soc. London*, vol. 95, pp. 65–87, Jan. 1805.
- [142] M. Zhang, P. Dobriyal, J. T. Chen, T. P. Russell, J. Olmo, and A. Merry, “Wetting transition in cylindrical alumina nanopores with polymer melts,” *Nano Lett.*, vol. 6, no. 5, pp. 1075–1079, 2006.
- [143] P. E. De Jongh and T. M. Eggenhuisen, “Melt infiltration: An emerging technique for the preparation of novel functional nanostructured materials,” *Adv. Mater.*, vol. 25, no. 46, pp. 6672–6690, 2013.
- [144] E. Dujardin, T. W. Ebbesen, H. Hiura, and K. Tanigaki, “Capillarity and Wetting of Carbon Nanotubes,” *Science (80-. )*, vol. 265, no. 5180, p. 1850 LP-1852, Sep. 1994.

- [145] D. Schebarchov and S. C. Hendy, "Uptake and withdrawal of droplets from carbon nanotubes," *Nanoscale*, vol. 3, no. 1, pp. 134–141, 2011.
- [146] E. W. Washburn, "The Dynamics of Capillary Flow," *Phys. Rev.*, vol. 17, no. 3, pp. 273–283, Mar. 1921.
- [147] B. Y. Cao, M. Yang, and G. J. Hu, "Capillary filling dynamics of polymer melts in nanopores: Experiments and rheological modelling," *RSC Adv.*, vol. 6, no. 9, pp. 7553–7559, 2016.
- [148] E. Kim, Y. Xia, and G. M. Whitesides, "Polymer microstructures formed by moulding in capillaries," *Nature*, vol. 376, p. 581, Aug. 1995.
- [149] J. L. Lutkenhaus, K. McEnnis, A. Serghei, and T. P. Russell, "Confinement effects on crystallisation and curie transitions of poly(vinylidene fluoride-co-trifluoroethylene)," *Macromolecules*, vol. 43, no. 8, pp. 3844–3850, 2010.
- [150] C. L. Jackson and G. B. McKenna, "The melting behavior of organic materials confined in porous solids.," *J. Chem. Phys.*, vol. 93, no. 12, p. 9002, 1990.
- [151] K. Shin, E. Woo, Y. G. Jeong, C. Kim, J. Huh, and K. W. Kim, "Crystalline structures, melting, and crystallisation of linear polyethylene in cylindrical nanopores," *Macromolecules*, vol. 40, no. 18, pp. 6617–6623, 2007.
- [152] E. Woo, J. Huh, Y. G. Jeong, and K. Shin, "From homogeneous to heterogeneous nucleation of chain molecules under nanoscopic cylindrical confinement," *Phys. Rev. Lett.*, vol. 98, no. 13, pp. 1–4, 2007.
- [153] T. M. Chung, T. C. Wang, R. M. Ho, Y. Sen Sun, and B. T. Ko, "Polymeric crystallisation under nanoscale 2D spatial confinement," *Macromolecules*, vol. 43, no. 14, pp. 6237–6240, 2010.
- [154] R. M. Michell *et al.*, "The crystallisation of confined polymers and block copolymers infiltrated within alumina nanotube templates," *Macromolecules*, vol. 45, no. 3, pp. 1517–1528, 2012.
- [155] R. M. Michell, I. Blaszczyk-Lezak, C. Mijangos, and A. J. Müller, "Confinement effects on polymer crystallisation: From droplets to alumina nanopores," *Polym. (United Kingdom)*, vol. 54, no. 16, pp. 4059–4077, 2013.
- [156] B. D. Hamilton, J. M. Ha, M. A. Hillmyer, and M. D. Ward, "Manipulating crystal growth and polymorphism by confinement in nanoscale crystallisation chambers," *Acc. Chem. Res.*, vol. 45, no. 3, pp. 414–423, 2012.
- [157] J. M. Ha, J. H. Wolf, M. A. Hillmyer, and M. D. Ward, "Polymorph Selectivity under Nanoscopic Confinement," *J. Am. Chem. Soc.*, vol. 126, no. 11, pp. 3382–3383, 2004.
- [158] M. C. García-Gutiérrez *et al.*, "Confinement-induced one-dimensional ferroelectric polymer arrays," *Nano Lett.*, vol. 10, no. 4, pp. 1472–1476, 2010.
- [159] V. Cauda, S. Stassi, K. Bejtka, and G. Canavese, "Nanoconfinement: An effective way to enhance PVDF piezoelectric properties," *ACS Appl. Mater. Interfaces*, vol.

- 5, no. 13, pp. 6430–6437, 2013.
- [160] K. Choi, S. C. Lee, Y. Liang, K. J. Kim, and H. S. Lee, “Transition from Nanorod to Nanotube of Poly(vinylidene trifluoroethylene) Ferroelectric Nanofiber,” *Macromolecules*, vol. 46, pp. 3067–3073, 2013.
- [161] V. Cauda *et al.*, “Confinement in oriented mesopores induces piezoelectric behavior of polymeric nanowires,” *Chem. Mater.*, vol. 24, no. 21, pp. 4215–4221, 2012.
- [162] H. Wu, W. Wang, H. Yang, and Z. Su, “Crystallisation and orientation of syndiotactic polystyrene in nanorods,” *Macromolecules*, vol. 40, no. 12, pp. 4244–4249, 2007.
- [163] M. K. Lee and J. Lee, “Fabrication of ferroelectric polymer nanocrystals with tunable morphologies,” *Cryst. Growth Des.*, vol. 13, no. 2, pp. 671–678, 2013.
- [164] C. Fu, X. Wang, X. Shi, and X. Ran, “The induction of poly(vinylidene fluoride) electroactive phase by modified anodic aluminum oxide template nanopore surface,” *RSC Adv.*, vol. 5, no. 106, pp. 87429–87436, 2015.
- [165] J. Xue, Y. Xu, and Z. Jin, “Interfacial Interaction in Anodic Aluminum Oxide Templates Modifies Morphology, Surface Area, and Crystallisation of Polyamide-6 Nanofibers,” *Langmuir*, vol. 32, no. 9, pp. 2259–2266, 2016.
- [166] J. T. Chen *et al.*, “Fabrication of polymer nanopeapods in the nanopores of anodic aluminum oxide templates using a double-solution wetting method,” *Macromolecules*, vol. 47, no. 15, pp. 5227–5235, 2014.
- [167] M. Steinhart *et al.*, “Coherent kinetic control over crystal orientation in macroscopic ensembles of polymer nanorods and nanotubes,” *Phys. Rev. Lett.*, vol. 97, no. 2, pp. 1–4, 2006.
- [168] Y. Ma, W. Hu, J. Hobbs, and G. Reiter, “Understanding crystal orientation in quasi-one-dimensional polymer systems,” *Soft Matter*, vol. 4, no. 3, p. 540, 2008.
- [169] K. Fukuda and T. Someya, “Recent Progress in the Development of Printed Thin-Film Transistors and Circuits with High-Resolution Printing Technology,” *Adv. Mater.*, vol. 29, p. 1602736, 2017.
- [170] J. O’Donnell, M. Kim, and H.-S. Yoon, “A Review on Electromechanical Devices Fabricated by Additive Manufacturing,” *J. Manuf. Sci. Eng.*, vol. 139, no. 1, p. 010801, 2016.
- [171] R. L. Truby and J. A. Lewis, “Printing soft matter in three dimensions,” *Nature*, vol. 540, no. 7633, pp. 371–378, 2016.
- [172] M. J. Renn, “Direct Write System,” US Patent 7270844, 2011.
- [173] J. R. Castrejon-Pita, W. R. S. Baxter, J. Morgan, S. Temple, G. D. Martin, and I. M. Hutchings, “Future, Opportunities and Challenges of Inkjet Technologies,” *At. Sprays*, vol. 23, no. 6, pp. 541–565, 2013.
- [174] E. B. Secor, “Principles of aerosol jet printing,” *Flex. Print. Electron.*, vol. 3, p. 035002, 2018.

- [175] OPTOMECH, “Aerosol Jet AJ 200 System User Manual,” 2016.
- [176] R. J. Lang, “Ultrasonic Atomization of Liquids,” *J. Acoust. Soc. Am.*, vol. 34, no. 6, pp. 6–8, 1962.
- [177] R. L. Peskin and R. J. Raco, “Ultrasonic Atomization of Liquids,” *J. Acoust. Soc. Am.*, vol. 35, no. 9, pp. 1378–1381, 1963.
- [178] T. D. Donnelly *et al.*, “Using ultrasonic atomization to produce an aerosol of micron-scale particles,” *Rev. Sci. Instrum.*, vol. 76, p. 113301, 2005.
- [179] C. Rodes, T. Smith, R. Crouse, and G. Ramachandran, “Measurements of the Size Distribution of Aerosols Produced by Ultrasonic Humidification,” *Aerosol Sci. Technol.*, vol. 13, no. 2, pp. 220–229, 1990.
- [180] R. Kumar and K. S. L. Prasad, “Studies on Pneumatic Atomization,” *Ind. Eng. Chem. Process Des. Dev.*, vol. 10, no. 3, pp. 357–365, 1971.
- [181] G. James and M. W. R., “Characteristics of pneumatic atomization,” *AIChE J.*, vol. 7, no. 2, pp. 312–318, 1961.
- [182] H. Y. Chen and H. L. Huang, “Numerical and experimental study of virtual impactor design and aerosol separation,” *J. Aerosol Sci.*, vol. 94, pp. 43–55, 2016.
- [183] S. Binder, M. Glatthaar, and E. Rädlein, “Analytical investigation of aerosol jet printing,” *Aerosol Sci. Technol.*, vol. 48, no. 9, pp. 924–929, 2014.
- [184] C. Goth, S. Putzo, and J. Franke, “Aerosol Jet printing on rapid prototyping materials for fine pitch electronic applications,” *Proc. - Electron. Components Technol. Conf.*, pp. 1211–1216, 2011.
- [185] A. Mahajan, C. D. Frisbie, and L. F. Francis, “Optimization of aerosol jet printing for high-resolution, high-aspect ratio silver lines,” *ACS Appl. Mater. Interfaces*, vol. 5, no. 11, pp. 4856–4864, 2013.
- [186] Y. S. Choi, J. A. Elliott, S. K. Kim, F. Williams, Y. Calahorra, and S. Kar-Narayan, “The effect of crystal structure on the electromechanical properties of piezoelectric,” *Chem. Commun.*, vol. 54, pp. 6863–6866, 2018.
- [187] J. Jakeš and S. Krimm, “A valence force field for the amide group,” *Spectrochim. Acta Part A Mol. Spectrosc.*, vol. 27, no. 1, pp. 19–34, 1971.
- [188] H. Isoda and Y. Furukawa, “Electric-Field-Induced Dynamics of Polymer Chains in a Ferroelectric Melt-Quenched Cold-Drawn Film of Nylon-11 Using Infrared Spectroscopy,” *J. Phys. Chem. B*, vol. 119, no. 44, pp. 14309–14314, 2015.
- [189] D. J. Skrovanek, P. C. Painter, and M. M. Coleman, “Hydrogen bonding in polymers. 2. Infrared temperature studies of nylon 11,” *Macromolecules*, vol. 19, no. 3, pp. 699–705, 1986.
- [190] Y. S. Zhou, Y. Liu, G. Zhu, Z. Lin, C. Pan, and Q. Jing, “In Situ Quantitative Study of Nanoscale Triboelectrification and Patterning,” *Nano Lett.*, vol. 13, pp. 2771–2776, 2013.

- [191] Y. S. Zhou *et al.*, “Manipulating nanoscale contact electrification by an applied electric field,” *Nano Lett.*, vol. 14, no. 3, pp. 1567–1572, 2014.
- [192] S. Li, Y. Zhou, Y. Zi, G. Zhang, and Z. L. Wang, “Excluding Contact Electrification in Surface Potential Measurement Using Kelvin Probe Force Microscopy,” *ACS Nano*, vol. 10, no. 2, pp. 2528–2535, 2016.
- [193] R. Oliver, “Characterisation techniques: electrical measurements by AFM,” 2013.
- [194] T. Jungk, A. Hoffmann, and E. Soergel, “Consequences of the background in piezoresponse force microscopy on the imaging of ferroelectric domain structures,” *J. Microsc.*, vol. 227, no. 1, pp. 72–78, 2007.
- [195] M. Smith, Y. Calahorra, Q. Jing, and S. Kar-Narayan, “Direct observation of shear piezoelectricity in poly-L-lactic acid nanowires,” *APL Mater.*, vol. 5, no. 7, p. 074105, 2017.
- [196] B. Wu, A. Heidelberg, and J. J. Boland, “Mechanical properties of ultrahigh-strength gold nanowires,” *Nat. Mater.*, vol. 4, no. 7, pp. 525–529, 2005.
- [197] Y. Calahorra, R. A. Whiter, Q. Jing, V. Narayan, and S. Kar-Narayan, “Localized electromechanical interactions in ferroelectric P(VDF-TrFE) nanowires investigated by scanning probe microscopy,” *APL Mater.*, vol. 4, no. 11, p. 116106, 2016.
- [198] M. E. McConney, S. Singamaneni, and V. V. Tsukruk, “Probing soft matter with the atomic force microscopies: Imaging and force spectroscopy,” *Polym. Rev.*, vol. 50, no. 3, pp. 235–286, 2010.
- [199] H. Liu, N. Chen, S. Fujinami, D. Louzguine-Luzgin, K. Nakajima, and T. Nishi, “Quantitative nanomechanical investigation on deformation of poly(lactic acid),” *Macromolecules*, vol. 45, no. 21, pp. 8770–8779, 2012.
- [200] B. Pittenger, N. Erina, and C. Su, “Quantitative Mechanical Property Mapping at the Nanoscale with PeakForce QNM,” 2009.
- [201] H. J. Butt, B. Cappella, and M. Kappl, “Force measurements with the atomic force microscope: Technique, interpretation and applications,” *Surf. Sci. Rep.*, vol. 59, no. 1–6, pp. 1–152, 2005.
- [202] R. a. Whiter, V. Narayan, and S. Kar-Narayan, “A Scalable Nanogenerator Based on Self-Poled Piezoelectric Polymer Nanowires with High Energy Conversion Efficiency,” *Adv. Energy Mater.*, vol. 4, no. 18, p. 1400519, 2014.
- [203] Dassault Systèmes BIOVIA, “BIOVIA Materials Studio Visualizer.” Dassault Systèmes, San Diego, 2014.
- [204] C. W. Bunn and E. V. Garner, “The Crystal Structures of Two Polyamides (‘Nylons’),” *Proc. Roy. Soc. A*, vol. 189, no. 1016, pp. 39–68, 1947.
- [205] M. Dosiere and J. J. Point, “Orientation of the boundary faces in nylon-11 lamellar crystals,” *J. Polym. Sci. Part B-Polymer Phys.*, vol. 22, no. 8, pp. 1383–1398, 1984.
- [206] H. Sun, “COMPASS: An ab Initio Force-Field Optimized for Condensed-Phase

Applications Overview with Details on Alkane and Benzene Compounds,” *J. Phys. Chem. B*, vol. 102, no. 38, pp. 7338–7364, 1998.

- [207] A. K. Rappé, C. J. Casewit, K. S. Colwell, W. A. Goddard, and W. M. Skiff, “UFF, a Full Periodic Table Force Field for Molecular Mechanics and Molecular Dynamics Simulations,” *J. Am. Chem. Soc.*, vol. 114, no. 25, pp. 10024–10035, 1992.
- [208] A. Datta, Y. S. Choi, E. Chalmers, C. Ou, and S. Kar-Narayan, “Piezoelectric Nylon-11 Nanowire Arrays Grown by Template Wetting for Vibrational Energy Harvesting Applications,” *Adv. Funct. Mater.*, vol. 27, p. 1604262, 2017.
- [209] Q. Gao and J. Scheinbeim, “Crystallisation studies of polymer blends of nylon-11/poly (vinylidene fluoride),” *Polym. J.*, vol. 35, no. 4, pp. 345–352, 2003.
- [210] X. Zhang, M. Shimoda, and A. Toyoda, “Investigation of phase structures and intermolecular interactions of nylon-11/polyepichlorohydrin blends,” *Polymer (Guildf)*, vol. 35, no. 20, pp. 4280–4286, 1994.
- [211] R. A. Whiter, Y. Calahorra, C. Ou, and S. Kar-Narayan, “Observation of Confinement-Induced Self-Poling Effects in Ferroelectric Polymer Nanowires Grown by Template Wetting,” *Macromol. Mater. Eng.*, vol. 301, pp. 1016–1025, 2016.
- [212] C. Ou *et al.*, “Template-Assisted Hydrothermal Growth of Aligned Zinc Oxide Nanowires for Piezoelectric Energy Harvesting Applications,” *ACS Appl. Mater. Interfaces*, vol. 8, no. 22, pp. 13678–13683, 2016.
- [213] F. L. Boughey, T. Davies, A. Datta, R. A. Whiter, S. L. Sahonta, and S. Kar-Narayan, “Vertically aligned zinc oxide nanowires electrodeposited within porous polycarbonate templates for vibrational energy harvesting,” *Nanotechnology*, vol. 27, no. 28, 2016.
- [214] D.-M. Shin *et al.*, “Bioinspired piezoelectric nanogenerators based on vertically aligned phage nanopillars,” *Energy Environ. Sci.*, vol. 8, no. 11, pp. 3198–3203, 2015.
- [215] V. Bhavanasi, D. Y. Kusuma, and P. S. Lee, “Polarization orientation, piezoelectricity, and energy harvesting performance of ferroelectric PVDF-TrFE nanotubes synthesized by nanoconfinement,” *Adv. Energy Mater.*, vol. 4, no. 16, pp. 1–8, 2014.
- [216] S-L Wu, J. I. Scheinbeim, and B. A. Newman, “The effect of melt processing conditions on the hydrogen-bonded sheet orientation and polarization of nylon 11 films,” *J. Polym. Sci. Part B Polym. Phys.*, vol. 34, pp. 3035–3053, 1996.
- [217] L. F. Brown, J. L. Mason, M. L. Klinkenborg, J. I. Scheinbeim, and B. A. Newman, “Ferroelectric nylon materials and their feasibility for ultrasound transducers,” *IEEE Trans. Ultrason. Ferroelectr. Freq. Control*, vol. 44, no. 5, pp. 1049–1059, 1997.
- [218] P. Frübing, A. Kremmer, R. Gerhard-Multhaupt, A. Spanoudaki, and P. Pissis, “Relaxation processes at the glass transition in polyamide 11: From rigidity to

- viscoelasticity,” *J. Chem. Phys.*, vol. 125, no. 21, pp. 214701-1–8, 2006.
- [219] E. W. Jacobs and J. C. Hicks, “Electric field induced morphological changes in nylon 11,” *Appl. Phys. Lett.*, vol. 44, no. 4, pp. 402–403, 1984.
- [220] D. K. and V Gelfandbeint, “Ferroelectric behaviour of  $\alpha$ -nylon 11,” *J. Phys. D. Appl. Phys.*, vol. 15, pp. L115-117, 1982.
- [221] Z. Y. Wang, H. Q. Fan, K. H. Su, and Z. Y. Wen, “Structure and piezoelectric properties of poly(vinylidene fluoride) studied by density functional theory,” *Polymer (Guildf)*, vol. 47, no. 23, pp. 7988–7996, 2006.
- [222] Y. L. Hong, T. Koga, and T. Miyoshi, “Chain trajectory and crystallisation mechanism of a semicrystalline polymer in melt- and solution-grown crystals as studied using  $^{13}\text{C}$ - $^{13}\text{C}$  double-quantum NMR,” *Macromolecules*, vol. 48, no. 10, pp. 3282–3293, 2015.
- [223] B. Z. Mei, J. I. Scheinbeim, and B. A. Newman, “The Ferroelectric Behavior of Odd-Numbered Nylons,” *Ferroelectrics*, vol. 144, no. 1, pp. 51–60, 1993.
- [224] H. H. E. R. Yu and L. J. Fina, “Electric Field-Induced Dipole Reorientation in Oriented Nylon 11 by In Situ Infrared Spectroscopy,” *J. Polym. Sci. Part B Polym. Phys.*, vol. 34, pp. 781–788, 1996.
- [225] A. J. Lovinger, “Ferroelectric Polymers,” *Science (80-. )*, vol. 220, no. 4602, pp. 1115–1121, 1983.
- [226] N. C. Banik, F. P. Boyle, T. J. Sluckin, and P. L. Taylor, “Theory of Structural Phase-Transition in Poly(vinylidene fluoride),” *Phys. Rev. Lett.*, vol. 43, no. 6, pp. 456–460, 1979.
- [227] Y. S. Choi *et al.*, “Control of Current Hysteresis of Networked Single-Walled Carbon Nanotube Transistors by a Ferroelectric Polymer Gate Insulator,” *Adv. Funct. Mater.*, pp. 1–9, 2012.
- [228] J. W. Stout and L. H. Fisher, “The entropy of formic acid. The heat capacity from 15 to 300°K. Heats of fusion and vaporization,” *J. Chem. Phys.*, vol. 9, no. 2, pp. 163–168, 1941.
- [229] H. Wu, Y. Higaki, and A. Takahara, “Molecular self-assembly of one-dimensional polymer nanostructures in nanopores of anodic alumina oxide templates,” *Prog. Polym. Sci.*, vol. 77, pp. 95–117, 2018.
- [230] D. Q. P. G. de Gennes, F. Brochard-Wyart, *Capillarity and Wetting Phenomena*. New York: Springer, 2004.
- [231] L. H. A. S. L. Lai, J. Y. Guo, V. Petrova, G. Ramanath, “Size-Dependent Melting Properties of Small Tin particles: Nanocalorimetric Measurements,” *Phys. Rev. Lett.*, vol. 77, no. 1, pp. 99–102, 1996.
- [232] M. J. D., J. Lawrence, P. R. Bruce, B. H. E., R. Mike, and S. Steven, “Differential Scanning Calorimetry (DSC),” in *Thermal Analysis of Polymers*, Wiley-Blackwell, 2008, pp. 7–239.

- [233] A. Galeski, "Strength and toughness of crystalline polymer systems," *Prog. Polym. Sci.*, vol. 28, no. 12, pp. 1643–1699, 2003.
- [234] S. C. Mathur, J. I. Scheinbeim, and B. A. Newman, "Piezoelectric properties and ferroelectric hysteresis effects in uniaxially stretched nylon-11 films," *J. Appl. Phys.*, vol. 56, no. 9, pp. 2419–2425, 1984.
- [235] J. I. Scheinbeim, S. C. Mathur, and B. A. Newman, "Field-Induced Dipole Reorientation and Piezoelectricity in Heavily Plasticized Nylon 11 Films," *J. Polym. Sci. Part B Polym. Phys.*, vol. 24, pp. 1791–1803, 1986.
- [236] C. Ou *et al.*, "Fully Printed Organic-Inorganic Nanocomposites for Flexible Thermoelectric Applications," *ACS Appl. Mater. Interfaces*, vol. 10, pp. 19580–19587, 2018.
- [237] I. Katsouras *et al.*, "The negative piezoelectric effect of the ferroelectric polymer poly(vinylidene fluoride)," *Nat. Mater.*, vol. 15, no. 1, pp. 78–84, 2016.